Advanced laser based spectroscopic techniques for trace gas detection based on optical cavity enhancement and multipass absorption cells

Johnny Chung Leung Chu

A thesis submitted in partial fulfilment of the requirements for the degree of
Doctor of Philosophy

The University of Sheffield
Faculty of Science
Department of Chemistry

September 2015

Acknowledgements

It would not have been possible for me to complete this PhD without receiving some help along the way. I would like to thank these people specifically. I am extremely grateful for all the guidance and advice while working with Dr. Robert Salter during my first year.

I would like to thank Dr. Mark Stringer for all of his advice and support received during the second year, especially how to deal with difficult experimental apparatus (and yes, Mark, I am finally writing this thesis...).

It would not have been possible for me to participate in this learning experience without my supervisor, Dr. Michael Hippler, with his eternal patience and ability to put up with my clumsiness (apologies again for killing the QCL chip) and guidance throughout.

I would like to thank my parents for the support during this PhD and thank them for not forcing me to do a business oriented undergraduate degree and their continued support through the PhD, even if they do not understand what I did.

This PhD would not have been possible without the funding from EPSRC/University of Sheffield (DTA) and Smiths Detection Watford's sponsorship of the final stages the PhD.

Abstract

Spectroscopy is a fundamental part of Physical and Analytical Chemistry. In this thesis, three advanced experiments based on laser spectroscopy are introduced for the first time which address several experimental topics for trace gas analysis. The implementation of a diode laser based gas phase Raman detector is introduced, capable of parts per million (ppm) detection limits. The spectrometer features a low power laser diode (10 mW) which is enhanced by power build up in an optical cavity. This new technique is characterised by recording spectra of N_2, O_2, H_2, CH_4 and benzene.

A second advanced laser based spectroscopy technique for trace gas detection, mid infrared cavity enhanced resonant photoacoustic spectroscopy (mid-IR CERPAS) is set up and characterised. This scheme uses optical cavity power build-up, optical feedback stabilisation and resonant photoacoustics. A single-mode continuous wave quantum cascade laser is coupled to a three mirror V-shape optical cavity. Gas phase species absorbing in the mid-IR are detected using the photoacoustic (PA) technique. Mid-IR CERPAS was characterised by measuring acetylene (limit of detection 50 ppt) and nitromethane (0.8 ppb). The mid-IR CERPAS equipment was also used to detect explosives' vapours; TNT (1.2 and 5.5 ppb), 2, 4-DNT (7 ppb), TATP (4 ppb) and explosives' taggants such as DMNB (11 ppb). Significant interferences from ambient water in lab air are observed and are overcome. Normalized noise-equivalent absorption coefficients are determined as $\alpha \approx 6 \times 10^{-10}$ cm^{-1} s$^{1/2}$ (1 s integration time) and 6×10^{-11} cm^{-1} s$^{1/2}$ W (1 s integration time and 1 W laser power).

Finally, a near infrared Herriott cell enhanced resonant photoacoustic spectroscopy spectrometer is set up and characterised. This scheme uses enhancement from the absorption pathlength by a multipass Herriott cell and detection of the gas phase species by resonant photoacoustics, Herriott cell enhanced resonant photoacoustics, HERPAS. A single-mode continuous wave near infrared external cavity diode laser is coupled to a Herriott cell. Absorbing gas phase species are detected using the photoacoustic (PA) technique which was characterised by measuring acetylene (150 ppb detection limit at 100 ms integration time). HERPAS was extended to measure several toxic industrial gases including hydrogen sulfide, ammonia and carbon monoxide. Normalized noise-equivalent absorption coefficients are determined for H_2S as $\alpha \approx 5.3 \times 10^{-9}$ cm^{-1} $s^{1/2}$ (1 s integration time) and 1.6×10^{-10} cm^{-1} $s^{1/2}$ W (1 s integration time and 1 W laser power).

These three novel advanced spectroscopic techniques allow the detection of IR-inactive and IR- active gas phased species with great sensitivities and selectivity and improve significantly current capabilities for trace gas phase detection.

Abbreviations

CEAS	cavity enhanced absorption spectroscopy
CRDS	cavity ringdown spectroscopy
CERPAS	cavity enhanced resonant photoacoustics spectroscopy
CW	continuous wave
ECDL	Extended cavity diode laser
DFB	distributed feedback
F	finesse
FWHM	full width half maximum
i.d.	internal diameter
InGaAs	Indium Gallium Arsenide
InP	Indium Phosphorous
LD	laser diode
LOD	limit of detection (defined as 3σ)
kHz	kilohertz
MHz	megahertz
mbar	millibar

mV	millivolt
mW	milliwatt
NEDL	Noise equivalent detection limit (defined as 1σ)
NNEA	normalised noise equivalent absorption
pm^2	picometers squared
ppmv	parts per million by volume
ppbv	parts per billion by volume
ppt	parts per trillion (10^9)
Q factor	quality factor
QCL	Quantum cascade laser
TICs	Toxic industrial chemicals
μ	micro
V	Volt
W	Watt
τ	decay time

Table of Content

Acknowledgements ii

Abstract iii

Abbreviations v

Table of Content vii

1. Introduction 11

  Absorption Spectroscopy 12

  Beer-Lambert Law 13

  Multipass Absorption Cell 13

    Herriott Cell 14

  Cavity Ring-Down Spectroscopy 16

    Pulsed Cavity Ringdown Spectroscopy 18

    Continuous Wave Cavity Ringdown Spectroscopy 20

  Optical feedback stabilisation of diode lasers 23

  Cavity designs 24

  Photoacoustic detection 28

  Raman 32

    Wavelength and Intensity dependency 38

  Light Sources 39

    Fabry Pérot lasers 40

    Distributed feedback laser diode 41

Extended Cavity Diode Laser 41

2. Cavity Enhanced Raman Spectroscopy with optical feedback for gas phase analysis and spectroscopy 45

Introduction 46

Experimental 49

Results and Discussion 53

Hydrogen 55

Methane 58

Benzene 62

Nitrogen and Air 65

3. Mid-Infrared Cavity Enhanced Resonant Photoacoustic Spectroscopy 71

Introduction 72

Experimental 74

Description of the Experimental Set-up 74

Characterisation of the optical cavity 79

Tuneability of the Quantum Cascade Laser 81

Results 91

Detection of Acetylene by mid-IR QCL CERPAS 91

Detection of Nitromethane by mid-IR QCL CERPAS 97

4. Cavity Enhanced Resonant Photoacoustic Spectroscopy – Explosives’ Vapours 103

Introduction 104

Experimental 106

Mid-IR CERPAS measurements 110

Water interferences 110

Interferences from vapours such as ethanol and n-hexane 114

Measuring 2,4,6-TNT vapour in a static cell at 1 atm................................... 117

Measurements under flow conditions and reduced cell pressure.................... 119

Direct air sampling under flow conditions and reduced pressure................... 129

Sampling via Solid Phase Microextraction (SPME)...................................... 131

Sampling of solids or liquids via heated vaporization 133

5. Trace gas detection of toxic industrial chemicals (TICS) by Herriott- cell enhanced resonant photoacoustic spectroscopy (HERPAS).. 136

Introduction 137

Experimental.. 141

Description of the Experimental Set-up 141

Data collection 157

Results and discussion.. 158

Sensitivity and detection limits.. 158

Other Toxic Industrial Gases 170

Interferents... 171

External influences.. 185

Further Investigations... 196

Power dependency 196

Duty cycle... 197

Distributed feedback laser 199

Wavelength Calibration/Correction 203

6. Conclusion 207

CERS 207

Mid-IR CERPAS 208

HERPAS 210

7. Future Work 212

8. References 217

1. Introduction

There is an ever present need to detect and monitor trace gases in many real-life applications. Much scientific research focuses on atmospheric monitoring such as analysing the Greenhouse Effect, acid rain, destruction of ozone, air pollution including health and safety monitoring of industrial applications, process control and detection of illicit compounds.

An ideal gas sensor should be highly selective and sensitive with good accuracy and precision, able to identify and discriminate the chemical of interest and possesses qualities such as a large dynamic range, ease of use, reliability, robust construction and, small size. Such a sensor should be capable of multi-component analysis and be cost effective.

Trace gas detection can be performed with a variety of methods, which can be characterised as spectroscopic and non-spectroscopic methods. Most common spectroscopic techniques involve observing an absorbance of light in the IR region by the target compound. Non-spectroscopic techniques typically involve gas chromatography (GC) or mass spectrometry (MS). GC and MS are very sensitive techniques but have respective drawbacks. For GC, a pure carrier gas is required and can have a slow turn-around time for each data point whereas for MS, the samples have to be pre-treated and are expensive to purchase. In addition, a calibration sample is required in order to calibrate the GC which limits its practical applications beyond the laboratory environment. Alternatively, electrochemical gas sensors are available for specific gases, with a resolution in the ppm range. Such sensors are compact and power efficient. However, they suffer from a characteristic slow response time when they are first powered on as it can take up to several minutes prior to settling to the final output value. In addition, electrochemical sensors suffer from “poisoning” under long term exposure to the target chemical which results in reduced sensitivity over time.[1,2]

Absorption Spectroscopy

Direct absorption spectroscopy forms the basis of analysing atoms and molecules in the gas phase, yielding the frequency dependent absorption cross section and the absolute concentration. Conventional absorption spectroscopy typically measures the difference in the intensity of light before and after transmission through a sample using the Beer-Lambert law. The basic set up consists of three components: a light source, a method to differentiate the wavelengths and a detector. The light source used can be either monochromatic or broadband. For a broadband source, a tool is required to distinguish different wavelengths. For this task, a prism or grating is most commonly used. Alternatively, a tuneable monochromatic source, e.g. laser, can be used to record a spectrum due to their narrow wavelength range.

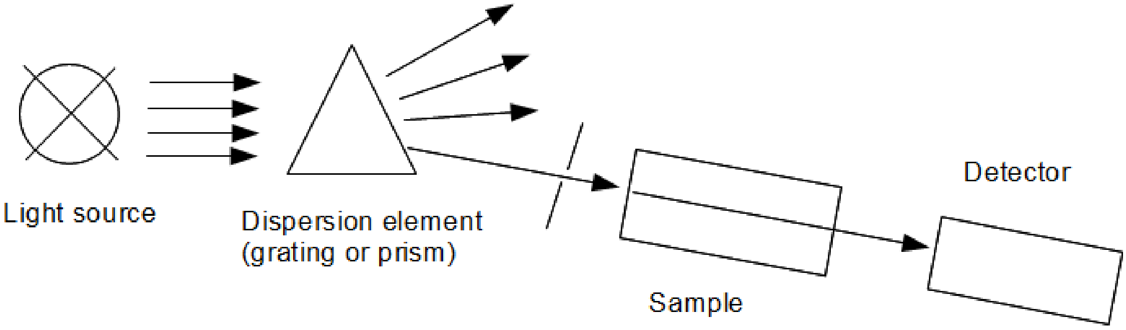

Figure 1 - A schematic of absorption spectroscopy for a broadband light source.

Beer-Lambert Law

The Beer-Lambert law defines the attenuation of light which is proportional to the concentration of sample (*N*) and the path length (L) of material travelled through while dependent on the material's specific absorption coefficient (σ).

$$I_{(t)} = I_0 \cdot e^{-\sigma.N.L} \qquad \textit{Equation 1}$$

The Beer-Lambert law has prerequisites that must be satisfied in order for it to be valid. Firstly, the incident light must be monochromatic and parallel. Secondly, the incident flux must not interfere with the atoms and molecules. Thirdly, the sampling species must act independently of each other. Fourthly, the sampling species must be homogenous in the interaction volume. Lastly, the sampling species must not scatter the radiation.

If any of these conditions are not satisfied then there will be deviations from the Beer-Lambert law and thus the logarithmic correlation between the transmitted and incident intensity is not obtained from the absorbing species.

However, in many practical cases these conditions are fulfilled and thus are applicable. The Beer-Lambert law is a simple model suitable for absorption of light by a dilute absorbing material which limits its practical applications.

Multipass Absorption Cell

As seen from the Beer-Lambert law (equation 1), it is possible to increase the sensitivity of detection by increasing either the concentration or the path length. Increasing the concentration is not always practical. For gas phase samples, the concentration is limited by the vapour pressure of the substance and thus increasing the optical pathlength is the sensible option. Pfund demonstrated a triple pass cell for atmospheric study in 1939.[3] The optical cell consists of a pair of spherical mirrors, separated by the focal length. Light for the source is focused through the centre hole of one mirror towards the facing mirror. The light is reflected twice before leaving through the centre aperture of the facing mirror. This design increased the pathlength somewhat but was soon surpassed by an alternative design by White,[4] now commonly referred to as the White cell. The White cell can be described as a descendent of the Pfund cell. It consists of three spherical mirrors where the input and output of the cell is at the same end as shown in Figure 2. The mirrors' separation is at the radius of curvature which is twice the focal length. The figure shows 4 passes, but this can be increased in increments of four passes. The large aperture of the light is maintained by the continual re-focussing by the spherical mirrors. This is particularly relevant for thermal light sources in the FTIR spectrometers which have a large aperture.

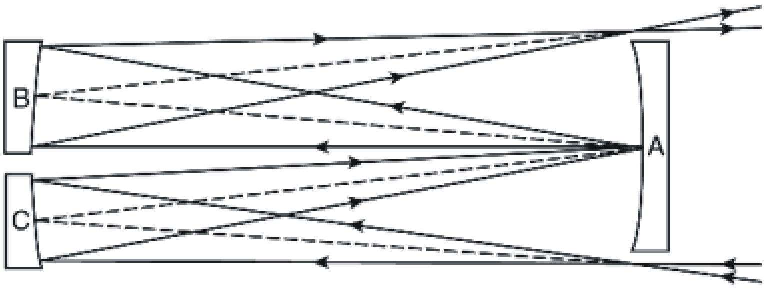

Figure 2 – Schematic of a White cell with the beam path shown. Image taken from Ref. 5.

Herriott Cell

With the advent of highly collimated light sources, higher numbers of passes were achievable with a Herriott cell. The Herriott cell $^{\text{design}}$ was first described in 1964.[6] It consists of a pair of opposing spherical mirrors where the light is injected through a hole in one mirror and is reflected back and forth between the two mirrors yielding typically an elliptical pattern of reflections (see Figures 3 and 4). Herriott cells were designed for optical absorption spectroscopy techniques where an exit hole is required to feed the outgoing light to a detector. A variant of the Herriott cell uses astigmatic mirrors instead of spherical mirrors, which causes a minor deviation to the reflected beampath.[7] The minor astigmatism can increase the optical pathlength significantly. It has been reported that pathlengths of up to 3000 metres are achievable at 1000 passes with mirror diameters of 7.5 cm.[8] The long pathlength reported utilised a "perturber", a mirror placed at the last reflection spot to start a new elliptical pathway. The beam strikes the perturbing mirror again, forming yet another elliptical axis (see Figure 3 and 4). In theory, it is possible to extend the pathlength as long as the reflection spots do not overlap with the entry or exit holes.

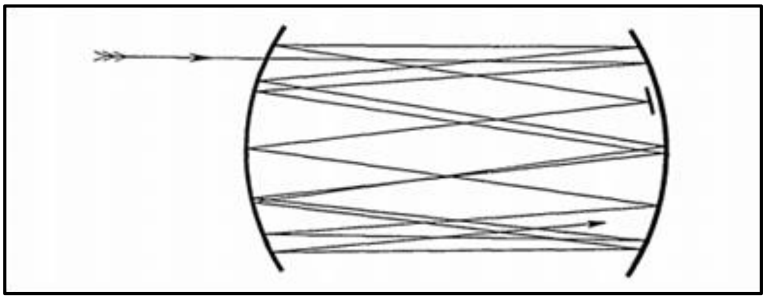

Figure 3 - Schematic showing the perturber mirror position and the reflected laser light.

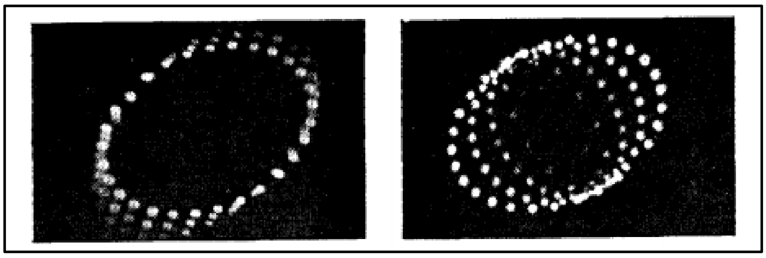

Figure 4 - Photographs depicting the multiple elliptical patterns on a mirror with perturber system. Left: The perturber expands the elliptical axis outwards from the axis. Right: The perturber shifts the elliptical pattern towards the upper right, reproduced from Ref. 8.

Other schemes of multipass cells have been reported such as toroidal/cylindrical multipass cells,[9,10] and multipass cells utilising cylindrical mirrors [11,12,13] instead of spherical mirrors.

Cavity Ring-Down Spectroscopy

Increasing the path length eventually leads to spectroscopy techniques which are able to accommodate multipass absorption cells such as White cells for FTIR, where light is reflected between a pair of mirrors typically tens of times yielding a maximum effective path length up to 100 m. Alternatively, light can be sent by a telescope towards a mirror several kilometres away which is reflected back and collected by a second telescope to a detector. This is known as Differential Optical Absorption Spectroscopy (DOAS).

An alternative approach giving the longest possible absorption path lengths is Cavity Ringdown Spectroscopy (CRDS). In the early 1980's, Herbelin *et al.*[14] devised a method to determine the reflectivity of mirrors. It was noticed that the measurements were dependent "on the ambient Pasadena air quality" which served as an indication of the extreme sensitivity to weak absorbers during their measurements at 514.4 nm (presumably NO_2 absorptions).[15] O'Keefe and Deacon[16] developed and presented the first CRDS experiment for spectroscopic absorption measurements and since then it has been utilised in numerous spectroscopic studies. The basic principle of CRDS is shown in Figure 5.

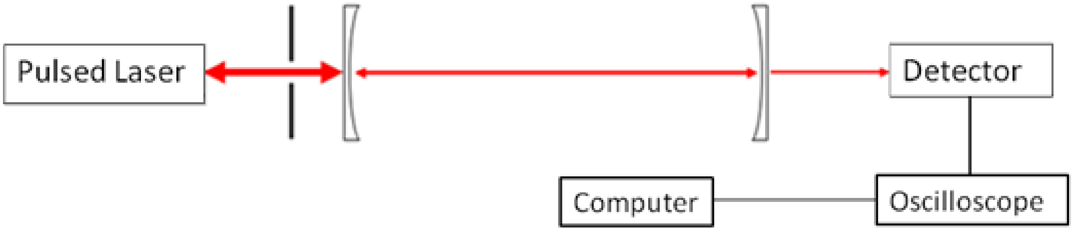

Figure 5 - A typical setup of a pulsed cavity ringdown spectrometer.

Light is coupled into the optical cavity composed of highly reflective mirrors (R > 99.9 %). The light that gets coupled into the cavity reflects back and forth within the cavity. The light is attenuated by absorption of the sample to an extent determined by its absorption coefficient (σ) as well as light leaking out from the mirrors due to imperfection in reflectivity. A perfect mirror (if it existed) cannot be used as it will not let light into the cavity. The light that leaks out is detected by the detector and is plotted as a function of time yielding an exponential decay with a time constant called the ringdown time. The higher the reflectivity the longer it takes the intensity to decrease. The ringdown time of the cavity can reach up to hundreds of microseconds which represent a path length of several kilometres (10 µs ≡ 3 km). In an empty cavity, the ringdown time is a single exponential decay determined by the reflectivity of mirrors and the optical path length between the mirrors. In a cavity with an absorbing species, additional loss is encountered; if the absorption follows the Beer-Lambert law, the result is still a single exponential decay with a higher decay rate or shorter ringdown time.

In a CRDS experiment, the ringdown time is measured from the time dependent intensity of light. In a linear cavity composed of two mirrors,

$$I(t) = I_0 \cdot e^{(-kt)} \qquad \textit{Equation 2}$$

$$k = \frac{(1-R)c}{l} + \sigma[A]c \qquad \textit{Equation 3}$$

where k is the decay rate, R is the reflectivity of the mirrors, c is speed of light, l is the length of the optical cavity, σ is the absorption coefficient and $[A]$ is the concentration of absorbing species.

The decay rate is separated into two segments. Firstly, it gives the decay rate of the empty cavity, *(1-R)c/l,* which is solely determined by the reflectivity of the mirrors and represents the baseline in the absence of an absorbing species. Secondly, it accounts for the additional attenuation from the absorbing species. The absolute absorption strength can be measured by subtracting the decay rate measured at absorbing frequencies from the rate at non-absorbing frequencies.

Pulsed Cavity Ringdown Spectroscopy

The first CRDS experiments were performed using pulsed laser sources, and pulsed CRDS is still widely used today. A typical pulsed CRDS involves a laser pulse, with duration shorter than the ringdown time, coupled into a linear cavity composed of two highly-reflective mirrors.

Pulsed CRDS has been performed in the IR,[17] visible[16,18] and UV[19,20] spectral regions. It can be applied as long as high reflectivity mirrors, fast response detector and tuneable pulsed lasers are available. The basic setup of pulsed CRDS is shown Figure 5 which consist of a pulsed laser, a ring down cavity, a detector, an oscilloscope and a computer. Pulsed lasers are typically available in the form of dye lasers and have high pulse energy. They cover the visible region and can also reach IR and UV regions via frequency doubling, mixing and Raman shifting.

The ringdown cavity consists typically of a pair of identical plano-concave mirrors. The radius of curvature of the concave mirrors is typically between 0.25 to 1 m placed in an optically stable configuration (see Cavity Design). Cavity lengths described in the literature vary greatly. For example, Berden *et al.*[21] reported a cavity length of just 3 cm while Le Grand and Le Floch[22] reported cavities with lengths up to 270 cm. The mirrors require alignment so that light is trapped in-between them and thus are placed in mounts which typically allow x and y directional movements. For measurements the cavity is built into an enclosure cell where the mirrors act as the entrance and exit points of the cell. It is not possible to have the cell inside the cavity as the reflection and absorption losses from the cell windows are too large which makes observation of the ringdown decay difficult.

The description above gives a somewhat simplified picture of CRDS. It implies that CRDS is independent of frequency but it is not because of cavity modes. An optical cavity is a kind of an etalon. Due to its boundary conditions, constructive interferences between reflections only occur if the cavity length is an integer multiple of the wavelength divided by two. A cavity can only support a number of longitudinal modes. Longitudinal modes are given by:

$$l = q\frac{\lambda}{2} \qquad \textit{Equation 4}$$

where l is the mirror separation, λ the light wavelength, and q is an integer. In practice, the mirror separation distance (l) is typically much greater than the wavelength of light and thus q is quite large (around the order of 10^4 to 10^6).

At very high spectral resolution, the cavity modes present a problem if a narrow absorption feature is between two cavity modes. In this case, this feature might be missed in a spectrum.

Pulsed lasers are characterised by the time bandwidth product, essentially derived from Heisenberg's energy/time uncertainty principle. The spectral bandwidth domain of the laser is directly related to the time domain of the pulse which means the shorter the pulse width, the larger the spectral bandwidth will be.

In order to get a smaller frequency domain, for spectroscopy at the highest resolution, one could utilise a continuous wave laser which by definition has a much smaller wavelength distribution (bandwidth) as the time domain is nominally infinite.

Continuous Wave Cavity Ringdown Spectroscopy

CRDS performed with continuous wave (CW) laser is known as CW CRDS in the literature, but is in fact not strictly a CW technique, because in order to observe an exponentially decaying light intensity within the cavity, the laser has to be switched-off at some point.

CW CRDS utilises a CW laser source instead of a pulsed one. The laser spectral bandwidth (also known as spectral resolution) is much smaller (typically on megahertz scale), which allows spectroscopy at highest spectral resolution.

Whether pulsed or CW CRDS is used depends on the application. For large wavelength range scanning, pulsed dye lasers are more practical since they usually span a much larger wavelength range than standard CW lasers. Their wavelength range in the visible can be extended by nonlinear processes like frequency doubling, mixing and Raman shifting into the UV and the IR regions. In contrast, CW lasers are only available at some limited wavelengths, and they can only be scanned over a relatively small wavelength range. CW laser diodes are relatively inexpensive, have relatively low power consumption and usually do not require any involved cooling using water chillers. An advantage of CW CRDS is the higher repetition rates that can be achieved compared to pulsed laser systems which typically run at 10 Hz pulse repetition rate. Another advantage is the increase in energy build up within the cavity which results from the longer time the laser can interact with the cavity and fill it with light energy. This higher laser power available within the cavity results in higher light intensity reaching the detector. This improves the signal to noise ratio on the ringdown curves and thus improves the sensitivity.

The experimental setup of CW CRDS is analogous to pulsed CRDS. CW light is coupled into the optical cavity consisting of a pair of highly reflective mirrors. Due to the smaller bandwidth and the longer coherence length of a CW laser, care must be taken to ensure only one mode is excited in the cavity, i.e., the cavity length must be an integer multiple of the laser wavelength divided by two (equation 4). If this resonance condition is achieved, light intensity builds up inside the cavity until, at equilibrium, as much light is leaking out of the cavity as is fed into it. In order to observe the ringdown decay in the optical cavity, the light intensity has to be monitored. A rise in intensity shows that the resonance condition is achieved, and the laser has then to be switched off rapidly by a fast switch such as an acousto-optical modulator. The light emitted from the cavity mirrors can be recorded and gives an exponential decay as shown in Figure 6. To monitor the energy build up, one could record the light leaking out of the cavity. When the light intensity exceeded a preset threshold, the laser light could be “switched off” via the use of an acousto-optical modulator and data acquisition of the decay curve triggered. The signal to noise ratio is higher than that of pulsed CRDS due to the increase in spectral resolution from the smaller bandwidth and the single mode coupling resulting in higher light intensities.

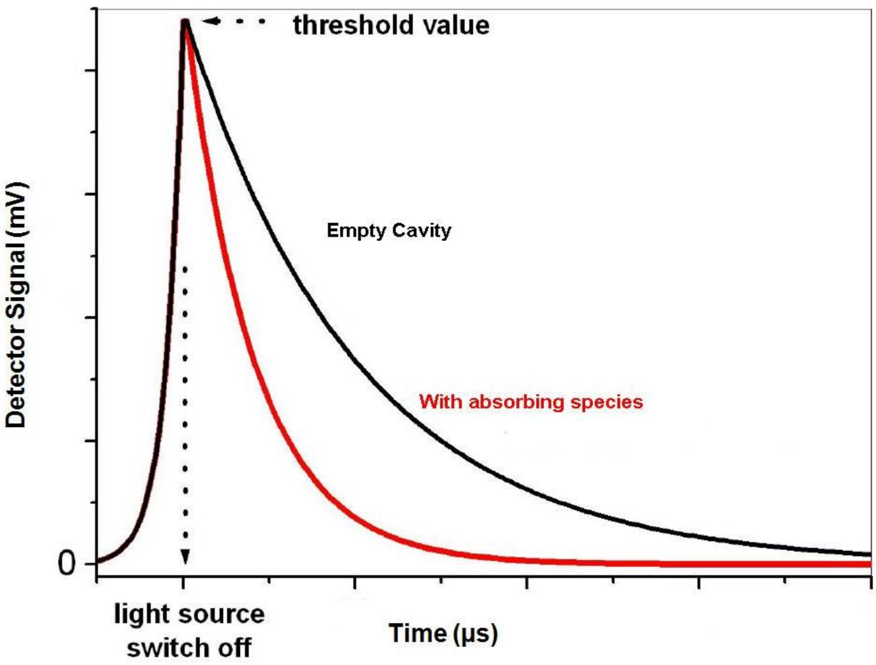

Figure 6 - Chart to show the difference in exponential decays between an empty cavity and one with an absorbing species from Ref. 23.

A fundamental problem encountered in CRDS is the difficulty in achieving a stable single mode coupling and stable energy build up. Anderson *et al.* originally did not stabilise the cavity and used randomly coupled light.[15] When the intensity reached a certain threshold, the laser was modulated by a Pockels cell and the data acquisition was started.[15] The initial performance was not great but was enough to stimulate interest in the field. More recently, active and passive stabilised cavity designs were applied successfully. Several research groups measured CW CRD absorption spectra, using passive stabilising techniques, by scanning the cavity length with a piezoelectric transducer until an optical resonance was found.[24,25,26] This allowed the cavity to be in resonance with the laser which increases the repeatability and reproducibility. An electronic feedback circuit was introduced to provide a correction voltage to the piezoelectric transducer to keep the optical resonance in the middle of the periodic modulation. Using this method, Romanini *et al.* were able to measure an overtone of C_2H_2 and achieve a sensitivity of 10^{-9} cm^{-1} at around 570 nm.[24]

It is also possible to scan the cavity without the need of an external optical switch. Hahn demonstrated such an approach where first the cavity mode is swept into resonance with the laser by changing the cavity length with a piezoelectric transducer.[27] After the observed light intensity reached a preset value, a voltage is sent to the piezoelectric transducer to move the cavity out of resonance by a quarter wavelengths within a microsecond. This moves the cavity mirrors out of resonance very rapidly which effectively replaces the fast external optical switch.[27] This approach is known as a cavity length modulation.

CRDS has the potential for highly sensitive absorption measurements and is widely used for detection of trace gas species. This has been demonstrated in the atmospheric monitoring of gases (ethene,[28] nitrogen dioxide,[29] acetylene[30]), aerosol extinction and absorption,[31,32] radicals in flames,[33] dissociation of molecules[20] to list a few. For a more in depth review of CW CRDS and CEAS please refer to reference [34]

Optical feedback stabilisation of diode lasers

Optical feedback occurs when a portion of the laser light is reflected back to the source by an external reflective surface. The optical feedback can enhance longitudinal mode selection which can be used to narrow the laser's spectral width. However, it can also "degrade the modulation response characteristics and increase intensity noise".[35] An example of unwanted optical feedback is present in the linear cavity, where the majority of light is directly back reflected by the first entry cavity mirror to the diode laser. The back reflected light will have no effect on the spectral width and will possibly damage the diode laser. An example of wanted optical feedback is light exiting the cavity. This will “seed” and stabilise the laser to lase at the exact wavelength required for the cavity. This will be beneficial as it would stabilize the laser coupling into the cavity which is important because diode lasers are intrinsically unstable, with fluctuating wavelength.

Cavity designs

For any cavity with two mirrors having the same radius of curvature to be stable, the cavity length (*d)* has to be within a certain range of the radius of curvature *(r)*. The relationship between the cavity length and radius of curvature for a stable cavity is shown below:

$$0 < d < r \qquad \textit{Equation 5}$$

or

$$r < d < 2r \qquad \textit{Equation 6}$$

In a stable cavity, light will be trapped within the cavity. A stable cavity is also more robust against misalignments. A special case exists for where the cavity length is equal to the radius of curvature. This is known as the confocal cavity and has the advantage that any direction of light coupled into the cavity will retrace its path due to the focusing effect from the curvature of the mirrors.

For cavities with two mirrors with different radius of curvature, it is customary to define a “resonator *g* parameter”, g_1 and g_2 to describe the laser resonator. These parameters are given by:

$$g_1 \equiv 1 - \frac{1}{r_1} \qquad \textit{Equation 7}$$

$$g_2 \equiv 1 - \frac{1}{r_2} \qquad \textit{Equation 8}$$

By using these two parameters, a resonator stability diagram can be plotted as shown in Figure 7.

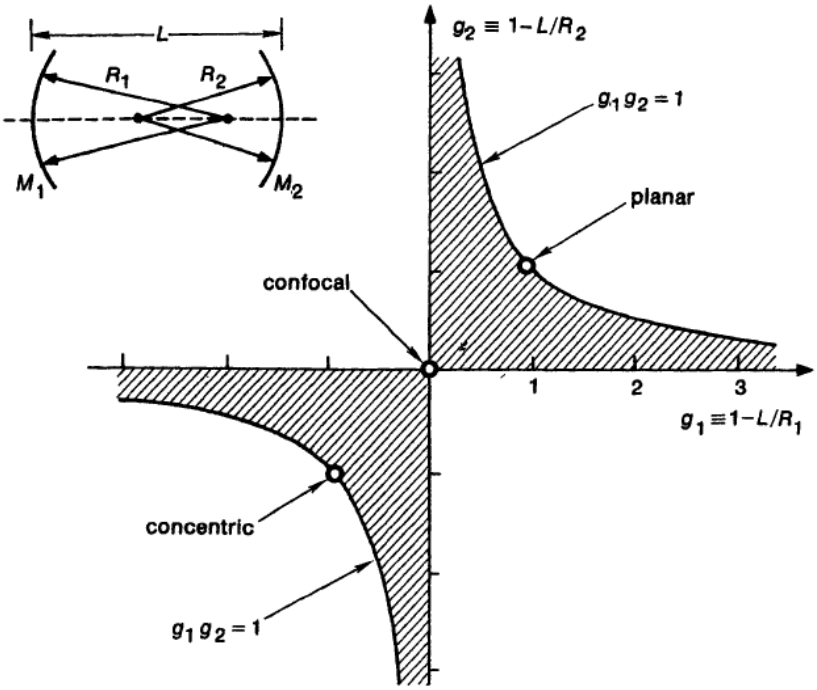

Figure 7 - A plot to show the stability regions of a two mirror optical cavity from Ref. 36.The shaded area represents the stable regions.

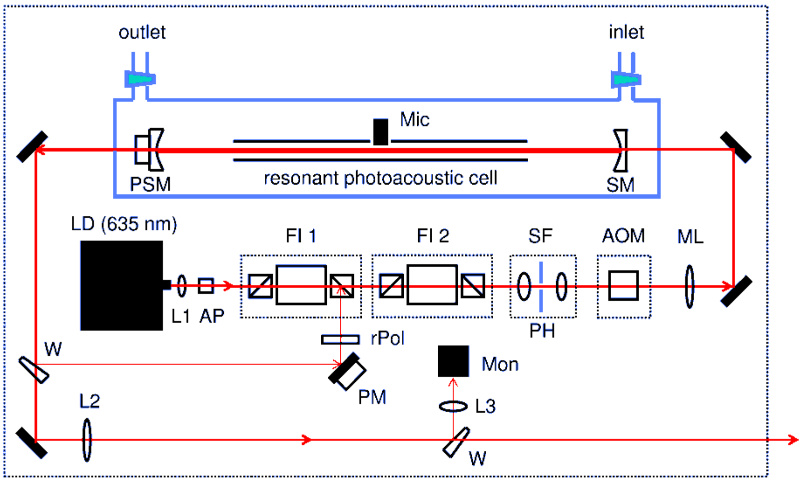

Figure 8 - Scheme of the 635 nm diode laser CERPAS experiment from Ref. 37 showing a linear optical cavity and Faraday isolators **FI** to avoid direct back reflections into the diode laser **LD**.

In most cavity enhanced experiments, a linear cavity with two mirrors is used, as shown for example in Figure 8 for the previous 635 nm cavity enhancement resonant photoacoustic experiment (CERPAS) in Dr Hippler's lab.[37] There are several advantages of a linear cavity, only two expensive high-reflectivity mirrors are used, the alignment is generally easier than other cavity designs such as ring, triangular, etc. However, there is an unwanted direct back reflection from the first cavity mirror, going straight back to the diode with high intensity. This is likely to damage the diode and will cause unstable operation due to unwanted optical feedback. Optical feedback from inside the cavity may be beneficial, because it stabilises the laser to the wavelength of the cavity, but other reflections are always to be avoided. For a linear cavity, these direct back reflections can be blocked by Faraday isolators which essentially transmit light only in one direction. To our knowledge, no Faraday isolators are available in the mid-IR, or if so, only at great expense. Also, it was not clear at the start of the project whether the QCL can accept any optical feedback, or whether the chip would be damaged by even small amounts of feedback. In the initial phase of the project, a study of alternative cavity designs which completely avoid direct back reflections using a 780 nm diode laser was performed.[38]

Non-linear optical cavities with a triangular beam path avoid direct back reflections (see Figure 9).[26] The back reflection from the first mirror (the entrance mirror) is reflected at an angle, and can be trapped by an iris or a beam dump. There are also no back reflections from the inside of the cavity, so there is no optical feedback in this design. If optical feedback from light inside the cavity is required for optical stabilisation, a mirror outside one of the exit cavity mirrors can reflect light back into the cavity and into the laser. As an advantage, the intensity of this feedback can be easily adjusted by an attenuator between the exit cavity mirror and the reflecting mirror outside the cavity. This design works quite well, but it has distinct disadvantages: it is not compact but uses quite a lot of space, so it would be difficult to put it into an enclosure. In addition, the angle of incidence on the high reflectivity mirrors is far way from 0° for which they are usually designed and specified, compromising their performance.

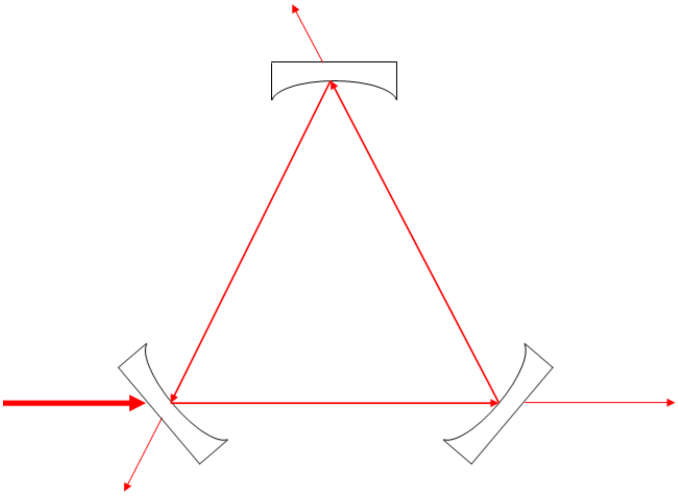

Figure 9 - Three mirror equilateral triangular cavity.

V-shaped cavities have the advantage that they are more compact and that the angle of incidence is much closer to 0°. In a particularly simple configuration, only 2 mirrors are required provided the cavity is confocal (see Figure 10). The direct back reflection is at an angle and can be blocked by an iris. Reflection from inside the cavity will go back to the laser and can be used for optical feedback and locking of the laser to the cavity. This cavity design has been reported in the literature before,[39] but it turned out to be very impractical and difficult to align; in particular the distance of the two mirrors is very critical in order to have a perfect confocal cavity. The design is unstable due to the confocal requirement. In view of these difficulties, it was decided not to pursue this design any further.

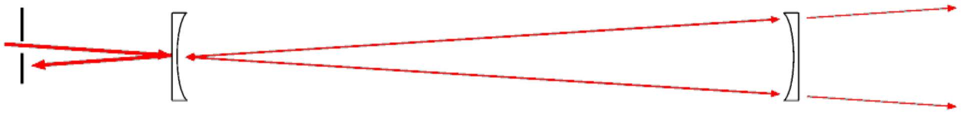

Figure 10 - Confocal two-mirror V-shaped cavity.

A V-shape cavity with three mirrors [40,41] does not have to be confocal, and it allows additional independent alignment of the third mirror (see Figure 11). The design is quite compact, and the angle of incidence on the cavity mirrors is 0° for the two exit mirrors, and close to 0° for the entrance mirror of the cavity. Direct back reflection is avoided, but optical feedback from within the cavity is still possible. The design proved to be very stable and easy to align.

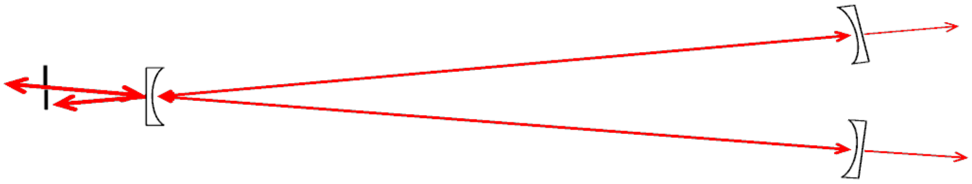

Figure 11 - Three-mirror V-shape cavity, as used in the present work.

Photoacoustic detection

The photoacoustic effect was discovered in solids by Alexander Graham Bell[42] in 1880 using a photophone. Soon, the photoacoustic (PA) effect was also discovered in liquids and gases by Bell *et al.*[43], Tyndall *et al.* [44], Rontgen *et al.*[45] and Preece *et al.*[46] Bell also described the principle of resonant photoacoustics. The basis of the photoacoustic effect is that a sound is generated when a material is illuminated from a modulated or pulsed light source. Molecules absorb light and are excited to higher electronic, vibrational and rotational states. The excited molecules then lose their energy by radiation (fluorescence), and/or by collisional deactivation. The excited molecules collide with other molecules, which converts the absorbed energy to heat. The localised transient heating and expansion generates a thermal and acoustic wave and the acoustic wave is picked up by a microphone. The process is shown in Figure 12.

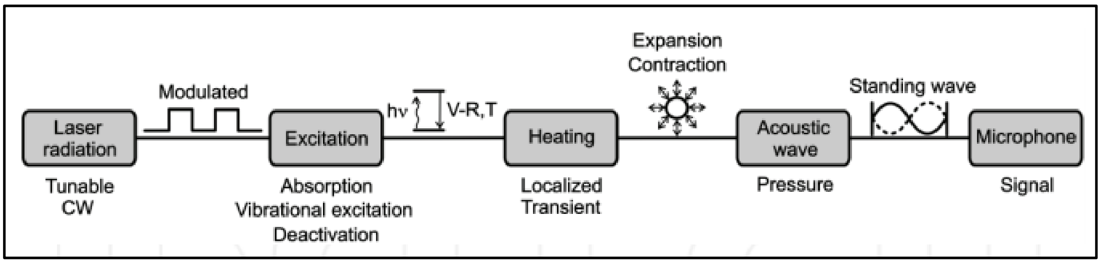

Figure 12 - Schematic of the physical processes for optical excitation of molecules in photoacoustic spectroscopy

The photoacoustic signal S can be expressed as:

$$S = C \cdot P \cdot \alpha \qquad \textit{Equation 9}$$

Where C is the instrument constant (or cell constant), P is the optical output power and α is the absorption coefficient which is defined as:

$$\alpha = \sigma \cdot c \qquad \textit{Equation 10}$$

where σ is the absorption cross-section and c is the concentration of the target gas. From equation 9, it is possible to see that there is a linear relationship between the photoacoustic signal and the sample concentration. The minimum detectable optical absorption coefficient α_{min} with a photoacoustic based sensor is typically defined as $S = N$, where $N$is the noise level. This allows us to define the minimum detectable or noise equivalent concentration c_{min} as:

$$c_{min} = \frac{\alpha_{min}}{N.\sigma} \qquad \textit{Equation } 11$$

In the present work, the limits of the detection (LOD) are defined as the 3 times the noise limits for each compound. The instrument constant C is dependent on the cell geometry, size and modulation frequency, the sensitivity of the microphone/transducer and the quality factor Q of the acoustic resonance which is defined as:

$$Q = \frac{f_0}{\Delta f} \qquad \textit{Equation } 12$$

wheref_0 and Δf are the resonance frequency and the half width of the resonance peak. The Q factor is a measure of bandwidth compared to the centre resonance frequency. Literature reports typical Q factors of 40 - 200 in longitudinal acoustic mode with resonant frequencies between 1 - 4 kHz.[47] A high Q factor system will be more selective compared to a system with a low Q factor as it will resonate over a much smaller frequency range. The width of the resonance peak is defined by the points where the amplitude is at 1/√2 value of the maximum peak value. Typically, in resonant photoacoustics, a cylindrical pipe is used to allow an acoustic resonance to be achieved which enhances the acoustic signal and increases sensitivity.

The development of lasers, monochromatic and collimated light sources allowed new areas of research into PAS. The first laser photoacoustic experiments were reported by Kerr and Atwood in 1960s.[48] High sensitivities of laser photoacoustics, in the ppb range, were demonstrated with CO_2 lasers, with the high optical output power (in the Watt range) and monochromaticity. In 1973, resonant photoacoustic spectroscopy with a Q-factor of greater than 100 was demonstrated by Dewey *et al.*[49] During the 1990s with the advent of semiconductor laser diodes operating in the near infrared range, accessing the ro-vibrational overtones, the flexibility of PA spectroscopy widened due to their reliability and modulation capabilities. Other new laser light sources such as quantum cascade lasers (QCL) and periodically poled lithium niobate (PPLN) optical parameter oscillators (OPOs) which operate in the fundamental infrared absorption spectral range (2.5 to 12 μm) have been developed and lower detection limits are reported. The increase in sensitivity is due to increase in absorption cross-section for the fundamental bands which can be several orders of magnitude larger than the overtone bands in the near infrared.

Photoacoustic spectroscopy is an inherently background-free technique as an acoustic contrast signal is detected (neglecting noise), only if an absorption occurs. This contrasts with the direct absorption techniques, such as Fourier transformed infrared spectroscopy (FTIR), where the background intensity must be monitored and the decrease in the intensity has to be observed. Photoacoustic spectroscopy requires a modulated or pulsed light source in order to generate an acoustic wave and detect an absorbing analyte. The modulated light enters the sample cell and is absorbed by the analyte. The optical absorption and the collisional energy transfer increases the temperature of the gas within the cell and leads to a periodic expansion and contraction of the gas at the modulation frequency. The pressure waves are picked up by a suitable sensor, e.g. capacitive microphones, silicon cantilevers,[50] microelectromechanical systems (MEMS),[51] quartz tuning forks.[52] The advantage of PA spectroscopy is that high sensitivity can be achieved in a relatively low volume. However, dependent on the light source used, acoustic noise from the environment or the laser itself limits its sensitivity due to unwanted pick up of acoustic noise.

Raman

An alternative spectroscopic technique to detect molecules is by Raman spectroscopy. The Raman effect was first experimentally observed and described in 1928 by Sir C.V. Raman in the liquid phase.[53] However, the theoretical principle of this effect was first predicted by A. Smekal.[54]

Raman spectroscopy involves an intense monochromatic incident beam passing through the sample. The monochromatic light is scattered into different frequencies which are recorded. This is given by the Bohr frequency condition.

$$h\nu = |E_1 - E_2| \qquad \textit{Equation 13}$$

E_1 and E_2 are the energies of two energy levels where a transition can occur. This relationship is typically expressed in terms of wavenumbers, $\tilde{\nu}$,

$$\lambda = \frac{c}{\nu} \qquad \textit{Equation 14}$$

where c is the speed of light. This equation is more typically expressed as wavenumbers, $\tilde{\nu}$, when used in spectroscopy.

$$\tilde{\nu} = \frac{1}{\lambda} \; or \; \frac{\nu}{c} \qquad \textit{Equation 15}$$

The unit of choice for wavenumber is the reciprocal centimetre (cm^{-1}). For Raman spectroscopy, the Raman spectra are presented as shifts from the incident light $\tilde{\mathrm{v}}_0$ and the scattered light is shifted with respected to it as given by:

$$\Delta\omega = \left(\frac{1}{\lambda_0} - \frac{1}{\lambda_1}\right) \qquad \textit{Equation 16}$$

where λ_0 is the incident light's wavelength and λ_1 is the inelastically scattered light.

Mie Scattering

"Mie scattering" of light is observed when the particles are comparable in size to the wavelength of the incident light, i.e. in aerosols particles or small droplets. The scattering gives no change in wavelength. The Mie scattering light intensity is much stronger than the Rayleigh or Raman scattering.

The Mie scattering has a strong angular dependency with preferential scattering into the forward direction of the incident light for small particles. Mie scattering can be used for particle sizing applications.

Rayleigh scattering

Rayleigh scattering occurs when the scatterers are small compared to the wavelength of the incident light, i.e. for gas phase molecules. The elastic scattering is called "Rayleigh scattering" where the wavelength is the same as the incident light. The scattering intensity is proportional to the intensity of incident light, a molecular dependent constant and the number density of scattering molecules.

Raman scattering

Raman spectroscopy is based on inelastic scattering of light. The spontaneous Raman effect can be explained via an energy diagram as depicted in Figure 13, using a simplified example, where the molecular system has two vibrational energy levels, the ground state, n = 0 and the excited state, n = 1. The energy separation is given as hv_m, where v_m is the molecular vibration frequency. The incident or excitation light induces a transition to a virtual energy level. The molecule can relax to the ground state via elastic (Rayleigh) or inelastic (Stokes and anti-Stokes) scattering.

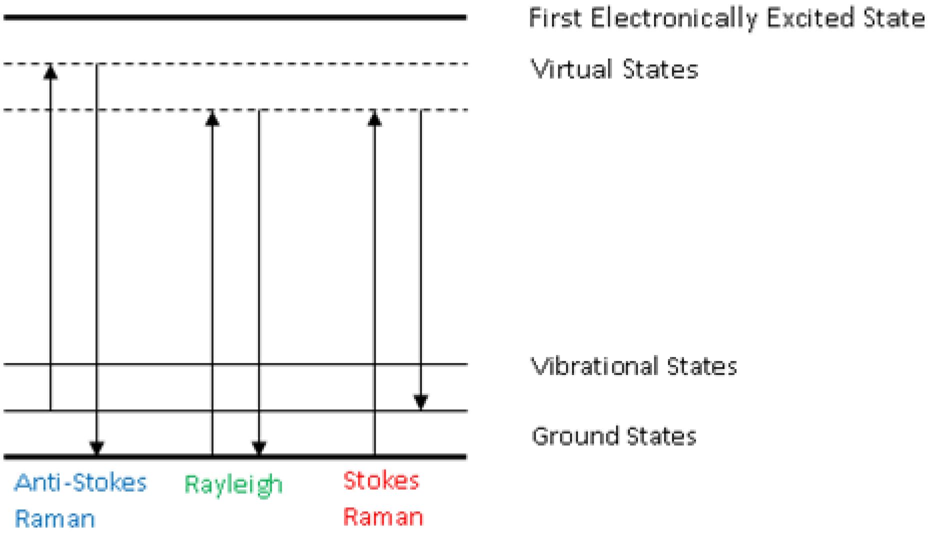

Figure 13 - A Jablonksi energy diagram for Rayleigh, Stokes and anti-Stokes Raman scattering

From the energy level diagram, it is possible to see that molecules can undergo inelastic scattering to give two different wavelength shifts, one where the energy gap is smaller, “Stokes shift” and one where it is larger, “anti-Stokes shift”.

The inelastic scattering from Raman scatting of molecules may be summarised as:

$$v_{Raman} = hv_L + \Delta E_{(vib,rot)} \qquad \textit{Equation 17}$$

where the $\Delta E_{(vib,rot)}$ is the energy difference between the initial state and the final state from the scattering process. Should the final state be higher than the initial state, there is a loss of energy of the released photon compared to the incident photon and thus $\Delta E_{vib,rot} < 0$. This is known as the Stokes Shift. On the other hand, should the final state be lower than the initial state, then $\Delta E_{vib,rot} > 0$ and this is known as the anti-Stokes shift.

The Stokes lines are much more intense compared to the anti-Stokes lines at room temperature due to the fact that anti-Stokes transitions can only occur when some of the molecules are already in a vibrationally excited state. At room temperature, the relative population between the ground state and the first excited state will mostly be close to 1, i.e., that most of the molecules will be in the ground state and only very few are in the excited state. The origin of the naming of Raman lines is from Stokes Law which states that the wavelength of the emission light must be higher than the wavelength of the incident light. The inelastically scattered light wavelength which followed the Stokes law were named Stokes lines and ones which did not were named anti-Stokes lines.

In order to observe any Raman scattering, there must be an induced electric dipole moment present. The molecular orbitals are distorted upon application of the electric field which is dependent on the square of the intensity. Alternatively, the polarizability of the molecule must change with the motions of the molecule, which can be expressed as:

$$\vec{P} = \alpha \cdot \vec{E} + \left(\frac{1}{2}\right) \beta \cdot \vec{E} \cdot \vec{E} + \left(\frac{1}{6}\right) \gamma \cdot \vec{E} \cdot \vec{E} \cdot \vec{E} + \cdots \qquad \textit{Equation 18}$$

where α, β and γ are tensors. A tensor is a group of numbers or functions which are transformed under a certain set of conditions when there is a change of coordinates, for example, an application of electric field in the *x* direction may produce a *y* or *z* component in the vector *P*, rather than just a parallel movement in the same direction as the applied electric field. The polarizability is typically approximated by the first polarizability tensor, α.

$$\vec{P} = \alpha \cdot \vec{E} \qquad \textit{Equation 19}$$

The electric field vector is assumed to be sinusoidal in nature,

$$\vec{E} = \vec{E}_0 \, cos(2\pi v_0 t) \qquad \textit{Equation 20}$$

This allows equation 20 to be rewritten as:

$$\vec{P} = \alpha \cdot \vec{E}_0 \, cos(2\pi v_0 t) \qquad \textit{Equation 21}$$

The polarizability tensor, α, can be expanded in a Taylor series:

$$\alpha = \alpha_0 + \left(\frac{\delta\alpha}{\delta Q_k}\right) Q_k + \cdots \qquad \textit{Equation 22}$$

which approximates the total polarizability along a given normal coordinate, Q_k.

The electric field vector was assumed to be a sinusoidal wave, Q_k then becomes:

$$Q_k = A_k \, cos(2\pi v t) \qquad \textit{Equation 23}$$

By substituting equation 23, back into equation 22, the polarizability tensor becomes:

$$\alpha = \alpha_0 + \left(\frac{\delta\alpha}{\delta Q_k}\right)_0 A_k \, cos(2\pi v t) \qquad \textit{Equation 24}$$

And substituting equation 24 back into equation 21 yields a fully expanded expression of the polarizability equation,

$$\vec{P} = \alpha_0 \cdot \vec{E}_0 \, cos(2\pi\nu_0 t) + \left(\frac{\delta\alpha}{\delta Q_k}\right)_0 A_k \cdot \vec{E}_0 \cdot cos(2\pi\nu t) \cdot cos(2\pi\nu_0 t) \quad \textit{Equation 25}$$

By using the product of the two cosines:

$$cos\,\alpha \cdot cos\,\beta = \frac{1}{2} cos\,(\alpha - \beta) + \frac{1}{2} cos(\alpha + \beta) \qquad \textit{Equation 26}$$

Then, equation 25 becomes:

$$\vec{P} = \alpha_0 \cdot \vec{E}_0 \, cos(2\pi\nu_0 t) + \frac{1}{2}\left(\frac{\delta\alpha}{\delta Q_k}\right)_0 A_k \cdot \vec{E}_0 \{ cos(2\pi t[\nu_0 - \nu]) + cos(2\pi t[\nu_0 + \nu])\}$$

Equation 27

The first term of equation 27 corresponds to the Rayleigh or elastic scattering. The second term contains the two shifts in frequency, $\nu_0 - \nu$ and $\nu_0 + \nu$. These new frequencies are the Stokes and the anti-Stokes shift.

Raman scattering occurs when a molecular vibration can change the polarizability. This change in polarizability is known as polarizability derivative. The selection rule for Raman is that there must be a change in polarizability when it undergoes a vibration, thus

$$\left(\frac{\delta\alpha}{\delta Q_k}\right)_0 \neq 0 \qquad \textit{Equation 28}$$

This selection rule defines that for a Raman transition to occur at least one component of the polarizability tensor must be non-zero. For a homonuclear diatomic molecule, a vibrational mode is Raman active as there is a change in the molecular polarizability when the atoms are displaced relative to each other.

For triatomic molecules, the selection rules mean that some vibrations may be Raman inactive. A homonuclear diatomic molecule has only one mode of vibration. For this molecule, there is no permanent dipole present in the equilibrium position due to the symmetry of the electron distribution. When the molecule undergoes a vibration, the symmetry does not change whilst the internuclear separations undergo small changes. This means that there is no dipole change and thus the vibration of a homonuclear diatomic molecule is IR inactive.

Wavelength and Intensity dependency

From the energy level diagram, it is possible to see that it is important that the excitation wavelength must be larger than the rotational/ vibrational energy levels spacings. However, it should not be resonant with higher energy states as other process such as fluorescence will be more efficient and mask the scattering signal (although being close to a resonance usually enhances the Raman effect). The non resonant requirement of the scattering processes means that the wavelength choice is not that important. This allows a wide variety of choice in laser wavelength from UV to IR. However, care must be taken to avoid accidental fluorescence since fluorescence is usually stronger than the Raman scattering, for example in the condensed phases typically 10^7 stronger.

The intensity of scattered light I_{scat} is dependent on the incident light intensity I_L as well as the wavelength as given in equation 29:

$$I_{scat} \propto C_m {\nu^4}_{scat} I_L \qquad \textit{Equation 29}$$

where C_m contains the information on the physical properties of the molecule, v_{scat} is the scattering photon frequency which for Rayleigh scattering is $v_{scat} = v_L$ but for Raman scattering it is $v_{scat} = v_L \pm v_{Raman}$.

From this equation, it can be seen that it is advantageous to use high frequency excitation wavelengths to increase Raman signals.

Light Sources

A blackbody radiator with an optical filter allows wide tunability over the IR region. This principle is demonstrated in filter based spectrometers. The fundamental absorption bands in the mid IR region can be reasonably covered by a blackbody radiator heated to 200 - 500 °C. The wide bandwidth of blackbody radiators allows multi-component analysis. This can be achieved with wavelength separation such as in FTIR spectrometers.[55] While blackbody radiators are suitable as a wideband light source, it is not energy efficient since intensity is so widely distributed. Lasers can offer higher spectral resolution, with more optical power per nanometre. Quantum cascade lasers (QCL) offer portable, power efficient mid-to far-IR laser light sources. QCL are semiconductor lasers which were first demonstrated by Faist *et al.* at Bell Laboratories, US, in 1994.[56] QCL are different to traditional semiconductor lasers which use interband transitions. QCL rely on intersubband transitions instead to generate the photons. Interband transitions in diode lasers rely on an application of current to populate electrons in the conduction band and light is emitted by the relaxation of these electrons into the holes of the valence band. The photon's energy is dependent on the difference in energy levels between the conduction and valence band. In intersubband transitions, electrons are injected into the conduction bands by applying a current. The electrons relax into lower energy level of the same conduction band. The transitions can occur multiple times which is typically dependent on the number of layers of the active material, also known as the superlattice. The intersubband transitions have the same energy levels and thus the same wavelength. This allows a much high optical power output, while maintaining single longitudinal operation.

Fabry Pérot lasers

Semi-conductor laser diodes are typically based on the Fabry-Pérot (FP) design which consists of an active medium enclosed within a pair of highly reflective facets.[57] The two facets are essentially an optical resonator which returns the stimulated photons back to the active medium to stimulate the emission of more photons of the same wavelength. The positive feedback will only occur if the separation of the facets is an integer multiple of the photon wavelength. This means that the laser will only support wavelengths which can fulfil the standing wave criteria. Each wavelength which can be supported by the optical resonator is called a longitudinal mode and in theory the resonator can support an infinite number of standing waves. However, in practice, the active medium can only provide gain within a small number of wavelengths. Thus, only wavelengths which are supported by the active medium and fulfil the standing wave criteria of the optical resonator will be radiated. Also, in order to lase, only the longitudinal modes where gain exceeds the loss of photons can generate laser emission. FP lasers provide "lump" feedback and thus, typically end up with a number of simultaneous longitudinal modes present in the emission spectra but they can support relatively high output power. However, the multimode nature of FP diodes makes them unsuitable for spectroscopic work as precise measurement of the wavelength is constantly required. Novel techniques such as multi-mode absorption spectroscopy have been reported which overcome the multiple emission wavelength issue with the use of modelling and fitting of expected absorption response profiles.[58,59,60]

Distributed feedback laser diode

A DFB laser diode is similar to a FP laser diode with the addition of a grating to prevent the emission of other than the desired wavelength. This forces the laser to operate in single longitudinal mode and even at high optical power output. DFB can be tuned a few nanometres by temperature tuning while maintaining single mode operation. Depending on the pulse length and current settings, one could chirp the laser to rapidly scan across a spectral range.[61]

Extended Cavity Diode Laser

External cavity diode lasers (ECDL) differ to FP laser diodes by replacing the fixed length optical resonator with a tuneable one. This is performed by coating one of the facets with an anti-reflection coating, resulting in reflectivity in the order of 0.1 %, and collimating the diverging light emission with a lens and a tuneable external mirror is used to complete the resonator. In theory, the tuneable mirror allows precise matching of the resonator to the laser’s emission so that emission is only supported at a single wavelength. In practice, further suppression of the interactivity optical feedback is required due to the presence of the intrinsic back reflection of the intra-facet light which affects the stability and spectral quality of the ECDL. This can be further suppressed by using an angled waveguide to intersect the AR coated facet at an angle to remove most of the unwanted feedback.[62] This reduces the effective reflectivity to below 0.01 %. This single-angled-facet gain chip gives the best possible performance for broadband tuneable ECDL.

The most common configuration, known as a Littrow configuration,[63] uses a diffraction grating to select the wavelength. Depending on the orientation of the grating, the first order light is reflected back towards the active medium to provide the positive feedback to stabilise the laser. The disadvantage of this configuration is that the output beam direction changes with the grating and is inconvenient for many applications. This can be avoided by allowing the output laser light to exit from the normal mirror of the gain chip.[64] To achieve this, the reflectivity of the mirror is typically reduced from 30 % to 10 %. Another variation of wavelength tuneable ECDL is the Littman-Metcalf design,[65] where an adjustable mirror, rather than rotating the grating, is used for the selection of the feedback wavelength. The light is collimated and then diffracted by a grating. The first order diffraction reflects off the mirror, back into the grating where it is diffracted for a second time before feeding back to the active medium. The two diffraction steps cause high losses, resulting in lower maximum output power. However, this design has higher side mode suppression yielding narrower linewidths. A schematic of an ECDL in the Littman configuration is shown in Figure 14.

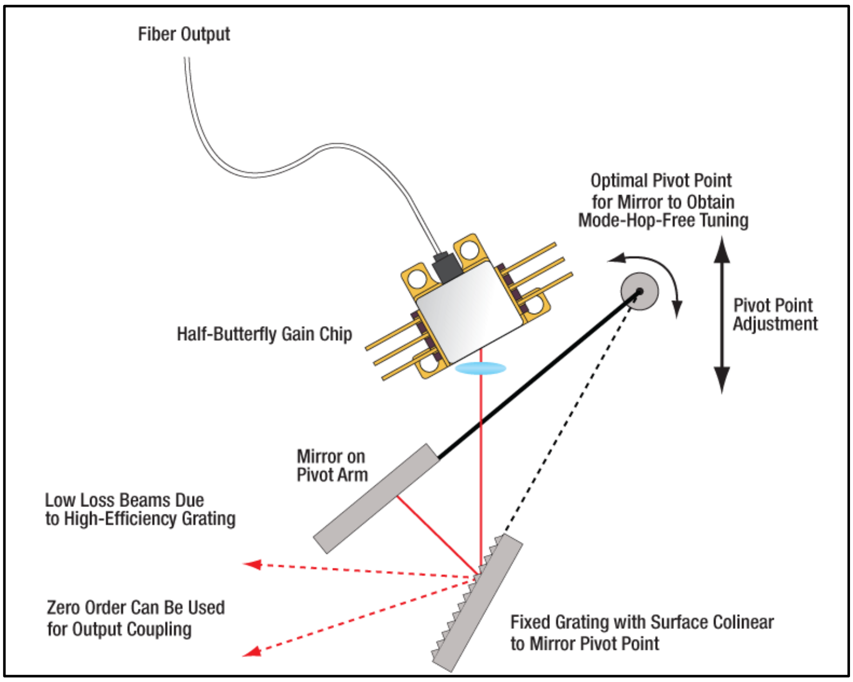

Figure 14 - Schematic of a fiber coupled ECDL in a Littman configuration – taken from Ref. 66.

This thesis aims to introduce several novel laser based spectroscopic techniques for sensitive detection of gaseous phases molecules using Raman, mid-IR and near-IR absorption spectroscopy. In Chapter 2, cavity enhanced Raman spectroscopy (CERS) with optical feedback will be introduced. In Chapter 3, mid-IR cavity enhanced resonant photoacoustic spectroscopy (CERPAS) is introduced with the experimental and results for detection of acetylene and nitromethane. Explosives' and taggants' vapours measured with mid-IR CERPAS are introduced in Chapter 4 along with introduction of the vapour generator (provided by Smiths Detection Watford Ltd). Near-IR HERPAS is presented in Chapter 5 along with measurements of various toxic industrial gases and chemical interferents as well as evaluation of extra influences. A summary of all of the work above is presented in Chapter 6.

2. Cavity Enhanced Raman Spectroscopy with optical feedback CW diode lasers for gas phase analysis and spectroscopy

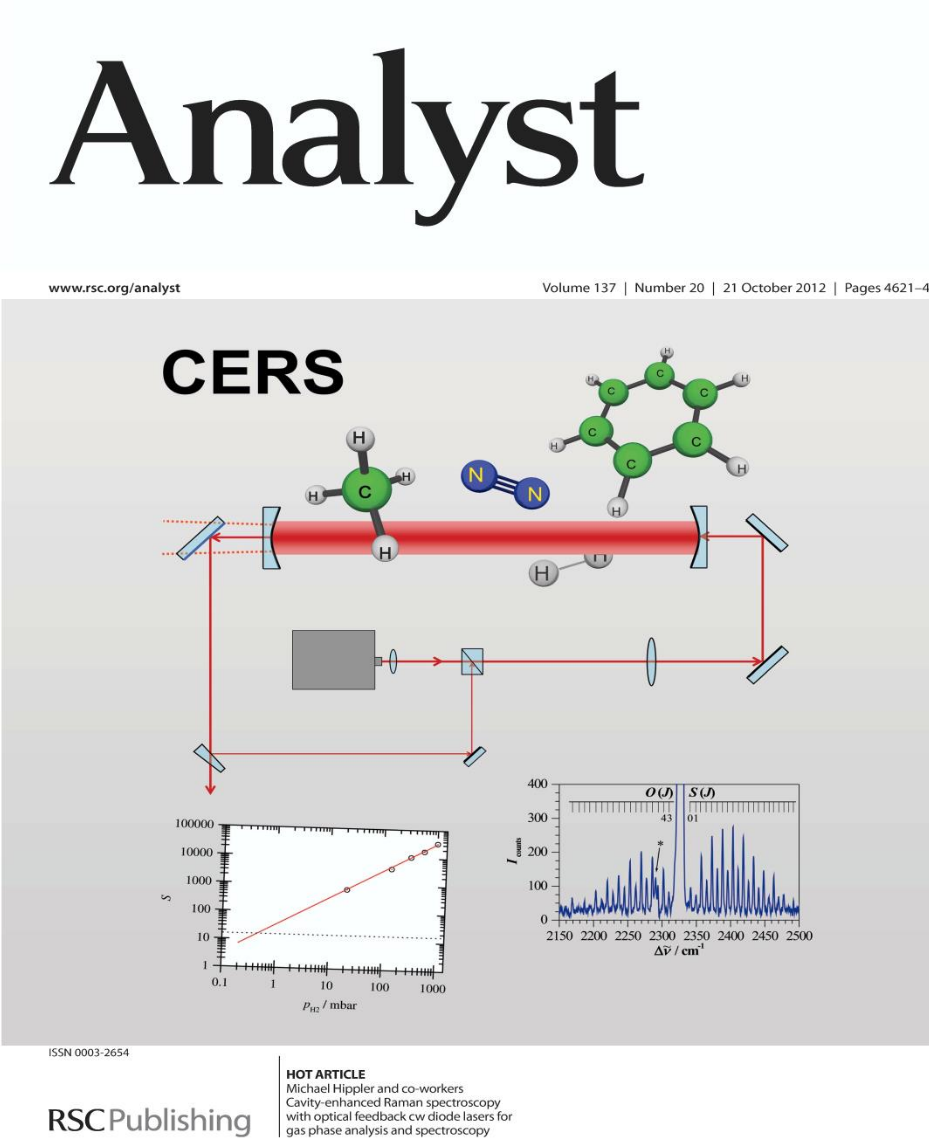

Analyst

www.rsc.org/analyst

Volume 137 | Number 20 | 21 October 2012 | Pages 4621–4

CERS

ISSN 0003-2654

RSC Publishing

HOT ARTICLE
Michael Hippler and co-workers
Cavity-enhanced Raman spectroscopy
with optical feedback cw diode lasers for
gas phase analysis and spectroscopy

The following work was published in *Analyst* 137 (2012), 4669-4676.

Introduction

Vibrational spectroscopy is a powerful method for quantitative analysis. For direct absorption techniques, molecules have high absorption cross section in the mid/far-IR. As discussed in the introduction, the light sources are not particularly efficient and IR absorption spectroscopy is insensitive to homonuclear diatomic molecules such as nitrogen, oxygen, hydrogen. One technique to detect these molecules is Raman spectroscopy but it is not widely used in the gas phase due to low cross-sections for spontaneous Raman scattering. More promising Raman schemes are based upon stimulated Raman spectroscopy techniques such as inverse Raman spectroscopy,[67] coherent anti-Stokes Raman spectroscopy (CARS), [68] or photoacoustic stimulated Raman spectroscopy (PARS).[69,70.] However, these techniques involve complex arrangements and require two different wavelengths from high power lasers.

As Raman signals scale linearly with laser power, the intrinsic low sensitivity of spontaneous Raman spectroscopy can be partly overcome by using higher power lasers. Another method is to place the Raman cell inside the laser resonator together with the gain medium. This utilises the highly effective laser power circulating within the laser cavity (intracavity laser Raman spectrometer).[71] Another method is to use an external optical cavity and use the build-up of power within the cavity. The simplest configuration for this would be the linear cavity, consisting of a pair of highly reflective mirrors placed in along the optical axis. The power build-up within the cavity can be of several orders of magnitude under optimal condition such as frequency stabilisation of the laser to the cavity, the efficient coupling of the laser to the cavity.[72,73,74,75,76,77] The power build-up within the optical cavity can be exploited to enhance the generation of spontaneous Raman signals (cavity-enhanced Raman spectroscopy, CERS).[78,79] The first practical applications, to our knowledge, include the work by Taylor *et al.*, who in 2001, stabilised a 1 W, 532 nm laser to a short, linear cavity by an electronic feedback mechanism, and observed Raman signals from hydrogen in a 90° collection geometry.[80] A Raman cell was placed inside the optical cavity, but the cell windows introduced significant optical losses, limiting the enhancement factor to around 50. Ohara *et al.* used an approach described previously by King, Pittaro and co-workers, where an antireflection (AR) coated laser diode is coupled into a linear cavity.[81] The laser diode as stabilised to the diode by the optical feedback from the back reflection of the cavity mirror. This in essence creates two separate optical resonators. The Raman signals were again collected at 90° collection geometry. By having the two separate optical resonators, theoretically speaking, it may appear difficult to have both in resonance simultaneously. However, it appears that several longitudinal modes are always coupled into the optical cavity and is actually quite difficult to select just one resonance. This negatively impacts on the spectral bandwidth of the apparatus to 30 cm^{-1} full width half maximum (FWHM), which is not satisfactory for gas phase spectroscopy. Li *et al.* reported the use of a multi-pass cell in a near confocal cavity coupled with a 200 mW laser.[82] The multi-pass cell in theory achieves more than 50 passes and actually yields a power build up of 9 W with a detection limit of 6 ppm for CH_4. It must be noted that the cavity scheme used there is different to the work presented before as it is a non resonant cavity.

In this work, we introduce a novel approach, where a standard 635 nm diode laser (without AR coating) is coupled into an external linear optical cavity. The laser is stabilised to the cavity by optical feedback from light exiting the cavity. Compared to previous approaches, this avoids direct back-reflections and allows better feedback control with single mode operation. Power build-up of light by three orders of magnitude occurs. Raman light is collected in a forward scattering collection geometry. After a detailed description of the experimental set up, the principle of cavity enhancement including the effect of mirror reflectivity within the Raman emission region is discussed, and the performance of the apparatus is characterised by recording Raman spectra of H_2, air, CH_4 and benzene vapour, showing that CERS is a powerful technique for sensitive, selective and quantitative gas phase analysis.

Experimental

The experimental scheme of cavity enhanced Raman spectroscopy with optical feedback CW-diode laser is shown in Figure 15.

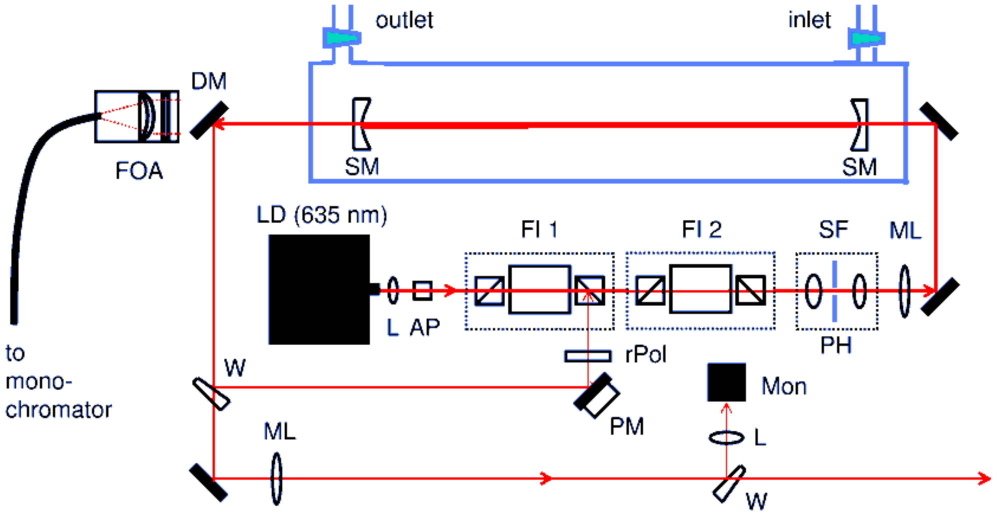

Figure 15 - Experimental scheme of cavity enhanced Raman apparatus.

The diode laser (HL6322G) lasing at 635 nm is collimated with an aspheric lens **L1** (focal length f =1.45 mm, 0.55 NA), and made circular by an anamorphic prism pair **AP**. After the anamorphic prism pair, the laser beam has a diameter of ca. 1.5 mm. The laser diode is mounted on a temperature stabilised mount (Thorlabs TCLDM9, Newton, NJ) and driven by an OEM diode current and temperature controller (Thorlabs ITC102). The diode is typically driven at 65 mA and at a temperature of 14.5°C, yielding 10 mW at 635 nm. The lasing wavelength can be changed by ca. 10nm by operating between 0 - 40 °C and fine tuned by adjusting the current. Two Faraday isolators **FI** (OFR, IO-3D-633-PBS, 30 - 36 dB isolation each) were used to provide optical isolation against back reflections to the laser diode. They also allow the controlled feedback by injection seeding via the exit polarising beam splitter cube of the first Faraday isolator. A mode matching lens (f=40 cm) **ML** couples the laser radiation in to the centre of the optical cavity. The optical cavity consists of a pair of high reflectivity mirrors **SM** (Newport Supermirrors, Irvine, CA, R > 99.99 %, 1 m curvature) in a linear configuration. The mirrors are separated at a distance of 35 cm and are assembled on an optical cage system (Thorlabs). After the cavity, there is a dichroic mirror **DM** (Semrock RazorEdge LPD01-633RS-25) which separates the pump light from the Raman radiation. Some of the 635 nm light is diverted back to the diode via the exit port of the FI by a glass wedge **W**. The feedback light is attenuated by a linear film polarisor on a rotating mount **roll**. To match the phase of the feedback light to the diode laser, mirror PM in the feedback loop is mounted on a low voltage piezoelectric actuator. The light exiting the cavity is made parallel by lens ML and directed in to photodiode by a glass wedge **W** and monitored by a photodiode **Mon**. It is possible to use the remaining light intensity for wavelength calibration but this was not used and is just blocked off. The optical cavity is enclosed in a vacuum tight glass enclosure with glass windows (BK7) with gas inlet, outlet taps and a vacuum gauge. This allows the gas cell to be filled with a gas mixture in a controlled manner or to allow the cell to be operated under gas flow conditions. The windows are mounted at a slight angle in order to reduce the back reflection. At future implementations the windows will be placed at Brewster’s angle to completely eliminate the issue.

In order to couple the laser light into cavity, the laser wavelength must be matched to a multiple of the cavity length. Two methods could be used to achieve this. Firstly, is to use cavity length modulation by mounting **SM2** on a stack of piezoelectric actuators which is driven using a positive offset modulation signal. This lengthens and shortens the cavity on a micrometre scale which at a certain point the cavity length must be a multiple of the laser’s wavelength. This method however has the disadvantage that the modulation signal cannot be too high frequency (<1 kHz) nor can the amplitude be too large as it may irreversibly damage the piezoelectric actuator. The alternative method is to use current modulation of the laser diode. As mentioned before, the lasing wavelength can be fine tuned by changing the current. In this case, the current was modulated around a fixed cavity mode (using a saw-tooth waveform at 1.5 kHz), the wavelength of the laser diode changes by the current modulation until it is locked into a longitudinal cavity mode by optical feedback. During the locking (resonance), the light intensity is coupled into the cavity (single mode) a power build up occurs. As the current modulation continues, the locking will be lost after some time. It is important to choose a suitable offset and modulation amplitude in order to get the resonance in the middle of the modulation waveform, giving a duty cycle of ca. 50 %. Compared to previous approaches,[78,79,81] this active optical feedback locking can be applied to standard laser diodes without AR coating, it avoids direct back-reflections and it allows better feedback control with well-defined single mode operation which is essential for highest spectral resolution.

An electronic feedback circuit (lock in amplifier and feedback loop based on Ref. 83, is employed to keep the optical resonance in the centre of each modulation period by constantly adjusting the diode current. If the optical resonance deviated from the middle of the modulation period, the lock-in amplifier produces an error voltage. This error voltage is smoothed (low pass filtering), integrated and amplified in a PI controller (proportional plus integral controller), the error signal is fed back as an offset to the injection current modulation to the laser diode driver. It is important to note that only that the same cavity mode is excited and that no scanning of the laser wavelength is required for Raman spectroscopy.

The phase matching of the feedback light to the diode laser is accomplished by a second electronic circuit (based on Ref. 84) which also provides an error signal controlling the PZT of the mirror PM. In perfect phase matching, the tuning from current modulation gives a perfect symmetrical transmission signal from the cavity. By differentiating and integrating the monitor signal, a perfectly symmetrical signal yields a zero error voltage. However, for an asymmetrical signal, it will yield a signed error signal. After smoothing, the error signal is integrated and amplified in a PI controller and fed to the PM until the transmission signal becomes symmetrical. The active optical feedback locking can be applied to standard laser diodes without AR coating as it avoids the direct back-reflections and better feedback control and a well-defined single mode operation, which is essential for spectroscopy at the highest spectral resolution.

The Raman scattered light passes through the dichroic mirror and into the optical assembly FOA. The light is filtered again by a Raman long pass filter (Semrock RazorEdge LPRE-633.0-S-25) to further attenuate the remaining 635 nm light and focused with a lens (f = 25.4 mm) into a 50µm multimode optical fibre with 0.22 NA. The fibre carries the Raman light to a monochromator and camera. In one experiment, a compact spectrometer was used (Ocean Optics USB4000) with 25 µm entrance slit, 1200 lines per mm holographic grating and 3648 pixel diode array CCD detector operating at room temperature. This yields a spectral range between 514-816 nm with a specified resolution of 0.57 nm at 600 nm. Using an excitation wavelength of 635nm, this corresponds to a Raman Shift of -3700 to +3500 cm^{-1}, with a resolution of 15 cm^{-1}. A higher performance spectrometer was also used (Shamrock 750 with Andor iVac CCD camera). The fibre was coupled using a pair of plano-convex lenses (f=35 mm after fibre, f=150 mm in front of entrance slit). The spectrometer has f =

750 mm focal length and F/6.5 and is typically used with a 120 µm entrance slits width. The spectrometer is equipped with 3 different gratings of different blaze (1200, 600 and 150 lines/mm, blazed at 750, 600 and 800 nm respectively). The CCD camera has 1650 x 200 pixels and pixel size of 16 µm x 16 µm and is typically cooled to -50 °C to reduce the thermal noise and to allow for longer integration times. The high resolution grating allows Raman shifts in intervals of 500 cm^{-1} to be measured with a resolution of 0.8 cm^{-1}. The calibration of the monochromator was performed using the emission from a Neon lamp.

Gases and vapours used for characterisation of the performance of the instrument include hydrogen (CK gas, N6.0 grade), methane (CK gas, 5.0 grade), benzene vapour (Sigma Aldrich 99.8 %, anhydrous) and standard lab air. Dissolved air in benzene was extracted by freeze-pump- thaw cycles. The other gases were used as is without further purification. The gas pressures with the cell are monitored with capacitance manometers (MKS Baratron, 1000 mbar and 100 Torr full range).

Results and Discussion

At 635 nm, the mirror reflectivity was determined as R = 99.988 %, in the linear configuration, by using the cavity ring-down measurement (exponential decay time of 9.87 µs). Using the optical feedback, including all the electronic controls, it is possible to couple the light into the cavity and power build up occurs typically at 1.5 kHz with a 50 % duty cycle. From previous experiments, it was estimated that the power build-up of the cavity was from 10 mW externally to 2.5 W inside the cavity. The Raman light is collected at a 0° forward scattering geometry. When compared to the 90° collecting angle, it is not possible to position the lens as close to the scattering medium but the light from the entire scattered medium is sampled thus resulting in a higher observed scattered signal. In the forward collection geometry, the scattered light has to pass through the cavity exit mirror. The transmittance of mirror can be seen in Figure 16, where it is possible to see that some Raman shifts are in the high reflectivity range of the mirror.

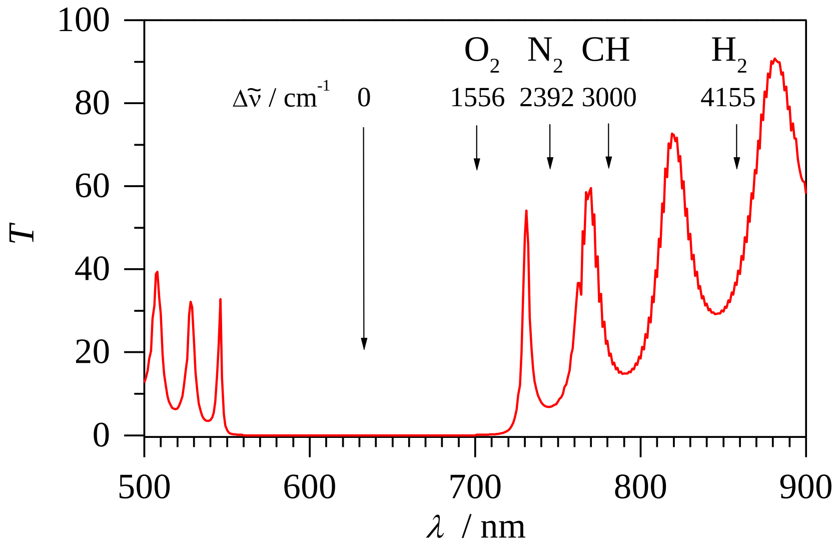

Figure 16 - Transmittance T of the high reflectivity cavity mirrors. The laser excitation wavelength and several Raman transitions are indicated with arrows.

For these Raman shifts, it was surprising that one could observe these transitions at all; however, the cavity effectively stores the light within cavity and it leaks out slowly. Even though 50 % of the forward scattered light will exit from the “wrong” mirror, thus lost for detection, the same amount is made up for from the backward scattered light which will reach the FOA from the reflection. In practice, there should be no loss of Raman intensity as long as there are no significant absorption losses from the mirrors or absorption from with the cavity. This was observed from the Raman transitions of the simultaneous sampling of N_2 and O_2, even though the respective reflectivity values are different.

Hydrogen

The cell was filled with one bar of H_2 at room temperature and a Raman spectrum was recorded using the high resolution grating (1200 lines/mm) over 50 seconds. Figure 17 shows the Raman spectrum of H_2.

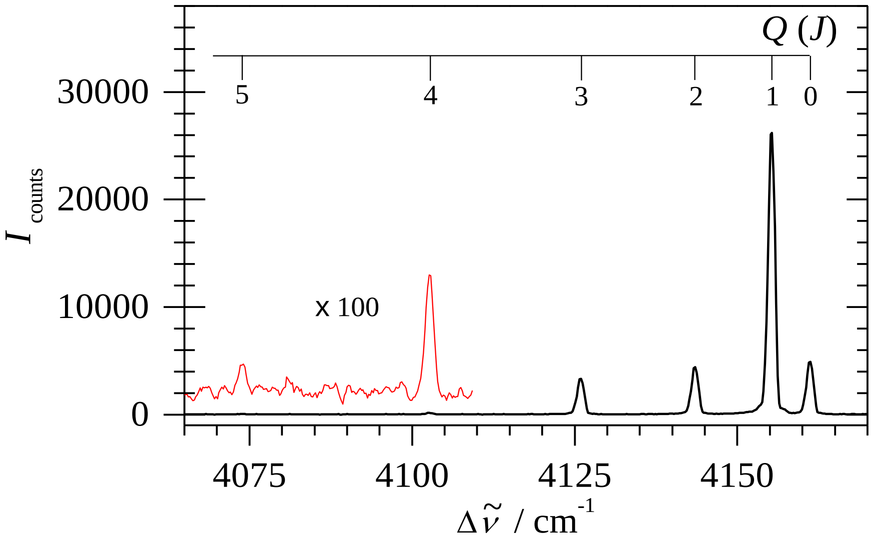

Figure 17 - Overview of Cavity Enhanced Raman spectrum of Hydrogen (1 bar H_2, 1200 lines/mm grating, 50 s integration). The red trace on the left is amplified by a factor of 100 to show the very weak Raman transitions more clearly.

The spectrum is dominated by the rotationally resolved *Q*-branch transitions of the vibrational fundamental (4161.14 cm^{-1}). The relative intensities of the recorded spectrum are in perfect agreement with the previously measured using photoacoustically detected stimulated Raman spectroscopy (PARS) of H_2.[70] There is a 3:1 intensity ratio between the odd and even J values caused by the ortho- and para-H_2 nuclear spin statistics. The strongest feature observable is the *Q*(1) line with a signal to noise ratio of approximately 1000:1 at 50s integration time. It is possible to observe the subsequent *Q*-branch lines up to *Q*(5), which has a term value of 1740.21

cm^{-1} above the ground state, J = 0, and is very weakly populated at room temperature.[85]

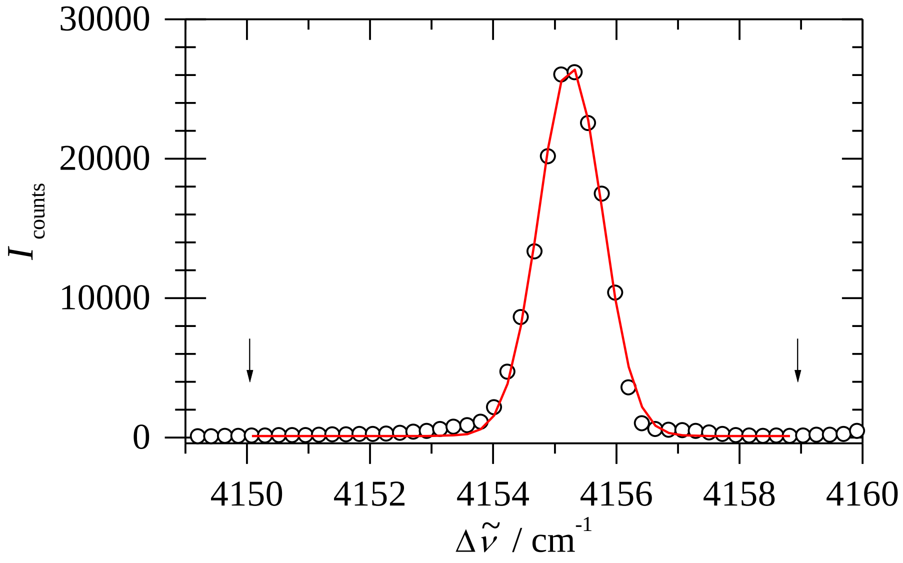

Figure 18 - *Q*(1) line of the H_2 Raman transition. The circles are the experimental data and the red line shows the Gaussian fit curve.

The *Q*(1) transition was fitted using a Gaussian line shape centred at 4155.25 cm^{-1} with a FWHM of 1.03 cm^{-1} as shown in Figure 18. The observed linewidth is due to the instrument bandwidth of the grating used. For quantitative analysis of the hydrogen concentration, the *Q*(1) transition was integrated and measured against pressure for use in a calibration plot. The use of peak area for quantitative analysis is limited by one difficulty, the determination of the baseline. It is a common procedure to “zero” the baseline of a region without any spectral features. However, this outcome of this technique is subjective to each user and difficult to perform especially at low concentrations where lower levels of signal to noise are observed. To overcome this, one could continue to integrate the peak area using a constrained Gaussian fitting (centre 4155.25 cm^{-1}, FWHM 1.03 cm^{-1}) with the area and the baseline as variables. The area given would be correlated to the pressure of the gas (hydrogen in this case) in a calibration plot. Using this procedure, no baseline manipulation is required. The cell was filled with different pressures of H_2 (1 bar to 21 mbar) and cavity enhanced Raman spectra were obtained. The calibration plots are shown in Figure 19. At 1 bar, the area under the Gaussian curve is 34988 +/- 332 counts per cm. In addition, 11 spectra of the empty cells were obtained and the observed standard deviation of the baseline is 16 counts per cm. This can be used to as an estimate for the noise level for H_2 detection. This gives a noise detection limit of 0.46 mbar for H_2 at 50s integration time and 10 mW excitation, equivalent to 460 ppmv in a gas mixture at 1 bar. Using longer integration times and a stronger laser source, it will be possible to lower the detection limits into the low ppmv or even ppbv range. A previously reported system, PARS, has a detection limit of 40 ppmv at 58 s detection time and 4.6 ppmv at 256 s. For CERS, using only a low powered laser diode, it is possible to use it for trace gas detection of H_2. The rotational level populations can give information about the temperature as well as the abundance of the ortho- and para-isomers of hydrogen. It is expected that other isotopomers of hydrogen will yield similar performances. A potential application is to detect the production of radioactive tritium gas for the nuclear power industry.

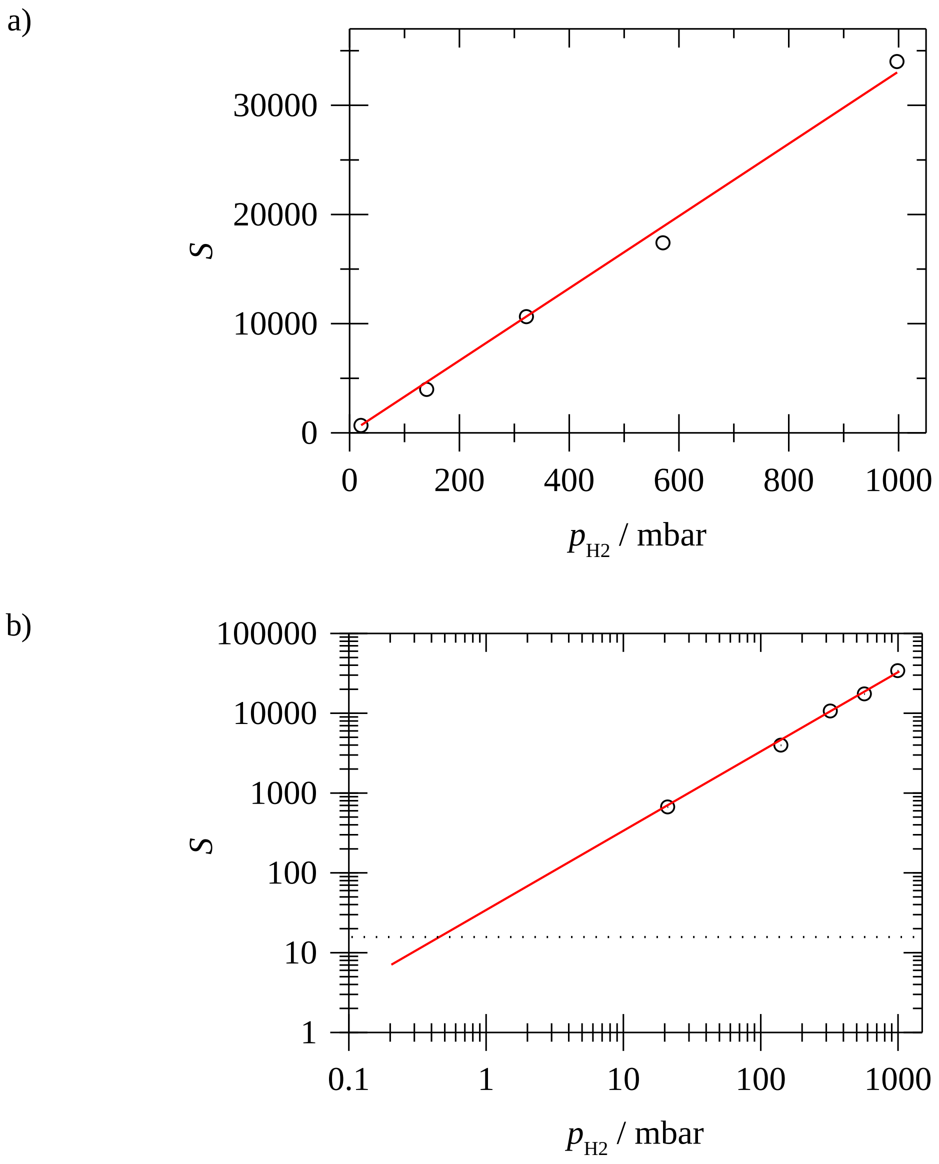

Figure 19 - Calibration plot of the integrated $Q(1)$ line of H_2 (S, arbitrary units; obtained by Gaussian fits) versus H_2 pressure. One standard deviation corresponds approximately to the symbol size used. a) Linear scale, b) logarithmic scale, including the noise limit of a 50 s spectrum (dotted line). The solid line is a fit line through the origin. The fit line intersects the noise limit at 0.46 mbar H_2

Methane

Methane is a tetrahedral molecule which is highly symmetrical (T_d symmetry).

Methane is the simplest hydrocarbon and is the main ingredient in natural gas. It is also produced from biological processes and is a significant contributor to the greenhouse effect after CO_2 and water. Methane has a complex rovibrational spectrum. The spectrum is complicated by the Rotation-vibration (Coriolis) interactions which spoil the simplicity of the highly symmetric molecule by lifting the degeneracy of rovibrational levels, and strong anharmonic Fermi resonances which couple CH-stretching and bending modes. [86,87,88,89,90,91,92] Methane has four vibrational modes described below. The vibrational levels are grouped into resonance polyads given below:

$$N = v_1 + v_3 \ + 0.5\ (v_2 + v_4) \qquad \textit{Equation 30}$$

where v_1 and v_3 represent CH-stretching and v_2 and v_4 CH-bending quanta. The CH-stretching fundamentals are near 3000 cm^{-1}, the CH-stretching fundamentals v_1 and v_3, the CH-bending overtones $2v_2$ and $2v_4$, and the combination band $v_2 + v_4$. The Raman spectrum in this region is dominated by the Q-branch of the totally symmetric v_1 band at 2917 cm^{-1}.

The Raman spectrum is dominated by the Q-branch of the v_1 totally symmetric CH stretching at 2917 cm^{-1}. A Raman spectrum from 2800 - 3050 cm^{-1} was recorded with one bar of methane, with the high resolution grating (1200 lines/mm) and a CCD camera integration time of 20s as shown in Figure 20a. The signal to noise ratio for the methane spectrum is excellent. The peak height for the Q-branch is 55530 counts whereas the noise level, as characterised as the standard deviation for the baseline region where there were no Raman transitions, is about 20 counts.

Looking beyond the strong transition at 2917 cm^{-1}, it is possible to see much weaker signals. These features are not noise but very weak ro-vibrational transitions. In Figure 20b, a weak transition of the F_2 component of v_3 near 3020 cm^{-1} is shown with a simulated Raman spectrum obtained from the STDS program with the molecular parameters from the Dijon group. In the simulation program, the room temperature was assumed to be 296 K, and the stick spectrum was convoluted with a Gaussian line shape with 1.1 cm^{-1} FWHM. The 1.1 cm^{-1} FWHM is chosen as it is the specified resolution of the monochromator grating used. There is a very good agreement of the Raman transitions intensities between the recorded (2650 - 3110 cm^{-1}) and stimulated spectra. However, occasionally, there are some differences in intensities observed for some very weak transitions. These deviations may be caused by isotopomers of methane, imperfections in modelling of low Raman transitions or from yet to be characterised methane Raman transitions. This shows that CERS has the potential to refine the theoretical analysis of methane transitions and ro-vibrational energy levels.

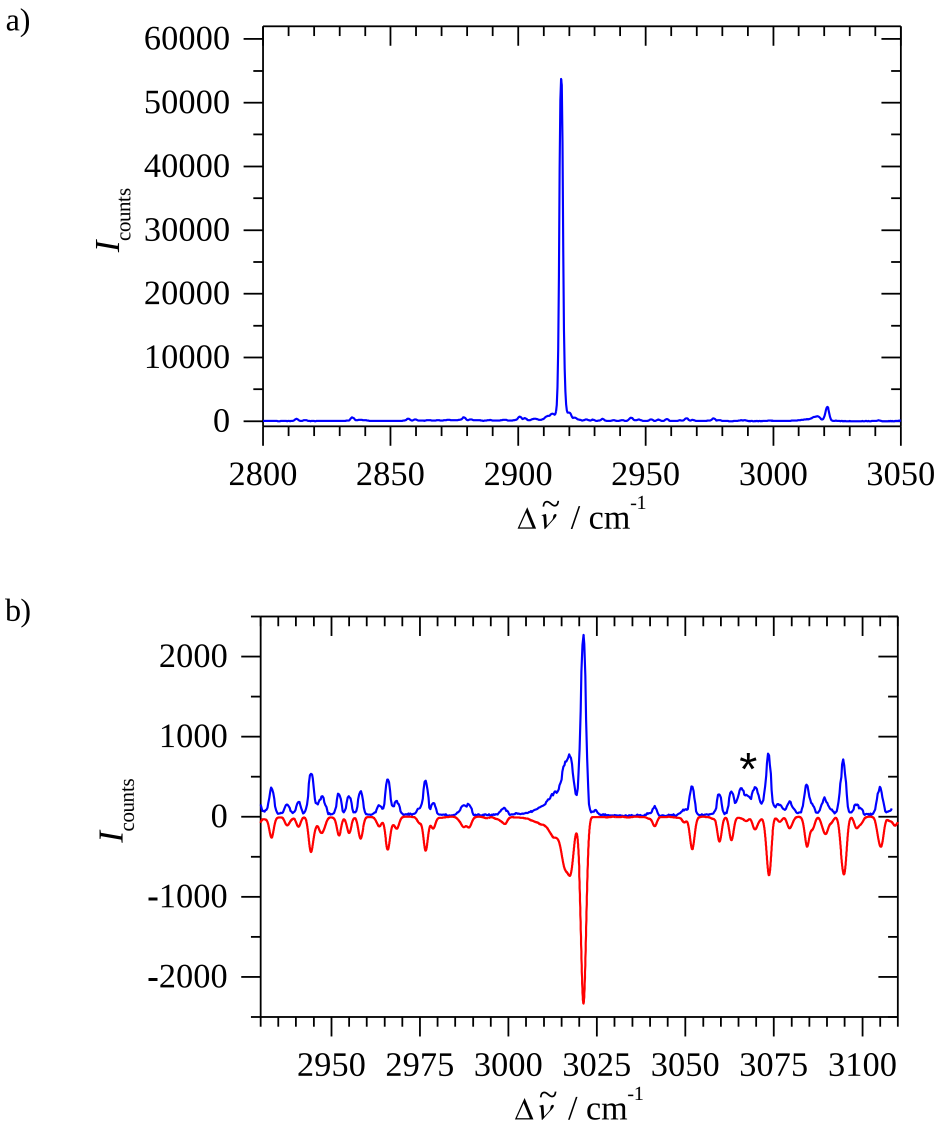

Figure 20 - Cavity-enhanced Raman spectrum of methane (1 bar CH_4, 1200 lines/mm grating, 20 s integration time) in the CH-stretching range. a) Overview. b) Detail (upper trace), together with a simulation of the spectrum (lower trace, intensities mirrored).

To calculate a detection limit for methane for the CER spectrometer, the spectral fitting procedure used before was used. The *Q*-branch of the ν_1 band at 2905- 2930 cm^{-1} was fitted with a Gaussian curve. The Gaussian has a centre at 2917 cm^{-1} with a FWHM of 1.3 cm^{-1}. With 1 bar of methane, an area of 91200 ± 600 counts cm^{-1} was obtained for the Gaussian line shape. With that knowledge, several spectra of the empty cell were recorded under the same experimental conditions in order to establish the baseline noise. The 2907-2930 cm^{-1} regions of the baseline spectra were fitted with a constrained Gaussian fit with the position and FWHM fixed at 2917 cm^{-1} and 1.3 cm^{-1}, only allowing the offset and area to vary. Eight of the empty spectra were processed and yielded a standard deviation of 17 counts per cm. This serves as an estimate for the noise limit for the spectra fitting procedure. Using these values, for 1 bar of methane, the noise equivalent detection limit is 0.19 mbar with a 20 s integration time at 10mW excitation. This corresponds to 190 ppmv in 1 bar.

Benzene

Benzene ($^{12}C_6H_6$) is a highly symmetric molecule with a centre of inversion and 20 normal vibrations of which 10 are doubly degenerate. The only transitions from the ground state that are Raman active are the A_{1g} and E_{2g} vibrational states. Benzene has 4 fundamental normal modes between 3048 and 3074 cm^{-1} which are essentially CH stretching modes: the Raman active (A_{1g}) and v_7 (E_{2g}) and the IR active CH stretching fundamental v_{20} (E_{1u}) and the Raman and IR inactive v_{13} (B_{1u}). There are additional local modes which are the result of normal vibrations coupled by Darling-Dennison overtones and further anharmonic resonances. Furthermore, the CH stretching modes are known to be strongly coupled with CH bending modes by Fermi resonances, where one quantum of v_s is exchanged with 2 quanta of v_b. All the vibrational CH stretching and bending modes of the same symmetry with common polyad quantum number, N, are strongly coupled and mixed by Fermi, Darling-Dennison and further anharmonic resonances, where $N = v_s + 0.5 \text{ x } v_b$.

The cavity-enhanced Raman spectrum of benzene vapour (vapour above the liquid, at room temperature) was recorded with an integration time of 20 s in the region of the CH stretching fundamental near 3000 cm^{-1}.

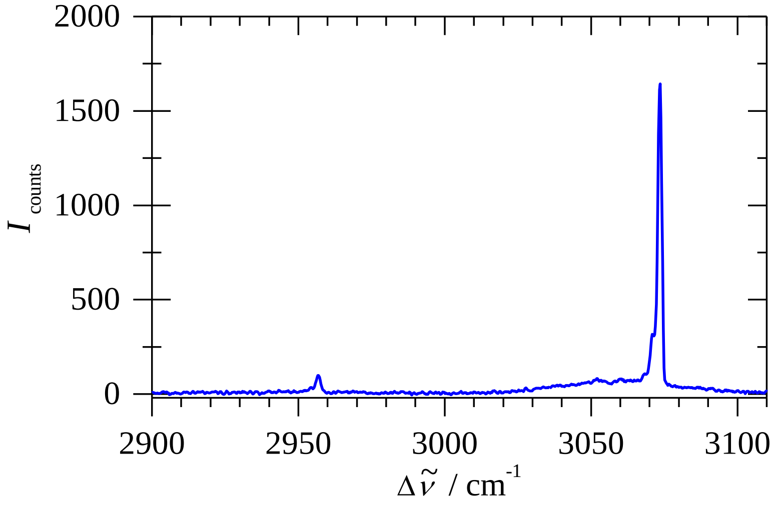

Figure 21 - Cavity-enhanced Raman spectrum of benzene vapour (vapour above liquid at room temperature, ca. 130 mbar; 1200 lines/mm grating, 20 s integration time) in the CH-stretching range.

Figure 21 shows the CER spectrum near the CH stretching fundamental of 3080 cm^{-1}. The spectrum is dominated by the *Q*-branch of the totally symmetric ν_2 fundamental peak at 3073.6 cm^{-1}. To the side of the *Q*-branch, there are broad extended wings due to rotational contours of the *O*, *P*, *Q* and *S*- branches. Upon closer inspection, it is possible to see the hot bands from the v_6 and $2v_4$ on the low wavenumber side of the *Q*-branch and the much weaker degenerate v_7 mode at around 3057 cm^{-1} which overlaps with the *O* and *P*- branches of the ν_2 band. At 2957 cm^{-1}, the overtone of the $2v_2$ mode is present. This overtone is likely to have obtained its intensity from the Fermi resonance with the v_2 band.

At 20s integration, the peak intensity for the v_2 Q-branch is 1650 counts. The standard deviation of the baseline is about 17 counts as obtained by the statistical analysis of the spectrum where no Raman transition occurred. This would lead to a signal to noise ratio of approximately 100:1. For gas phase Raman spectroscopy, it is common to use integration times of several hours. With longer integration times it will be possible to obtain more detailed Raman spectrum which can yield more relevant information about the coupling of the vibrational modes and the intramolecular dynamics. An estimate of the detection limit was calculated from integrating the Raman intensity of the Q-branch between 3060-3080 cm^{-1}. Gaussian line shape fitting was not used in this case as the additional Q-branch contours including the hot band transitions are unsymmetrical. The baseline intensity was estimated from integrating the region of 2980-3000 cm^{-1} which shows no Raman transition and is close enough to the Q-branch to give an estimate of the background signal. For the 20 s spectrum of benzene at 130 mbar vapour pressure, an integral of 4440 counts cm^{-1} was obtained. The procedure was repeated for the empty cavity and yielded a standard deviation of 37 counts cm^{-1}. This gives a noise equivalent detection limit of 1 mbar of benzene vapour at 20 s integration time. With longer integration times, a low ppmv detection limit for benzene can be achieved. The reason why longer integration times were not used is the enclosure sealing agent used (Apiezon Wax). This sealing agent is particularly miscible with toluene and other aromatic analogues. For this reason, it was decided that long exposure times was probably not a good idea due to the risk of benzene vapours dissolving the black wax seals which are required to keep the cell air tight.

Nitrogen and Air

The cavity-enhanced Raman spectrum of 1 bar of ambient laboratory air is shown in Figure 22, taken with an exposure time of 20 s with the low resolution grating (150 lines/mm) to allow an overview. The spectrum is dominated by the *Q*-branches of oxygen at 1556 cm^{-1} and nitrogen at 2329 cm^{-1}. The *Q*-branches have a FWHM of about 15 cm^{-1}, consistent with the instrumental bandwidth of the low resolution grating. Closer inspection shows that the *Q*-branches are accompanied by very weak and unresolved broad *O*- and *S*-rotational contours. In addition, a very weak Raman transition at 2917 cm^{-1} is noticed which is due to traces of methane left in the cell after a previous methane measurement (see below). By comparison with simulated spectra at room temperature, it is estimated that O_2 Raman features, including the *O*- and *S*-branch wings, extend roughly from 1300-1800 cm^{-1}, and N_2 from 2000-2600 cm^{-1}. After carefully zeroing the baseline, integration within these limits gives an area of 41265 counts cm^{-1} for O_2, and 119590 counts cm^{-1} for N_2. O_2 is a somewhat stronger Raman scatterer than N_2; using the constants from Ref. 93, a differential Raman scattering cross section of 2.1×10^{-35} m^2 sr^{-1} at 635 nm excitation is calculated for O_2, and 1.6×10^{-35} m^2 sr^{-1} for N_2. Correcting for these different scattering efficiencies, the ratio of O_2 to N_2 in air is then determined as 0.27:1 by the integrated intensities in the Raman spectrum, in almost perfect agreement with the expected abundance by volume in air. Observed intensities seem not to be distorted by different values of mirror transmittance at different spectral regions.

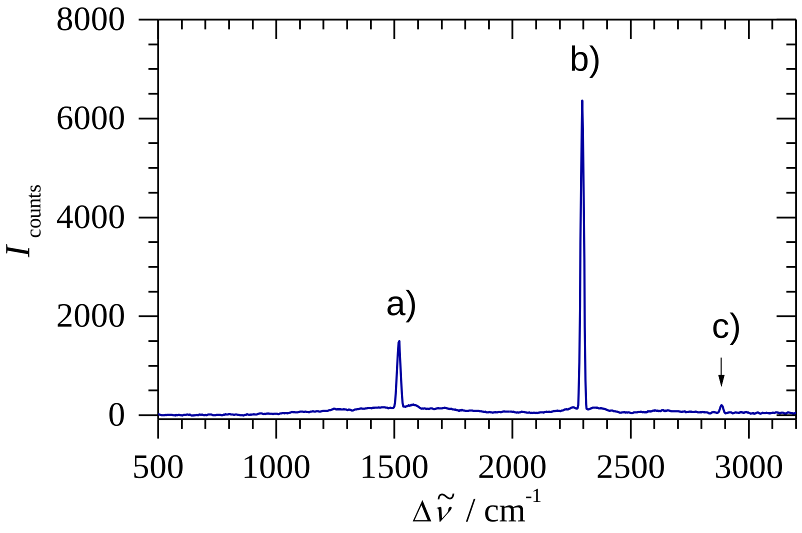

Figure 22 - Overview cavity-enhanced Raman spectrum of 1 bar lab air at room temperature, 20 s exposure, 150 lines/mm low resolution grating. a) O_2, b) N_2, and c) traces of CH_4 left in the cell after a previous experiment.

To demonstrate that cavity-enhanced spectra can also be obtained with a battery operated, portable apparatus, the Raman output was coupled into the USB4000 spectrometer which is powered by the USB port connection to the computer. With a battery operated computer (laptop) and battery operated laser diode, a very compact and portable apparatus can be obtained. Figure 23 shows the Raman spectrum of 1 bar of ambient air. At 60 s exposure time, a S/N ratio of about 25 is achieved, comparing the peak height of the N_2 *Q*-branch with the standard deviation of the baseline. The lower S/N ratio is mainly due to the CCD array in the USB4000 which is operated at room temperature, whereas the -50 °C cooling of the Andor camera greatly reduces thermal noise. The *Q*-branches of O_2 and N_2 have a FWHM of about 15 cm^{-1}, consistent with the specified instrumental bandwidth. Integrating O_2 and N_2 Raman bands after zeroing the baseline, and considering the different Raman scattering cross sections, an O_2 to N_2 ratio of 0.26 (by volume) is obtained for air, again in good agreement with expectation.

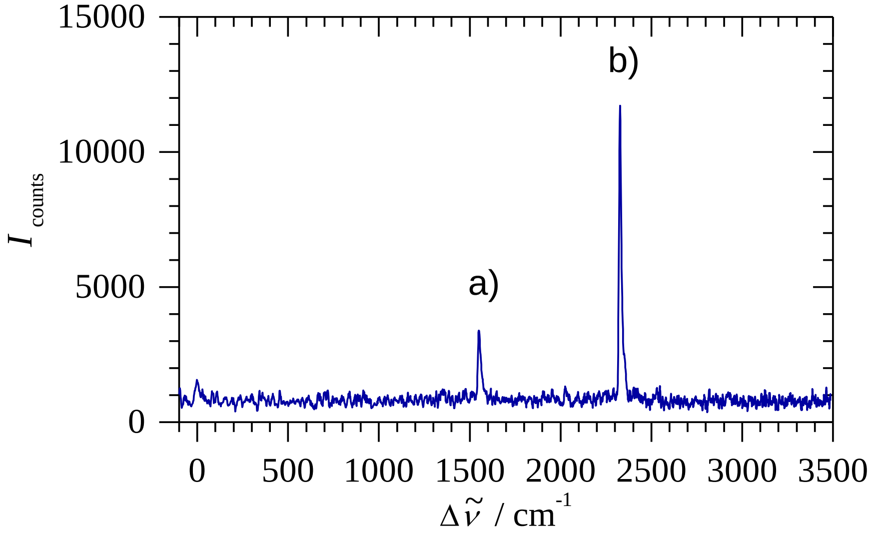

Figure 23 - Cavity-enhanced Raman spectrum of 1 bar lab air obtained with the USB4000 spectrometer, 60 s exposure. a) O_2, b) N_2.

Using the Shamrock monochromator with the high resolution grating and Andor camera, Raman spectra of N_2 in 1 bar of air are obtained as shown in Figure 24. Figure 24a shows the unresolved *Q*-branch of $^{14}N_2$ at 2329 cm^{-1} which dominates the spectrum. The contour has a FWHM of about 3.0 cm^{-1}, determined by the instrumental bandwidth and spectral congestion by overlapping *Q*-branch transitions. After averaging four 100 s exposures, the spectrum has a S/N of about 870, with a peak height of 14820 counts and a baseline noise of about 17 counts (standard deviation of baseline). In addition, the much weaker *O*- and *S*-branch transitions can be clearly seen (Figure 24b). In the rotationally resolved $^{14}N_2$ Raman spectrum, intensity alternations are due to the 6:3 nuclear spin statistical weight for even and odd *J*, respectively. Between the *O*(5) and *O*(6) transition, the *Q*-branch of the isotopomer $^{14}N^{15}N$ is apparent at 2290.5 cm^{-1} (marked with the asterisk in Figure

24b) with a peak height of 125 counts. Due to partial overlap of the spectral wings with the *O*-transitions, the peak height is chosen as a measure of $^{14}N^{15}N$ abundance. Compared with the peak height of the $^{14}N_2$ *Q*-branch, a relative abundance of 0.8 % of the $^{14}N^{15}N$ isotopomer is measured, close to the expected value of 0.73 %. This shows the suitability of CERS with low power diode lasers for quantitative isotopomer measurements, for example in isotope tracer experiments.

The Gaussian fitting procedure introduced before cannot be applied to estimate a limit of detection for $^{14}N_2$, since the *Q*-branch contour has an asymmetric line-shape. Instead, the area of the *Q*-branch is integrated from 2310 - 2340 cm^{-1}, and from this value, the integral of the spectrum between 2120 - 2150 cm^{-1} is subtracted. In the second region, there are no noticeable Raman transitions, so this value may serve as an estimate for the baseline of the spectrum. For 1 bar of air, an area of 55 954 counts cm^{-1} is thus obtained. To estimate the noise level of this measurement, this procedure was repeated for 8 scans with 100 s exposure (no averaging) in an empty cell, giving a standard deviation of 184 counts cm^{-1} for the area. A noise equivalent detection limit of about 2.6 mbar N_2 is thus estimated for 100 s exposure time and 10 mW excitation. This value is higher than the 0.46 mbar H_2 at 50 s integration time, even considering the larger differential Raman scattering cross section of H_2, (3.6×10^{-35} m^2 sr^{-1}, calculated with constants from Ref. 88), showing the improvement afforded by the spectral fitting procedure if it can be applied.

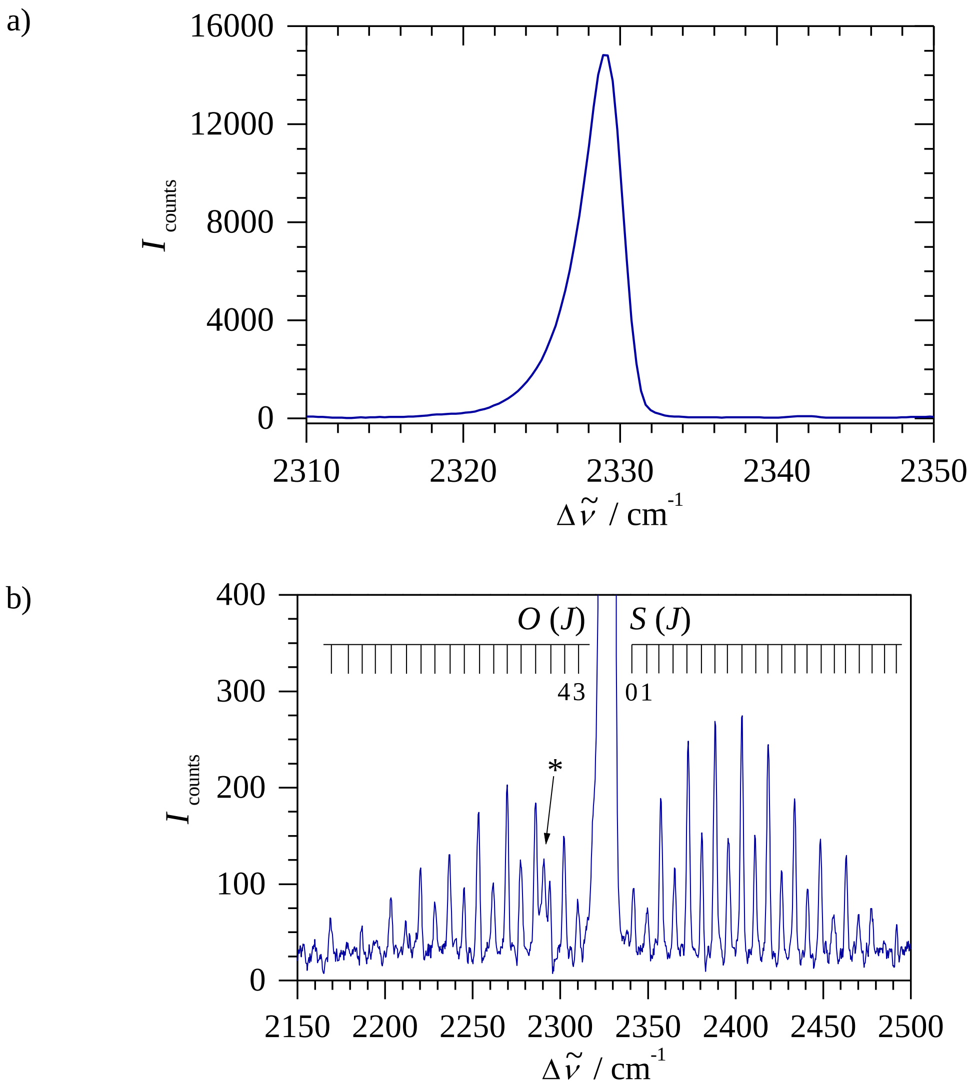

Figure 24 - Cavity-enhanced Raman spectrum of N_2 (1 bar lab air, high resolution grating, 4 scans with 100 s exposure each averaged). a) *Q*-branch contour, b) rotationally resolved *O*- and *S*-branches. The position of the *Q*-branch of the $^{14}N^{15}N$ isotopomer is marked by an asterisk.

In conclusion, a variant of cavity enhanced Raman spectrometer was set up, using a 10 mW 635 nm laser diode, with optical feedback to from an external optical cavity. A few Watts of power was periodically built up within the cavity (1.5 kHz, 50 % duty cycle), which allows easy observation of the spontaneous Raman signals collected at a forward collection geometry. The variations in mirrors reflectivities do not affect the Raman signals observed. Excellent linearity was demonstrated with a variety of gases and noise equivalent detection limits in the order of ppm range by volume is achieved (at 1 bar). A Gaussian spectral fitting procedure (if applicable) was also demonstrated. The low power consumption and compact layout means that the apparatus can be made to be battery operated and portable for field use.

CERS is potentially a new standard for gas phase Raman detection, especially for the possible future energy source, hydrogen, which cannot be easily detected by alternative spectroscopic means. High sensitivity and selectivity of analysis of gas mixtures can be carried out with Raman spectroscopy due to high spectral resolution. Possible analytic application involve isotopic tracer analysis ($^{14}N/^{15}N$) and elevated presence of tritium.

CERS can also be used for more fundamental applications, for example to study vibrational interactions, intramolecular vibrational energy redistribution on fast timescales by high resolution spectroscopy, or to refine the theoretical analysis of molecular energy levels and potential energy hypersurfaces.

3. Mid-Infrared Cavity Enhanced Resonant Photoacoustic Spectroscopy

Molecules with IR-active vibrations can be detected by IR absorption spectroscopy, usually with much greater sensitivity than with Raman spectroscopy (see previous chapter). This chapter deals with cavity enhanced resonant photoacoustic spectroscopy (CERPAS), a very sensitive detection method developed originally by Hippler and co-workers and demonstrated in the visible; this technique is ported to the more sensitive mid-IR regions in the present work. The mid-IR CERPAS was originally set up by Dr. Mark Stringer and myself to detect explosives (see chapter 4). In this chapter, measurements of the water, acetylene and nitromethane are described to characterise the mid-IR CERPAS apparatus. This work was done partly in collaboration with Dr. Mark Stringer, a research associate in Dr. Hippler's group.

Introduction

Absorption of light at characteristic wavelengths allows unique identification, and compounds in a mixture can be differentiated by their spectroscopic signatures. At present, the most sensitive optical absorption techniques are either based on cavity-enhancement or photoacoustic detection. In cavity based techniques, light is coupled into an optical cavity composed of two or more high-reflectivity mirrors (reflectivity $R > 99.9$ %). Due to many reflections within the cavity, extremely long effective absorption path lengths of the order of some km can be achieved. This greatly increases the sensitivity. In the two major implementations of this principle, either the decaying light intensity is observed (cavity-ringdown spectroscopy, CRDS) [89,94,95,96] or the accumulated absorption of light (cavity-enhanced absorption spectroscopy, CEAS).[97,98,99] CRDS and CEAS are direct optical absorption methods which suffer from the fact that only a small fraction of light is absorbed and the small difference of strong signals with absorption and without absorption is the measure of concentration. Amplification of light signal does therefore not directly increase sensitivity. In photoacoustic spectroscopy, after absorption of light, molecules transfer their excitation via collisions with other molecules into local heating.[100,101] The associated weak pressure wave is a sound which can be detected by a microphone. Since this is essentially a zero background method, the microphone signal can be amplified which increases sensitivity, until background noise becomes dominant. In a particularly sensitive implementation of photoacoustic detection, the acoustic excitation occurs in an acoustic resonator (e.g., an organ pipe) at an acoustic resonance frequency which enhances signals (resonant photoacoustic spectroscopy).[100, 101]

Hippler *et al.* have recently introduced a combination of cavity-enhancement and resonant photoacoustic spectroscopy for ultratrace gas analysis, cavity-enhanced resonant photoacoustic spectroscopy (CERPAS).[37] In this approach, a diode laser is coupled into an optical cavity composed of two highly reflective mirrors. Inside the cavity, laser power builds up and absorbing species are detected by photoacoustics. Coupling is modulated to an acoustic resonance, finally achieving sensitivities comparing favourably with cavity-ringdown spectroscopy. In the scheme, a single-mode CW diode laser (10 mW, 635 nm) is coupled into a high-finesse linear cavity and stabilized to the cavity by optical feedback. Inside the cavity, a build-up of laser power to at least 2.5 W occurs. Absorbing gas phase species inside the cavity are detected with high sensitivity by the photoacoustic effect using a microphone embedded in the cavity. To increase sensitivity further, light coupling into the cavity is modulated at a frequency corresponding to a longitudinal resonance of an organ pipe acoustic resonator (f = 1.35 kHz, $Q \approx 10$). The technique has been characterized by measuring very weak water overtone transitions near 635 nm. Normalized noise-equivalent absorption coefficients are determined as $\alpha \approx 4.4\times10^{-9}$ cm^{-1} s$^{1/2}$ (1 s integration time) and 2.6×10^{-11} cm^{-1} s$^{1/2}$ W (1 s integration time and 1 W laser power). These sensitivities compare favourably with existing state-of-the-art techniques. As an advantage, CERPAS is a "zero-background" method which increases selectivity and sensitivity, and its sensitivity scales with laser power.

Fundamental vibrational transitions in the mid-IR are up to 10000 times stronger than the weak water overtones in the original CERPAS study. Porting the CERPAS technique into the mid-IR would therefore greatly increase sensitivity. In the past, tuneable mid-IR laser sources were difficult to achieve and to operate, but with the advent of new quantum cascade lasers, the mid-IR region can now conveniently be accessed. Here, we report a CERPAS setup using a QCL system lasing around 7.5 µm and characterise performance by measuring acetylene and nitromethane.

Experimental

Description of the Experimental Set-up

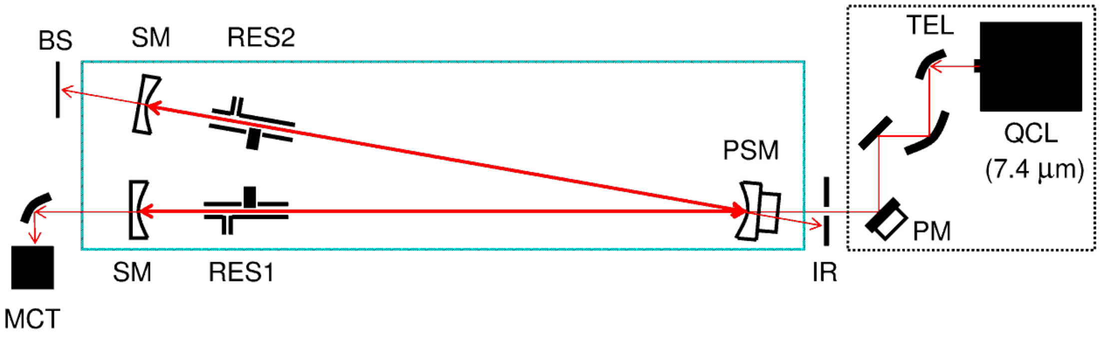

Figure 25 - Scheme of the QCL-CERPAS setup for ultratrace gas detection. QCL: CW-single-mode quantum cascade laser, lasing around 7.5 µm with 100 mW; TEL: beam shaping telescope, with 2 gold-coated off-axis parabolic mirrors (first focal length 2", second 3"). PM: mirror, mounted on a piezoelectric transducer to allow optical feedback; IR: iris to block direct back reflection from cavity entrance mirror; PSM: highly reflective cavity entrance mirror, mounted on a piezoelectric transducer to allow mode matching; RES: acoustical resonator tube (glass, 54 mm long, 8 mm i.d.), with microphones and inlet for gas stream to be measured; SM: highly reflective cavity exit mirrors; BS: beam stop; MCT: MCT detector.

The optical set-up is shown schematically in Figure 25. In short, the optical setup consists of a V-shaped cavity with arm length l = 75 cm and a separation of the two exit mirrors of d = 5.5 cm. After one of the exit mirrors, an off-axis parabolic mirror focuses exiting light on a MCT detector (EG&G Optoelectronics, J15D14-M960) which allows monitoring of light intensities. Focusing turned out to be very important. The detector has only a small detection area (1 mm^2) and is not sampling the entire beam without focussing. Due to the excitation of higher transverse optical modes in the cavity which are interfering with each other, the detector then sees interference patterns, sometimes strong signals due to positive interference, and sometimes weak signals due to destructive optical interference. These interferences can change very rapidly and in an unpredictable way. Initially, the light exiting the optical cavity was not focussed and the weak optical signals indicated wrongly that alignment has been lost, and triggered a lengthy realignment procedure. However, it was discovered that this is simply an artefact. By focusing the outgoing beam to the detector, the detector samples the entire beam and is not affected by interference patterns anymore.

The mirror mounts are heated with resistors to approximately 50 °C, and the temperature is monitored by thermistors. The mirrors (LohnStar Optics; mirrors on loan from Prof. Orr-Ewing, Bristol) are highly reflective between 7 to 8.5 μm (specification R = 99.94 %). The concave mirrors have a radius of curvature of 5 m. The optical cavity and the acoustic resonators are contained in a glass enclosure equipped with CaF_2 windows. The acoustic resonators consist of a 54 mm long glass tube with 8 mm i.d. Each resonator has three microphones (Knowles, EK-23024) attached to it in the middle of the resonator tube (see Figure 26). The resonators have a resonance frequency of about 3 kHz. Microphone signals are first filtered by a home-built analogue multiple feedback band-pass filter with a Q-factor of 5 and 7x amplification (see Figure 27), and then further processed by home-built lock-in amplifiers (following the design in Ref. 83) with 100x input amplification and 10x amplification of the integrated output. The acoustic resonator tube has an inlet connected to 1/8" Teflon tubing to allow flow measurement of gases; in a flow configuration, one possible configuration would be to use resonator 1 to sample an analyte gas stream, and resonator 2 to measure lab air as reference and to cancel out some systematic (e.g., water absorptions) and random (e.g. noise in the lab) acoustic noise sources. This noise cancellation scheme is expected to increase the signal-to-noise ratio for ultratrace detection. In the present setup, however, static cell measurements were performed under reduced total pressure, and all microphone signals were simply added together.

Figure 26 - Photograph of one of the acoustic resonator tubes, with microphones, supply inlet and heating wire attached.

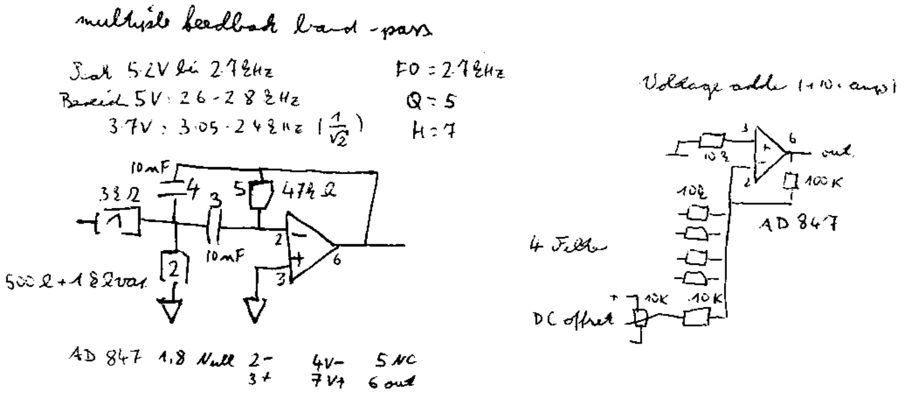

Figure 27 - Sketch of the electronic circuit used for the electronic band-pass filter (notes from Dr. Hippler).

The continuous-wave (CW) mid-IR light source is a tuneable external cavity quantum cascade laser (Daylight Solutions, TLS-21074), tuneable from 1330 - 1390 cm^{-1} (7.52 - 7.20 μm) with about 50 - 120 mW power. The laser output is single longitudinal mode, linearly polarized and has a specified line width of 50 MHz. The laser head is cooled by an external water chiller and kept at around 15 °C. By moving the grating of the external cavity of the laser, laser wavelength can be tuned. The laser also allows external current modulation which allows fine tuning of the wavelength. The length of the measurement optical cavity has to be a multiple of the laser wavelength in order to support optical resonances and to allow power build-up by positive interferences to occur. To achieve this mode matching, the entrance mirror of the optical cavity is put on a piezoelectric transducer and a voltage applied until an optical resonance has been achieved. For effective optical feedback to the QCL, the return path has also to be a multiple of the laser wavelength (phase matching). This is achieved by putting the steering mirror in front of the optical cell on a piezoelectric transducer which is adjusted by applying a voltage. The piezoelectric assemblies are home-built using 150 V piezoelectric activators (Thorlabs, AE0505D16F) and a 150 V driver (Thorlabs TPZ001). The laser beam is slightly widened and made parallel by a beam shaping telescope consisting of 2 gold-coated off-axis parabolic mirrors (first focal length 2", second 3"; Edmund Optics NT47-098 and NT63-195). The beam has been characterised using a mid-IR beam profiler (Dataray Inc., WinCamD; on loan from Laser2000). The beam is nearly circular with a diameter between 2 and 3 mm (see Figure 28).

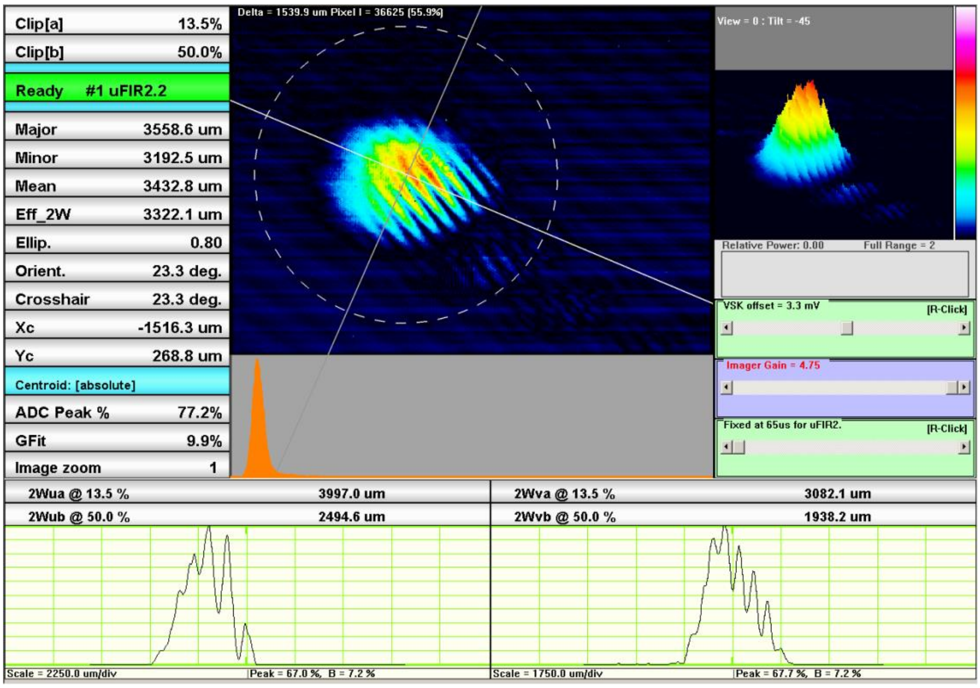

Clip[a] 13.5%

Clip[b] 50.0%

Ready #1 uFIR2.2

Major 3558.6 um

Minor 3192.5 um

Mean 3432.8 um

Eff_2W 3322.1 um

Ellip. 0.80

Orient. 23.3 deg.

Crosshair 23.3 deg.

Xc -1516.3 um

Yc 268.8 um

Centroid: [absolute]

ADC Peak % 77.2%

GFit 9.9%

Image zoom 1

Delta = 1539.9 um Pixel I = 36625 (55.9%)

View = 0 : Tilt = -45

Relative Power: 0.00 Full Range = 2

VSK offset = 3.3 mV

Imager Gain = 4.75

Fixed at 65us for uFIR2.

2Wua @ 13.5 % 3997.0 um

2Wub @ 50.0 % 2494.6 um

2Wva @ 13.5 % 3082.1 um

2Wvb @ 50.0 % 1938.2 um

Scale = 2250.0 um/div

Peak = 67.0 %, B = 7.2 %

Scale = 1750.0 um/div

Peak = 67.7 %, B = 7.2 %

Figure 28 - Screen shot from the mid-IR beam profiler characterising the laser beam ca. 1 m after the beam-shaping telescope.

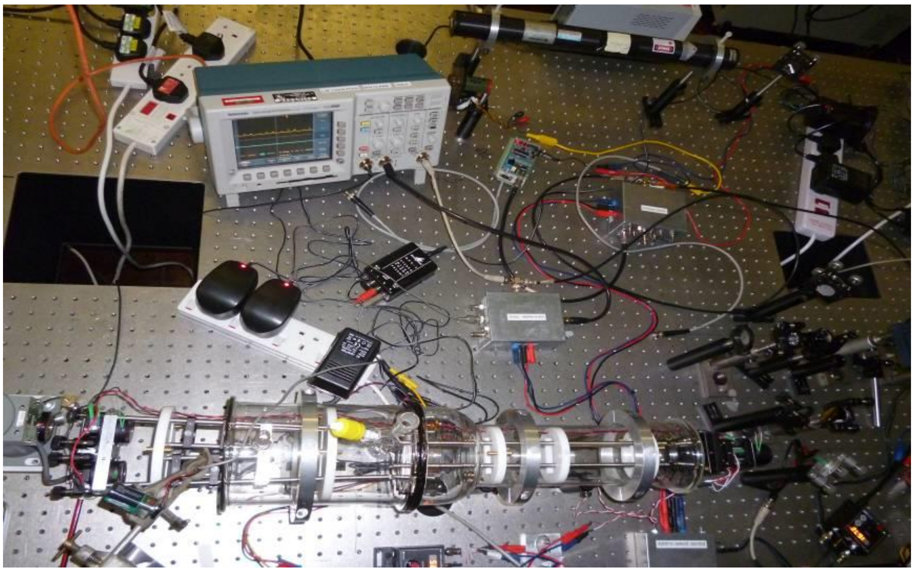

Figure 29 - Photograph of the open optical cell.

Characterisation of the optical cavity

In order to characterise the performance of the optical cavity and of its mirrors, cavity ringdown experiments have been performed. By switching off the laser coupling into the cavity, cavity-ring down signals can be obtained in the experimental set-up. Light intensity is monitored with the MCT detector. If the light intensity is above a given threshold, light has been coupled into the cavity. By applying a square voltage pulse with a fast rising edge to the current modulation entrance of the QCL system, the laser is pushed out of resonance and thus effectively switched-off. Figure 30 shows a typical ringdown trace obtained. The decaying light intensity is described by

$$I(t) = I_0 \exp(-k\,t)\,, \qquad \textit{Equation 31}$$

$$k = \alpha c + (1-R)\,c\,/\,l\,, \qquad \textit{Equation 32}$$

where k is the exponential decay constant, α the absorption coefficient, c the speed of light and l = 75 cm the arm length of the V-shape optical cavity. Strictly, equation 32 is derived for a linear cavity, but a V-shape cavity can be considered as a folded linear cavity. The parameter $(1-R)\,c\,/\,l$ represents the baseline in the absence of an absorber. These equations are derived for monochromatic light and apply to the present experiment, where the laser bandwidth is much narrower than the absorption line width and where only one cavity mode is excited. Anderson *et al.*[102] have derived expressions for the finesse of the cavity F and the quality factor Q of the optical cavity in terms of the cavity decay time, $\tau = 1/k$,

$$F = \pi \frac{c}{l} \tau \qquad \textit{Equation 33}$$

$$Q = 2\pi\nu\tau \qquad \textit{Equation 34}$$

where v is the optical frequency (note Ref. 102 contains an additional factor 2 in F, because there the round trip is used and not the cavity length).

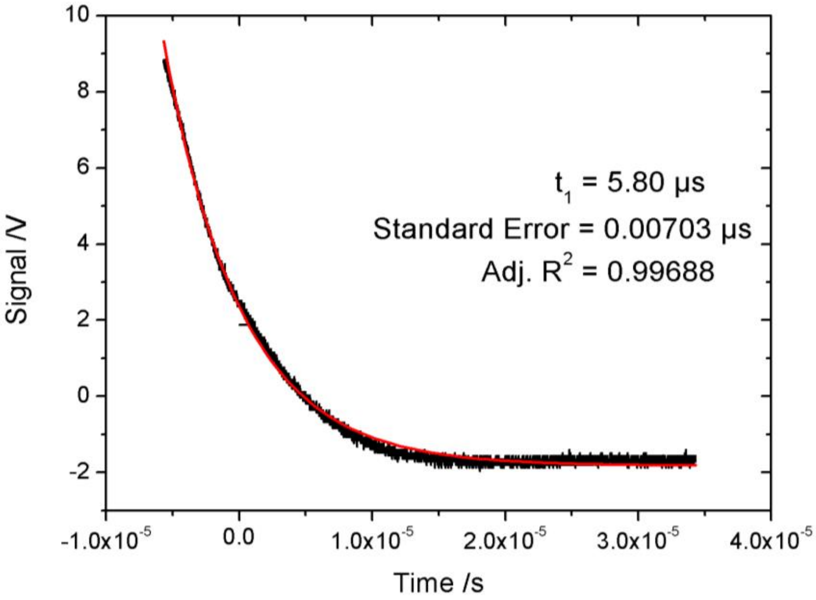

Figure 30 - An exponential decay (red) of the empty cavity, with an exponential fit (red) for a decay time τ = 5.8 µs, as observed with the V-shaped cavity near 1346.0 cm^{-1} (weak water line), open to lab air.

The apparatus utilised two resonators. For the detection of ultratrace vapours, one possible configuration would be to use resonator 1 to sample an analyte gas stream, and resonator 2 to measure lab air as reference. and to cancel out some systematic (e.g., water absorptions) and random (e.g. noise in the lab) acoustic noise sources. This noise cancellation scheme is expected to increase the signal-to-noise ratio for ultratrace detection. The acoustic signals are first filtered with an analogue band-pass, and then processed in an analogue lock-in amplifier which is referenced to the laser current modulation frequency taking appropriate phase shifts into account. To demonstrate the principle of difference detection, a droplet of water was placed in the sample resonator 1, whilst the reference resonator 2 is open to the quite dry lab air (approximately 20 % relative humidity at the 20 °C ambient temperature). In this way, resonator 1 will have a higher water vapour concentration (approaching 100 % relative humidity at the 20 °C ambient temperature) than the reference resonator. Figure 31 shows an oscilloscope screenshot showing the difference in signal amplitude from the sample resonator and the reference resonator under these conditions. In theory, if both resonators sample the same gas stream, the response will be identical and a null signal will result from the difference.

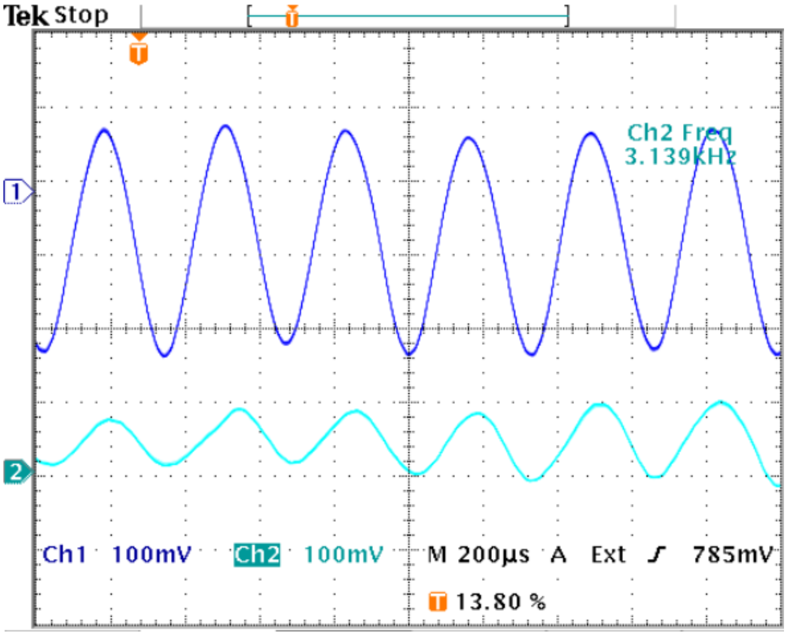

Figure 31 - Oscilloscope screenshot, showing photoacoustic signals from very weak water absorptions at 1355.9 cm^{-1} within 1 atm lab air. Lower trace: reference resonator, measuring quite dry lab air; upper trace: resonator loaded with water droplet to increase water pressure.

Tuneability of the Quantum Cascade Laser

A key requirement for the quantum cascade laser is that it is continuously tuneable. Water is one of the most important interferences in the optical detection in the mid-

IR, and the narrow water absorption lines have to be avoided. Figure 32 shows water absorptions in the region of the mid-IR QCL system.

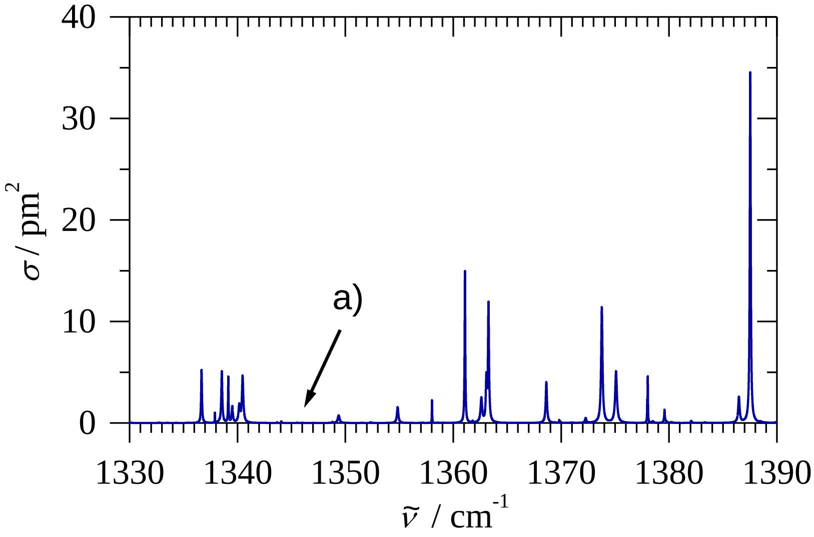

Figure 32 - Water vapour transitions within the tuning range of the QCL laser system, as obtained from the most recent and most accurate data base of water transitions (Ref. 103), where the stick lines have been convoluted with 298 K Doppler broadening and 1 atm air pressure broadening to mimic the actual lab air spectrum.

In an external cavity laser system, the laser chip output facet should be antireflection (AR) coated to avoid unwanted optical feedback. Optical feedback is provided by the grating of the external cavity, and by moving the grating angle, the laser is forced to lase at a wavelength given by the grating. The pivot of this movement should be precisely aligned so that the angular movement coincides with a changing of the cavity length to ensure that the cavity length remains always a multiple of the laser wavelength. If there is residual reflectivity in the laser chip, or if the pivot movement of the grating is not perfectly synchronised, the laser will not change its wavelength smoothly, but will hop between modes. The laser system purchased (Daylight Solutions, TLS-21074) is supposed to be continuously tuneable without mode-hops, providing single-longitudinal mode high resolution CW output. It turned out, however, that the QCL laser has a very peculiar tuning behaviour. By turning the grating within the QCL system, a smooth tuning should be possible. Figure 33 shows the output power of the laser as a function of wavelength. Apparently the laser is tuneable from 1330-1389 cm^{-1} (7.519-7.205 µm) with about 50-120 mW power. However, it was found that the laser actually just jumps from one mode to another one, with a typical mode spacing between 0.5 and 1 cm^{-1}. This is demonstrated in Figure 33, showing the measured power directly after the QCL laser as a function of the nominal wavenumber. The actual wavenumber is the value at the maximum of each "ripple", and this wavenumber is not changing, until it jumps to another value at another ripple.

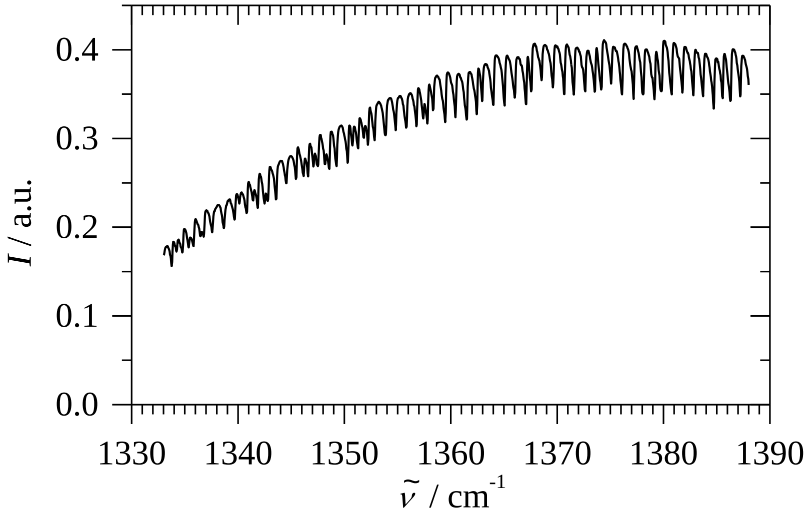

Figure 33 - Output power of the tuneable mid-IR QCL as a function of wavelength. The peak power is about 120 mW. The output shows mode-hopping tuning behaviour.

Since the typical full width at half maximum (FWHM) of water lines in the atmosphere is about 0.1 cm^{-1}, only, water lines cannot be reliably measured. This behaviour is shown in Figure 34, where a direct transmission measurement of lab air under ambient conditions (22 °C, 11 % relative humidity measured, corresponding to a water partial pressure of about 2.2 Torr) was made by placing the power meter as detector of transmitted intensity at about 2 m distance to the QCL laser. At 2 m, a significant amount of light is absorbed at one of the stronger water lines, resulting in an observed dip of intensity. Since the laser is not tuning smoothly, however, only measurements at wavenumbers indicated by crosses are actually made, resulting in completely distorted line shapes and even missing of entire lines.

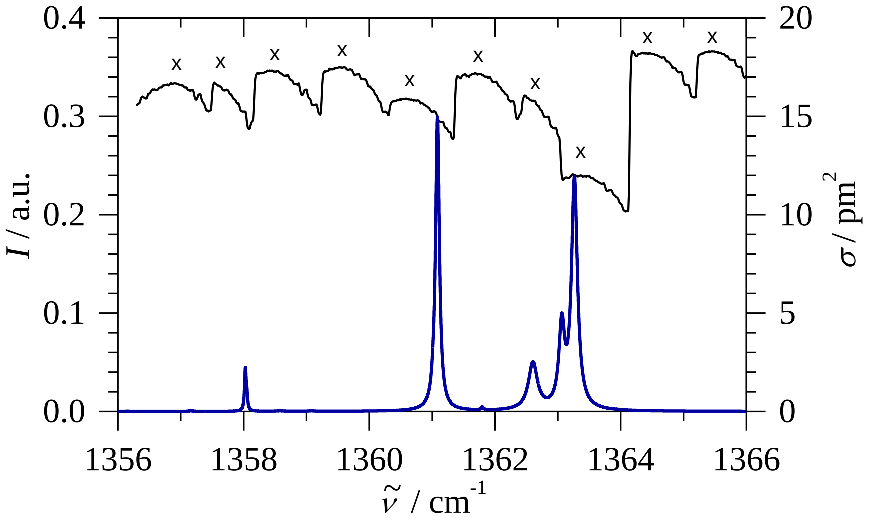

Figure 34 - Measured transmitted intensity at 2 m distance (black) and actual water lines from the data base (blue).

After extensive trials, it was found that the laser can be tuned continuously by temperature tuning, in addition to grating tuning. In temperature tuning, the temperature of the laser head is adjusted. At different temperatures, the laser chip will expand/contract slightly thus changing the length of the parasitic laser chip cavity and thus changing the wavelength of the mode. This was confirmed by measuring the actual wavelength with an FTIR spectrometer (Mattson Instruments, GL-2020, 0.4 cm^{-1} resolution), see Figure 35. A temperature tuning coefficient -0.0687 cm^{-1}/K is obtained. The laser can be tuned within a 10 K range (10 to 20 °C laser head temperature), provided that the grating is tuned synchronously.

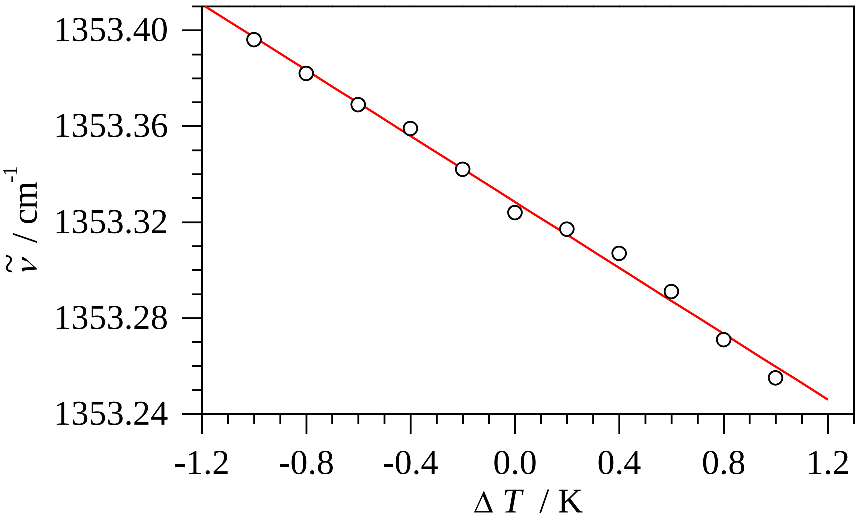

Figure 35 - Measured wavenumber of QCL as a function of temperature.

With this tuning method, first measurements with the cavity were obtained by a variant of cavity-enhanced absorption, where the transmitted intensity after the cavity is measured. To demonstrate this, a very weak water absorption line (the location is marked with arrow in Figure 32 but is too weak to be actually seen) was measured. These lines have about 1/1000 of the intensity of the strongest water lines within the QCL lasing range. Figure 36 shows the cavity-enhanced spectrum obtained with 3 water lines. Each measurement point represents a reading with a sampling time of approximately 1 s.

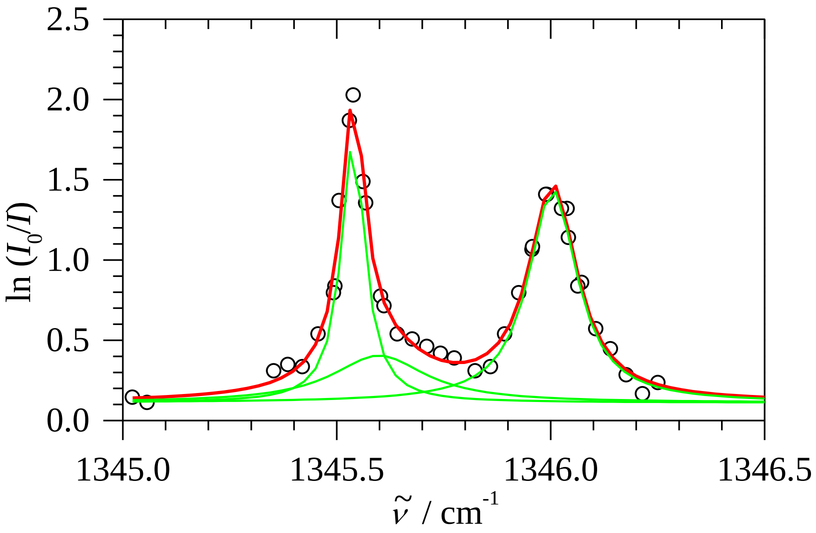

Figure 36 - Cavity-enhanced spectrum of water lines in the atmosphere (ca. 2.2 Torr water vapour pressure). Circles are experimental points; the green curves are fitted Lorentzians adding up to the red curve.

Figure 37 displays the same experimental spectrum, but overlaid with the theoretical spectrum from the data base, showing near perfect agreement in line positions and intensities. The very weak line between the 2 stronger lines is presumably due to the water isotopomer HDO at natural abundance; there seems to be a slight discrepancy between measured and theoretical intensity for this line which might well be due to inaccuracies of the data base for extremely weak lines.

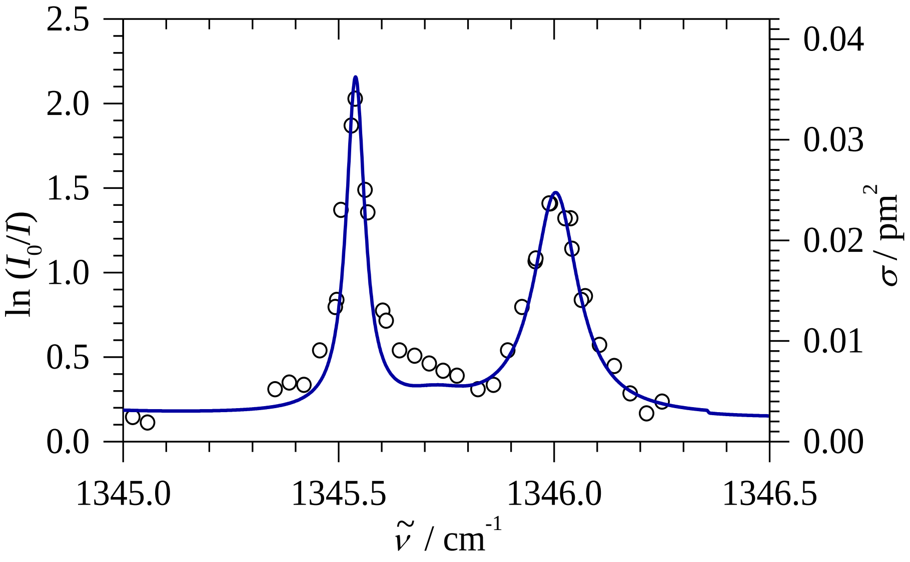

Figure 37 - Experimental spectrum of water from Figure 36, overlaid with a theoretical spectrum from the HITRAN 2012 database (blue).[104]

By tuning the grating and the temperature, as well as monitoring the wavelength with a FTIR spectrometer, the QCL laser can be reliably tuned to obtain high-resolution spectra, or to avoid strong water absorption lines in the detection of broader absorption features.

In most cavity enhanced experiments, a linear cavity with two mirrors is used. The advantages of a linear cavity are that only two expensive high-reflectivity mirrors are used, the alignment is generally easier, and it is much easier to achieve stable single-mode operation. As a distinct disadvantage, however, there is an unwanted direct back reflection from the first cavity mirror, going straight back to the diode with high intensity. This is likely to damage the diode and will cause unstable operation due to unwanted optical feedback. Optical feedback from inside the cavity is beneficial, because it stabilises the laser to the wavelength of the cavity, but other reflections are always to be avoided. For a linear cavity, these direct back reflections can be blocked by Faraday isolators which essentially transmit light only in one direction. Faraday isolators were not available in the mid-IR and are still not available at the QCL lasing range. Non-linear optical cavities with a triangular or V-shaped [40] beam path avoid direct back reflections (see Figure 11). The back reflection from the first mirror (the entrance mirror) is reflected at an angle, and can be trapped by an iris or a beam dump. It was decided to use a V-shape cavity with three mirrors. The design is quite compact, and the angle of incidence on the cavity mirrors is 0° for the two exit mirrors, and close to 0° for the entrance mirror of the cavity. Direct back reflection is avoided, but optical feedback from within the cavity is still possible. The design proved to be very stable and easy to align.

By modulating periodically the current supplied to the QCL laser, the wavelength of the QCL is changing and finds optical resonances within the optical cavity, resulting in build-up of light power inside the cavity. This can be seen as an increase of light exiting the cavity. By adjusting the cavity length with a piezo-electric transducer (mode-matching) and by encouraging optical feedback back into the QCL by adjusting one of the steering mirrors outside the cavity by another piezo-electric transducer (phase-matching), stable, periodic optical resonances are obtained. This is demonstrated in Figure 38. Once such a periodic resonance is found, it will stay in resonance up to typically a minute or more; slight manual adjustment of the two transducers is required to keep the resonance for prolonged periods of time. Mode- and phase-matching is done manually; the system is mechanically quite stable, and only minor adjustments are required to keep the cell in resonance. In a future implementation, these adjustments can be made automatic using simple analogue electronic circuits, as described in Ref. 83. If light absorption occurs within the acoustic resonator, a photoacoustic signal is picked-up by the microphone (see Figure

38) which is largest if the modulation frequency corresponds to an acoustic resonance mode of the resonator (resonant photoacoustics).

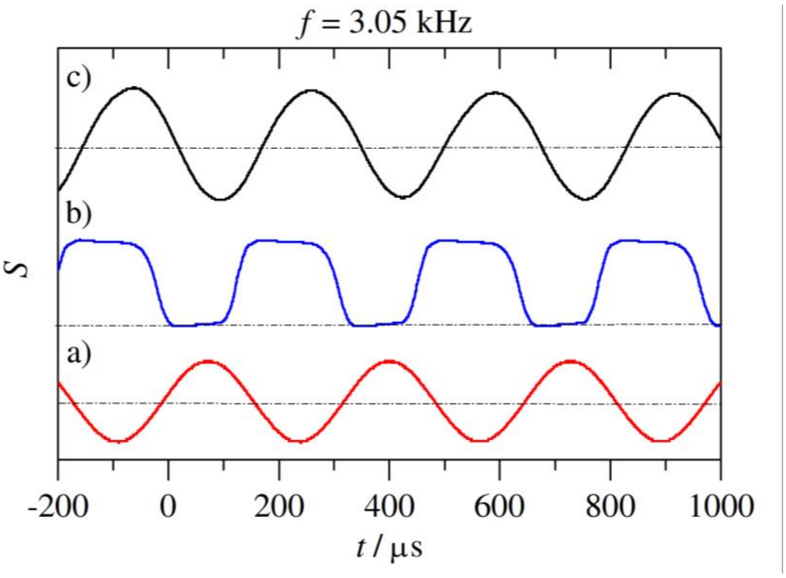

Figure 38 - Periodic signals from the QCL-CERPAS setup:

a) Sine modulation applied to the QCL driving current; the modulation frequency of 3.05 kHz corresponds to a longitudinal acoustic resonance.

b) Optical power build-up within the cavity, as observed by the MCT detector;

c) Resonant photoacoustic signal from very weak water absorptions at 1355.9 cm^{-1} of 1 atm lab air inside the cavity.

Peak photoacoustic signals of water absorption near 7.4 μm within 1 atm lab air were measured as a function of modulation frequency (see Figure 39). The data are well described by a Lorentzian distribution peaking at the acoustic resonance frequency f = 3.05 kHz, which corresponds to the longitudinal resonance frequency of the 54 mm long glass tube in air. The quality factor Q is defined as the ratio between the resonant frequency f and the frequency bandwidth at $1/\sqrt{2}$ of the maximum of the resonant profile. For the present set-up, $Q \approx 15$ is determined. Typical Q values reported in literature are between 40 and 200 for longitudinal resonators.[47] Note that a mechanical chopper is not required for resonant PAS in the present set-up.

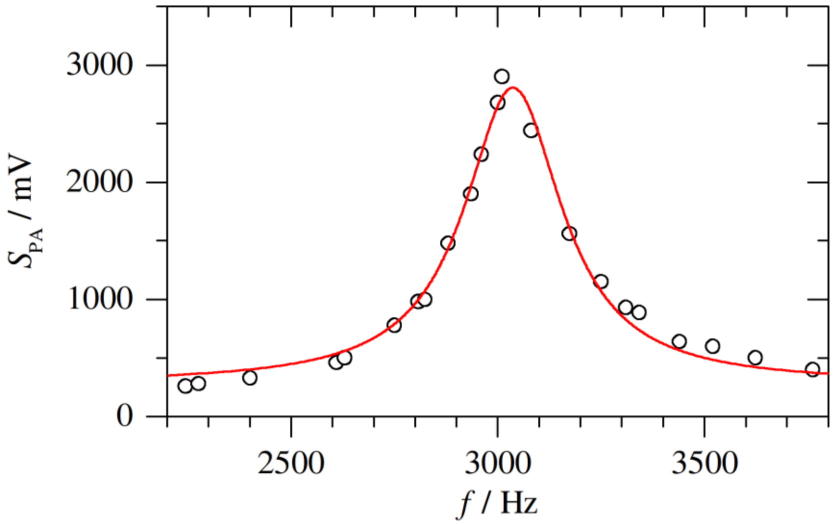

Figure 39 - Peak photoacoustic signal of water absorption near 7.4 µm within 1 atm of lab air at various modulation frequencies, together with a Lorentzian fit curve.

The resonance behaviour of the acoustic tube was further investigated by Fourier-transforming the time domain photoacoustic signal by the digital oscilloscope used (Tektronix TDS 3032B), see Figure 40. At a modulation frequency of 3.05 kHz, the acoustic spectrum is clearly dominated by the longitudinal resonance frequency fundamental at 3.05 kHz of the 54 mm long glass tube in air. The first longitudinal overtone can be seen as a weak peak near 6.10 kHz. In addition, there is some low frequency noise present.

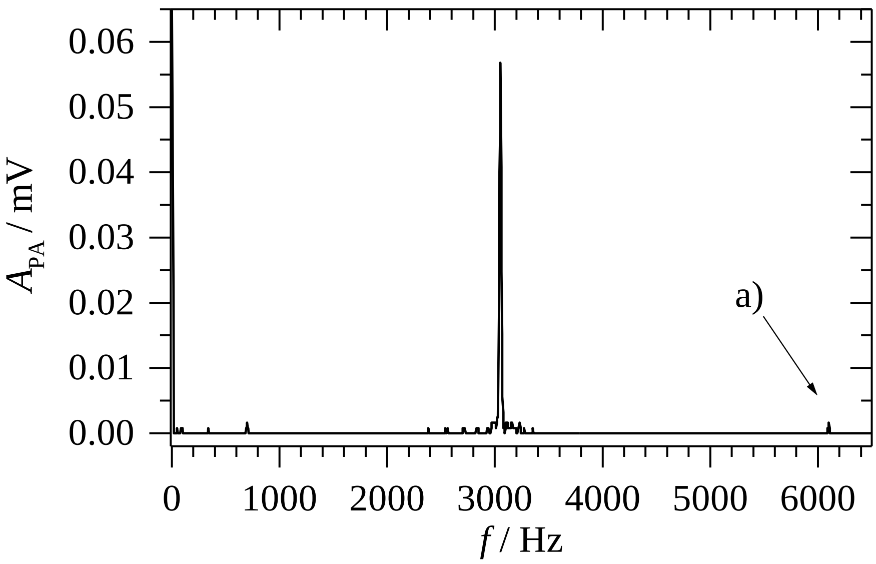

Figure 40 - Fourier-transform of the time domain photoacoustic signal, with the QCL-CERPAS modulated at 3.05 kHz. A is the magnitude (RMS) of the Fourier-amplitude. a) shows the position of the first longitudinal acoustic overtone of the resonator.

Results

Detection of Acetylene by mid-IR QCL CERPAS

Defined concentrations of acetylene in 1 atm N_2 were prepared on a gas handling vacuum line. Acetylene (BOC gas) was purified by repeated freeze-pump-thaw cycles under liquid N_2 cooling. Nitrogen from a high-purity nitrogen generator was added after passing through a cold trap at liquid N_2 temperature to remove some lower volatility impurities, in particular remaining traces of water. Gas pressures were measured with capacitance pressure gauges (Baratron). In a first step, about 10 mbar of acetylene was diluted with N_2 to a total pressure of about 1 atm in a 20 L glass container. A sample of this first dilution step was measured by FTIR spectroscopy, and the spectrum obtained was compared with a literature spectrum from the Pacific Northwest National Laboratory (PNNL database, Ref. 105) confirming the identity of acetylene and showing good quantitative agreement confirming our gas handling and dilution procedures. In further dilution steps, about 10 mbar of a mixture was further diluted with N_2 to a total pressure of about 1 atm in a 20 L glass container. After 4 - 5 such dilution steps, concentrations of acetylene in the low ppm to low ppb range in 1 atm N_2 were finally prepared and transferred to the measurement cell. In the cell, the pressure was typically reduced to 100 mbar (see below). Despite care taken to minimise water contamination, it was not possible to completely avoid water traces in our samples (typically some ppm water in 1 atm acetylene/N_2 mixture). Interferences due to water will be discussed below.

In the region accessible to the QCL laser system, acetylene has rotationally resolved transitions due to the R-branch of the $v_4 + v_5$ vibrational band; the strongest lines, $R(9)$ and $R(11)$, have peak cross sections of about 57 pm^2 at room temperature (RT) and at 1 atm air/N_2 pressure broadening. The region is affected by water absorptions. In trace gas analysis of air samples, it will be almost impossible to avoid sampling water as well. Even under laboratory conditions, it is very difficult to keep water vapour concentrations low enough that they will not affect trace measurements of acetylene in the low ppb region. Care has to be taken to choose a line for analysis which does not suffer from water interferences. The $R(11)$ line seems to be best suited, since it is strong and has no water lines in its vicinity. To demonstrate the effect of water interferences, and how to avoid these interferences, the $R(13)$ line at 1361.727 cm^{-1} was chosen. At 50 pm^2 peak cross section (RT, 1 atm air pressure broadening), the line is one of the strongest lines in the R-branch. It has two medium strength water absorption lines next to it, at higher and at lower wavenumbers, and a weak water line very close at slightly higher wavenumber (see Figure 41 for a simulation). At 1 atm pressure broadening, the two medium strength water lines combine their feet to effectively shift the baseline where the $R(13)$ line is, and the weak water line next to acetylene partially overlaps the $R(13)$ line (Figure 41), which in combination makes trace analysis of acetylene difficult. To avoid this interference, the sample was measured under reduced pressure to minimise pressure broadening. At 100 mbar total pressure (with N_2 as buffer gas), the acetylene line is well separated from the close weak water line, and the nearby medium strong water lines do not combine noticeably to shift the baseline. Diluting an air sample from 1 atm to 100 mbar decreases the number of analyte molecules by a factor of ten. However, since the acetylene lines become narrower, and peak absorption cross section thus increases by almost 10 (see Figure 41), the decrease in concentration is almost offset. For the $R(13)$ line the peak cross section increases from 50 pm^2 at 1 atm to 462 pm^2 at 100 mbar total pressure. At 100 mbar, photoacoustic signals are still supported; if anything, the microphones seem to be even slightly more sensitive in this region. As an additional benefit, ambient noise is better shielded from the measurement cell due to the pressure difference between outside and inside creating an acoustical impedance mismatching.

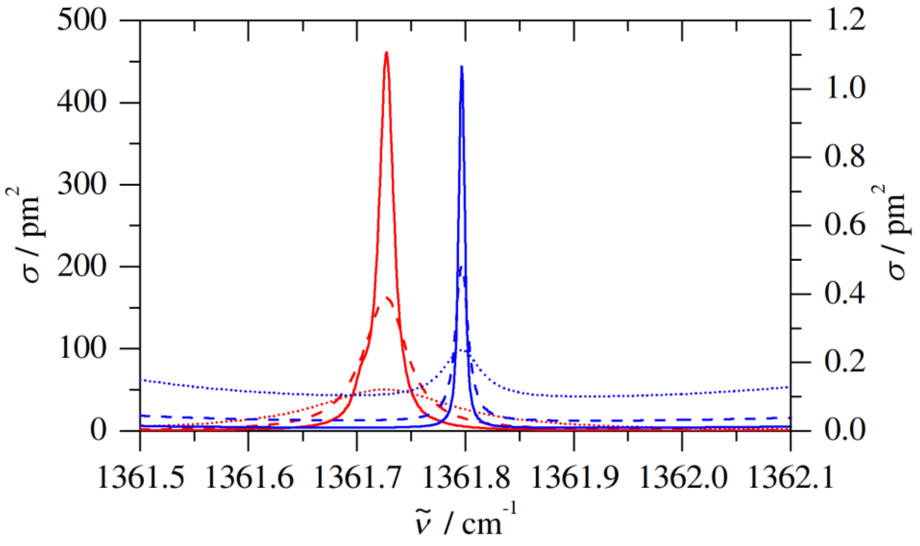

Figure 41 - Simulated spectra of acetylene (red; y-axis on the left) and water (blue; y-axis on the right), using spectral data obtained from a data base of water transitions (Ref. 103) and acetylene transitions (HITRAN 2012, Ref. 104), where the stick lines have been convoluted with 298 K Doppler broadening and 1 atm (dotted lines), 300 mbar (dashed lines) and 100 mbar (solid lines) air pressure broadening.

Figure 42 shows a measured CERPAS spectrum of 6.4 ppm acetylene in 1 atm N_2, reduced to 300 mbar total pressure in the photoacoustic cell and Figure 43 shows 360 ppb acetylene in 1 atm N_2 reduced to 100 mbar. The red line shows a Lorentzian fit of the *R*(13) line of acetylene and the blue curve a Lorentzian fit of the weak absorption line due to some residual water vapour. It is clear that working at 100 mbar almost completely avoids water interferences at the *R*(13) peak position.

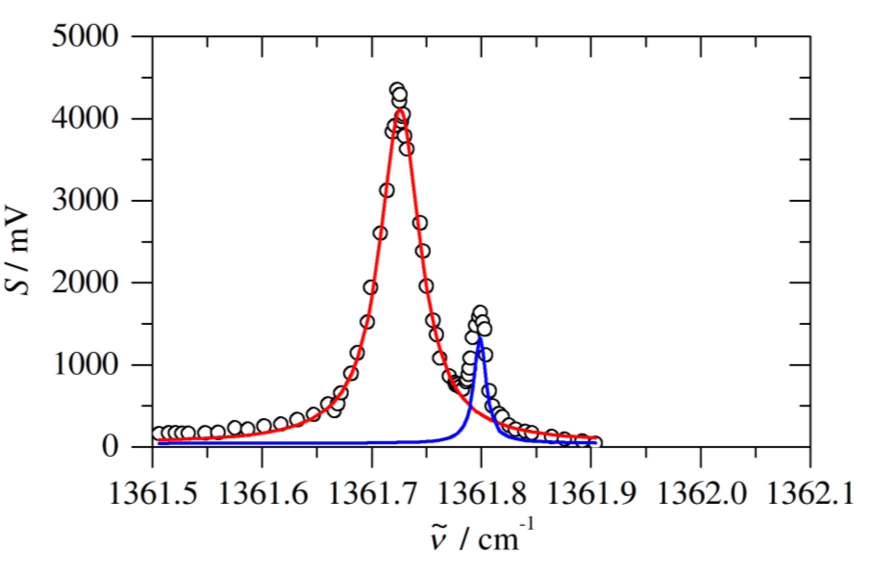

Figure 42 - CERPAS spectrum of 6.4 ppm acetylene in 1 atm N_2, reduced to 300 mbar total pressure (x10 amplification setting). The red line shows a Lorentzian fit of the *R*(13) line of acetylene, and the blue curve a Lorentzian fit of the weak absorption line due to some residual water vapour.

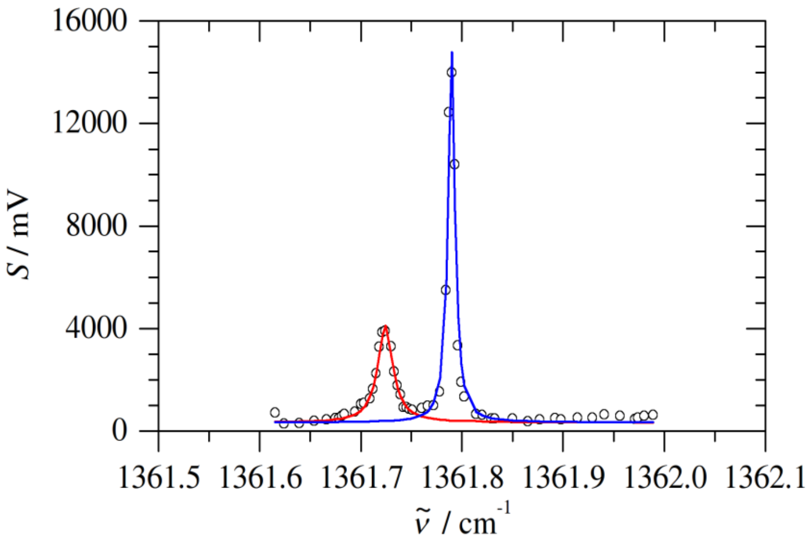

Figure 43 - CERPAS spectrum of 360 ppb acetylene in 1 atm N_2, reduced to 100 mbar total pressure. The red line shows a Lorentzian fit of the *R*(13) line of acetylene, and the blue curve a Lorentzian fit of the weak absorption line due to some residual water vapour.

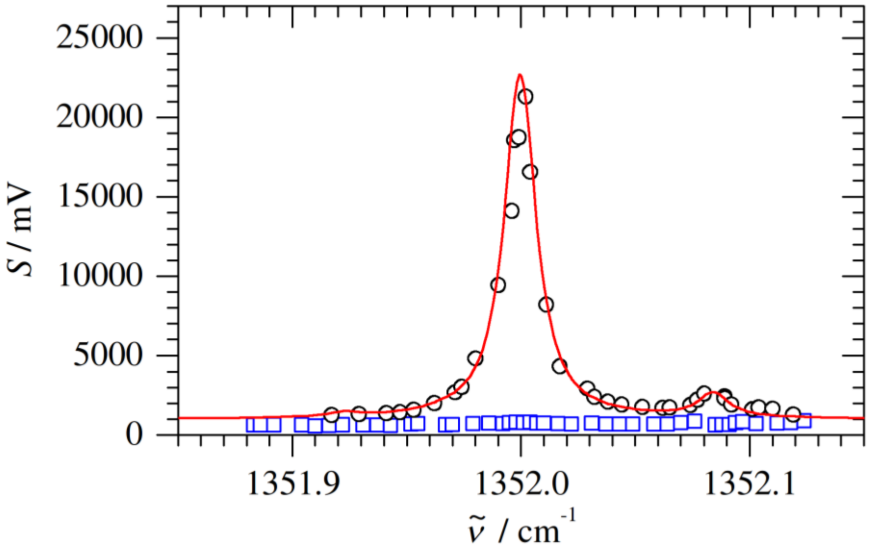

Figure 44 - CERPAS spectrum of the $R(11)$ line of 145 ppb acetylene C_2H_2 in 1 atm N_2, reduced to 100 mbar total pressure (circles, black), and a background measurement of 100 mbar N_2 (squares, blue). The red solid line is a simulated spectrum of C_2H_2 (HITRAN 2012, with 298 K Doppler broadening and 100 mbar air pressure broadening, including an offset.

To demonstrate the linearity of the detection scheme and to estimate a detection limit, acetylene mixtures in the range of high ppb to low ppb in 1 atm N_2 have been prepared and measured at 100 mbar total pressure, see Figure 45. Good linearity in the calibration plot is observed. The corresponding noise level at 1 s integration time is about 0.5 mV (x100 amplification setting); the corresponding noise equivalent detection limit for acetylene detection on the $R(13)$ line would be about 50 ppt in 1 s integration time. With a concentration of 50 ppt in 100 mbar and an absorption cross section $\sigma = 462$ pm^2, this corresponds to a noise equivalent absorption coefficient $\alpha \approx$ 6×10^{-10} cm^{-1} s$^{1/2}$ (1 s integration time), and assuming a linear power dependence, normalising the 100 mW QCL laser to 1 W gives 6×10^{-11} cm^{-1} s$^{1/2}$ W (1 s integration time and normalised 1 W laser power). These values are close to the values obtained previously for the 635 nm setup,[37] which shows essentially a balance between higher laser power available in this experiment (100 mW vs. 10 mW), but somewhat worse mirror reflectivities in the mid-IR (99.96 % vs. 99.988 %).

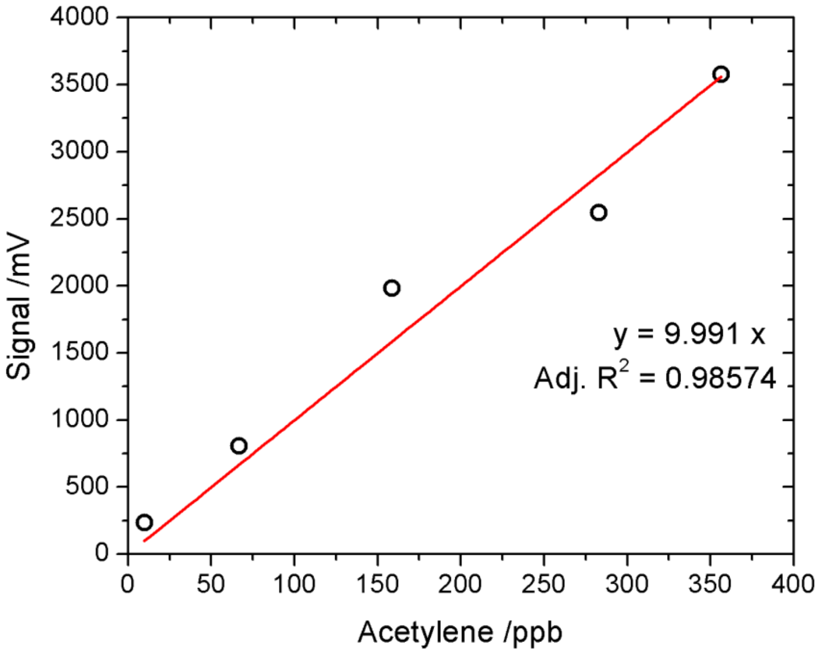

Figure 45 - Calibration plot for detecting acetylene on the peak absorption of the *R*(13) line. Acetylene in 1 atm N_2, reduced to 100 mbar total pressure (x100 amplification setting). The noise equivalent detection limit at 1 s integration time is 50 ppt acetylene.

Detection of Nitromethane by mid-IR QCL CERPAS

Analogous to the sample preparation described before, defined concentrations of nitromethane in 1 atm N_2 have been prepared on a gas handling vacuum line. Nitromethane (AlfaAesar, 98+ %) was purified by repeated freeze-pump-thaw cycles. Nitrogen from a high-purity nitrogen generator was added after passing through a cold trap at liquid N_2 temperature to remove some lower volatility impurities, in particular remaining traces of water. Gas pressures were measured with capacitance pressure gauges (Baratron). In a first step, about 10 mbar of nitromethane was diluted with N_2 to a total pressure of about1 atm in a 20 L glass container. A sample of this first dilution step was measured by FTIR spectroscopy, and the spectrum obtained was compared with a literature spectrum from the Pacific Northwest National Laboratory (PNNL database, Ref. 105), confirming the identity of nitromethane and showing good quantitative agreement confirming our gas handling and dilution procedures. In further dilution steps, about 10 mbar of a mixture was further diluted with N_2 to a total pressure of about 1 atm in a 20 L glass container. In the measurement cell, the pressure was typically reduced to 75 mbar to avoid water interferences since it was not possible to completely avoid traces of water vapour in our samples.

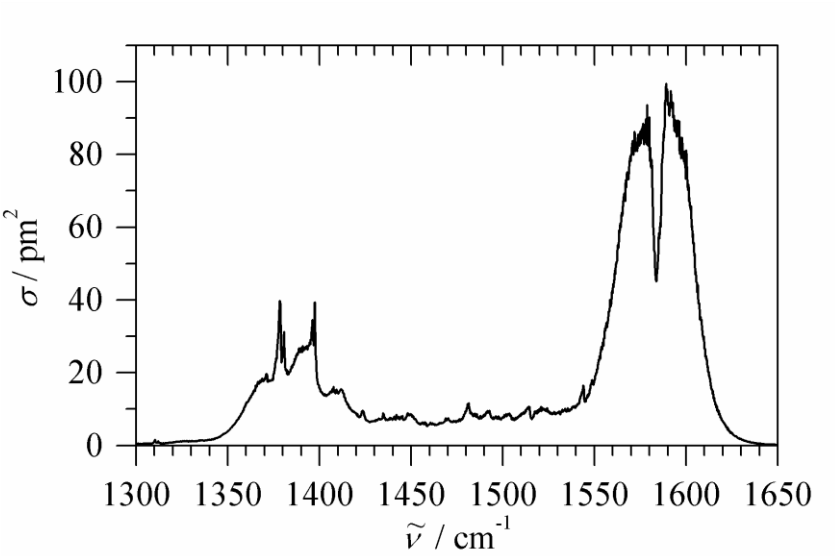

Figure 46 - PNNL reference spectrum of nitromethane in 1atm N_2 (Ref. 105).

Figure 46 shows an overview literature FTIR spectrum of nitromethane[105] in the 1300 - 1650 cm^{-1} region. With our QCL laser, we cannot access the stronger absorption features near 1580 cm^{-1} (asymmetric NO_2 stretching vibration). The weaker features in the 1350 - 1400 cm^{-1} range (symmetric NO_2 stretching vibration) can be accessed, but they suffer from water absorptions as interferences, as indicated in Figure 47. For reliable spectroscopic detection of nitromethane, a spectral region should be chosen which is as less affected by water absorption. As an additional requirement, the absorption for nitromethane quantitative analysis should be a narrow peak and not a broad absorption feature to allow discrimination against possible interferences by a short spectral scan. This will greatly increase selectivity of the detection scheme. Taking these two considerations into account, the absorption feature at 1380.65 cm^{-1} was selected for spectroscopic detection, as indicated by the arrow in Figure 47. Figure 48 shows a CERPAS spectrum of 670 ppb nitromethane in 1 atm N_2, reduced to 75 mbar total pressure to minimise the effect of nearby water absorption lines (the feature on the right at 1380.624 cm^{-1}, see Figure 48). Comparing the CERPAS spectrum with the FTIR spectrum, a narrowing of the absorption and some additional structure is noted. This is not unexpected, since the CERPAS spectrum at 75 mbar total pressure has much less pressure broadening than the 1 atm reference spectrum.

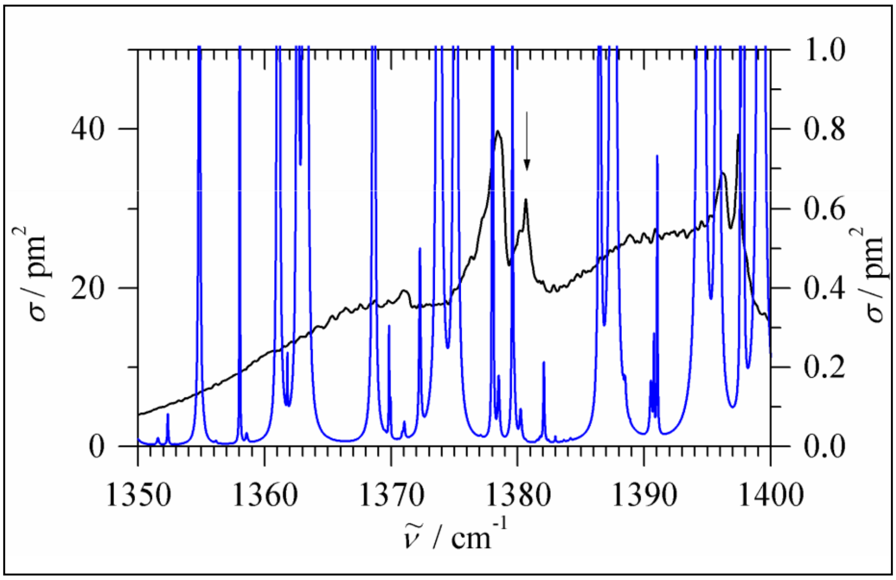

Figure 47 - Black line, *y*-axis on the left: PNNL reference spectrum of nitromethane in 1 atm N_2 (Ref. 105). Blue line, *y*-axis on the right: Water absorptions are simulated from a

database,[105] where the stick lines have been convoluted with 298 K Doppler broadening and 1 atm air pressure broadening.

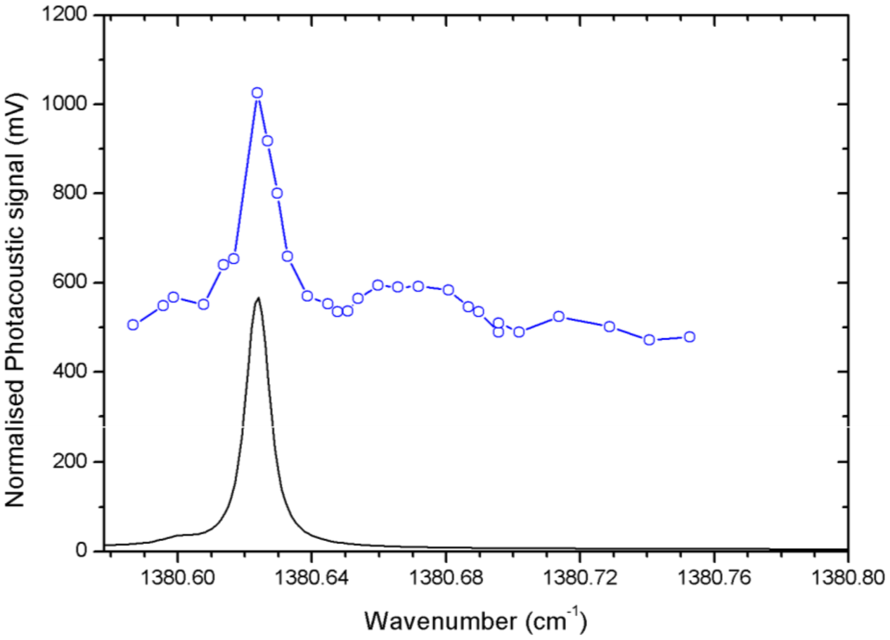

Figure 48 - CERPAS spectrum of 670 ppb nitromethane in 1 atm N_2, reduced to 75 mbar total pressure (x100 amplification setting), open circles/blue line. The feature at 1380.624 cm^{-1} is a weak water line due to water traces present in the sample. The black line shows water absorptions simulated from a database,[105] where the stick lines have been convoluted with 298 K Doppler broadening and 75 mbar air pressure broadening, scaled so that the intensity matches the CERPAS spectrum.

To demonstrate linearity of detection and to extrapolate a detection limit, six different concentrations of nitromethane between 71 ppb and 23 ppm have been measured. A plot of the signal of the nitromethane peak at 1380.674 cm^{-1} versus concentration (in 1 atm N_2, but further reduced to 75 mbar total pressure) is shown in Figure 49. Good linearity is observed. The calibration line intersects the 0.5 mV noise floor (1 s integration time) at a concentration of about 1 ppb, which thus gives an estimate for the noise equivalent detection limit at1s integration time by our CERPAS approach. This value is in good agreement with the 50 ppt noise equivalent limit for acetylene, taking into account the much larger absorption cross-section for the *R*(13) acetylene line (= 462 pm^2) compared to the 1380.674 cm^{-1} nitromethane feature (about 30 pm^2 in the 1 atm reference spectrum; note that at 75 mbar, the true absorption cross section might be higher due to reduced pressure broadening).

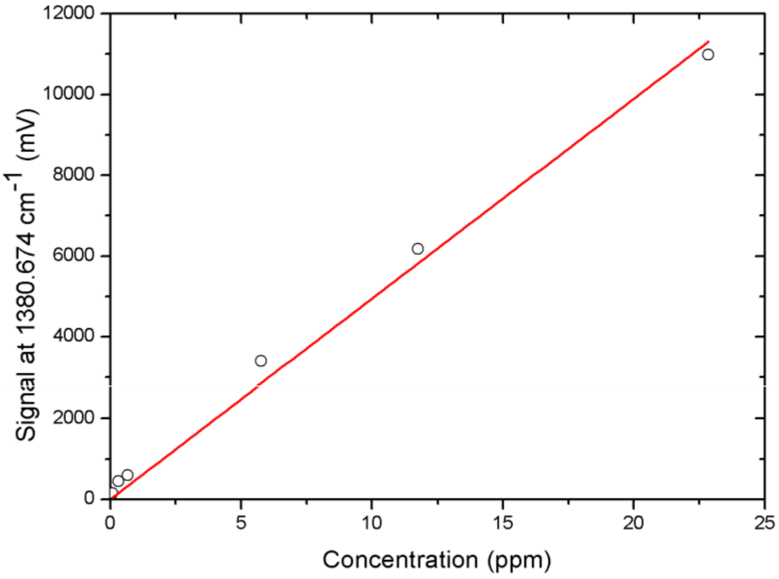

Figure 49 - Calibration plot for nitromethane on the peak absorption at 1380.674 cm^{-1}. Nitromethane in 1 atm N_2, reduced to 75 mbar total pressure (x100 amplification setting). The noise equivalent detection limit at 1 s integration time is about 1 ppb nitromethane.

To conclude, a mid-IR spectrometer using a 7.4 um EC-QCL and a V-shaped optical cavity composed of three highly reflective mirrors capable of trace gas detection has been demonstrated. The V-shaped cavity geometry avoids the unwanted back-reflection whilst allowing efficient coupling of light into the optical cavity. This gives rise to a power build-up with the cavity and also stabilises the QCL to the optical cavity. The cavity has two acoustic resonator tubes within the beam path; these resonators are equipped with microphones which enable photoacoustic detection of light absorption. Since light is coupled into the cavity periodically at a frequency matching the acoustic resonance frequency of the resonators, sensitive detection of absorption is possible (resonant photoacoustics) which is enhanced by the power build up in the optical cavity (cavity-enhanced resonant photoacoustic spectroscopy, CERPAS). The QCL is “broadly” tuneable in the mid-IR around 7.5 µm. With this apparatus, a noise-equivalent detection limit of 50 ppt C_2H_2 in 100 mbar N_2 is obtained at 1 s integration time. Nitromethane was also analysed at a further reduced pressure of 75 mbar of N_2 with a detection limit of 1 ppb.

After the completion of this work, we became aware of a recent publication by Tittel *et al.*[106] where a similar approach has been used to measure water at 960 cm^{-1} with a noise equivalent absorption of 1.9 $x10^{-10}$ cm^{-1} $Hz^{-1/2}$ with a normalised noise equivalent absorption of 1.1 x 10^{-11} cm^{-1} W $Hz^{-1/2}$. The two methods are comparable in performance.

4. Cavity Enhanced Resonant Photoacoustic Spectroscopy – Explosives' Vapours

Based on the characterisation of the mid-IR CERPAS setup described in the previous chapter (chapter 3), the setup is used in a particularly relevant and also challenging application of ultratrace gas analysis, the detection of explosives' vapours by IR spectroscopy.

This project was funded under the Innovative Research Call in Explosives and Weapons Detection (2010), a cross-government programme sponsored by a number of government departments and agencies under the CONTEST strategy, the University of Sheffield and Smiths Detection Watford Ltd; the work described here has been undertaken in collaboration with Dr. Mark Stringer, a research associate in Dr. Hippler's group.

Introduction

Vapour detection of explosives is a challenge for physical chemistry due to very low vapour concentrations under ambient conditions (see Table 1)[107,108]. Actual vapour pressures might even be substantially lower due to concealment. It is therefore clear that detection with extreme sensitivity is required. In addition, detection should be highly selective in order to avoid false positive alarms. Advanced explosives detection techniques are therefore required for crime prevention. Ion mobility spectrometry (IMS) is widely used which is extremely sensitive (sub-ng levels), but to minimise false alarm rates, sensitivity is compromised.[109] Optical spectroscopy provides an alternative for vapour detection of explosives. Absorption of light at characteristic wavelengths allows unique identification, and compounds in a mixture are differentiated by their spectroscopic signatures (see Figure 50). Due to very low vapour pressures, extremely sensitive optical detection is required.

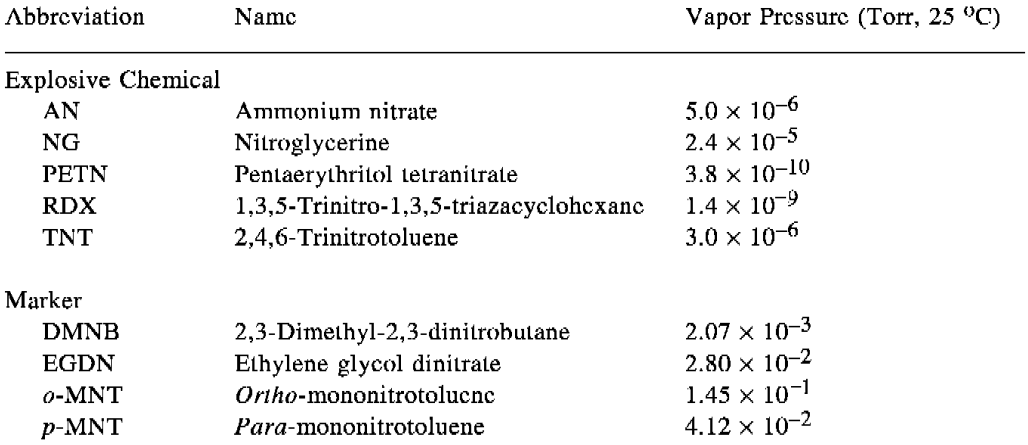

Abbreviation	Name	Vapor Pressure (Torr, 25 °C)
Explosive Chemical		
AN	Ammonium nitrate	5.0×10^{-6}
NG	Nitroglycerine	2.4×10^{-5}
PETN	Pentaerythritol tetranitrate	3.8×10^{-10}
RDX	1,3,5-Trinitro-1,3,5-triazacyclohexane	1.4×10^{-9}
TNT	2,4,6-Trinitrotoluene	3.0×10^{-6}
Marker		
DMNB	2,3-Dimethyl-2,3-dinitrobutane	2.07×10^{-3}
EGDN	Ethylene glycol dinitrate	2.80×10^{-2}
o-MNT	*Ortho*-mononitrotoluene	1.45×10^{-1}
p-MNT	*Para*-mononitrotoluene	4.12×10^{-2}

Table 1 - Vapour pressures of some explosives and common markers at room temperature from Ref. 108.

Prior work using laser photoacoustics (LPAS) with a quantum cascade laser has been reported by Patel *et al.*[110] In their work, their apparatus also characterised acetylene (2.5 ppb at 1σ, where a signal to noise ratio of 1) as well as TNT (0.1 ppb at 1σ).

However, there is a lack of detail in the methodology and several important details are missing such as how the spectra were collected, optical pathlength utilised, whether resonant photoacoustics were utilised, etc. A rough comparison of the sensitivity can be made. For acetylene, mid-IR CERPAS is more sensitive by 1 order of magnitude, (0.14 and 2.5 ppb respectively) while for TNT, CERPAS is less sensitive by 1 order of magnitude (1.2 ppb and 0.1 ppb). It should be noted that acetylene is a relatively easy gas to detect and analyse especially with IR absorption spectroscopy. From the results reported, Patel appears to suggest that TNT is easier to detect compared to acetylene.

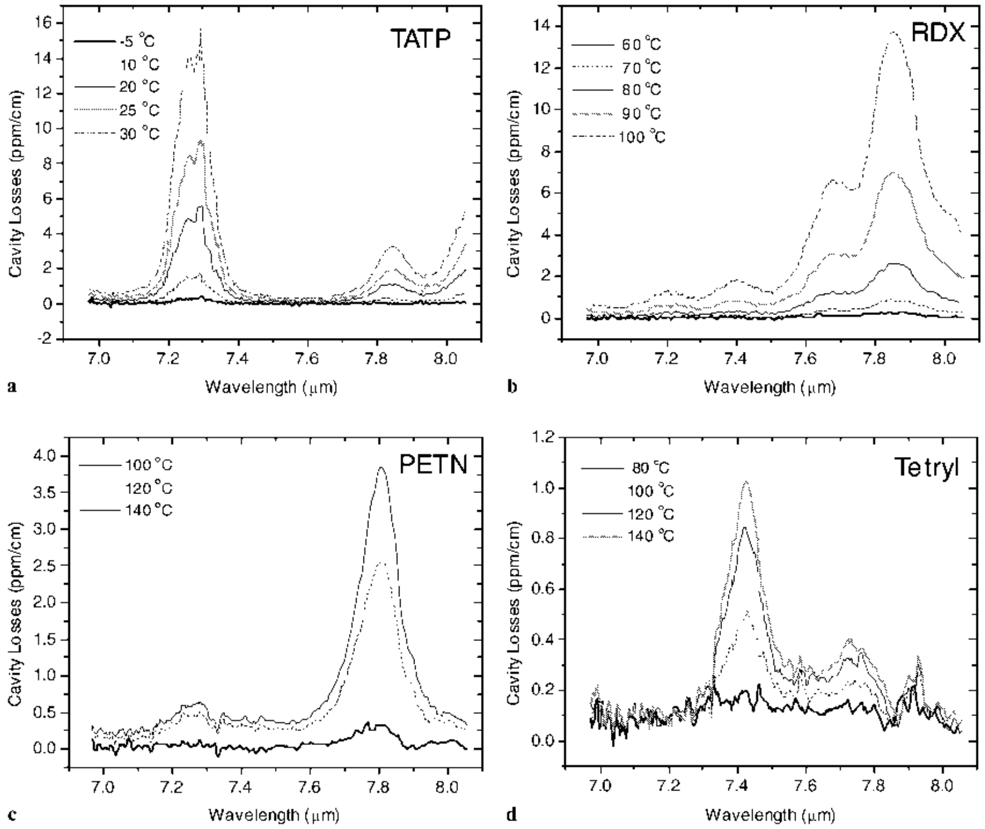

Figure 50 - Mid-IR absorption spectra of some explosives' vapours, in the 7-8 μm region (figure adapted from Ref. 111).

In this chapter, the mid-IR CERPAS apparatus described in the previous chapter is used to detect explosives’ vapours with quantum cascade lasers lasing in the mid-IR near 7.5 μm. In this region, strong vibrational absorptions occur which are characteristic for explosives, in particular but not exclusively vibrations of the NO_2 group (see Figure 50). Different explosives have characteristic shifts which allow their discrimination. Vapour-phase spectra of some common explosives (e.g., TNT, TATP) and explosives markers or taggants (e.g., DNT, DMNB) are acquired and interferences are assessed. The technique can be extended to other spectral regions as well which are characteristic for explosives, their precursors or decomposition products.

Experimental

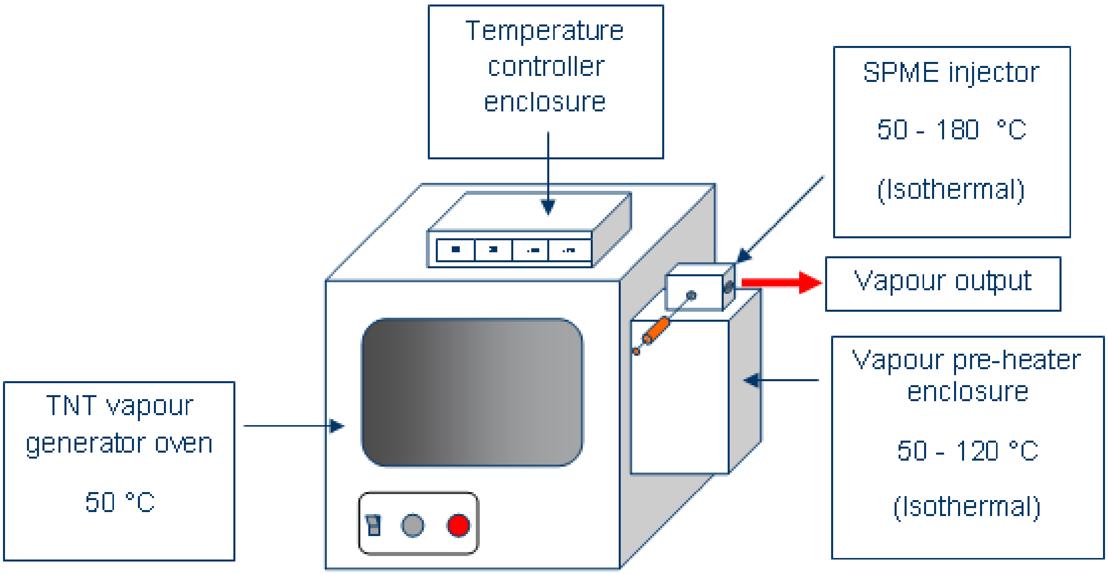

Figure 51 - Schematic of vapour generator (on loan from Smiths detection Watford Ltd., a collaborator and sponsor of this project).

Defined vapour concentrations are generated in a home-built vapour generator (Smiths Detection Watford Ltd, following a design in Ref. 112), see Figure 51. In this generator, a small coil containing the solid from which vapour is to be measured (e.g., TNT) is placed in an oven kept at a controlled temperature between typically 35-55

°C. A low flow of nitrogen (typically 10 mL/min) transfers the equilibrium vapour; by further diluting this flow with air or nitrogen (up to 6 L/min), low vapour concentrations are generated in a reproducible way. After passing a hot injector port, the vapour output is then transferred via specially coated 1/4" steel tubing (Silcosteel) to the acoustic resonators within the optical cell. The coupling between the 1/4" transfer line and the 1/8" inlet of the resonator is "loose", that is the resonator only samples the 4-5 L/h at atmospheric pressure, and disregards any excess flow. An external pump maintains a defined pressure (typically 300 mbar) within the measurement cell, as measured by capacitance pressure gauges (Baratron). The hot injector port allows inserting a solid-phase microextraction (SPME) fibre into the flow. The SPME fibre can absorb vapours above solids or liquids (headspace sampling) and releases these vapours at the elevated temperature (typically 50 - 100 °C) in the injector port. Photographs of the final experimental set-up are shown in Figure 52.

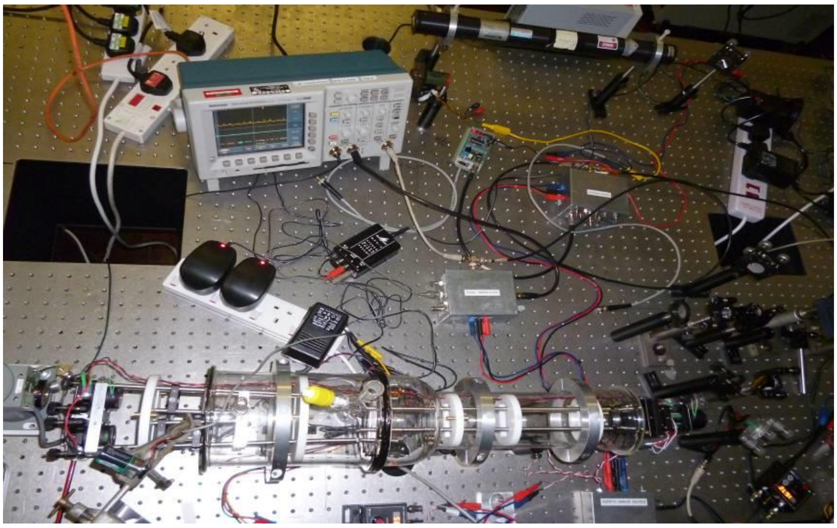

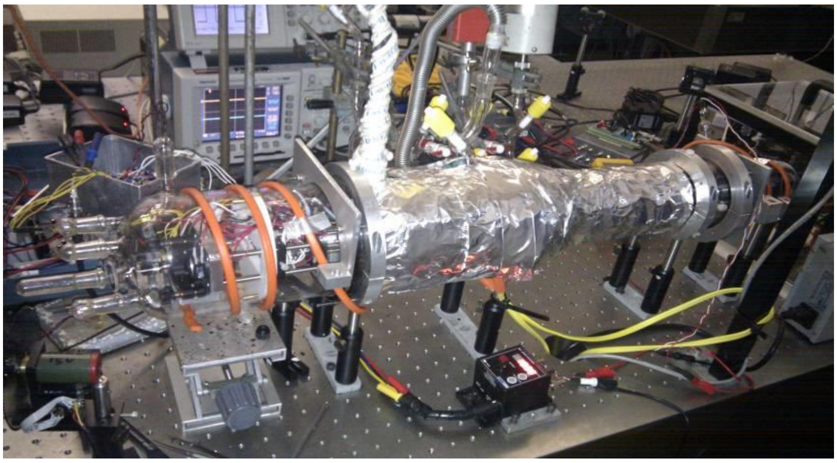

Figure 52 - Photographs of the open (top) and closed (bottom) optical cell.

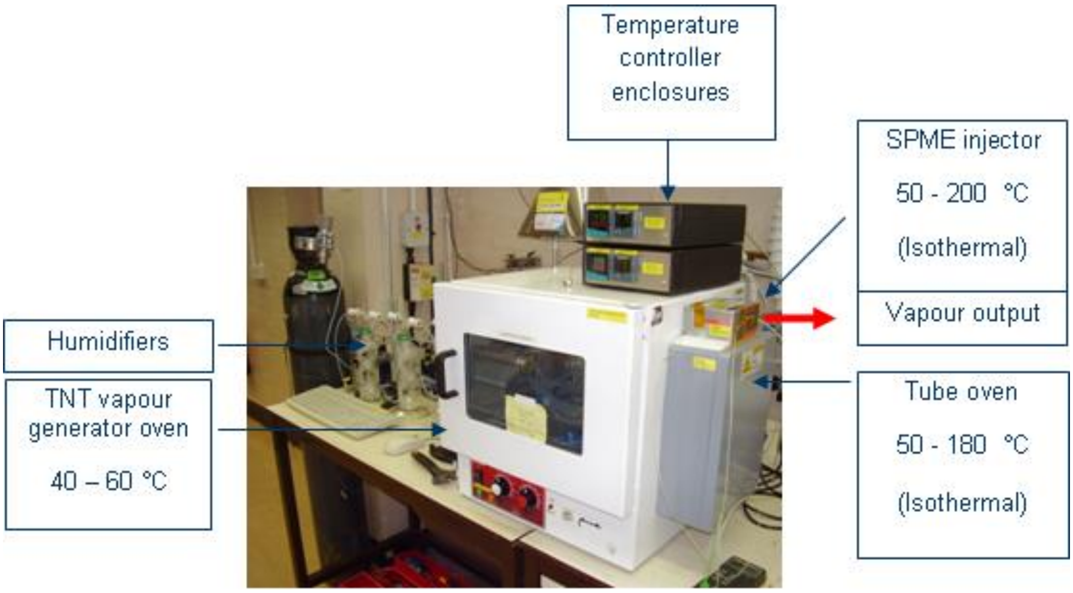

Figure 53 - Photographs of the vapour generator system (provided by Smiths Detection Watford Ltd.)

At a wavelength away from water absorption lines, a ringdown time of $\tau = 2$ μs was measured, corresponding to an effective optical path length of 600 m within the empty optical cavity. A mirror reflectivity of $R = 99.88$ %, a finesse $F = 2500$ and quality factor $Q = 5 \times 10^8$ of the optical cavity follow. These measurements were made at the end of 2011. At a repetition at the end of 2012, the ringdown time of the empty cavity fell to $\tau = 1$ μs, corresponding to an effective optical path lengths of 300 m, R = 99.75 % and finesse F = 1250. This deterioration of performance is most likely due to contamination of the mirrors, possibly due to condensation, and can probably be rectified by taking the cell apart and cleaning the mirrors carefully.

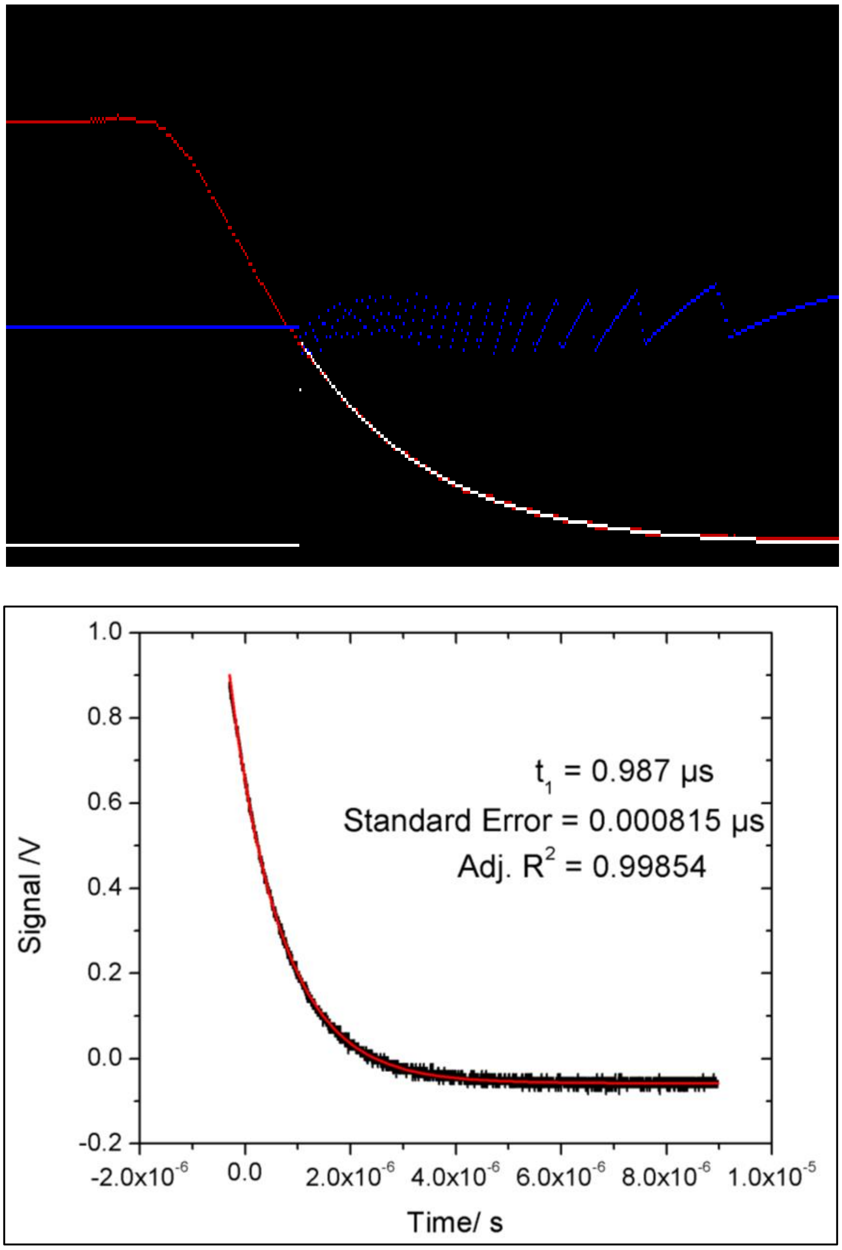

Figure 54 - Screenshot of an exponential decay (red), together with an exponential fit (white) and residuals (×10, blue) for a decay time τ = 1 μs, as observed with the V-shaped cavity near 1346.0 cm^{-1} (weak water line), open to lab air.

Mid-IR CERPAS measurements

Water interferences

In mid-IR absorption spectroscopy, water absorption backgrounds are a fundamental interference due to the ubiquitous presence of water. Even small traces of water can severely interfere with ultratrace gas detection due to the high sensitivity of measurements. This has the potential to severely limit the explosives vapour detection capability. At first, looking at the water vapour absorption spectrum, there was the expectation that there should be spectral regions where there is no significant absorption due to water (see Figure 55).

However, on closer inspection, it becomes apparent that at atmospheric pressure the water absorption lines have broad spectral wings due to pressure broadening which overlap to form an almost continuous absorption (see Figure 56).

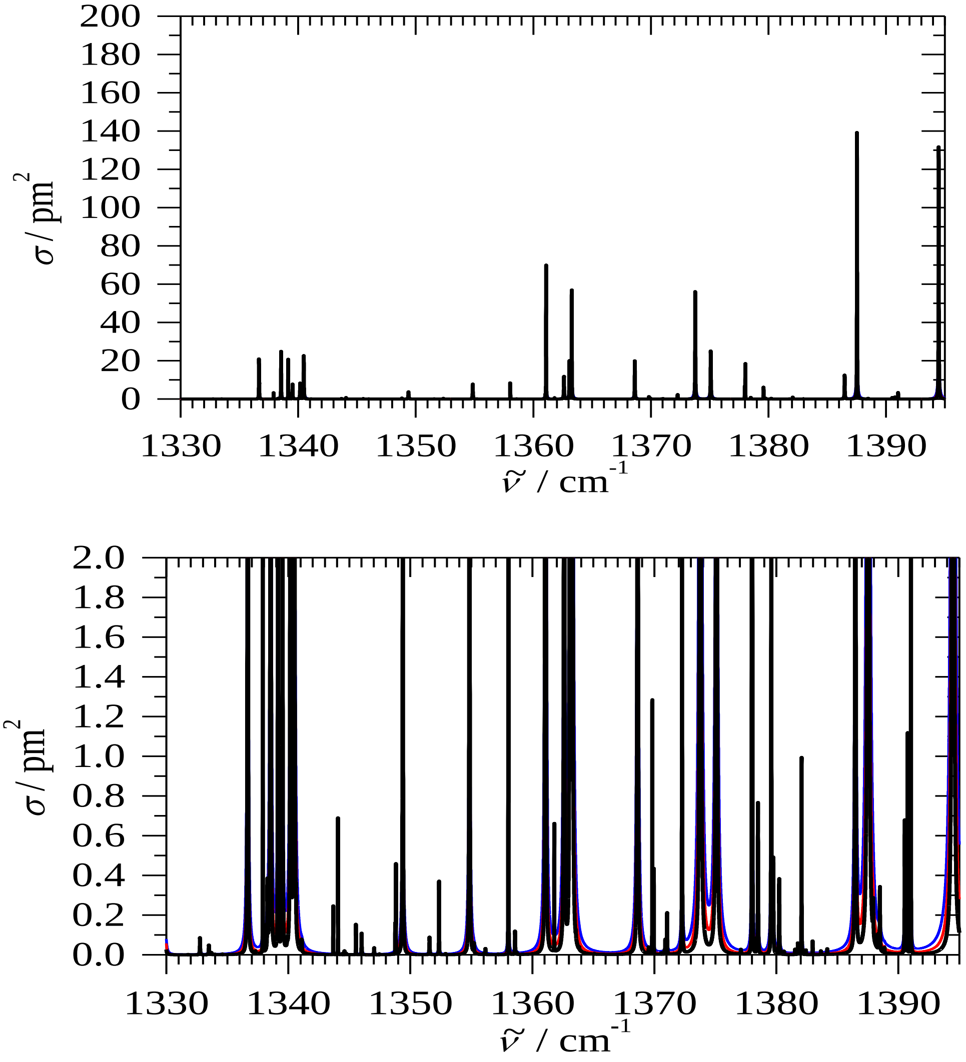

Figure 55 - Absorption cross sections of water vapour, at different full scales. A stick spectrum from Ref. 103 was convoluted with RT Doppler and 1 bar air pressure broadening. The colours represent different the cross sections at different pressure: blue 1 atm, red 300 mbar, black 100 mbars.

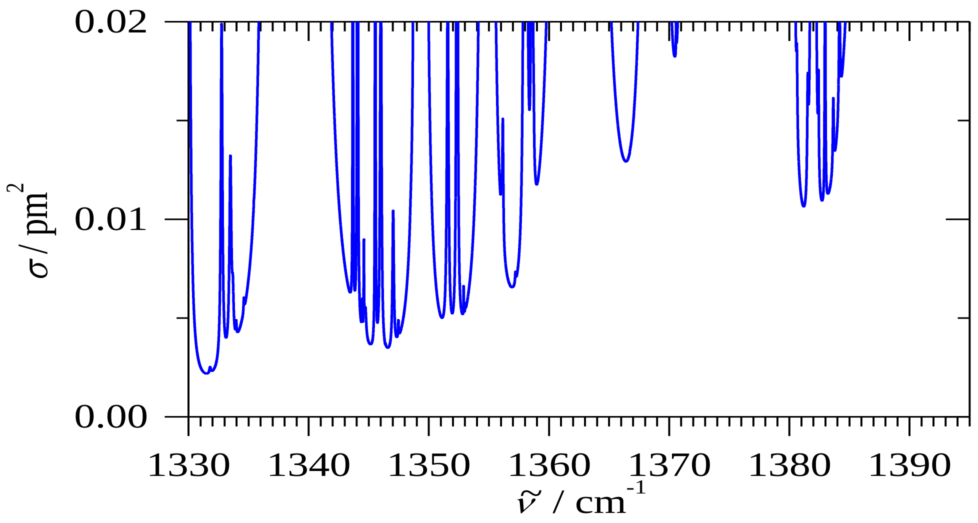

Figure 56 - Detail of the water absorption spectrum of Figure 55. Stick spectrum from Ref. 103 with room temperature Doppler and 1 bar air pressure broadening.

This continuum is very low; whereas peak absorption cross-sections of water in the spectral range which is used for explosives vapour detection reach about 15 pm^2, the continuum has a representative cross section of only 0.005 pm^2. However, due to the ubiquitous presence of water, even this very low remaining absorption is enough to mask the very weak explosives vapour absorptions. This is not a problem at all for TATP, which has a relatively high vapour pressure and can therefore be seen very clearly, but it is difficult to detect say TNT vapour against this background. Background cancellation by the two resonators works to an extent, but cannot completely eliminate this problem. To reduce the introduction of water as much as possible, the apparatus is purged with a flow of nitrogen, and the vapour generator uses nitrogen as flow gas, and not humid air. Including a cold trap filled with dry ice (CO_2) in the nitrogen and air supply line to the vapour generator and to the sampling cell almost completely removes any traces of water left.

If water contamination cannot be avoided, then a possibility to minimize its effect is to take measurements under reduced pressure. Simulations of the pressure dependence of water absorptions (see Figure 57) were performed, and found that by reducing the working pressure from 1 bar to 0.5 or 0.2 bar, the water continuum is reduced significantly due to reduced pressure broadening. Photoacoustic detection at reduced pressure has also the advantage that environmental noise from outside the enclosure is much reduced. It does not make the experimental set up more involved, since a pump has to be used anyway to flow sample into the enclosure for analysis. In the range of the mid-IR QCL used, there are several distinct wavenumbers which are suitable for measuring broad absorption features such as TNT vapour without much interference from water (see Figure 57).

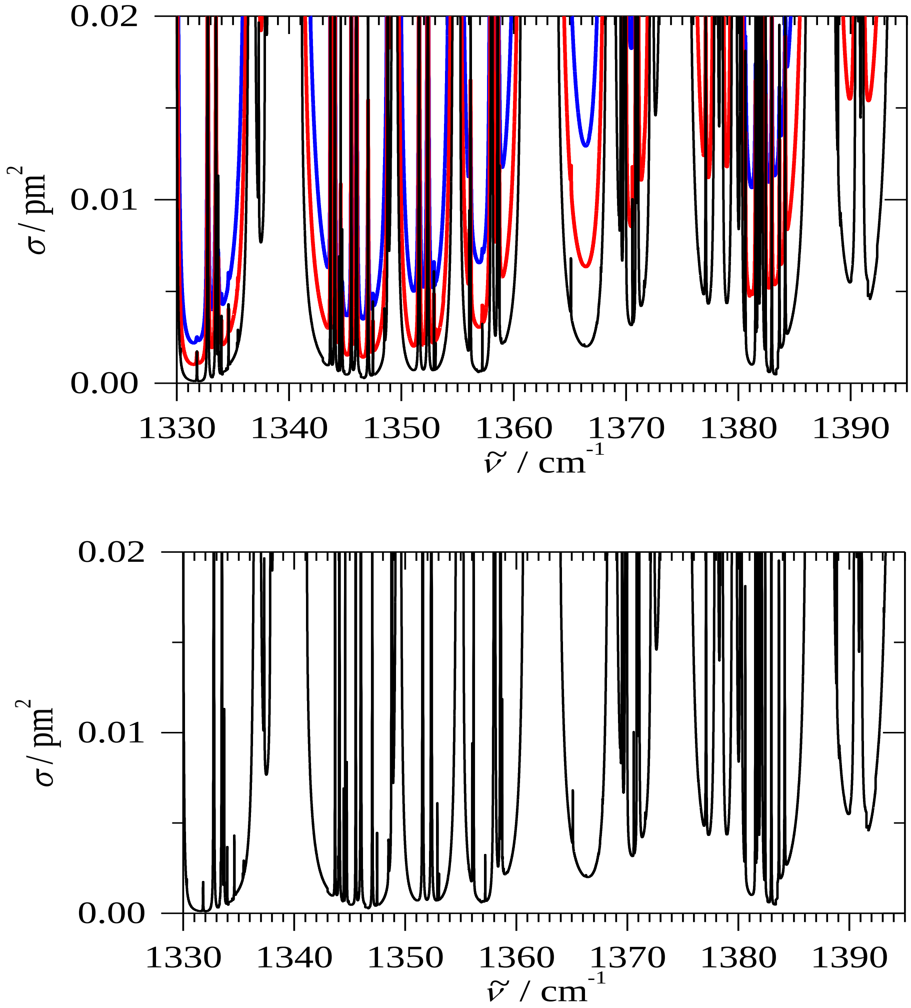

Figure 57 - Absorption cross sections of water vapour, simulated for 1 bar (blue curve), 0.5 bar (red curve), and 0.2 bar (black curve) air pressure.

Interferences from vapours such as ethanol and n-hexane

Water is a small molecule with large rotational constants resulting in rotationally resolved absorption lines in the IR. These lines can be avoided if pressure broadening is minimised. Medium sized and large molecules, however, most often have very broad vibrational absorption features without rotational resolution under standard conditions. Although the spectral region around 1350 cm^{-1} has been chosen because it encompasses characteristic absorptions of explosives vapours, other molecules have sometimes broad absorption features which may extend into this range and thus interfere with explosives detection. Examples are provided by ethanol and n-hexane which have CH_3-bending vibrations near 1400 cm^{-1} with *P*-branch wings extending to lower wavenumbers (see Figure 58 and 59). Since concentrations of these volatile solvents can easily exceed concentrations of explosives vapours, false positive alarms may result. False positive alarms can be minimised, however, by spectral discrimination. Explosives often have a pronounced, relatively sharp peak absorption between 1340 and 1380 cm^{-1} with a FWHM of less than 20 cm^{-1} (see Figure 59 for TATP, and also the following sections). By taking measurements on-peak and off-peak of such an absorption feature, selectivity is greatly increased and allows positive identification since interferents have a different spectral behaviour. Although spectral discrimination will minimise false positive alarms, such interfering absorptions can potentially mask explosives signatures and temporarily blind the detector. In "real" applications, it has to be investigated further how this will affect and limit the feasibility of mid-IR detection of explosives vapours in practice.

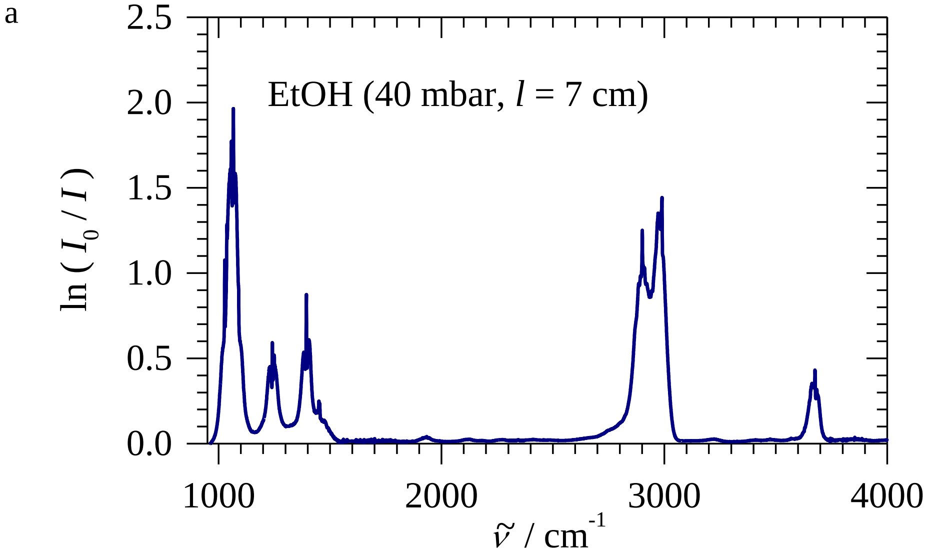

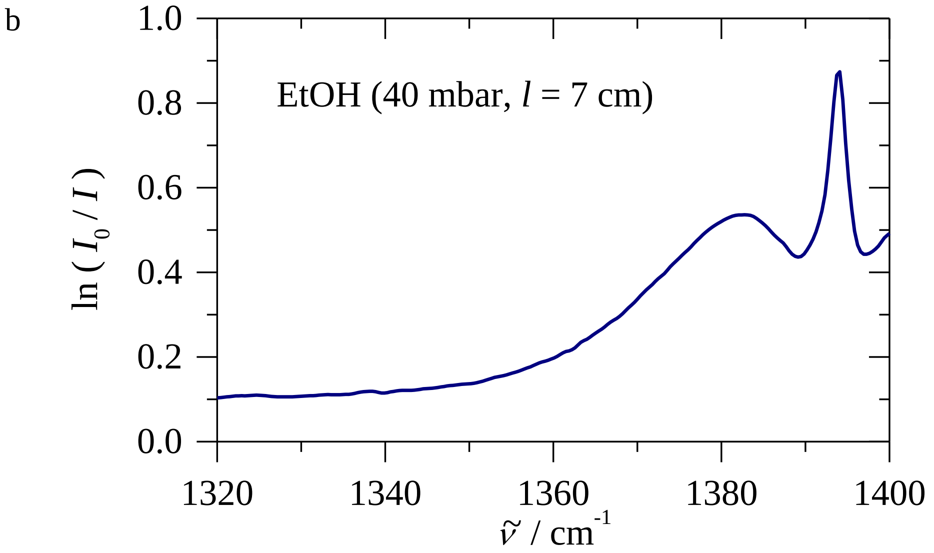

Figure 58 - a) Overview FTIR absorption spectrum of ethanol vapour (40 mbar, l = 7 cm). b) Magnified FTIR absorption spectrum covering the QCL lasing range

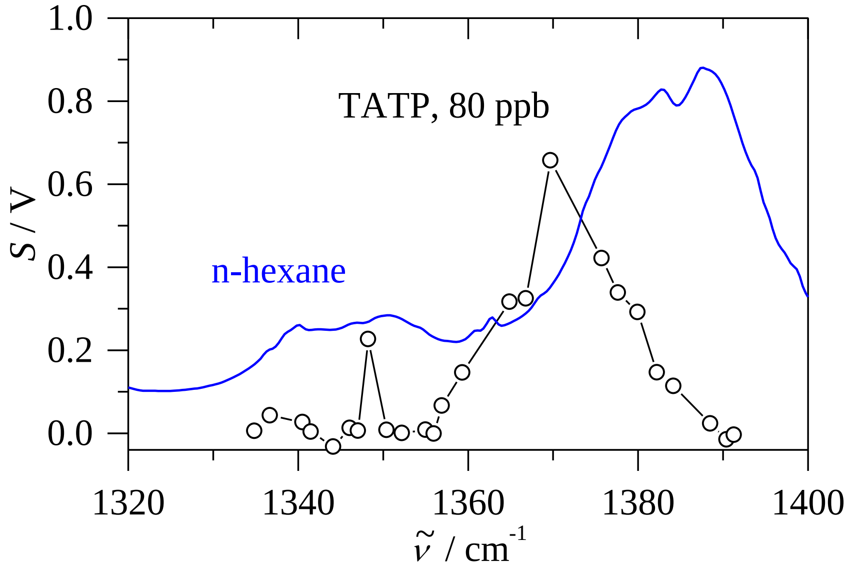

Figure 59 - FTIR spectrum of n-hexane (blue) with a TATP measurement superimposed (black).

Measuring 2,4,6-TNT vapour in a static cell at 1 atm

In one measurement configuration, the cell is filled with 2,4,6-TNT vapour traces diluted in nitrogen, as provided from the vapour generator. In this experiment, a 10 mL/min nitrogen flow over purified TNT (supplied by The Royal Ordnance plc, Bridgewater) at 56 °C is saturated with TNT vapour; this flow is then further diluted by pure N_2 to obtain a defined concentration of TNT in 1 atm N_2. The mixture is transferred to the cell which has been evacuated previously. Measurements are taken at 940 mbar total pressure in the cell under static conditions (no flow). Only the sampling photoacoustic resonator is used (the reference resonator experienced a technical fault in this particular experiment). Signals are taken at 1347 cm^{-1} (7.41 µm), close to the peak of the symmetric NO_2-stretching vibration of TNT (Figure 60).

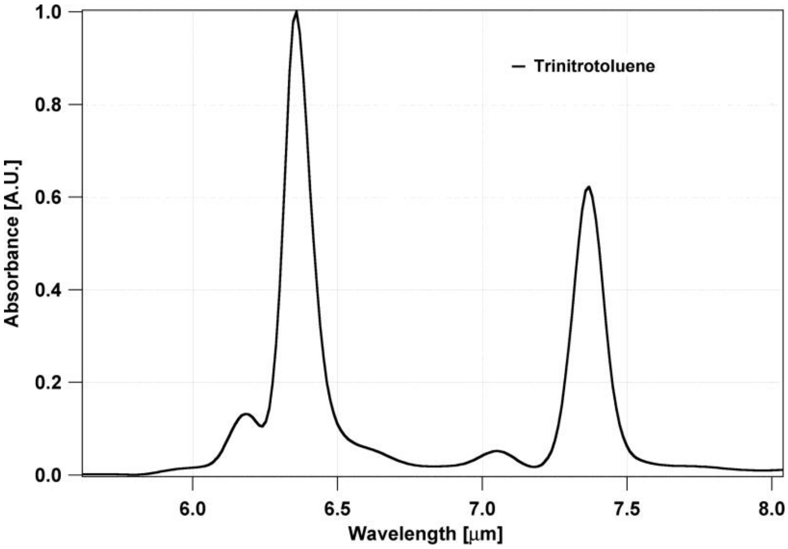

Figure 60 - TNT absorption spectrum (reproduced from Ref. 113).

Setting the vapour generator to 28 ppb TNT in N_2, a good linear correlation is observed between photoacoustic signals (as given from the lock-in detectors) and the optical resonance strengths (measured with a separate lock-in detector; proportional to the optical power circulating in the cavity). Measurements were then repeated with 10 ppb and 5 ppb TNT. The photoacoustic signal strength shows good linearity with the TNT vapour pressure (see Figure 61 and Figure 62). In these experiments, each data point corresponds to a measurement with 1 s integration time. In a separate experiment, the noise level of the photoacoustic setup (without laser on) was also determined, given as the standard deviation σ of the baseline signal. If this noise level is included in the calibration plot of Figure 62, a noise equivalent detection limit of 1.2 ppb TNT in 1 atm N_2 at 1 s integration time is deduced. In principle, sub-ppb detection of TNT in 1 atm would be possible with longer integration time, stronger laser power, or better cavity mirrors with more power build-up in the optical cavity.

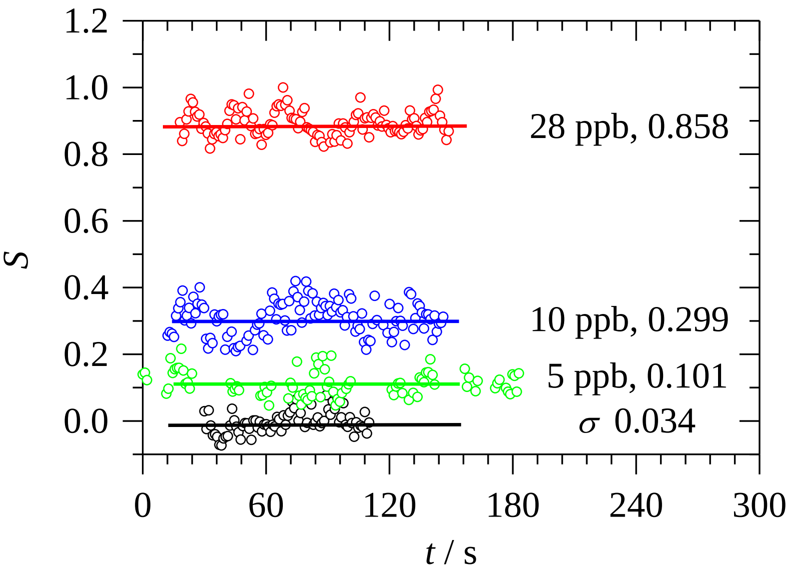

Figure 61 - Photoacoustic signals for 28 ppb, 10 ppb and 5 ppb TNT in 1 atm N_2, together with noise background. The noise background has a standard deviation of 0.034 (arbitrary units; voltage signal from lock-in detector) which may serve as the noise limit for TNT detection in the current setup. Each data point represents a measurement with 1 s integration.

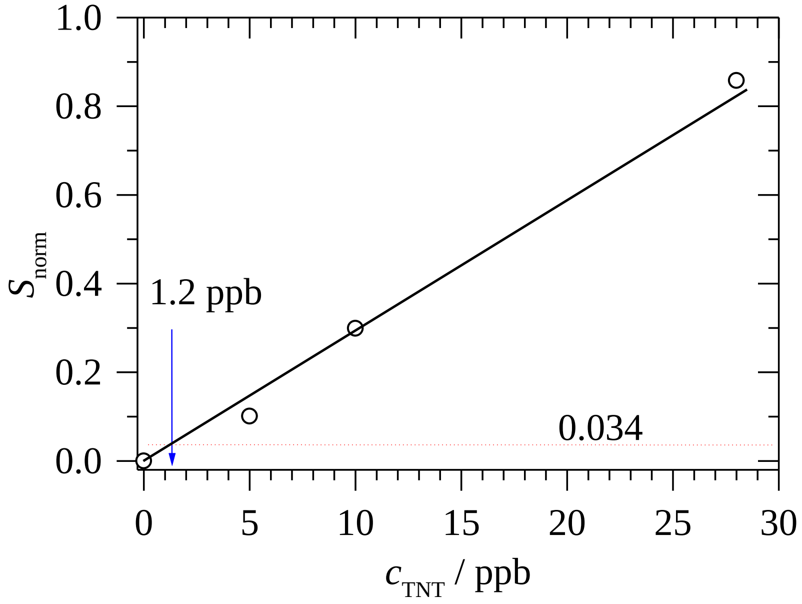

Figure 62 - Calibration plot of photoacoustic signal versus TNT vapour pressure in 1 atm N_2. The noise level (from the standard deviation of the background in Figure 61) and the resulting noise-equivalent detection limit at 1 s integration time are indicated.

Measurements under flow conditions and reduced cell pressure

2,4,6-TNT vapour

A measurement in a static cell close to atmospheric pressure yields the best detection limit, since flow noise is avoided and the vapour is fully sampled and not further diluted by operating the cell under reduced pressure. However, this is not the preferred mode of operation, since it takes too long to evacuate the cell and then fill it again with the analyte, and also, under atmospheric pressure, water interferences are expected to be an issue due to pressure broadening of water absorption lines.

Preferred is a mode of operation where the analyte flows through the resonators, and where the total pressure within the cell is reduced. In such an experiment, TNT from the vapour generator was flowing through the acoustic resonators, while the pressure inside the cell was kept at 0.3 bar by the pump. The TNT in the vapour generator was kept at 60 °C, with an equilibrium vapour pressure corresponding to approximately 1 ppm. A 10 mL/min flow of N_2 was further diluted by pure N_2 flows and then transferred and sampled at 4 L/h through the acoustic resonator. Signals from both resonators were averaged and processed in lock-in amplifiers. Signals were normalised to laser power assuming linear power dependence. Data points represent 1 s integration time. Although the response time of the apparatus is reasonably fast (see also below), it turns out that TNT vapour is rather "sticky" and considerable time is needed for complete equilibration after changing a concentration setting on the vapour generator. This is presumably due to adsorption of TNT on surfaces within the vapour generator, the transfer lines and the measurement cell. Before starting measurements at a new concentration, the system was allowed to equilibrate for a full day. Figure 63 shows a spectral scan of 32 ppb TNT, together with a background measurement of pure N_2. The absorption profile is well described by a Gaussian line shape with centre 1350 cm^{-1} and 18 cm^{-1} FWHM. Subsequent measurements were done on 6 selected wavenumbers, as indicated in Figure 63. These points characterise the absorption shape of TNT and allow spectral discrimination against interferents and backgrounds.

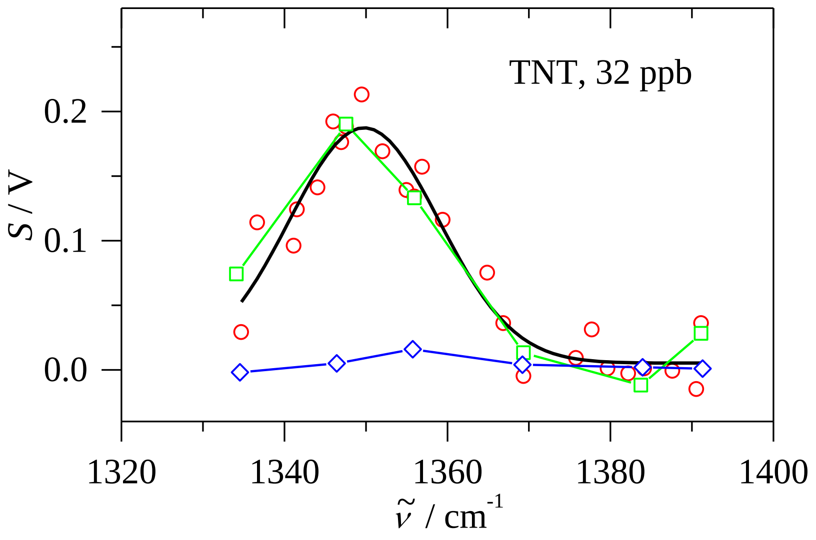

Figure 63 - Spectral scan of 32 ppb 2,4,6-TNT (red circles) with a Gaussian fit; background flow of pure N_2 (blue); and a typical 6-point scan of 32 ppb TNT (green squares).

Experiments were repeated at 32, 24 and 12 ppb to obtain a calibration line. In the calibration, the difference of the signal at 1347 cm^{-1} (close to the peak position) and 1384 cm^{-1} (off peak) was taken as a measure of TNT concentration. This difference procedure cancels most non-resonant backgrounds and interferents. In addition, a measurement of pure N_2 provided the background. The standard deviation of the background data at 1 s integration was 0.032 V which serves as an estimate of the noise level. The calibration (Figure 64) shows good linearity. The fit line crosses the 0.032 V noise level at 5.5 ppb which represents the noise-equivalent detection limit at 1 s integration time in the flow measurements under reduced pressure. Considering that the concentration (amount of substance per volume) is reduced inside the cell due to the reduced pressure, this result is in good agreement with the 1.2 ppb detection limit derived before for the static cell at atmospheric pressure. Since the equilibrium vapour pressure of TNT at room temperature corresponds to about 5 ppb, the detection limit for TNT has to be improved if the apparatus is to be used for TNT detection in this mode of operation. This should be possible, either by longer integration times, more powerful mid-IR lasers, better high-reflectivity mirrors and hence stronger power build-up, or by using a TNT pre-concentrator.[114]

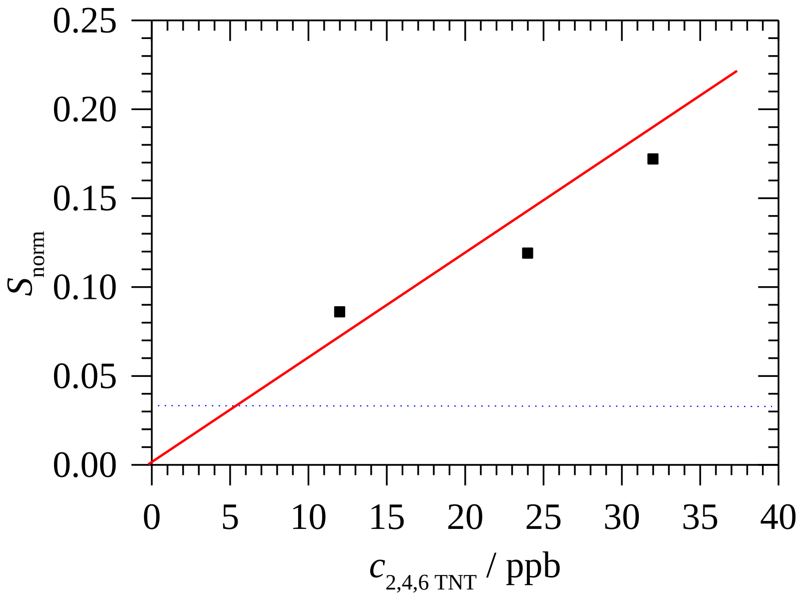

Figure 64 - Calibration plot of difference signal versus TNT fractions in 0.3 bar N_2 with a calibration line. The dotted line represents the noise level at 1 s integration time.

2,4-DNT vapour

In a further experiment, 2,4-DNT vapour from the vapour generator was measured to characterise the performance of the apparatus. 2,4-DNT is a common residue and marker for TNT. At room temperature, it has an equilibrium vapour pressure of about 10^{-4} Torr corresponding to 150 ppb in 1 atm. The DNT at the vapour generator was kept at 45 °C with an equilibrium vapour pressure corresponding to 4 ppm. 10 mL/min of a nitrogen flow, further diluted by additional nitrogen flows to give defined DNT concentrations, transferred the mixture to both acoustic resonators under flow conditions. The pressure inside the cell was kept at 0.3 bar. Signals from both resonators were averaged, detected in lock-in amplifiers and normalised to laser power assuming linear power dependence. Under these flow conditions, samples are replenished continuously, resulting in a fast response time. However, due to adsorption of DNT vapour on surfaces within the transfer lines, the resonators and the cell, accurate measurements require more time for complete equilibration. After changing concentration settings on the vapour generator, the flow through the resonators was left for at least 1 hour to ensure good equilibration before measurements were taken. Each data point represents 1 s integration time. Figure 65 shows the spectrum of 130 ppb DNT obtained together with a background scan of pure N_2. The data are well represented by a Gaussian absorption line peaking at 1354 cm^{-1} with 17 cm^{-1} FWHM, slightly shifted compared to the TNT absorption.

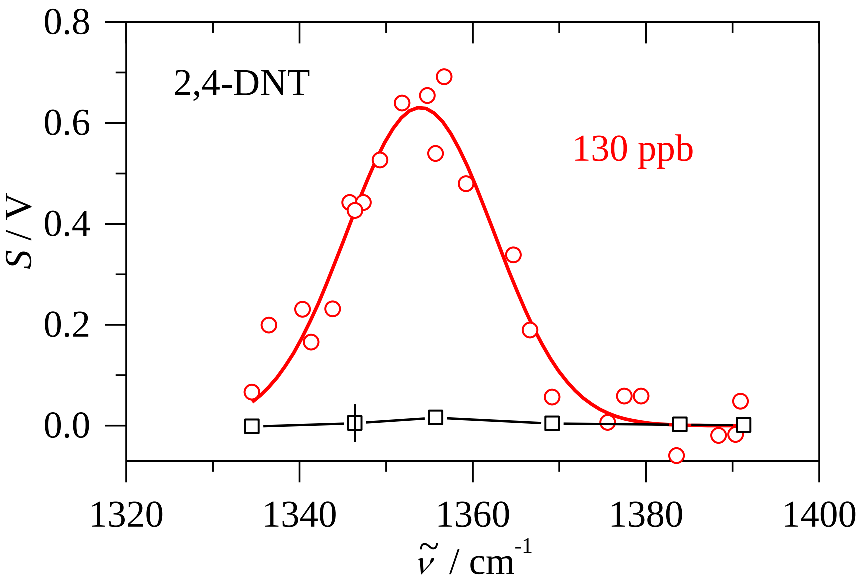

Figure 65 - Spectral scan of 130 ppb 2,4-DNT (red) together with a Gaussian fit, and of a background flow of pure N_2 (black). The bar on one of the background data points represents the estimated uncertainty of a measurement.

To obtain a calibration line and to determine a detection limit, measurements were made at 130, 98, 50, 25 and 13 ppb DNT in N_2. Only five spectral positions were measured, as indicated by the background data points in Figure 65, since they represent the DNT absorption profile reasonably well. Taking measurement at different wavenumbers is a recommended procedure to assess possible interferences by spectral discrimination in "real" applications. The difference of a measurement at 1356 cm^{-1} (close to peak absorption) and 1384 cm^{-1} (off peak) was taken as a measure of concentration. Such a difference measurement has the advantage that common broad spectral interferences and noise backgrounds are partially cancelled. In addition, a background measurement was taken with a pure nitrogen flow. The background had a standard deviation of its baseline of 0.032 V which may serve as an estimate of the noise level at 1 s integration time. The calibration plot is displayed in Figure 66, showing good linearity. The calibration line crosses the noise level at 7 ppb which is the noise-equivalent detection limit for detection of DNT in N_2 under flow conditions in a 0.3 bar measurement cell at 1 s integration time. Considering that TNT and DNT have somewhat different peak absorption cross sections, this result is compatible with the 5.5 ppb for TNT. Since 2,4-DNT has an equilibrium vapour pressure corresponding to about 150 ppb at room temperature, it is expected that DNT can be detected under "real" conditions with the present apparatus.

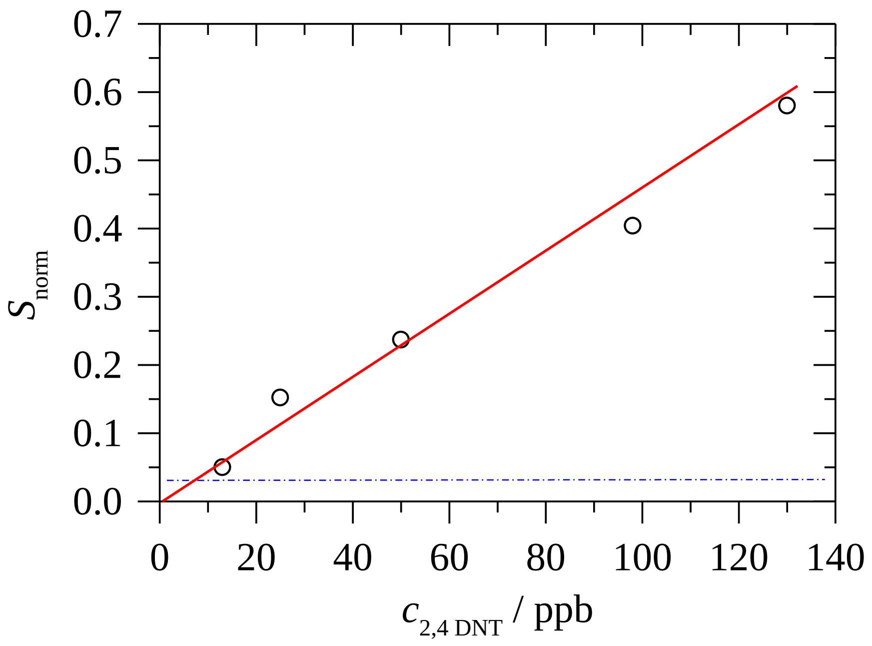

Figure 66 - Calibration plot of difference signal versus 2,4-DNT fraction in N_2 with a calibration line. The dotted line represents the noise level at 1 s integration time, as estimated from the standard deviation of a background measurement.

DMNB vapour

DMNB (2,3-dimethyl-2,3-dinitrobutane) is a volatile compound used as a taggant for explosives (e.g., for RDX which itself has an extremely low vapour pressure). Specially trained sniffer dogs are very sensitive to DMNB and can detect concentrations in the high ppt range in air.[115] Its vapour has been measured with the CERPAS apparatus. In the vapour generator source, DMNB was kept at 32 °C with an equilibrium vapour pressure corresponding to 2.4 ppm. By dilution with N_2 flows, defined DMNB fractions between 95 and 24 ppb in 1 atm N_2 were obtained; each acoustic resonator sampled 4 L/h of this flow, while a pump kept the pressure inside the cell at 0.3 bar. Figure 67 shows a spectral scan of 95 ppb DMNB. There are at least two different absorption features present in this spectrum. The stronger peak is well described by a Gaussian line shape with peak at 1345.5 cm^{-1} and FWHM of 13.5

cm^{-1}. The spectrum is similar to a solid phase spectrum obtained with an FTIR instrument (Bruker Alpha, 0.8 cm^{-1} resolution) with an attenuated total reflection (ATR) unit (see Figure 68). Peak positions in the solid phase spectrum are 1340, 1378 and 1394 cm^{-1}. There are some minor changes in peak positions and line shapes compared to the vapour spectrum which is to be expected for solid phase vibrational spectra. To obtain a calibration line, the difference of the reading at 1347 cm^{-1} (near the peak) and 1369 cm^{-1} (in-between two absorption features) was taken as a measure of concentration, resulting in a very good linearity (see Figure 69). The calibration line crosses the 0.032 V noise level at 11 ppb DMNB in 1 atm N_2; this serves as an estimate for the noise equivalent detection limit at 1 s integration time. As before, note that concentrations inside the resonators are lower due to the reduced pressure (0.3 bar compared to 1 atm). Since the equilibrium vapour pressure of DMNB at room temperature (25 °C) corresponds to about 2.6 ppm in 1 atm, spectroscopic detection of DMNB is feasible with sensitivity similar to detection dogs.

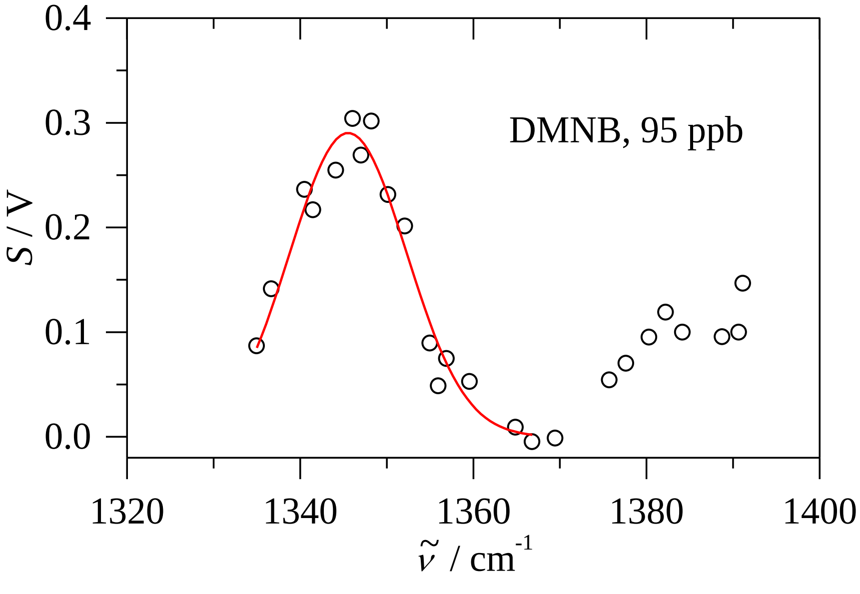

Figure 67 - Spectrum of 95 ppb DMNB with a Gaussian fit of the main absorption.

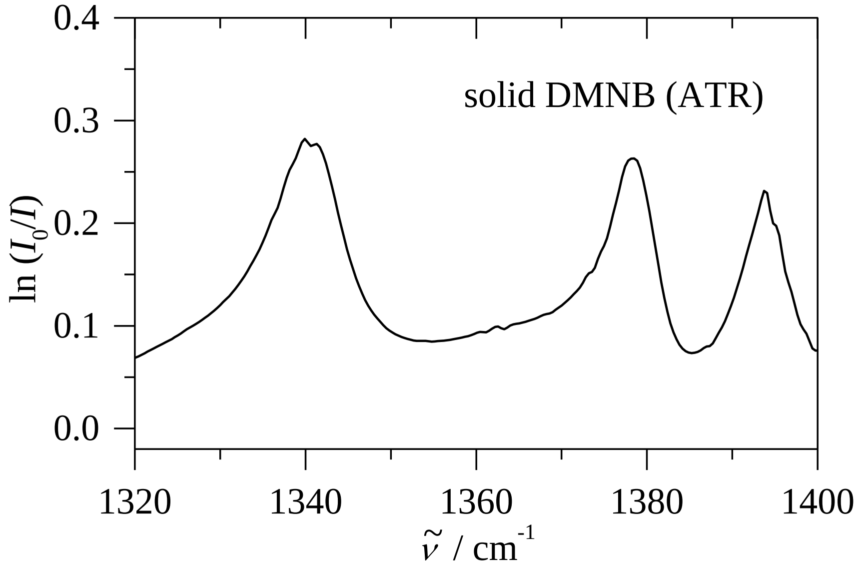

Figure 68 - FTIR-ATR absorption spectrum of solid DMNB.

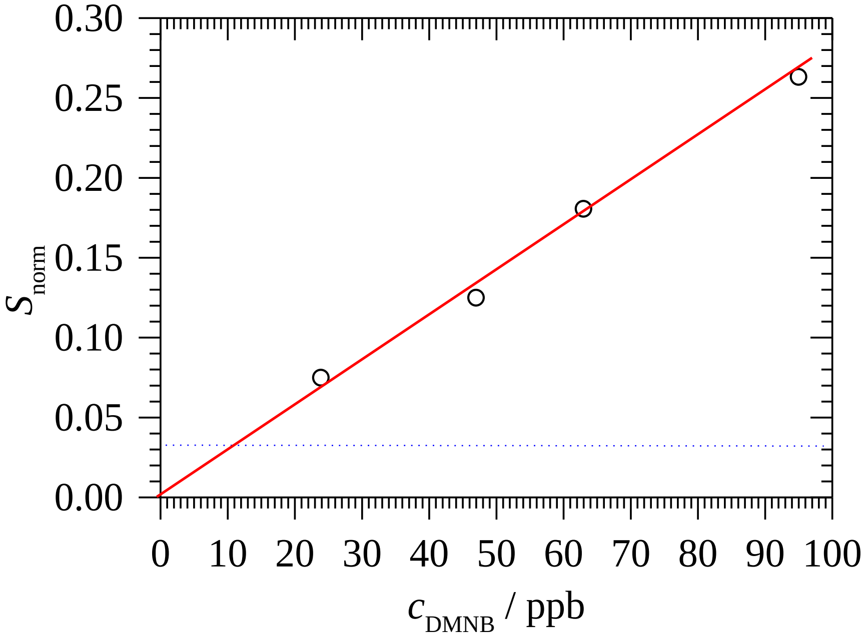

Figure 69 - Calibration line of differential signal versus DMNB fraction in N_2. The dotted line represents the noise level from a background measurement.

TATP vapour

TATP (triacetone triperoxide, the trimer of acetone peroxide) is a high explosive which can be easily prepared using standard household chemicals. Since TATP is structurally different to other explosives which contain the nitro-group as explosophor (functional group that makes a compound explosive), it can be difficult to detect with standard techniques (IMS, MS). It has a relatively high vapour pressure at room temperature. Fortunately, it has a rather strong carbonyl stretching absorption band within the range of the mid-IR QCL used. In the experiment, TATP (Accustandard, 97.7 % purity diluted in hexane to 10 mg/mL, the hexane left to evaporate to give white TATP crystals) was kept at 32 °C in the vapour generator with about 120 ppm TATP at equilibrium. The concentration was diluted by a strong flow of N_2, giving about 80 ppb TATP in 1 atm N_2. This flow was transferred to the acoustic resonators (sampling 4 L/h for each resonator) within the cell at reduced pressure of 0.3 bar. As before, signals from both resonators were averaged, processed in lock-in amplifiers and normalised to laser power assuming linear power dependence. Figure 70 shows the spectral scan obtained for 80 ppb TATP. In a separate experiment, hexane (the solvent used for TATP) was measured. The spectrum shown in Figure 70 does not seem to be affected by hexane absorptions; hexane has some broad absorptions in this region which peak around 1390 cm^{-1}. The TATP absorption band peaks around 1370 cm^{-1} with FWHM of about 12 cm^{-1} in an asymmetric line shape which is not well represented by a Gaussian or Lorentzian function. There is a minor, secondary sharp absorption around 1348 cm^{-1} which is not an outlier or artefact since it has been observed in several repeat experiments. It is not due to hexane. It is unclear at present whether this belongs to TATP or to a yet unknown impurity. The main absorption at 1370 cm^{-1} has a peak signal of about 0.65 V. With the previous noise level of 0.032 V, a noise equivalent detection limit of 4 ppb TATP in 1 atm N_2 is estimated at 1 s integration time. Due to the high vapour pressure of TATP at room temperature, mid-IR CERPAS is thus suitable to detect traces of TATP vapours.

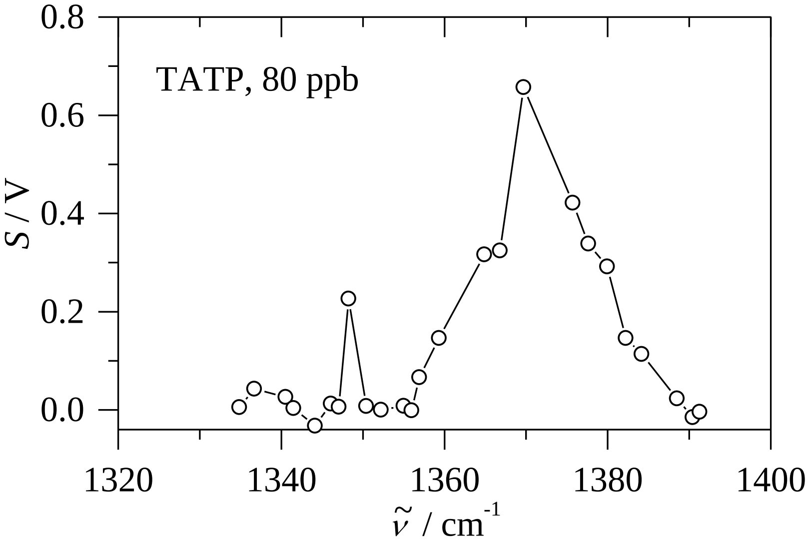

Figure 70 - Spectral scan of 80 ppb TATP in 1 atm N_2, in a flow cell under reduced pressure (0.3 bar).

Direct air sampling under flow conditions and reduced pressure

In a "real" application, air samples could be analysed by flowing air through the resonators while keeping a reduced pressure inside the cell. To demonstrate this principle, a 1/8" Teflon sampling tube with length 30 cm was attached to the resonators. The cell was kept at 0.3 bar with a pump, while lab air was flowing via the sampling tube into the resonators and into the cell. A clamp on the sampling tube restricted the flow to about 4L/h for each resonator. As before, signals from both resonators were averaged, processed in a lock-in amplifier and normalised to laser power. In one experiment, the sampling tube was pointing inside a container with 2,4-DNT at room temperature with an equilibrium vapour pressure corresponding to about 150 ppb. Detection was at 1356 cm^{-1}, close to the peak position of 2,4-DNT absorption. Figure 71 shows the time-dependent signal obtained from the apparatus (each data point represents 1 s integration time). At a), the sampling tube was pointing towards the DNT source, at b), the tube was withdrawn. A reasonably fast response time is observed, with a 90 % rise time of about 20 s. The decay time is somewhat slower, about 2 min, presumably due to some DNT vapour adhering to the surfaces or more time being required to completely pump off the sampling cell.

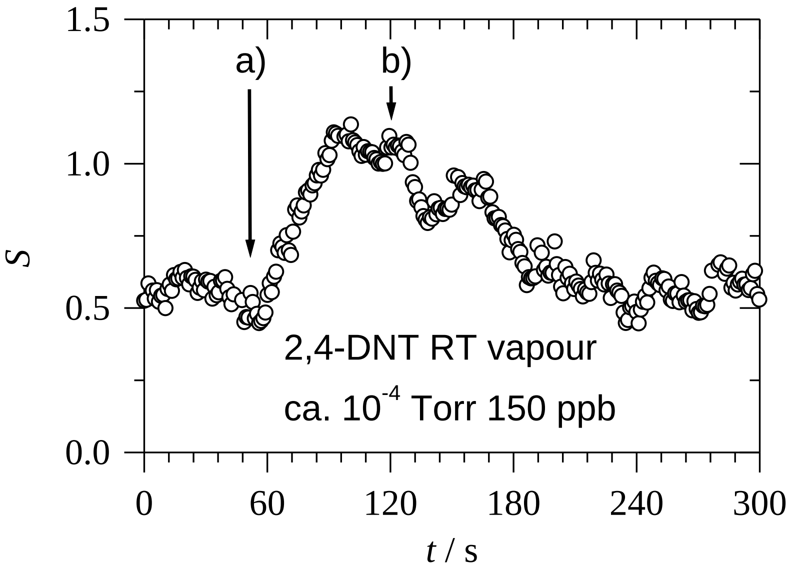

Figure 71 - Direct air sampling with traces of 2,4-DNT vapour (ca. 150 ppb). Arrow a) indicated time when the 2,4-DNT vapour was introduced to the sampling tube. Arrow b) indicates when the sampling tube was withdrawn from the 2,4-DNT source.

In another demonstration, the sampling tube was pointing into a container with 4-MNT (*para*-mononitrotoluene) at room temperature. With 50 ppm in 1 atm, 4-MNT has a much higher equilibrium vapour pressure at room temperature. Detection was again at 1356 cm^{-1}, close to the peak position of 4-MNT absorption. The signal rises within a response time of less than 1 min exceeding the amplification range of the lock-in amplifiers (Figure 72). After withdrawing from the container, the signal falls with a slower time constant, presumably due to vapour adhering to surfaces or due to restrictions of the pump speed. In conclusion, direct air sampling under flow conditions and reduced pressure is suitable for "real" applications of trace gas detection by optical spectroscopy with a fast response time.

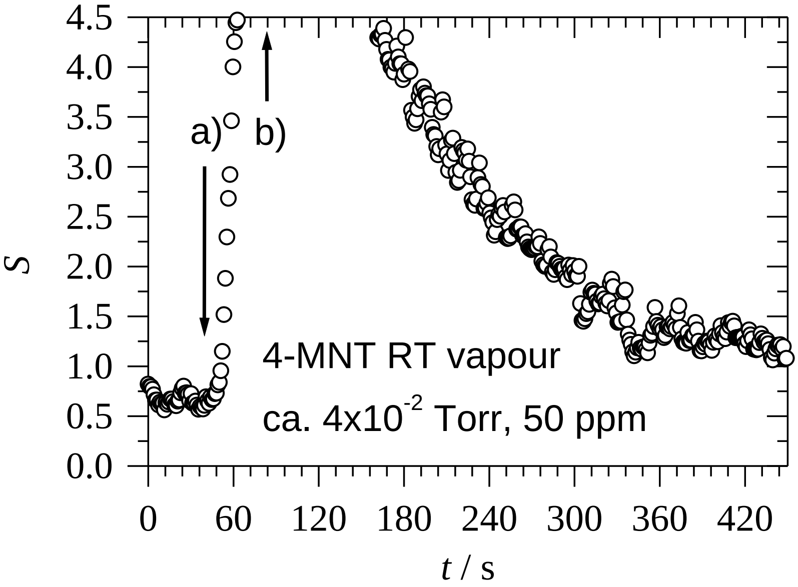

Figure 72 - Direct air sampling with 4-MNT vapour (ca. 50 ppm). Peak signals are exceeding the amplification range of the lock-in amplifiers used. Arrow a) indicate when MNT is directly sampled and b) indicates time when sampling tube was withdrawn from MNT sample.

Sampling via Solid Phase Microextraction (SPME)

A SPME fibre is a specially coated fibre which is protected inside a barrel of a syringe. By pushing the plunger of the syringe, the fibre can be exposed beyond the tip of the syringe. By exposing the fibre, vapours can be absorbed onto it (usually at room temperature) or released in a hot injector port. To demonstrate headspace sampling using a SPME fibre (Supelco 57324-U, coated with polydimethylsiloxane PDMS), the fibre was loaded for about 6 s sampling of the headspace above solids or liquids. The fibre then released the absorbed vapours into the hot injector port of the vapour generator at 60 °C, where a 400 mL/min flow of N_2 picked up the vapours and transferred it to the measurement cell. Each of the two resonators inside the cell sampled 4 L/h of this flow. The pressure inside the cell was maintained at 0.3 bar using a pump. As before, signals from both resonators were averaged, processed by lock-in amplifiers and normalised to laser power. Each data point represents 1 s integration time. In one experiment, the fibre was loaded for 6 s above a container with 4-MNT at room temperature with a vapour concentration corresponding to approximately 50 ppm. Figure 73 shows the time response from the detector monitoring absorption at 1356 cm^{-1}, close to the peak position of 4-MNT absorption. The signal rises with a fast time response within about 10 s. After ca. 2 min, the fibre has released all 4-MNT vapour and the reading is back at the baseline. In another experiment (not shown), the fibre was loaded with vapour for 6 s above TATP crystals. Monitoring at 1365 cm^{-1} (close to peak), a tremendous signal was observed exceeding the 5 V limit of the lock-in amplifiers. After a few minutes, the fibre had released all absorbed vapour and the reading went down back to the baseline. In a control experiment, loading the fibre with TATP and monitoring at 1331 cm^{-1} (off-peak) gave virtually no signal. Hexane, the solvent used in TATP solutions, has very large signals on both locations if sampled via the SPME fibre.

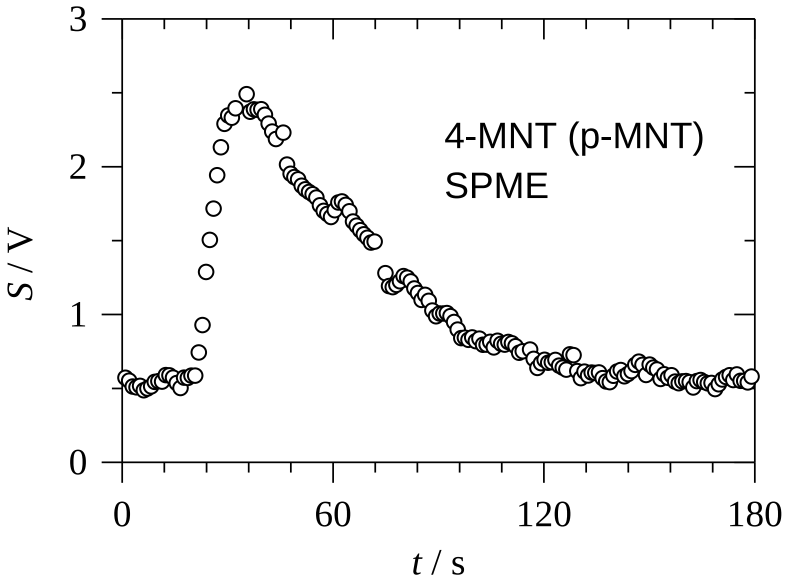

Figure 73 - Time response of the detector after sampling 4-MNT vapour with a SPME fibre. See text for detail.

Sampling of solids or liquids via heated vaporization

Solid and liquid samples can also be measured by putting them into the hot port of the vapour generator, where the samples release vapours due to heated vaporization. As before, these vapours are picked up by a stream of N_2 and transferred to the cell for measurement. The hot port temperature was between 50 and 80 °C. As a demonstration, a small 2,4-DNT crystal was placed into the hot port. Figure 74 shows the time response of the detector monitoring at 1356 cm^{-1}, close to the peak of 2,4-DNT absorption. Within a few seconds, the signal rises and exceeds the amplification range of the lock-in amplifiers used. In potential applications of this sampling technique, swabs could be tested for traces of explosives, to give one relevant example.

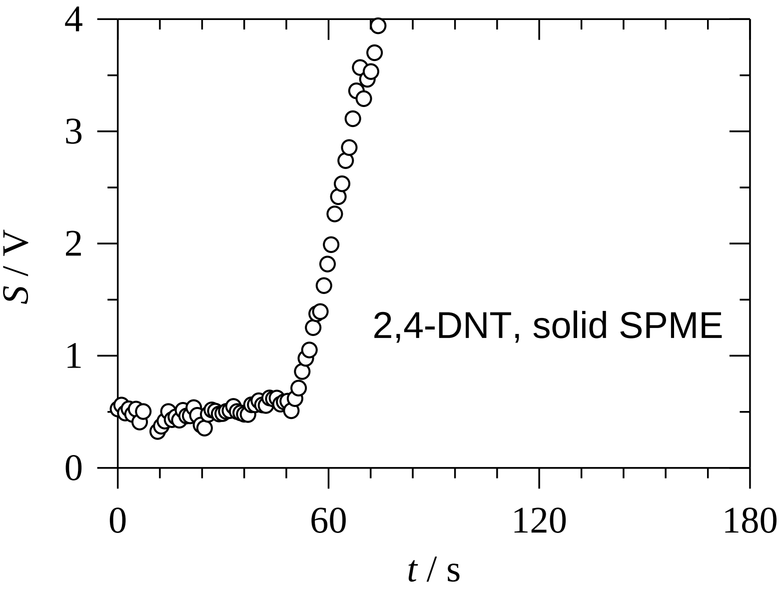

Figure 74 - Time-dependent signal resulting from the heated vaporization of a 2,4-DNT crystal inside the 60 °C hot port, monitoring at 1356 cm^{-1}, close to the peak of 2,4-DNT absorption.

In conclusion, mid-IR CERPAS has been combined with an explosives' and taggants' vapour generator to detect and analyse a variety of explosives' and taggants' vapours (TNT, DNT, MNT, DMNB & TATP) under static and flow measurements. Military grade explosives typically have very low vapour pressures and are difficult to detect by spectroscopic methods. The apparatus was able to detect TNT down to 1.2 ppb (at 1 atm) under static conditions and 5 ppb under flow conditions (300 mbar, 4 L/h) in nitrogen. Spectral regions were identified to avoid water interference in order to prevent false positive signals. Additional sampling techniques, solid phase microextraction and direct solid/liquid sampling was also demonstrated with DNT to show the possible implementation of swab sampling.

5. Trace gas detection of toxic industrial chemicals (TICS) by Herriott- cell enhanced resonant photoacoustic spectroscopy (HERPAS)

The cavity enhanced photoacoustic detection techniques (CERPAS) introduced in the previous chapters provide highest sensitivity, but they are somewhat experimentally involved and quite sensitive to misalignments and environmental influences. Compromising on sensitivity, more traditional and perhaps more robust multipass techniques can be combined with photoacoustics detection. In this chapter, such an approach is investigated and characterised, Herriott- cell enhanced photoacoustic spectroscopy (HERPAS) in the near IR for the detection of toxic industrial chemicals (TICs).

This project was sponsored by Smiths Detection Watford, in order to investigate innovative optical spectroscopic methods to detect toxic industrial gases by their near IR optical spectrum.

Introduction

Toxic industrial chemicals (TICs) are chemicals that are manufactured, stored, transported and used in large quantities throughout the United States and the world for manufacturing and/or research. These chemicals can be gases, liquids and solids which pose a chemical hazard, i.e., toxic, carcinogenic, mutagenic, reprotoxic, endocrine disruptors, corrosive or physical hazards, such as flammable, combustible or explosive. Toxic industrial chemicals are a concern for the security services as they can be easily deployed as a chemical warfare agent (CWA) by terrorist organisations and in asymmetric warfare scenarios with relative ease of procurement. While TICs are less lethal than conventional CWAs on a gram to gram basis, they are readily available in large quantities and can be easily mass produced, especially for state sponsored terrorism. Toxic industrial chemicals are ranked by a hazard index and are split into three categories: high, medium and low.[116] A high hazard chemical indicates a widely available, high toxicity chemical that is easily vaporised. A medium hazard chemical is one which rates highly in some of the categories but lower on others such as the availability, physical state or toxicity. Low hazard chemicals indicate the chemical is unlikely to be a hazard unless the circumstance indicates otherwise. A table of common toxic industrial chemical sorted into the respective categories are shown in Table 2 sourced from Ref. 116. Most of the chemicals have an associated immediately dangerous to life or health limits (IDLH). These IDLH values were originally developed for respirator selection criteria in the mid 1970’s. Current IDLH values from National Institute for Occupational Safety and Health (NIOSH, USA) are established to ensure workers can escape from a contaminated environment in the event of a respiratory protection equipment failure. In establishing IDLH values, the following conditions must be assured:[117]

1. "The ability to escape without loss of life or immediate or delayed irreversible health effects. (Thirty minutes is considered the maximum time for escape so as to provide some margin of safety in calculating an IDLH value.)"
2. "The prevention of severe eye or respiratory irritation or other reactions that would hinder escape."

It should be noted that IDLH limits give the maximum exposure limits for a given chemical before irreversible health effects are suffered or death. Other exposure limits include the permissible exposure limits (PEL) from Occupational Safety and Health Administration (OSHA) or recommended exposure limit (REL) from NIOSH. For example, ammonia has an IDLH value of 300 ppm, PEL value of 50 ppm, REL value of 25 ppm (time weighted average concentration over 10 hour working day during a 40 hour working week).

HIGH	**MEDIUM**	**LOW**
Ammonia	Acetone cyanohydrin	Allyl isothiocyanate
Arsine	Acrolein	Arsenic trichloride
Boron trichloride	Acrylonitrile	Bromine
Boron trifluoride	Allyl alcohol	Bromine chloride
Carbon disulfide	Allyl amine	Bromine pentafluoride
Chlorine	Allyl chlorocarbonate	Bromine trifluoride
Diborane	Boron tribromide	Carbonyl fluoride
Ethylene oxide	Carbon monoxide	Chlorine pentafluoride
Fluorine	Carbonyl sulfide	Chlorine trifluoride
Formaldehyde	Chloroacetone	Chloroacetaldehyde
Hydrogen bromide	Chloroacetonitrile	Chloroacetyl chloride
Hydrogen chloride	Chlorosulfonic acid	Cyanogen
Hydrogen cyanide	Crotonaldehyde	Diphenylmethane-4'-diisocyanate
Hydrogen fluoride	Diketene	Ethyl chloroformate
Hydrogen sulfide	1,2-dimethyl hydrazine	Ethyl chlorothioformate
Nitric acid, fuming	Dimethyl sulfate	Ethylene imine
Phosgene	Ethylene dibromide	Ethyl phosphonothioicdichloride
Phosphorus trichloride	Hydrogen selenide	Ethyl phosphonous dichloride
Sulfur dioxide	Iron pentacarbonyl	Hexachlorocyclopentadiene
Sulfuric acid	Methanesulfonyl chloride	Hydrogen iodide
Tungsten hexafluoride	Methyl bromide	Isobutyl chloroformate
	Methyl chloroformate	Isopropyl chloroformate
	Methyl chlorosilane	Isopropyl isocyanate
	Methyl hydrazine	N-butyl chloroformate
	Methyl isocyanate	Nitric oxide
	Methyl mercaptan	n-propyl chloroformate
	N-butyl isocyanate	Parathion
	Nitrogen dioxide	Perchloromethyl mercaptan
	Phosphine	Sec-butyl chloroformate
	Phosphorus oxychloride	Sulfuryl fluoride
	Phosphorus pentafluoride	Tert-butyl isocyanate
	Selenium hexafluoride	Tetraethyl lead
	Silicon tetrafluoride	Tetraethyl pyrophosphate
	Stibine	Tetramethyl lead
	Sulfur trioxide	Toluene 2,4-diisocyanate
	Sulfuryl chloride	Toluene 2,6-diisocyanate
	Tellurium hexafluoride	
	Tert-octyl mercaptan	
	Titanium tetrachloride	
	Trichloroacetyl chloride	
	Trifluoroacetyl chloride	

Table 2 - Common chemicals sorted into the respective hazard categories.

It is thus important to detect TICs with high sensitivity and selectivity. Selectivity is a particular concern to avoid false alarms. In this chapter, spectroscopic near-IR detection in a Herriott multipass cell combined with resonant photoacoustics is introduced and its performance characterised. Laser photoacoustics has been used for trace gas detection,[118] as discussed in the introduction. Various attempts to improve the sensitivity have been reported. These include detecting the PA signal by a micromechanical cantilever.[50,119] Another replaces the microphone with a quartz tuning fork, which can offer a compact detection system.[52] Alternatively, one could increase the optical pathlength as shown in the previous chapter with cavity enhancement. However, implementation of a cavity enhanced system is typically more labour intensive and more susceptible to mechanical instability. A compromise between a single pass and cavity enhanced photoacoustics technique is a multipass enhanced PA. This was demonstrated by Goldan et al.[120] with a multipass consisting of a planar mirror and a concave mirror. This enhanced the signal by a factor of 10. Hornberger demonstrated this principle further with 50 reflections with α of 2.6 x10^{-9} cm^{-1} at 130 mbar.[121]

Experimental

Description of the Experimental Set-up

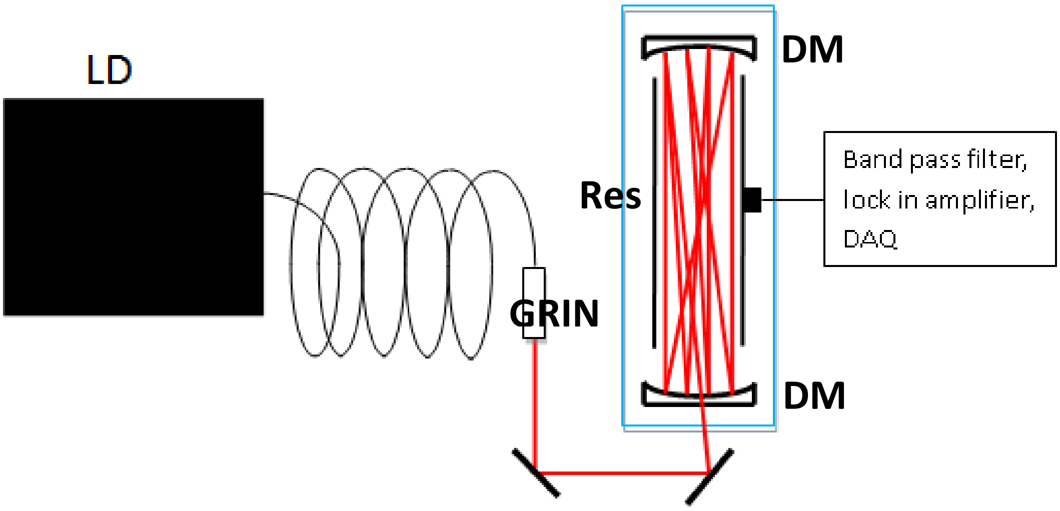

Figure 75 - Experimental scheme of the ECDL HERPAS setup for trace gas detection. **LD**: CW-single mode extended cavity diode laser, lasing at 1550 nm with 35 mW**. GRIN**: Graded-index lens collimator, **Res**: acoustic resonator tube (glass, 80 mm long, 11 mm i.d.), with a microphone, **DM**: dichroic mirrors.

The optical setup is shown in Figure 75. The set up consists of an acoustic resonator tube within a Herriott cell with mirror separation of 11 cm. The Herriott cell consists of a pair of concave dichroic mirrors (Thorlabs, 25.4 mm diameter, CM254-100-E04). The mirrors[122] have a radius of curvature of 100 mm and are highly reflective between 1200 - 1600 nm at 45° angle of incidence (AOI) and 1300-1800 nm at 8° AOI. The optical cell and the acoustic resonator tube are enclosed in a glass enclosure equipped with glass windows. The acoustic resonator tube consists of an 80 mm long glass tube with 11 mm internal diameter. The resonator has one microphone (Knowles, EK-23024) attached to it in the middle of the resonator tube. The microphone has a wide frequency response range which starts at 100 Hz and extends to the 10 kHz as shown in Figure 76.

The acoustic resonator has a resonance frequency of about 2.2 kHz. Microphone signals are first filtered by a home-built analogue multiple feedback band-pass filter[123] with a *Q*-factor of 5 and 7 times amplification (see Figure 77), and then further processed by home-built lock-in amplifiers[83] with 1000 times input amplification. The continuous wave near infrared (NIR) light source is a tuneable external cavity diode laser (Thorlabs, TLK-L1550M) tuneable from 1480 - 1610 nm (6200 - 6650 cm^{-1}). The laser output is single longitudinal mode with a specified linewidth of 100 kHz. The laser chip is bonded to a single-mode fibre and its polarisation is dependent on stress applied on the fibre. [124,125,126,127,128]

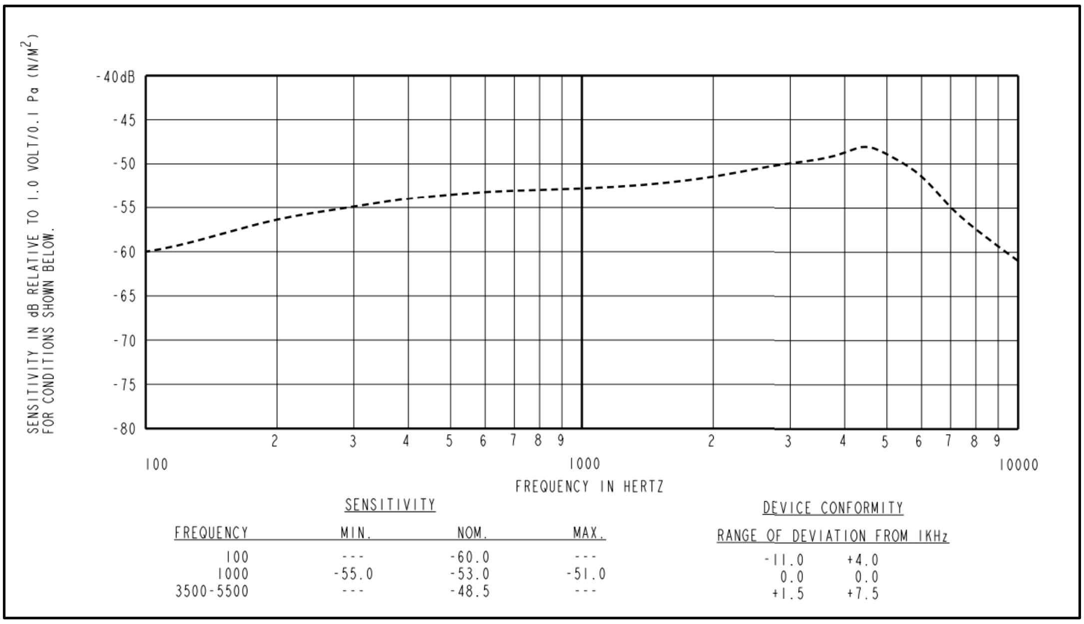

SENSITIVITY

FREQUENCY	MIN.	NOM.	MAX.
100	---	-60.0	---
1000	-55.0	-53.0	-51.0
3500-5500	---	-48.5	---

DEVICE CONFORMITY

RANGE OF DEVIATION FROM 1KHz	
-11.0	+4.0
0.0	0.0
+1.5	+7.5

Figure 76 - Frequency response of the Knowles electret microphone from manufacturer's specification sheet.

At the time of purchase, single-mode, polarisation-maintaining optical fibre was not conveniently available, meaning that while the output is linearly polarised, the polarisation plane changes depending on the experimental conditions.

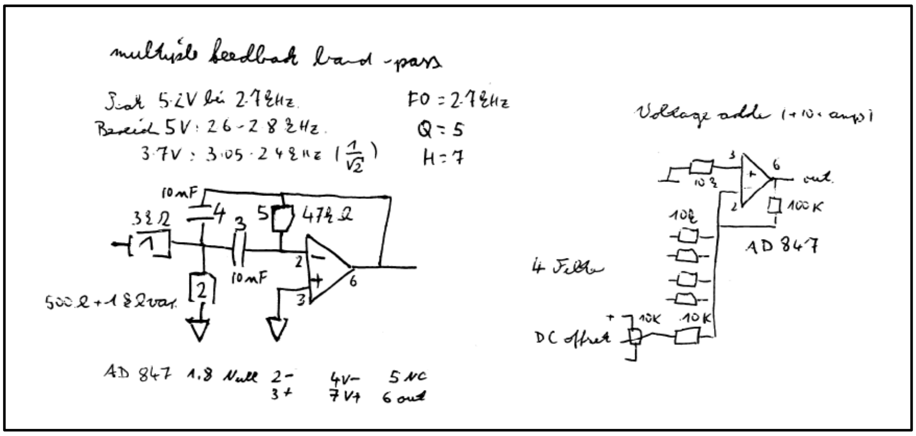

Figure 77 - Sketch of the electronic circuit used for the electronic band-pass filter (from Dr. Hippler's notes).

The laser chip is cooled by a thermoelectric cooler maintained at 25 °C. The ECDL is arranged in the Littman configuration where the laser emits some light from the uncoated end of the gain element. The wavelength can be tuned by altering the separation of the feedback mirror, the position being controlled by a DC servo motor (Thorlabs Z812). The laser has a useful optical output from 1610 to 1495 nm, which corresponds to the feedback mirror actuator extension from 11 – 2 mm. The laser system was found to be continuously tuneable with very few instances of mode hops. The laser system was suitable for use without any alignment and mode hop free spectra were recorded easily.

Characterisation of the Herriott cell

For the purpose of this investigation, a Herriott cell was constructed. A pair of 25.4 mm concave dichroic mirrors (Thorlabs CM254-100-E04, radius of curvature 100 mm) was aligned coaxially. The mirrors were mounted on modified two axis mirror mounts to allow minor repositioning in the *x* and *y* axes. The Herriott cell has a mirror separation of 11 cm. The entry hole was drilled using a diamond tipped drill bit (diameter, 1.5 mm, Eternal Tools) approximately 4 mm off the optical axis. An off-axis entry hole was chosen as it allowed the reflected beam spots to form a circle around the optical axis which allows easier access when positioning the acoustic resonator to enclose the optical beampaths. The Herriott cell was aligned to the maximum number of spots visible using a frequency doubled Nd:YAG alignment laser, operating at 532 nm, as shown in Figure 79. The dichroic mirror is partially reflective to green light which allows a lot of the green light to pass through the dichroic mirror. In Figure 78, the reflected beamspots are shown on a piece of white card and each spot is labelled. Each successive beam spot on the mirror is rotated by >122° (61° per reflection) in the current configuration.

Figure 79 - Photograph of the ring pattern of (23) spots on a mirror and on a piece of card from a green alignment laser.

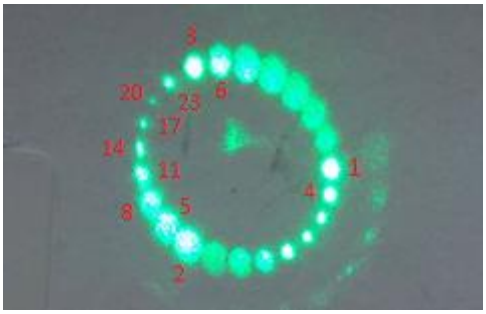

Figure 78 - Magnification of the individual green beam spots hitting the white card.

In order to characterize the performance of the Herriott cell for photoacoustic detection, two measurements, with and without Herriott cell enhancement (where the second mirror is blocked to prevent multipass reflections) were performed on water in 1 atm. of lab air observing a transition at 6726.25 cm^{-1}. It can be seen from Figure 80 that the additional 45 passes have increased the signal by a factor of 40. The noise limits are very similar, 273 and 287 µV for the single and 46 passes, respectively. The measurement was performed with only 100 times amplification rather than the usual 1000 times due to the large absorption cross section of the water line. This clearly shows that the Herriott enhancement increases the sensitivity of the apparatus significantly at very little cost.

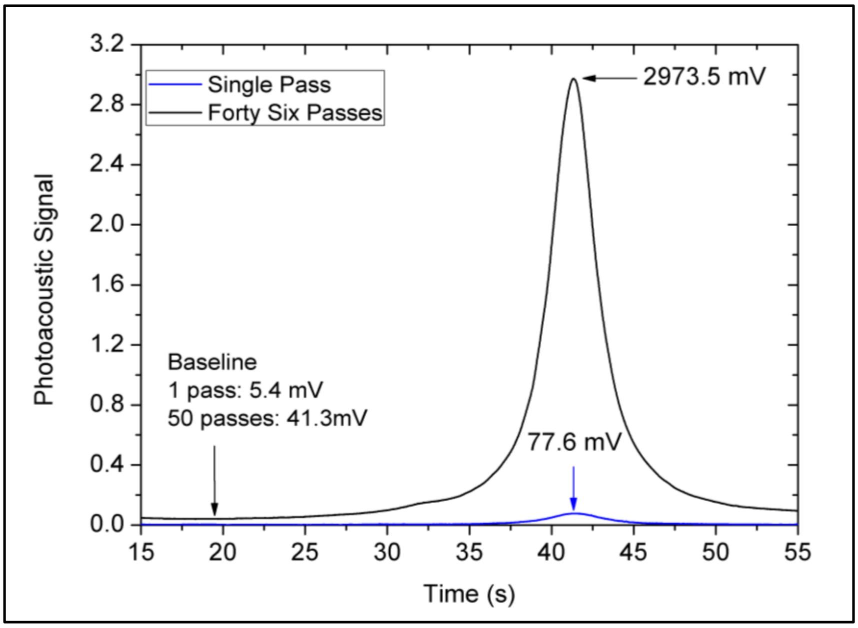

Figure 80 - Photoacoustic acoustic response of a water line near 6726 cm^{-1}at 1 atm. of air with and without Herriott cell enhancement.

Modulation of the laser

Initially the laser was modulated on/off with an optical chopper to achieve the acoustic resonance condition. An optical chopper consists of a spinning disc with a regular cut pattern driven by a DC motor. When the wheel spins, it periodically blocks the light. The optical chopper was operated at 2.2 kHz. This method was suitable for preliminary work, although several disadvantages were discovered. Firstly, the chopping frequency was not stable. The optical chopper's frequency was monitored by an onboard LED light-gate. The frequency is dependent on the DC supply voltage and if a minor ripple in voltage occurs, the frequency also varies. Secondly, the chopper is large and susceptible to mechanical interference such as small jolts which could affect the alignment of the light through the chopper wheel resulting in more or less light passing through the chopper, thus resulting in unequal on/off periods. Thirdly, 50 % of the laser output power is wasted during the chopping as the light is always on. Finally, there is no control over the phase of the chopper. One needs to be in control of the phase of either the photoacoustic signal or the modulating signal as the two need to be in phase for the maximum output signal from the lock in amplifier. The chopper also introduces acoustic noise which is difficult to filter out since by design it occurs at the acoustic resonance frequency of the PA acoustic resonator.

The solution to this was to electrically modulate the laser, i.e., switching on and off the laser at 2.2 kHz. The modulation was controlled by a delay generator (Stanford Research Systems, DG535) where the required frequency and amplitude are set and are fed as a gate signal to the laser driver. The second channel is then delayed by a user defined value to produce a phase shift which matches the photoacoustic response. This gate signal is fed to the lock-in amplifier as the reference signal. The use of the delay generator allows a very well defined modulation frequency and excellent phase matching resulting in maximum signal to noise output. Although a digital delay generator proved to be very convenient for this prototype system, in later implementations, a much simpler and cheaper analogue delay generator may be used.

Acoustic Resonator evaluation

When the modulation rate matches an acoustic mode of the resonator, an amplification effect of the acoustic wave occurs which increases the sensitivity. Typically, this enhancement is equal to the Q factor of the cell. A cylindrical cell can support 3 main acoustic modes: longitudinal, radial and azimuthal, see Figure 81.

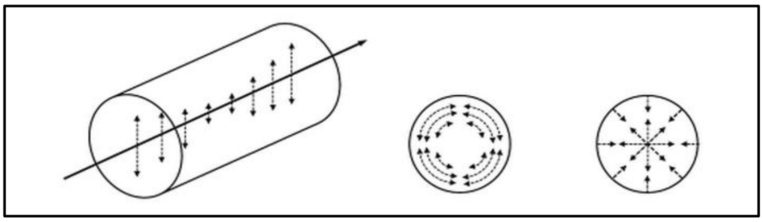

Figure 81 - Longitudinal, azimuthal and radial modes of a cylindrical tube reproduced from Ref. 101.

The peak photoacoustic signal of water in 1 atm. of lab air was measured as a function of modulation frequency as shown in Figure 82. The single Lorentzian fit gives a general quality factor for the measurement cell, yielding a Q factor of just over 46.7 (Δf 47.9 Hz, f_0 2237.4 Hz). Recent literature reports Q factors of 40 – 200 for longitudinal acoustic modes.[101] Hess *et al* [101] reported that higher Q factors can be obtained with a smoother internal surface of the acoustic resonator.

The data are best fitted with three Lorentzian functions which suggest the presence of three different acoustic modes. The primary acoustic mode, shown in green, is the longitudinal acoustic resonance from the 80 mm glass tube. There are additional minor peaks at 2.46 kHz and 2.212 kHz. These additional peaks are unaccounted for. At present, a theory is that these additional acoustic resonance modes may be from radial or azimuthal resonance modes. The enhancement factor of the resonant cell, defined as the maximum signal divided by the off-peak signal, is 34, close to the Q

factor, which shows the acoustic resonance enhancement of the sensitivity of the system.

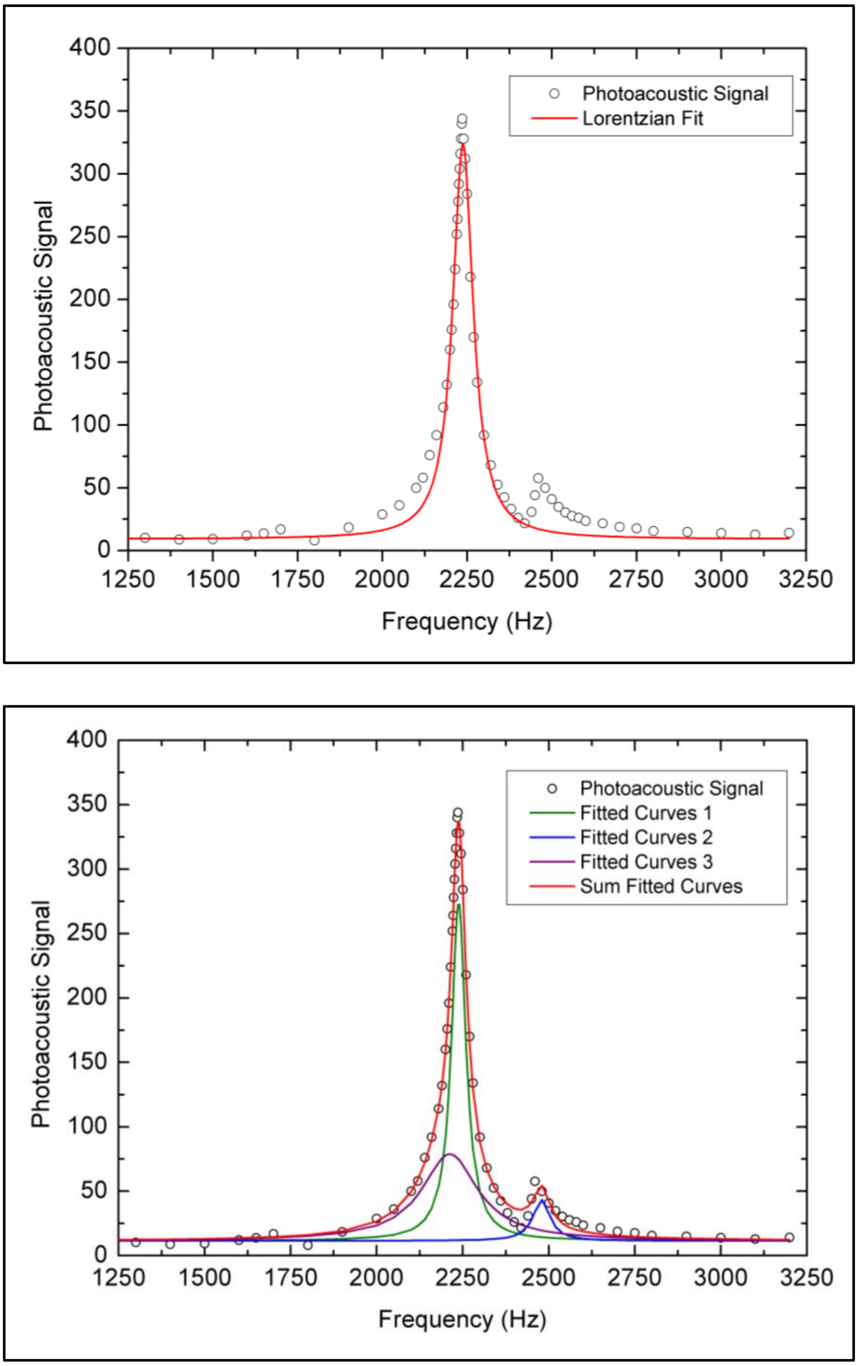

Figure 82 - Top: A Lorentzian fit of the primary resonance peak. Bottom: Three Lorentzian fits of the acoustic response peaks.

Metal resonator

To investigate whether a polished metal resonator provides an improved *Q* factor, a 55 mm long metal resonator with 12.5 mm i.d. was made and extrusion polished. This achieved a near-mirror like finish on the internal surface. The smaller resonator length allowed the two Herriott mirrors to be placed closer together, with a separation of 7 cm instead of 11 cm, making the design even more compact. To determine the *Q* factor and the resonance frequency, the peak photoacoustic response of a water line was measured in open lab air, without the glass enclosure (see Figure 83).

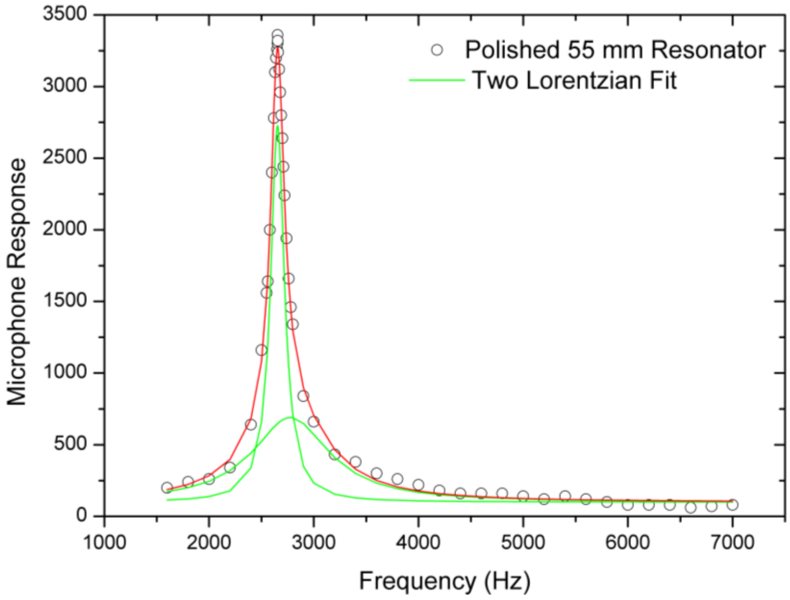

Figure 83 - Double Lorentzian fits of the peak photoacoustic response of a water line near 6726 cm^{-1} against the acoustic modulation frequency.

The resonance profile is best described by two Lorentzians. The polished metal acoustic resonator has a primary acoustic resonance frequency of 2653.6 Hz and a *Q* factor of 16.6. The presence of a secondary resonance peak (2778.1 Hz, *Q* factor: 3.1) which also contributes to the peak of the first acoustic response is also shown by the fitting. The *Q* factor of the metal resonator is not as high as might have been expected, and does not represent an improvement over a glass resonator.

Glass enclosure

The design of the glass enclosure appears to be as important as the resonator design, as the enclosure can affect the overall peak acoustic frequency, *Q*-factor and the enhancement factors of the resonator. To evaluate the effects of the glass enclosure, several configurations were tested, a glass cell without end caps, a single end cap, a single rounded end cap, the original end caps and a pair of different sized end caps (see photographs in Figure 84 and 85). All the acoustic resonance curves below were fitted by multiple numbers of Lorentzians until a good fit (R^2 value of 0.99 or above) is obtained.

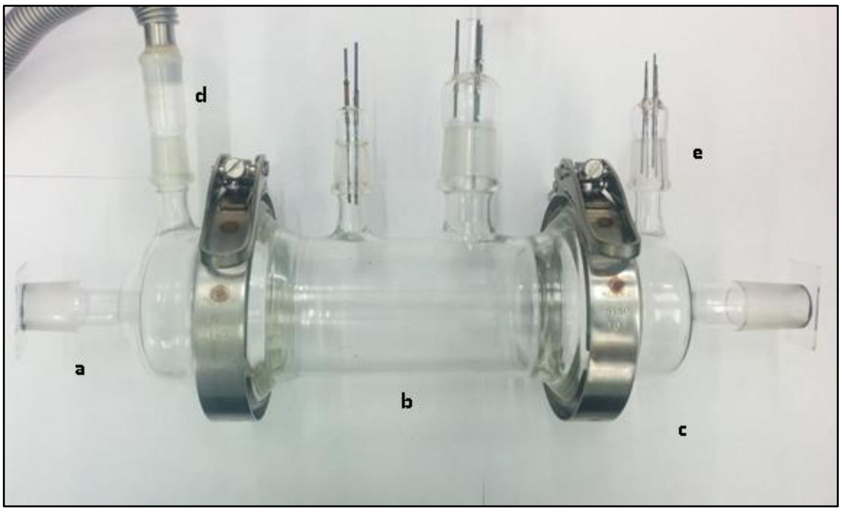

Figure 84 - Typical set up of the glass enclosure: a) Original entry end cap (near side), b) middle section, c) original exit end cap (far side), d) port to connect to gas handling line, e) B14 end cap – mentioned in later sections to determine the various effects of enclosure geometry on the photoacoustic response.

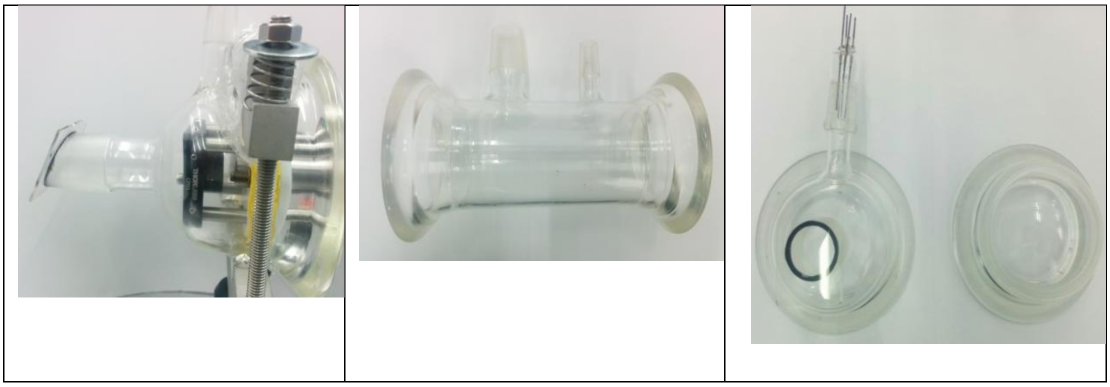

Figure 85 - Left: large entry end cap, the horizontal spout has a maximum diameter of 30 mm, centre: middle section of glass enclosure right: two exit end caps: original exit end cap, right: rounded end cap.

No end caps

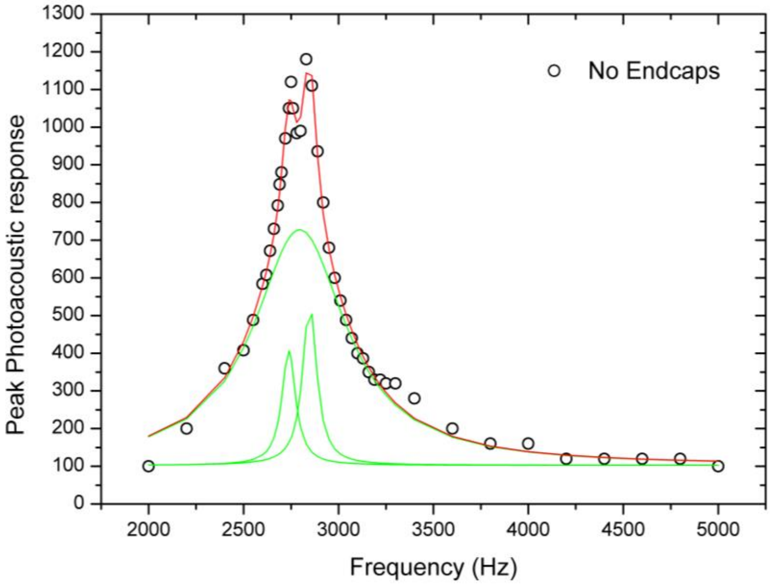

Figure 86 - Triple Lorentzian fit of the peak resonance response with no end caps present. R^2: 0.9942.

When no end caps are present, the mid-section of the glass enclosure appears to act as an additional open-open tube. The resonance curve is characterized by three peaks (Figure 86) at 2738, 2848 and 2796 Hz with *Q* factors of 31.2, 32.1 and 4.73, respectively. The original metal resonator's resonance frequency at 2635 Hz appears to have shifted to a higher value because of the glass enclosure, while the smaller resonance peak at 2778 Hz may have also been shifted and its magnitude increased.

Near end cap - ‘large size’

The metal resonator has a smaller diameter compared to the glass resonator and the entry angle is more obtuse. This required a larger optical entry port, see Figure 85. By placing the larger entry end cap on the near side (entry side) of the glass enclosure, one can see a difference in the acoustic resonance behavior Figure 87.

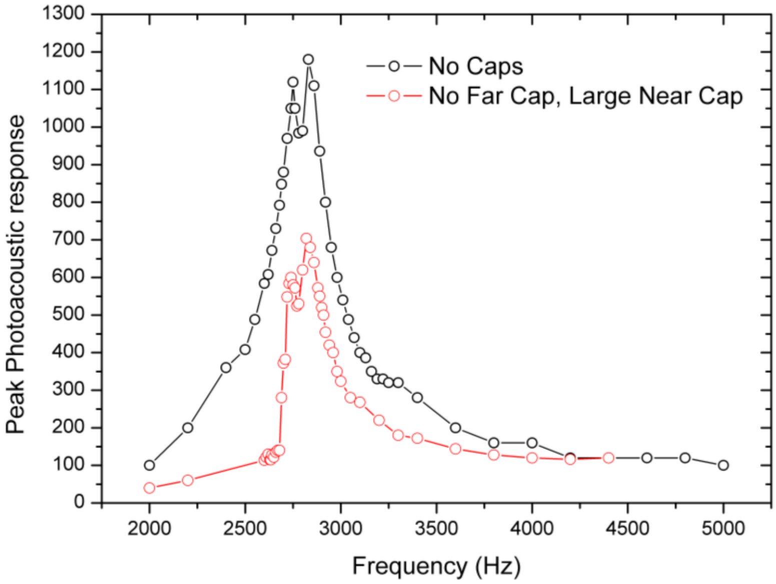

Figure 87 - Plot of the peak PA response of a water line against modulation frequency.

By adding an end cap, one would expect the peak resonance frequency to shift dramatically as the enclosure will have shifted from a pseudo open-open tube to a pseudo open-closed tube. However, it appears that this is not the case with the large entry end cap. The presence of the large entry end cap has dampened the photoacoustic response. The maximum acoustic signal is reduced by approximately half while keeping a similar frequency response.

Far end Cap - ‘rounded size’

A rounded end cap was trialed on the far side of the enclosure to determine its effect and frequency response is shown in Figure 88.

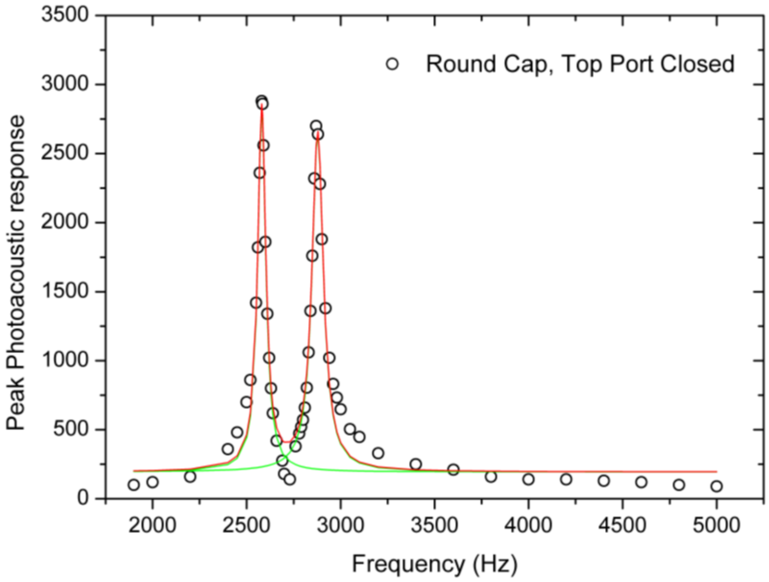

Figure 88 - Two Lorentzian fit of the peak photoacoustic response with a round end cap on the far side of the enclosure.

In this case, the primary resonance peak is shifted to 2580 Hz (*Q* factor: 50, enhancement factor: 17), which is an improvement compared to the large entry cap and just the plain metal resonator. The visible secondary resonance peak is also present 2875 Hz (*Q*: 39, enhancement factor: 16) which is clearly enhanced when compared to the previous example as shown in

Figure 89.

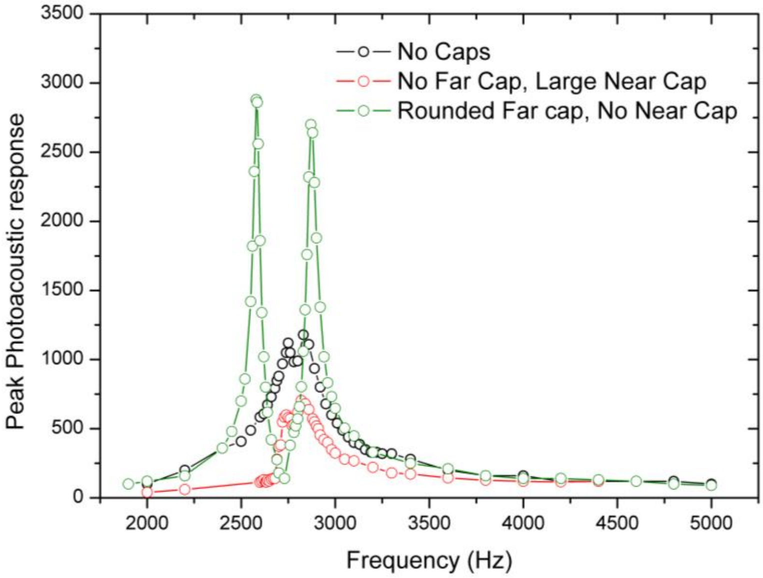

Figure 89 - Comparison of the photoacoustics response of the measurement cell without end caps, with a large near side end cap and a far side rounded.

It is also found that by unplugging one of the B14 caps on the mid-section of the glass enclosure, a shift in the photoacoustic response is visible as shown in Figure 90.

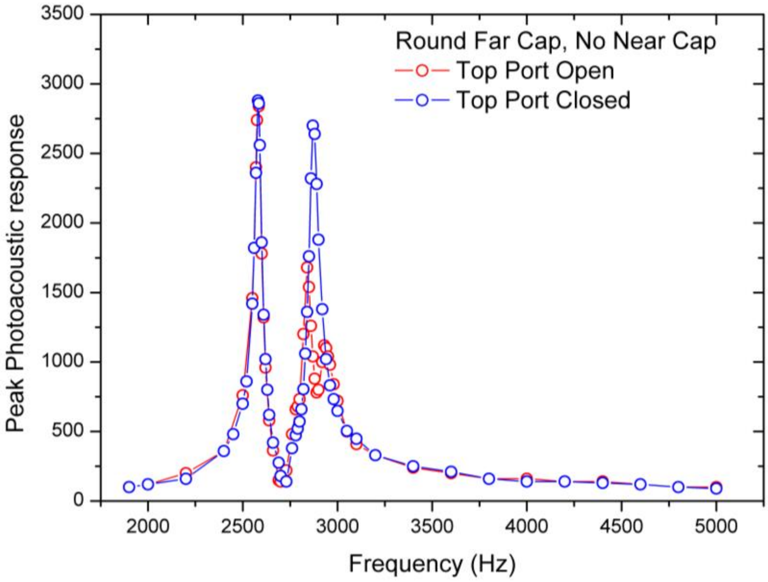

Figure 90 - Comparison of the photoacoustics response of the measurement cell with and without the B14 cap.

The removal of the B14 does not affect the primary resonance peak but splits the secondary resonance peak into two, 2840 and 2948 Hz with *Q* factors 69 and 38 respectively.

"Original" far cap, "large" near Cap

With the 'large' entry end cap, the resonance frequency and *Q* factor were re-measured. By enclosing the metal resonator within the measurement cell, the primary resonance frequency has shifted to 2635.8 Hz with a *Q* factor of 58. A more pronounced secondary resonance peak is also visible at 2903 Hz with a *Q* factor of 52, Figure 91.

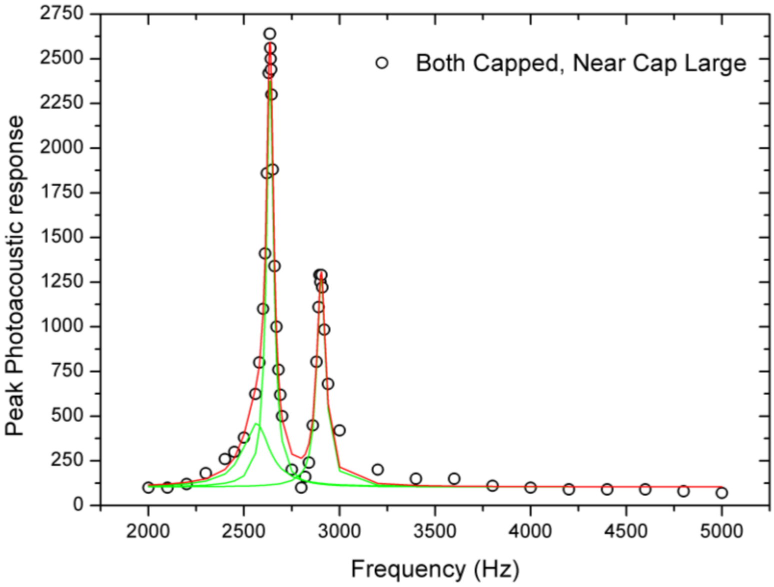

Figure 91 - A plot of the peak photoacoustic response of the polished metal resonator within the measurement cell with the large entry cap.

Original caps

By realignment of the optical path, it was possible to reduce the entry angle which allowed the use of the original end caps used before for the glass resonator (see Figure 92).

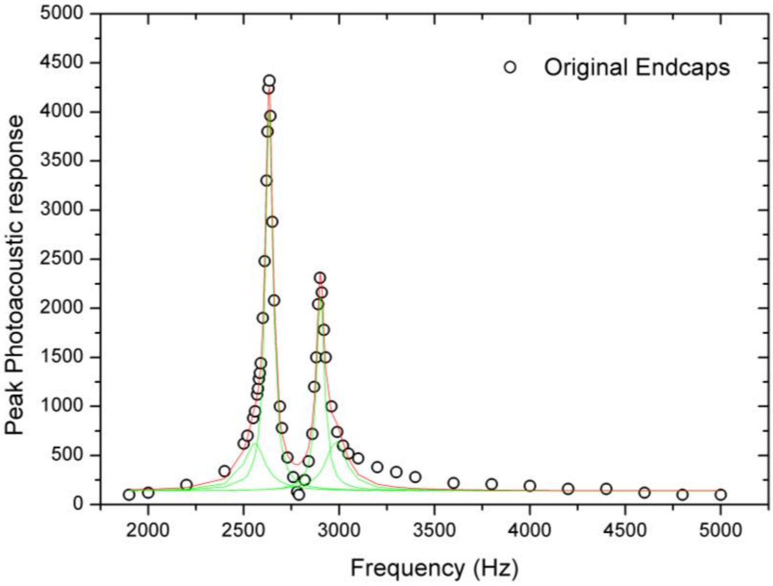

.

Figure 92 - Four Lorentzian fits of the peak photoacoustic response with the original end caps.

The primary acoustic resonance response is at 2633 Hz (*Q* factor 55, enhancement factor 34.8) with a secondary acoustic resonance at 2902 Hz (*Q* factor 58, enhancement factor 18). The original end caps have the largest overall *Q* and enhancement factors at the metal resonator's resonance frequency.

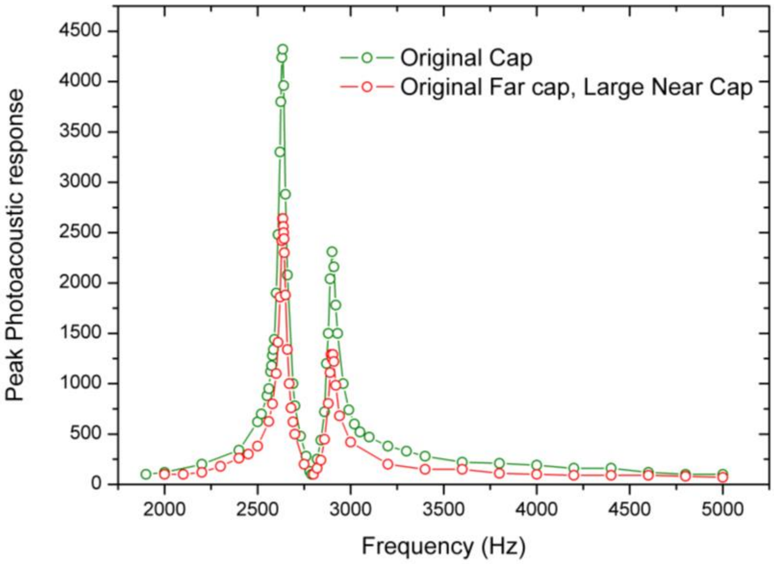

Figure 93 - Comparison of the frequency response of measurement cell with original caps and the combination of a large entry cap and an original cap.

In conclusion, the choice of the end caps is critical since it modifies the observed photoacoustic response of the acoustic resonator. It appears that the original end caps gave the biggest enhancement of all the end caps tested. In future work, the effect of the glass enclosure on the acoustic properties deserves to be investigated, for example with the use of an acoustic modelling software package, e.g. COMSOL (with the acoustics module) to identify the best enclosure configuration,[129] and verify the best configuration with a demonstrator.

Data collection

For each measurement, the processed output signal from the lock-in amplifier and the actuator’s extension length of the Littrow system were acquired by a data acquisition board (National instruments, PCI-6221), controlled by a home written LabVIEW program (see appendix for documentation).

Results and discussion

Sensitivity and detection limits

To characterise the sensitivity of HERPAS apparatus, acetylene and several TICs, ammonia, hydrogen sulfide and carbon monoxide, were analysed. Unless otherwise indicated, measurements refer to the glass resonator with the 'original' end caps. Care was taken to select absorption features which were free of unwanted water interference.

Acetylene

Acetylene (C_2H_2) has a very distinct absorption band with well-defined absorption lines. The $R(9)$ rotational line of the $(v_1 + v_3)$ vibrational combination band at 6578.6 cm^{-1} was selected as it was one of the strongest lines of this band at room temperature and since it is not affected by water absorptions. A defined gas mixture of acetylene and lab air was prepared on a vacuum line. The acetylene was transferred from a vintage BOC cylinder of unknown purity. A stock bulb was prepared by transferring 5 mbar of C_2H_2 to an evacuated glass bulb, purified by three cycles of freeze, pump, thaw and then made up to 1 atm. with lab air. For each concentration, a portion of the prepared gas mixture was transferred into the cell and made up to 1 atmosphere with lab air.

Figure 94 shows an overview spectrum of the R-branch of C_2H_2 at 6560 cm^{-1}. There is excellent agreement between the measured and simulated acetylene spectra from HITRAN database [104] where the simulated theoretical stick spectra have been broadened with room temperature Doppler broadening and 1 atm. of air pressure broadening. Within the 60 cm^{-1} range shown above, no evidence of mode hop behaviour was detected. The *R*(9) line was used to determine the limit of detection (LOD). The limit of detection is defined at the concentration equivalent to three times the noise level. All measurements here refer to a 100 ms integration time.

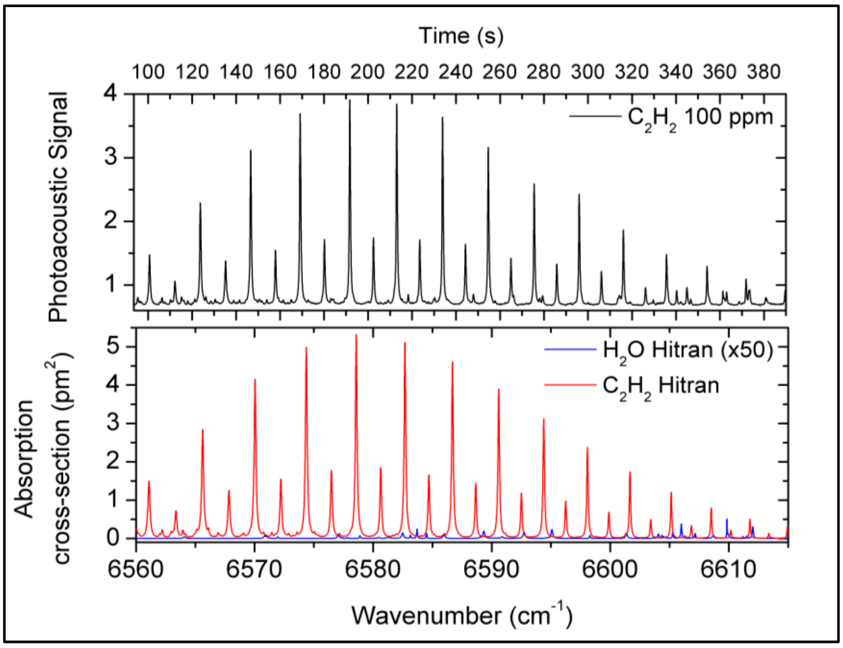

Figure 94 - Top: Measured spectrum of acetylene at 100 ppm. The majority of the *R*-branch is visible. Bottom: HITRAN simulation acetylene (red) and water (blue) at 1 atm., 298K. Water is amplified by a factor of 50 to allow easier observation.

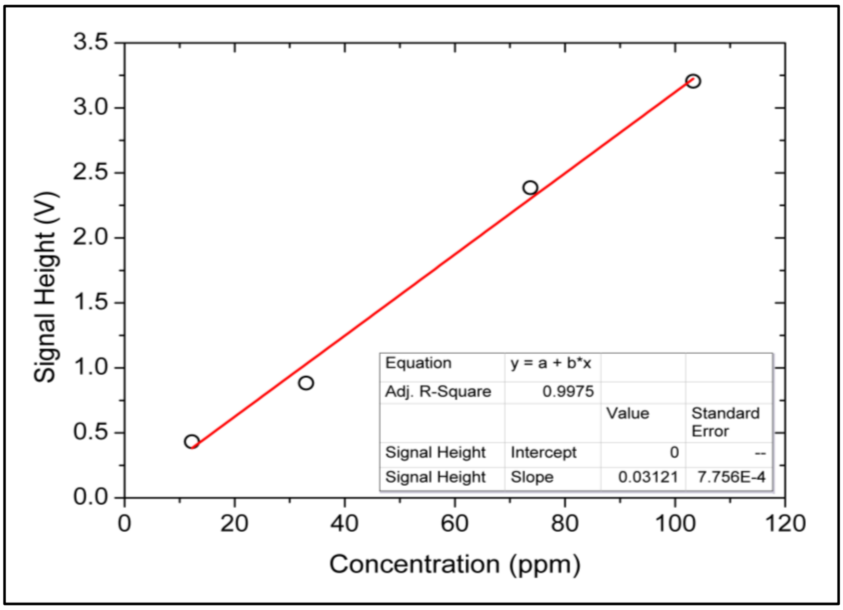

Figure 95 - A calibration line of acetylene ranging from 12 to 100 ppm against photoacoustic signal at room temperature and at 1 atm.

Figure 95 shows a calibration line of various concentration C_2H_2 against photoacoustic signal with good linearity. The noise level of the apparatus was determined at a region where there were no water absorptions. A noise level of 1.4 mV was determined. This corresponds to a limit of detection of 135 parts-per-billion (ppb) at 100 ms integration time. A comparison can be made with the mid-IR CERPAS (see Chapter 2); the noise equivalent detection limit (NEDL) for C_2H_2 was 150 part-per-trillion (ppt) at 1 s integration time. However, the mid-IR CERPAS had several systematic advantages. Firstly, the mid-IR laser had a nominal output of 100 mW compared to the 35 mW in the NIR, which will result in an increase of sensitivity by a factor of 3. Secondly, the $v_4 + v_5$ $R(9)$ was probed which is approximately ten times stronger compared to the $v_1 + v_3$ $R(9)$ line in the near IR, which will increase the sensitivity by a further factor of ten. However, the NIR HERPAS setup is considerably more convenient and user friendly.

Ammonia

Unlike acetylene, ammonia (NH_3) has a more irregular band pattern which requires a little preliminary work to identify suitable absorption lines for interference free detection. Figure 96 shows an overlay of the simulated NH_3 (red) and H_2O (blue) spectrum. It can be seen that the strongest NH_3 line at 6605 cm^{-1} is unsuitable for quantifying the concentration of ammonia in air due to the presence of a relatively strong water line which will cause inaccurate determination of NH_3 concentration. The next strongest lines are at 6568 cm^{-1} and 6612 cm^{-1} (labelled with 1 and 2 respectively). Line 1 is weaker than line 2 by approximately 60 % and there is a weak water absorption line which perfectly overlaps with the NH_3 line. The presence of such a small water absorption feature should not be a problem as the NH_3 absorption cross-section is orders of magnitudes stronger. Line 2 has the advantage that it is the second strongest line resulting in good sensitivity from HERPAS. However, the presence of a water line at 6612 cm^{-1} whose “foot” overlaps with an absorption line of NH_3 could be a cause for concern, especially at lower concentrations of ammonia.

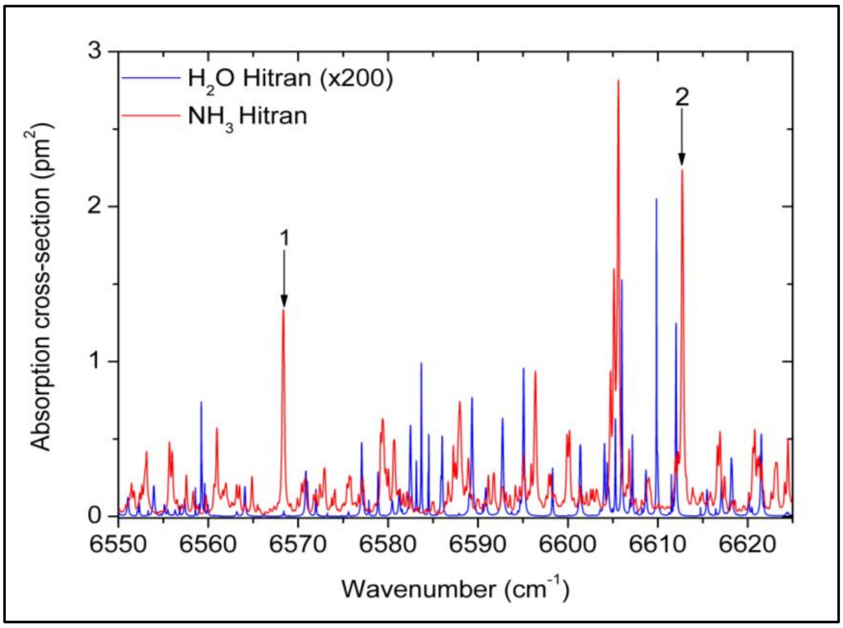

Figure 96 - HITRAN simulations of NH_3 and H_2O between 6550 and 6625 cm^{-1} at room temperature and 1 atm. of air. Line 1 is shown on the left and line 2 on the right.

In

Figure 97, excellent agreement is shown between the measured spectrum and the simulated spectra from HITRAN. In the baseline, there is a minor trough in the photoacoustic response, labelled with an asterisk, which is very likely to be caused by an external event. A more in depth discussion of external events will be performed in the later section of "External Influences". Using the peak value of line 1, several different concentrations were measured and analysed to determine the limit of detection. The LOD is 1.2 ppm in 1 atm. of air, at 100 ms integration time which is substantially below the immediately dangerous to life or health (IDLH) limit of 300 ppm.

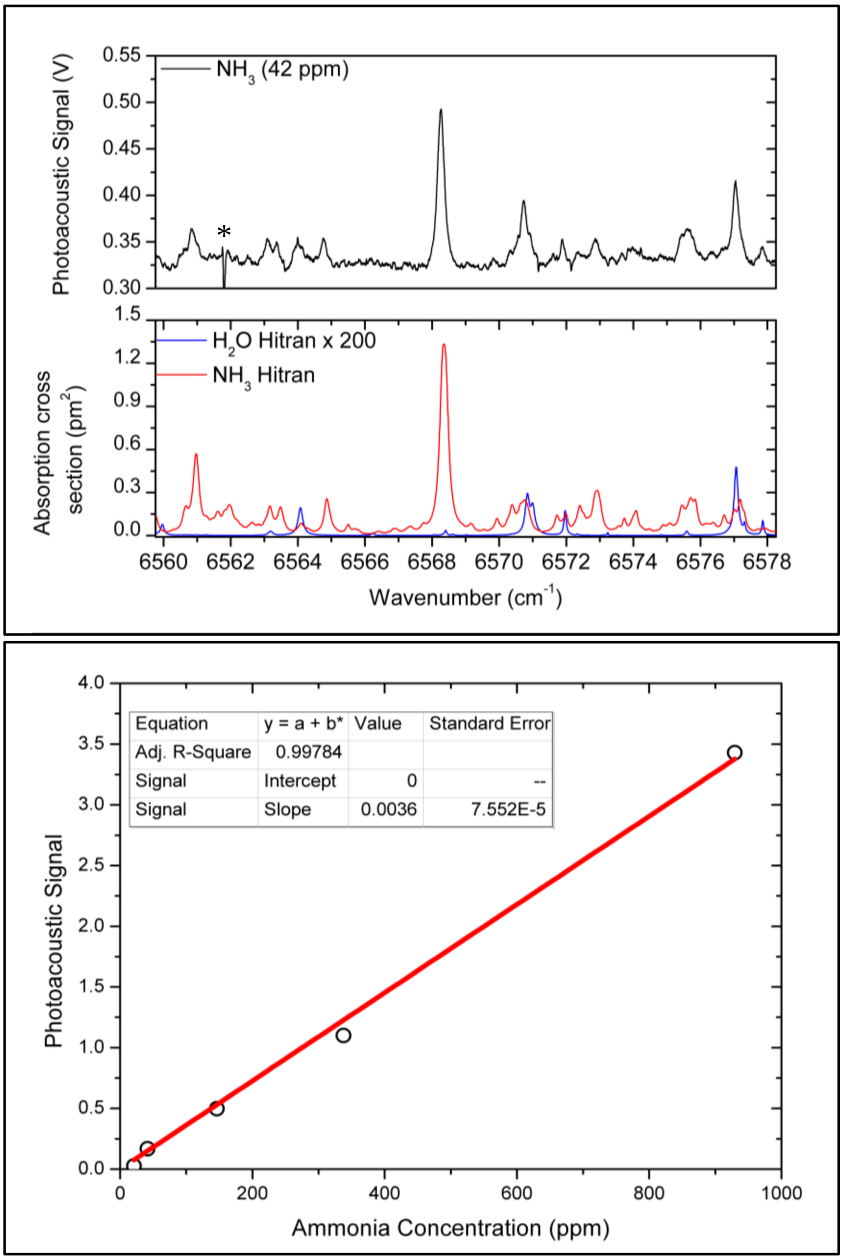

Figure 97 - Top: Measured spectrum of NH_3 at 42 ppm in 1 atm. of air. Middle: HITRAN simulation of ammonia and water at standard conditions. Bottom: Calibration plot of ammonia at varying concentrations using the line at 6568 cm^{-1}.

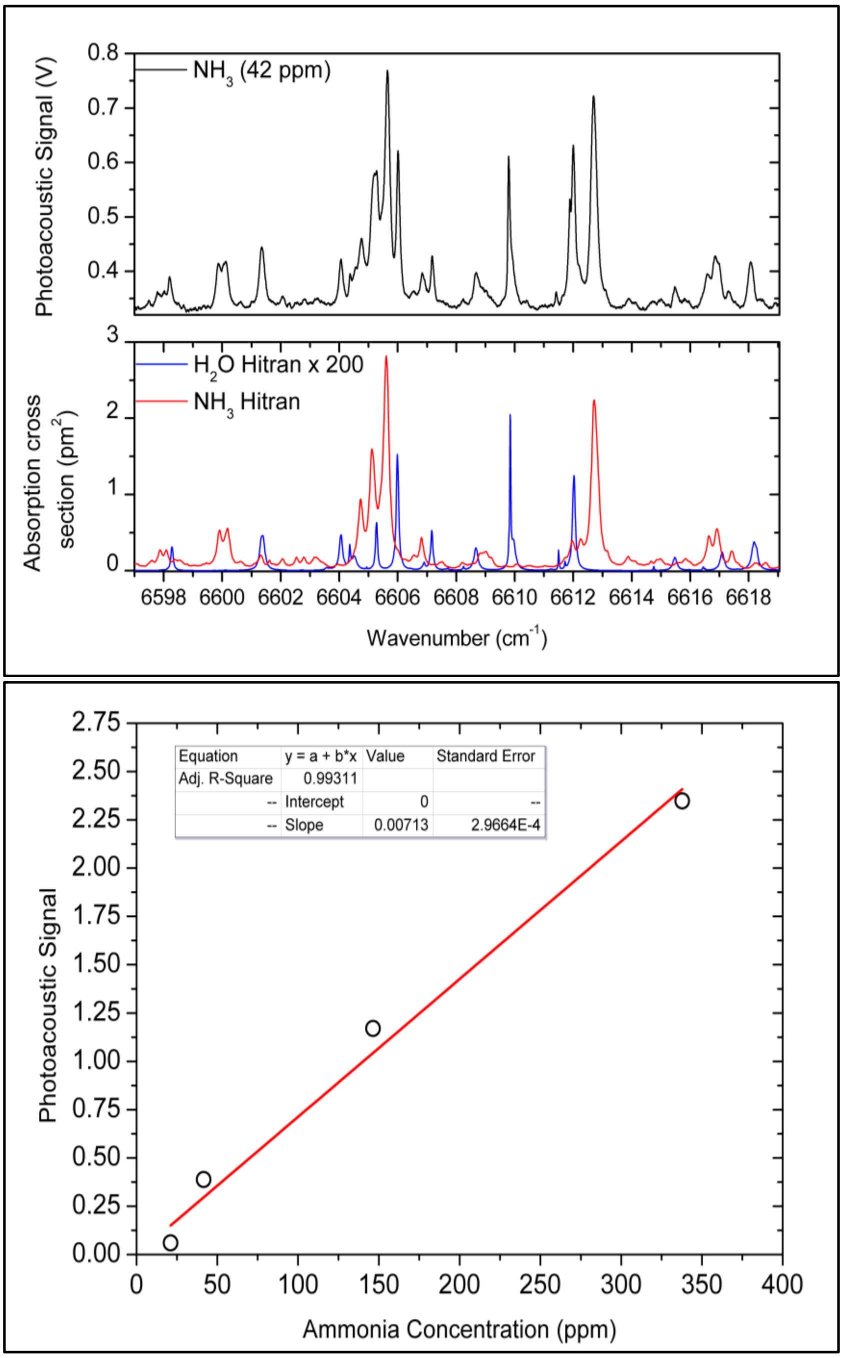

Figure 98 - Top: Measured spectrum of NH_3 at 42 ppm in 1 atm. of air, at 100 ms integration time. Middle: HITRAN simulation of ammonia and water at standard conditions. Bottom: Calibration plot of ammonia at varying concentrations using the line at 6612.7 cm^{-1}.

Using line "2" at 6612.7 cm^{-1}, again there is an excellent agreement between the measured and theoretical spectrum (see Figure 98). As an aside, there is a water line on the left of the strongest NH_3 line which has merged with a smaller ammonia line to form a broader peak. This suggests that not selecting the strongest absorption line was a fortuitous choice as the water line is likely to affect the true lineshape, increasing the apparent height of the ammonia signal and possibly yielding a false positive alarm. The calibration line yields a LOD of 0.6 ppm in 1 atm. of air, at 100 ms integration time which in consistent with the increase in absorption cross-section compared to line 1.

Hydrogen sulfide

Hydrogen sulfide (H_2S) has a rather low absorption cross-section even in the fundamental absorption band. In addition, the H_2S fundamental bands can be difficult to distinguish due to overlapping water bands. In the near infrared, there are much better opportunities to successfully detect and distinguish the individual H_2S lines as they are well removed from the strong H_2O lines. Three strong absorption lines from the $v_1 + v_2 + v_3$ combination band at 6362.9, 6363.9 and 6369.8 cm^{-1} are visible.[130] The strongest line at 6369.8 cm^{-1} was chosen as it is far away from strong water absorption features.

Figure 99 shows the excellent agreement between the measured and simulated spectrum in one atmosphere of lab air as well as excellent linearity for concentrations ranging from 50 to 723 ppm which are below and above the IDLH limits. The LOD is found to be 1.7 ppm in 1 atm. of air, at 100 ms integration time, once again far below the IDLH concentration limit of 100 ppm.

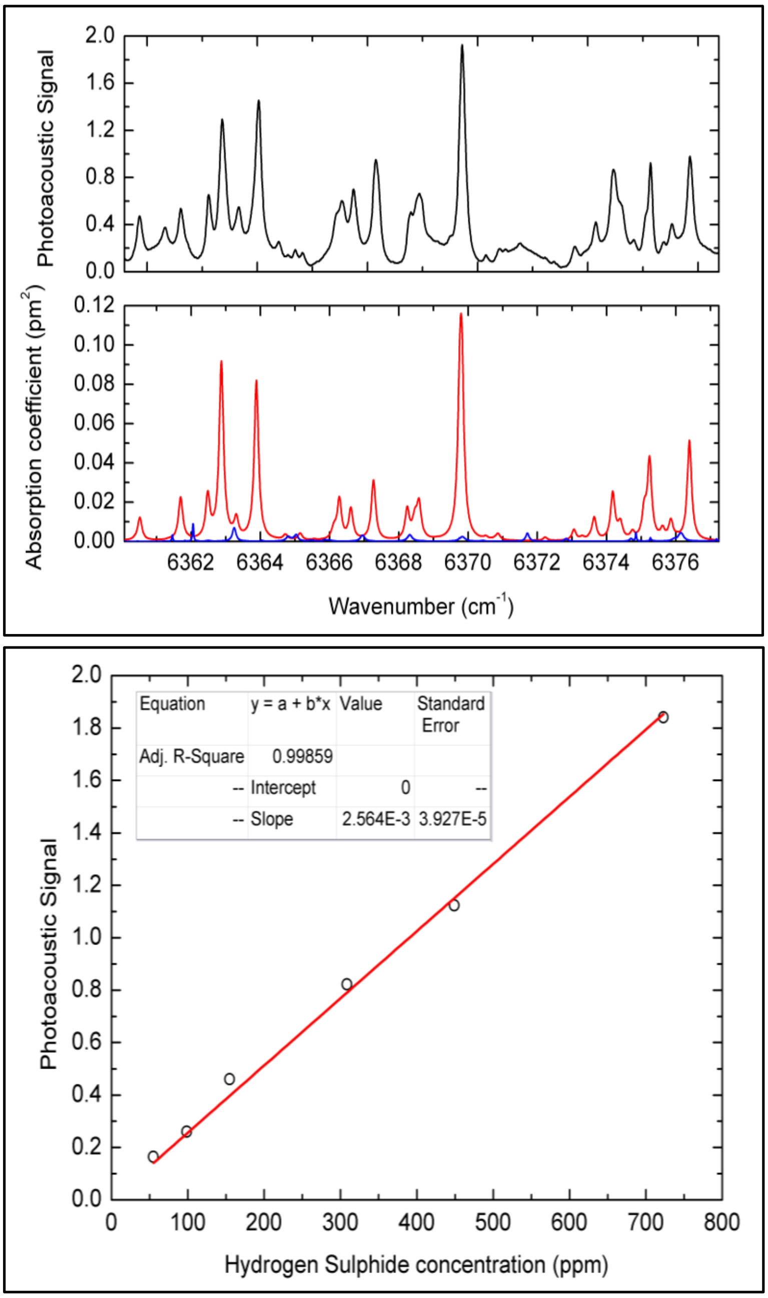

Figure 99 - Top: Measured spectrum of H_2S at 723 ppm in 1 atm. of air. Middle: HITRAN simulation of H_2S (red) and water (blue) at standard conditions. Bottom: Calibration plot of H_2S at various concentrations using the H_2S absorption line at 6369 cm^{-1}.

H_2S was also measured with the metal resonator to evaluate its performance in the shorter configuration. The same line was re-measured at various concentrations as shown in Figure 100. The gradient is much lower than the previous measurement of H_2S with the glass resonator, however, the noise is also lower as shown in Figure 102. This may be due to the fact that different microphones were used for the glass resonator and the metal resonator. The LOD is determined to be 2 ppm, very similar to the value for the glass resonator, so again the conclusion is that metal resonator does not offer significant advantages compared to a glass resonator.

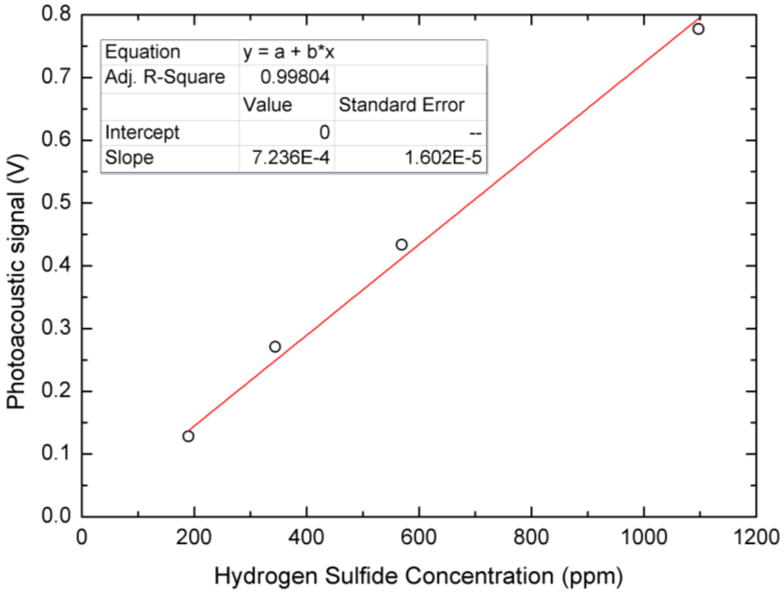

Figure 100 - Calibration plot of H_2S with the metal resonator.

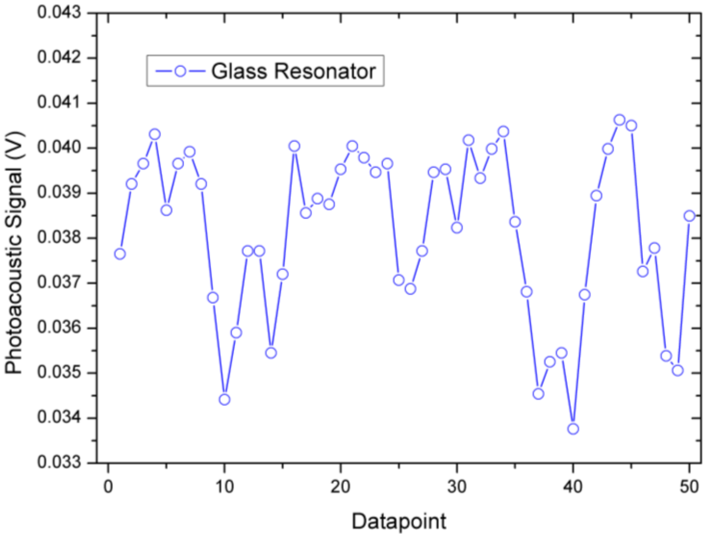

Figure 101- Noise profile from H_2S measurements from glass resonators

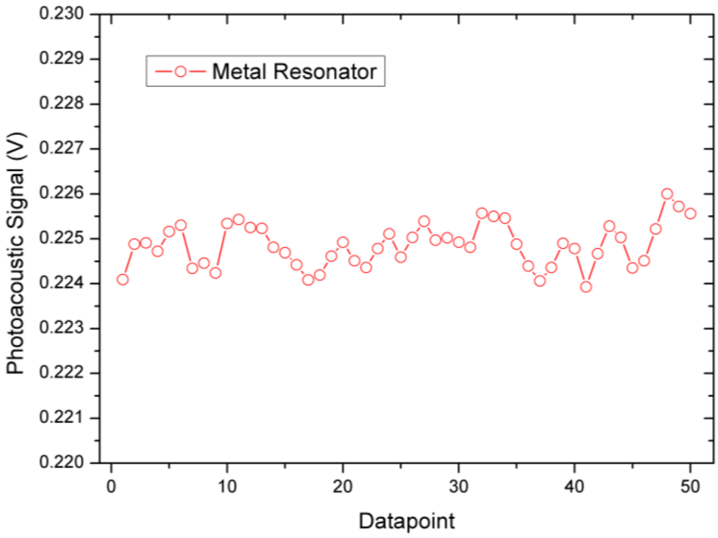

Figure 102 - Noise profile from H_2S measurements from metal resonators.

Carbon Monoxide

Carbon monoxide (CO) has the lowest absorption cross-section (≈ 0.012 pm^2) of all the tested TICs in this near infrared region and has easily recognisable ro-vibrational lines. In Figure 103, two different sets of absorption lines can be seen. The tighter packed lines on the left are the *R*-branch of CO_2 and the wider spaced lines to the right are from the *R*-branch of CO. In this scenario, care must be taken to avoid selecting a CO absorption line which is overlapped with any CO_2 absorption lines. The detection limit was determined using the *R*(8) line, labelled with an asterisk, as it is the first CO line with a large absorption cross-section which is clearly distinguishable from CO_2. Excellent linearity is observed in a dilutions series as shown in Figure 103. The LOD is found to be 28 ppm in 1 atm. of air, at 100 ms integration time which is significantly below the IDLH limit of 1200 ppm.

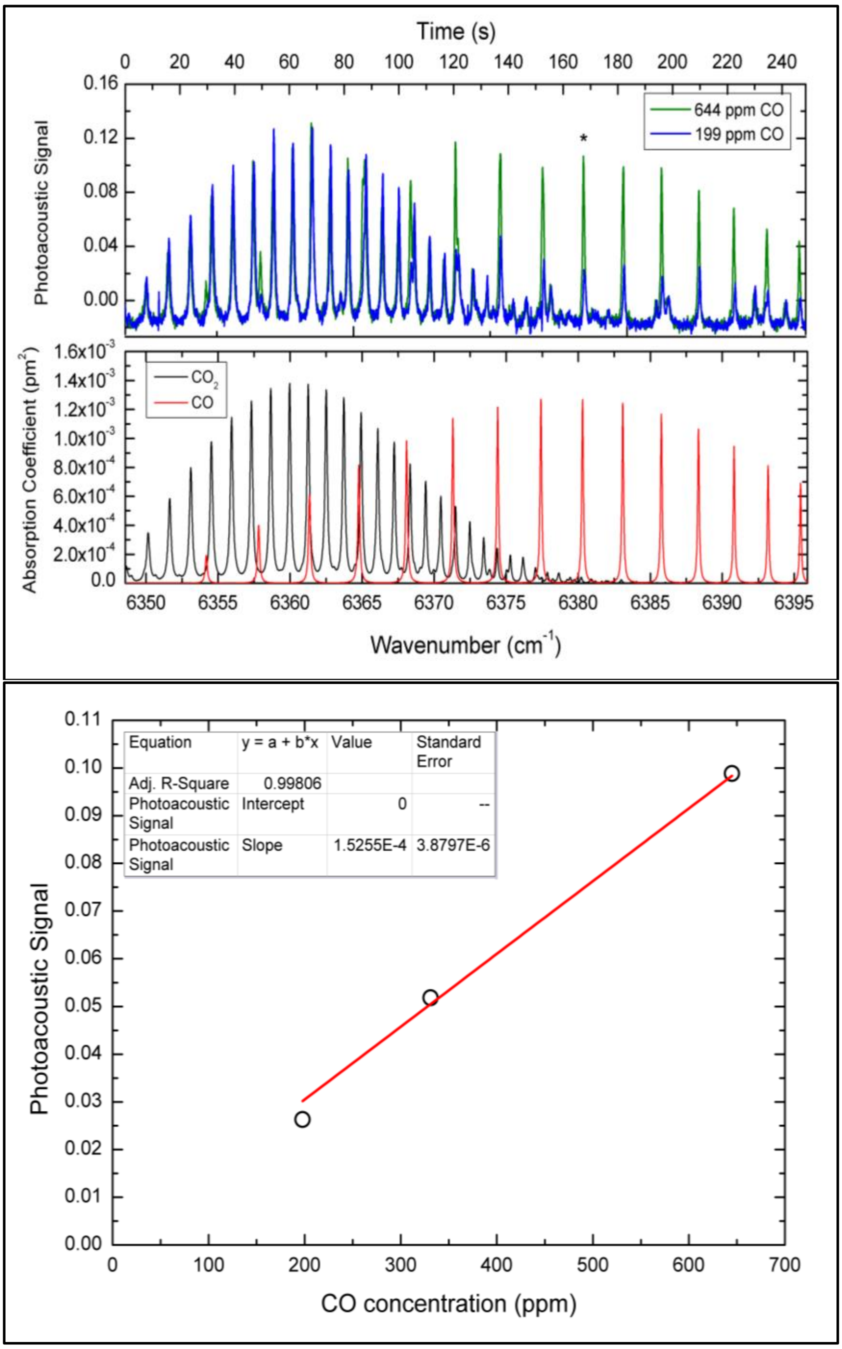

Equation	y = a + b*x	Value	Standard Error
Adj. R-Square	0.99806		
Photoacoustic Signal	Intercept	0	--
Photoacoustic Signal	Slope	1.5255E-4	3.8797E-6

Figure 103 - Top: Measured spectrum of CO (644 and 199 ppm) in 1 atmosphere of air. Middle: Simulation of CO and CO$_2$ at standard conditions. Bottom: Calibration line of the *R*(8) line of CO.

Other Toxic Industrial Gases

A search of spectral databases was undertaken to determine whether other TICs are theoretically detectable by the current ECDL system based upon the specification from the manufacturer (1470 - 1630 nm, 6130 - 6800 cm^{-1}).

Hydrogen Cyanide

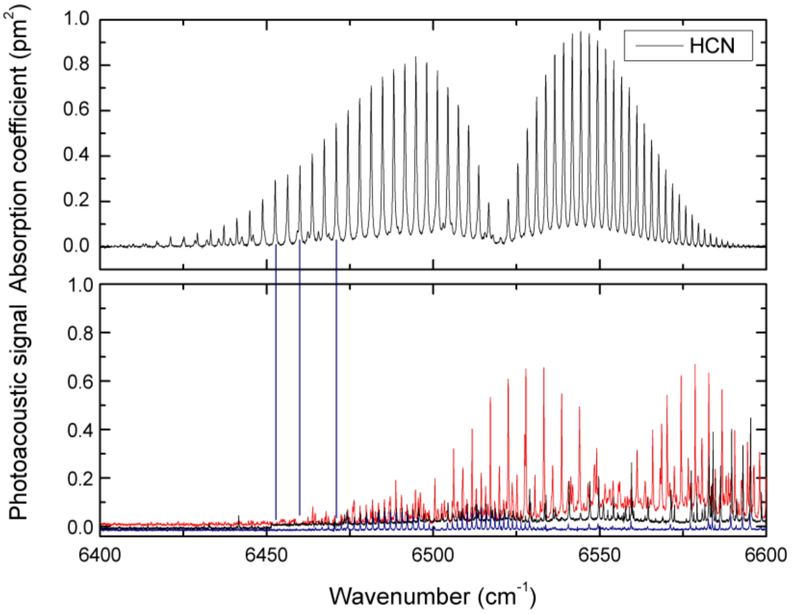

Figure 104 - Top: Theoretical absorption spectrum of hydrogen cyanide and HERPAS recorded spectrum of recorded chemical interferents.

From Figure 104, it can be seen that there are many absorption features present where hydrogen cyanide absorbs strongly; there are windows of opportunity in the range of the current ECDL system between 6450 - 6500 cm^{-1} where the absorption coefficients of HCN are still quite strong. Three particular lines (shown by the blue lines) have been identified as free from interferents as measured in the later section. By comparing the absorption coefficient, one can estimate a LOD of 0.4 - 0.8ppm. For comparison, the IDLH is 50 ppm.

Ethylene Dibromide

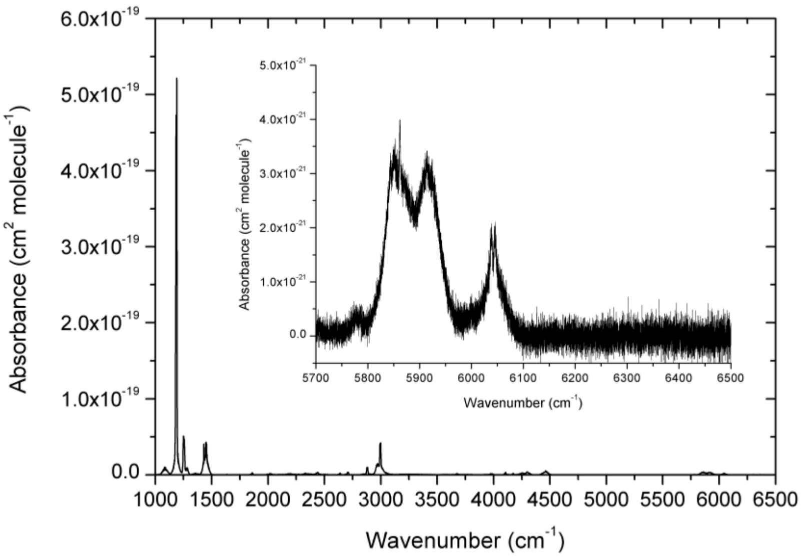

Figure 105 - Absorbance spectrum of ethylene dibromide extracted from Ref. 105

As can be seen from Figure 105, within the range of the current laser (1500 - 1600 nm, 6250 - 6670 cm^{-1}), there are no significant absorption features present and ethylene dibromide thus cannot be detected by the current system.

Other compounds are in a similar situation where there are no significant absorption features above 6200 cm^{-1}. These compounds are arsine (6136 cm^{-1}), acrolein (6170 cm^{-1}), allyl alcohol (6160 cm^{-1}) and carbonyl sulfide (6128 cm^{-1}), where close absorption bands are cited in parentheses.

Interferents

Using the current laser system, several possible interferents likely to be encountered in the field were analysed to evaluate their effects on HERPAS and to obtain spectra.

Methane

Methane (CH_4) is an odourless gas at standard conditions and an abundance of 1800 ppb in air. From literature, it is unlikely to be observable using the current HERPAS system as the absorption cross-sections are very weak, (strongest line 3.82 x 10^{-4} pm^2 at 1512.85 nm) between 1500 - 1600 nm).[104] At natural abundance, the predominant $v_2 + 2v_3$ combination overtone band at 1.33 µm and the $2v_3$ overtone band at 1.66 µm are not within the range of this laser diode as shown in Figure 106. [131] Figure 107 shows no signs of methane within the measured spectrum, while CO_2 and water peaks are clearly evident.

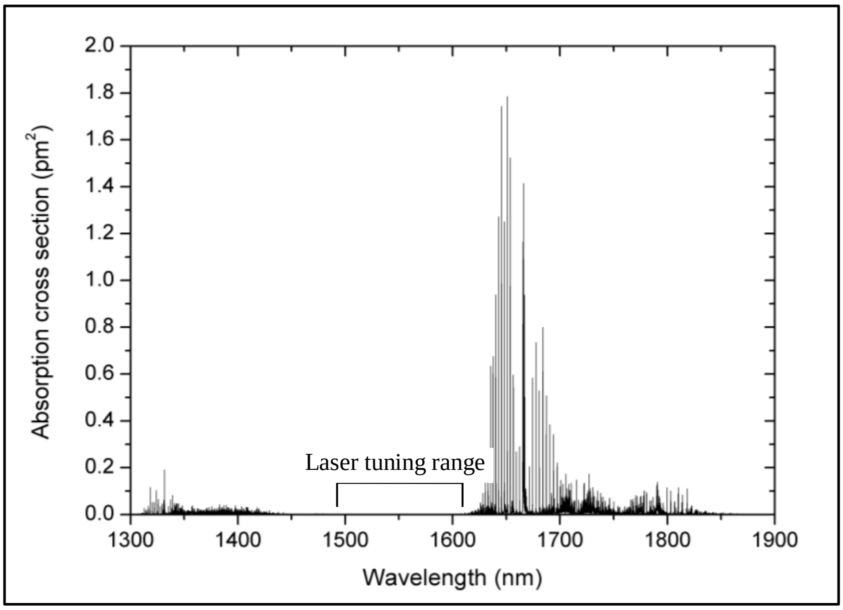

Figure 106 - Simulated spectrum of methane in the near IR range of the laser and beyond at 1 atm pressure broadening.

n-Hexane

n-Hexane is used to extract edible oils from seeds and oils and is a significant constituent in petrol whose fumes could be picked up when they system is deployed in the field. Hexane absorption bands in the NIR will arise from the second overtone C-H stretching and the C-H bending vibrations. However, in the current range of this laser, these absorption bands are not accessible as shown in Figure 106 as no distinguishable new bands can be observed, except from CO_2 and H_2O impurities.

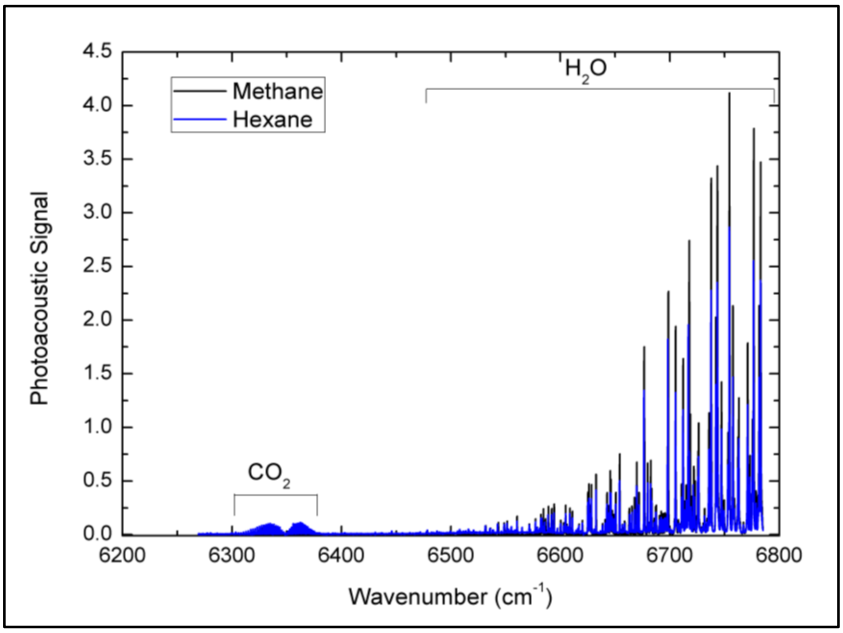

Figure 107 - Overlay of measured spectra of methane (974 ppm) and hexane (1174 ppm)

Natural Gas

Natural gas contains mainly methane, but also other hydrocarbons at much lower levels. Natural gas from the departmental gas supply was used without further purification. The gas was transferred into the cell by first purging a Teflon bag from a natural gas outlet to remove any traces of air and then filling it until full. The Teflon bag was then sealed and the gas was transferred from the bag to the cell via a vacuum line. Figure 108 shows that no peaks were observable with 1 atmosphere of natural gas. The two spikes are from external events which will be discussed later. Overall, there was no response from natural gas apart from an elevated baseline.

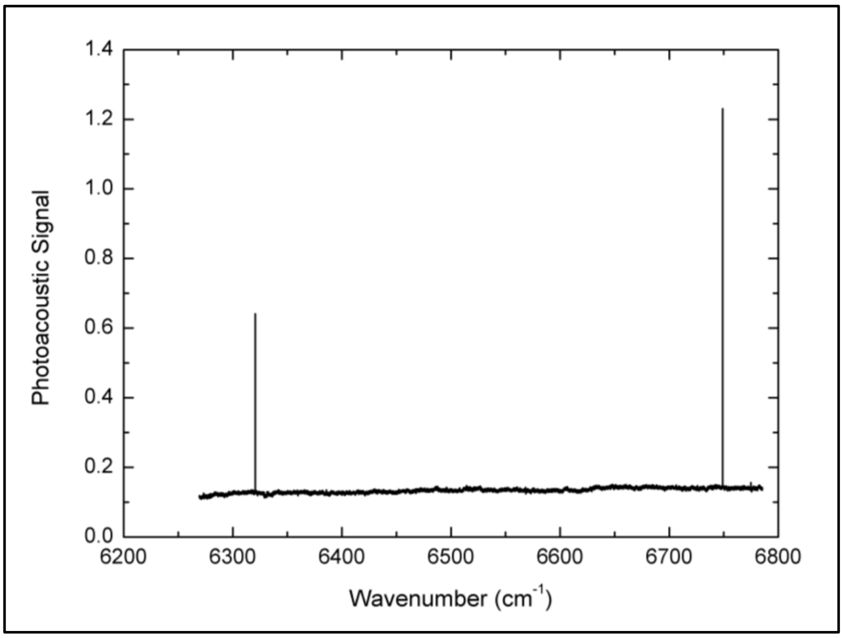

Figure 108 - A measured spectrum of 1 atmosphere of natural gas.

Methanol

Methanol is the simplest alcohol and has many uses ranging from camping fuel, as a solvent for industrial process and in bio-diesel production. HPLC grade methanol was purified by repeated freeze pump thaw cycles and its vapours were transferred to a glass balloon and made up to 1 atm. with lab air. The methanol/air gas mixture was then transferred to the measurement cell and diluted to the required concentration with more lab air.

Figure 108 shows the measured spectrum of 490 ppm of methanol in 1 atm. of lab air. In the region shown the O-H overtone band is very broad and is easily recognisable. With alternative fitting techniques, to correct for the broad methanol absorption, one could still determine the concentration of the TICs, a subject which will be discussed in more detail later.

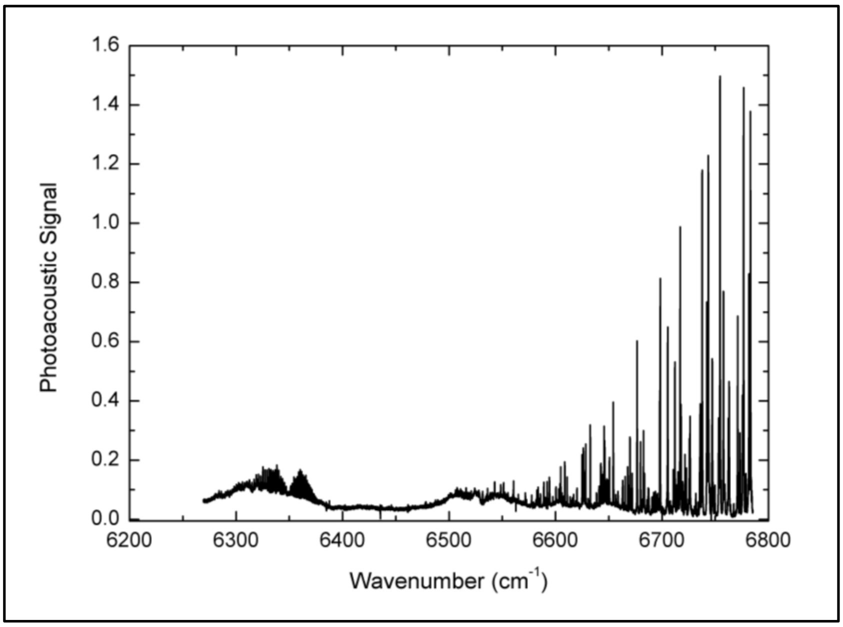

Figure 109 - A spectrum of 490 ppm of methanol. The O-H overtone bands are visible at 6325 cm^{-1} and 6530 cm^{-1}.

Ethanol

Ethanol is an important alkyl alcohol used recreationally and industrially. Annual production in 2012 reached 83 billion (10^9) litres. There is a significant concentration of ethanol in petrol or gasoline, with “E” numbers describing the percentage of ethanol by volume mixed with the petrol. A variety of ethanol: petrol blends are available from E5 to E85, with E10 being the most commonly used internationally. The presence of ethanol in fuel systems is likely to cause a slightly elevated ethanol concentration in close proximity to petrol driven cars, which might constitute an interference to the HERPAS system to TICs. Ethanol (VWR, 99.9 %) was purified by repeated freeze pump thaw cycles and its vapours was transferred to a glass balloon and made up to 1 atm. with lab air. The ethanol/air gas mixture was then transferred to the measurement cell and diluted to the required concentration with more lab air.

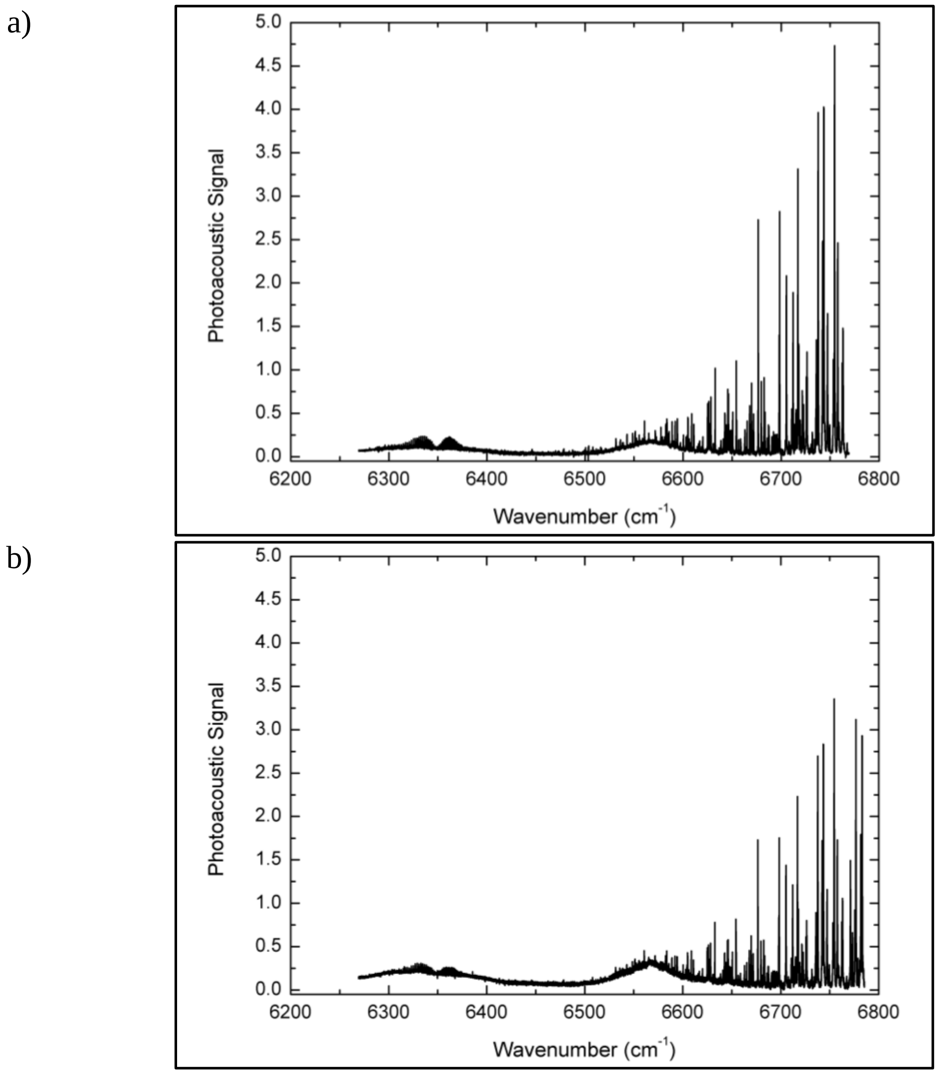

Figure 110 - a) A spectrum of 28 ppm ethanol, b) a spectrum of 795 ppm ethanol.

Figure 110 shows a typical measured spectrum of ethanol at 28 ppm in 1 atm of air. The OH absorption bands are present similarly as in methanol, with ethanol showing a more pronounced peak at 6560 cm^{-1}.

Perfume

Perfumes are classified by the concentration of aromatic compounds in a solvent into a variety of grades. They might also constitute interferents for HERPAS detection of TICs. Typically the solvent is ethanol or ethanol blended with water and can make up 80 % by volume of the perfume. A sample of perfume (Avon, City Rush, Eau de Parfum) was collected as below. The perfume was squirted ten times into a glass balloon and underwent three cycles of freeze, pump, thaw to remove the air present. A vapour pressure of 40 mbar was observed, where the majority can be attributed to ethanol. A sample with 0.49 % perfume was made up with lab air and measured with HERPAS as shown in Figure 111.

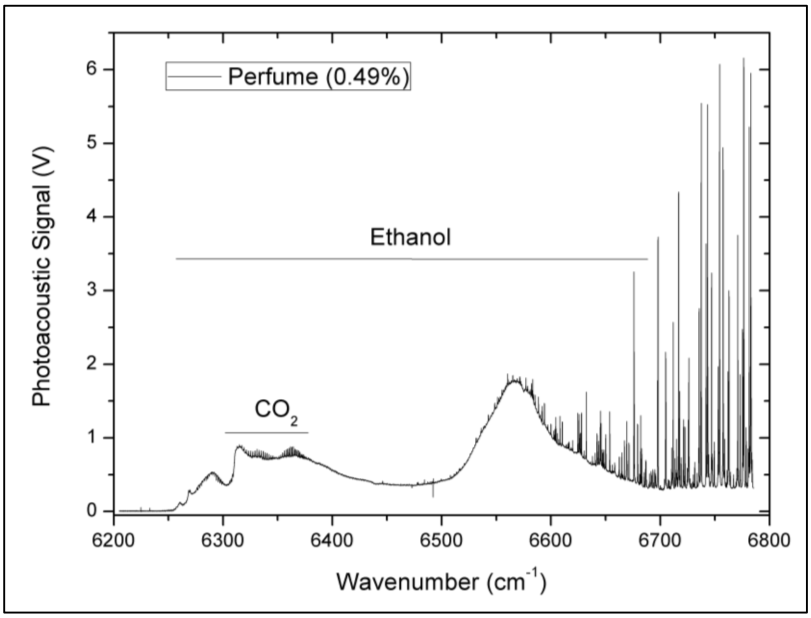

Figure 111 - A HERPAS spectrum of perfume at 0.49 % in 1 atmosphere of air.

It can be seen that the spectrum has the same broad response of the ethanol peaks (Figure 110) but more intense due to the increased concentration of ethanol. The distortion at 6310 cm^{-1} is from an artefact of the alignment of the ECDL and suggests realignment is required.

Petrol Exhaust

Another likely interferent is exhaust fumes from a petrol driven vehicle. A sample of petrol exhaust fumes was collected from a "warmed-up" car where the car has been idling for several minutes. This allows the catalytic convertor to be warmed up by the exhaust gases. An evacuated glass balloon was placed at the exhaust outlet and a sample was drawn into the balloon and transferred to the measurement cell. Figure

112 shows the resultant measured spectrum. It is possible to see an increase in CO_2 and water concentration. The presence of a weaker CO_2 band is just visible between 6470 and 6530 cm^{-1} as shown in Figure 112.

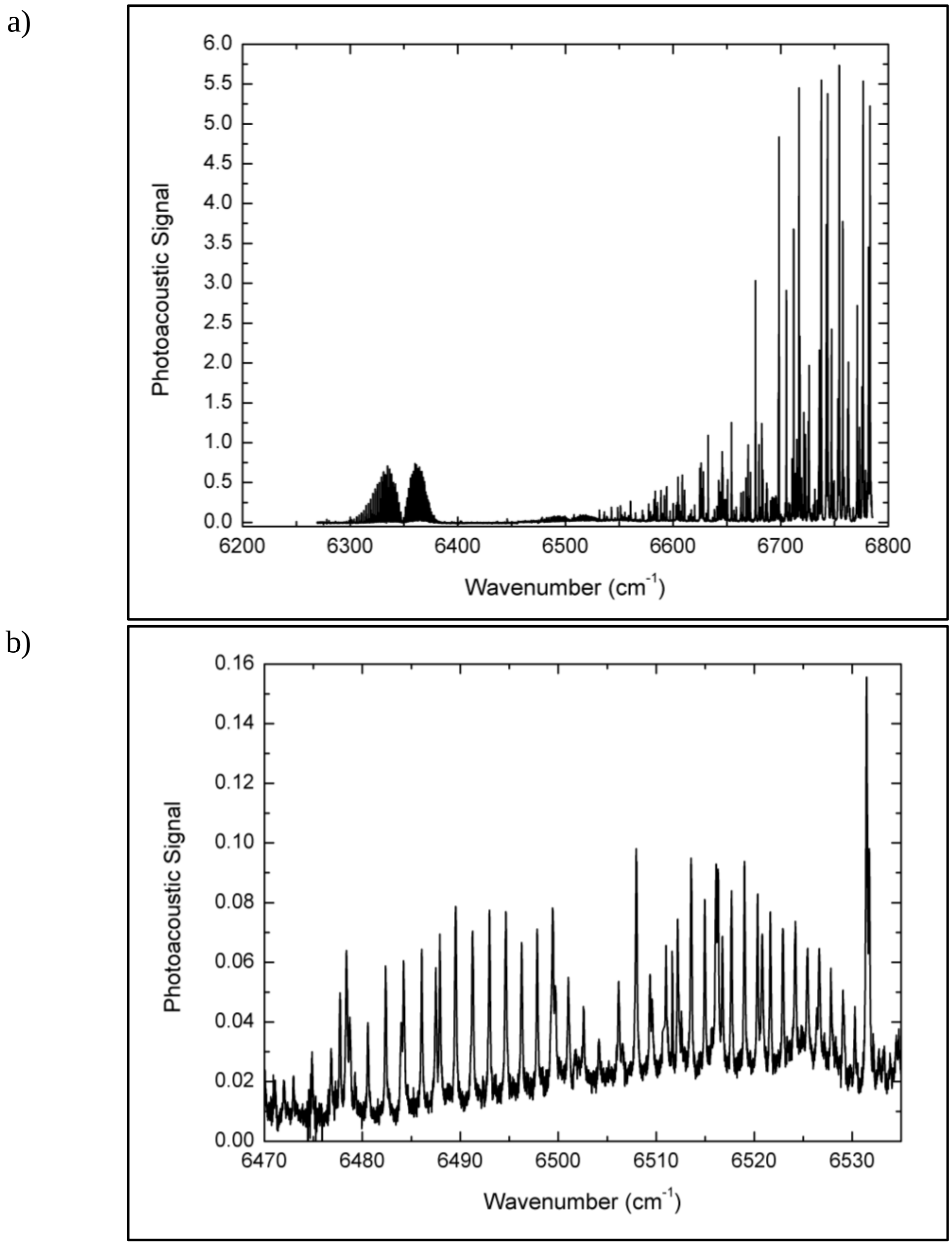

Figure 112 - a): Measured spectrum of 4 % petrol exhaust in 1 atm. of lab air. b): A much smaller CO_2 band at 6470 - 6530 cm^{-1}.

Diesel Exhaust

Diesel exhaust is another likely interferent to be encountered especially in the military sector. A sample of diesel exhaust fumes was collected from a “warmed-up” car as per the petrol exhaust collection. Figure 113 shows the resultant measured spectrum. It is possible to see an increase in CO_2 and water concentration and the presence of a weaker CO_2 band is visible between 6470 and 6530 cm^{-1}.

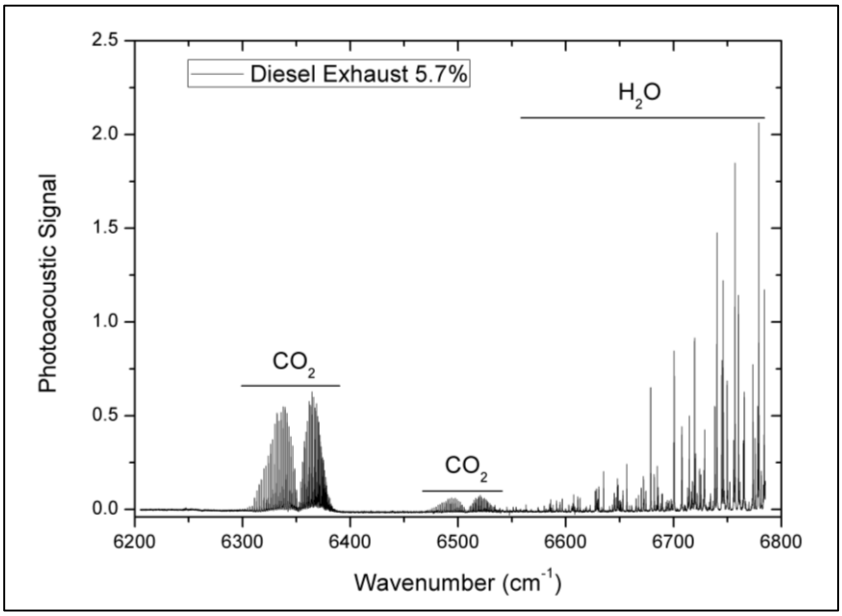

Figure 113 - Measured spectrum of 5.7 % diesel exhaust in 1 atm. of lab air.

Cigarette Smoke

For 2013, in the US, it was estimated that 18 % (42 million)[132] of the population are current cigarette smokers. Cigarette smoke was collected by sucking the smoke given off from the lit end of the cigarette into an evacuated balloon until the glass balloon was visibly smoky. The gas was transferred across to the measurement cell and diluted with air.

CO_2 and water vapour is clearly recognisable as per any recorded spectrum. An increased concentration of CO_2 is observed. In addition, C_2H_2 is also clearly present, with an estimated concentration of 21 ppb. Trace amounts of CO (≈ 66 ppm) are also present as shown in Figure 115 where directly identifiable peaks are shown in red as well as NH_3 (≈ 136 ppm) as shown in Figure 116.

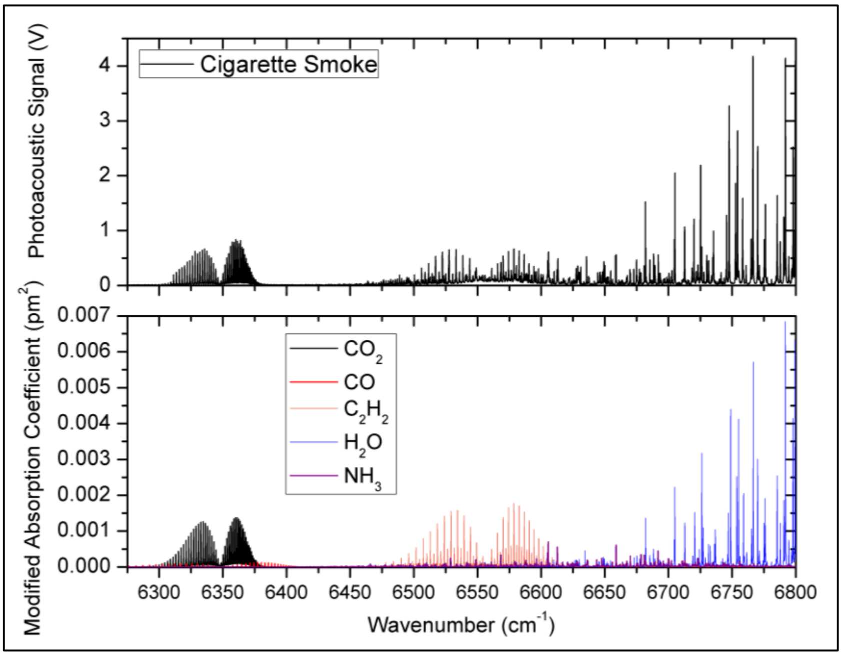

Figure 114 - Top: Measured HERPAS spectrum of cigarette smoke in one atmosphere of air. Bottom: Simulated spectrum of five observable components of cigarette smoke.

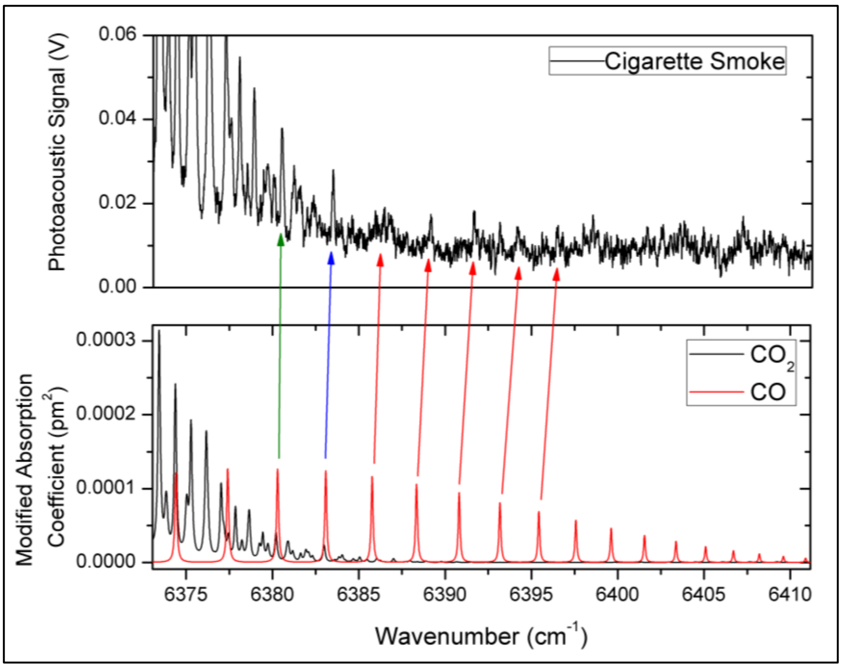

Figure 115 - Top: Magnified section of measured cigarette smoke HERPAS spectrum between 6370 - 6412 cm^{-1}. Bottom: corresponding theoretical spectrum.

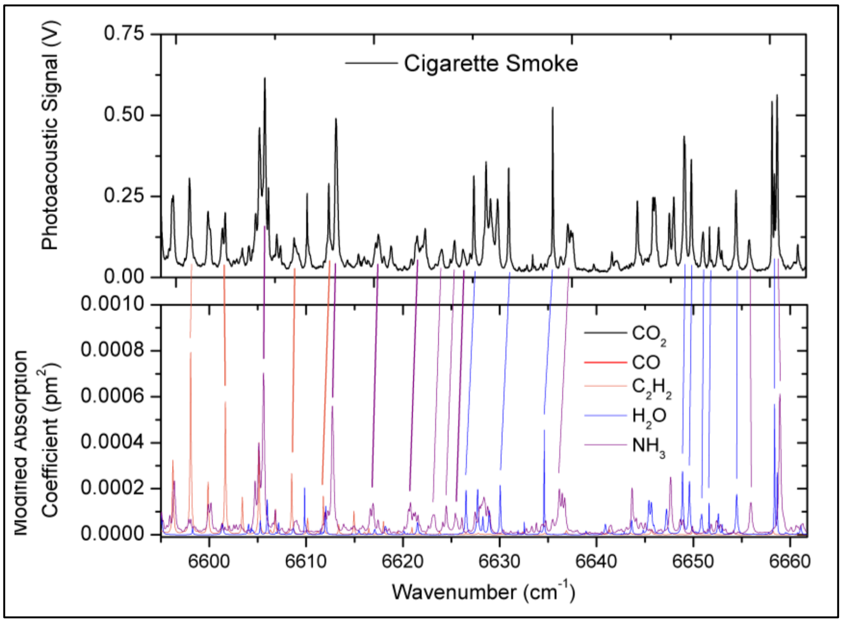

Figure 116 - Top: A magnified spectrum of cigarette smoke at 6595 - 6660 cm^{-1}. Bottom: theoretical spectrum showing the presence of C_2H_2, NH_3 and water, matched with the recorded spectrum with coloured lines.

Linearity of ethanol and hydrogen sulfide measurements

With high concentration of interferents, there was concern that TICs signals might be concealed or distorted by the interferents. Theory suggests that this is unlikely since PA is a highly linear technique with a very large dynamic range, unless the interferents and target molecules quench the laser light. A glass balloon filled with hydrogen sulfide and ethanol was made. For each measurement, a portion of the premade hydrogen sulfide/ethanol mixture was transferred across. Assuming that the mixtures equilibrated, the concentration for each measurement should be well defined.

Ethanol, as mentioned above, has a wide absorption band centred at 6330 cm^{-1}. Two options are available to determine the signal height of hydrogen sulfide. If one focused on the H_2S line position at 6369.8 cm^{-1}, the ethanol band is comparatively much broader and could be assumed to be effectively a flat elevated baseline where a simple baseline subtraction can suffice. The alternative is to fit the hydrogen sulfide absorption line with a Lorentzian line profile. While the absorption line is the convolution of a Lorentzian (pressure broadening) and Gaussian (Doppler broadening) profile yielding a Voigt profile, under standard conditions, the pressure broadening dominates and thus a good fit can be made by fitting a Lorentzian function as shown in Figure 117.

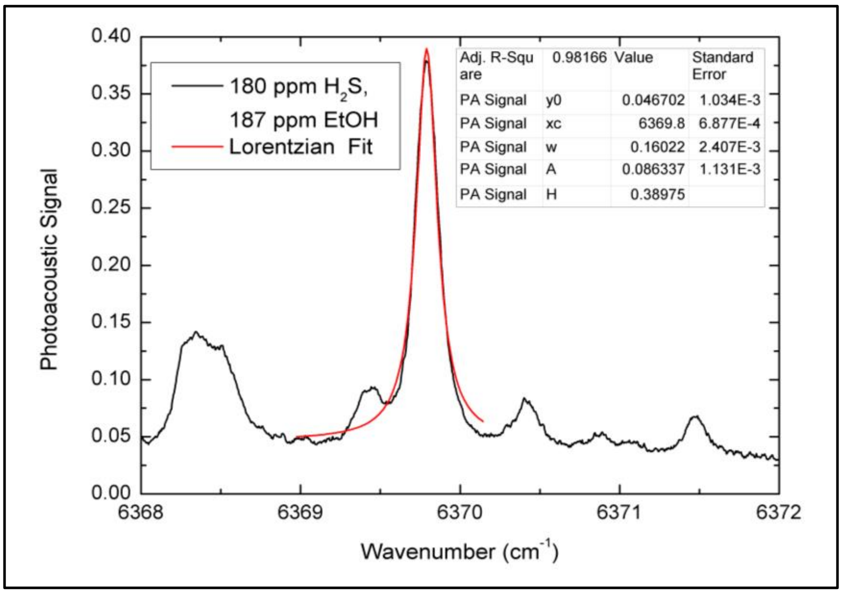

Figure 117 - Spectrum of hydrogen sulfide/ethanol mixture in 1 atm. of air. Lorentzian fitting is shown in red.

The fitting yields several important parameters: the baseline (*y0*), peak centre (*xc*), full width half maximum of peak (*w*), area of under the curve (*A*) and absolute height of the fitted peak (*H*).

From these parameters, one can interpret several things. Firstly, the baseline values correspond to the concentration of ethanol since the broad ethanol absorption feature essentially constitutes the baseline for the much narrower H_2S absorption line. Secondly, by subtracting the baseline (*y0*) from the absolute height (*H*) of the peak, one can determine the true peak height of H_2S, yielding a concentration for H_2S.

Thirdly, the area of the H_2S line also allows the determination of concentration of H_2S present in the cell by using the area instead of the peak height. All calibration plots are linear as expected. This suggest that even at high concentrations of an interferent with broad absorption features, one can still quantify the concentrations of the target molecule and also gain information about the interferent itself with the use of a Lorentzian fitting function.

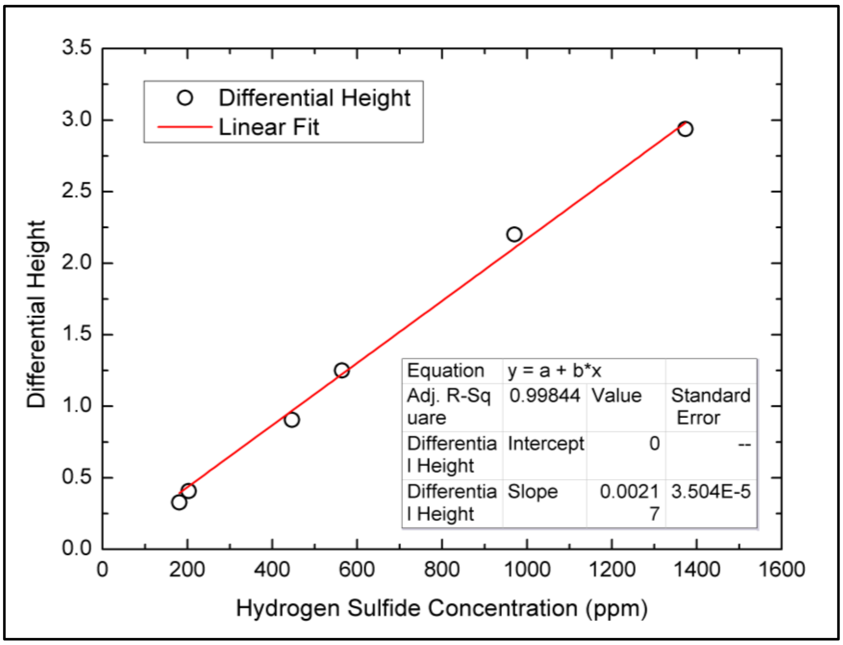

Equation	y = a + b*x		
Adj. R-Square	0.99844	Value	Standard Error
Differential Height	Intercept	0	--
Differential Height	Slope	0.00217	3.504E-5

Figure 118 - Calibration plot of hydrogen sulfide against differential peak height (*H* - *y0*)

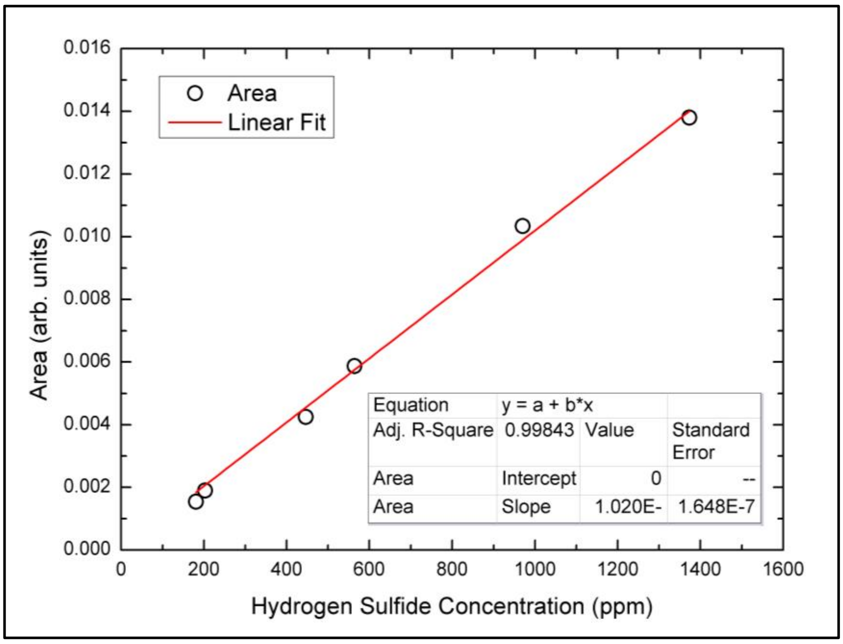

Figure 119 - Calibration plot of hydrogen sulfide against area under the curve (*A*)

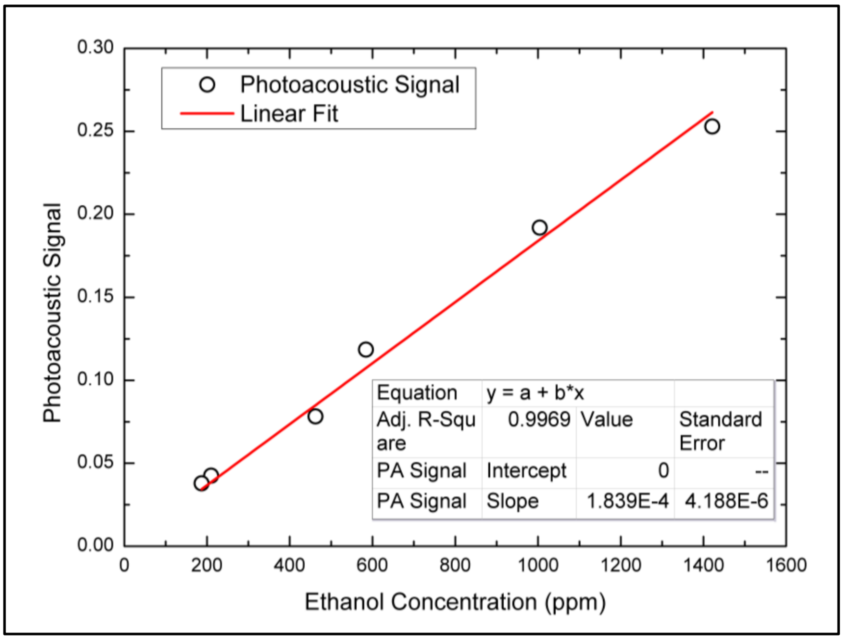

Figure 120 - Calibration plot of ethanol against baseline (*y0*)

To conclude, a near-IR photoacoustic spectrometer was demonstrated using a 1.55 µm ECDL and a Herriott cell composed of dielectric mirrors capable of trace gas detection. The Herriott cell increases the photoacoustic response by a factor of 40 compared to single pass laser photoacoustics. With this apparatus, a limit of detection (LOD) of 1.7 ppm H_2S (IDLH: 100 ppm) in 1 atm. of lab air is obtained at 100 ms integration time in a static cell measurement. LODs of 0.6 and 1.2 ppm for NH_3 (300 ppm), 28 ppm CO (1200 ppm) and 0.15 ppm C_2H_2 have been determined. Additionally, some possible interferents were analysed and were found to be easily avoidable. If the interferent has line resolved absorption spectrum at 1 atm, one can avoid any overlap between TICs' and interferents' absorption features. When the interferents' absorption features are broad and unavoidable, it is still possible to discriminate the TIC (H_2S) from the interferent (ethanol) by use of lineshape fitting. Overall, the effects of chemical interferent can be avoided or overcome.

External influences

Acoustic detection in HERPAS is performed with an electret microphone and such microphones are typically used in the human audible range. The electret microphone used (Knowles, EK-23024) has a response curve from 100 Hz to 10 kHz, peaking at 4.5 kHz as shown in Figure 76.[133] This means that the microphone is able to pick up any acoustic noise present, although electronic filtering and the lock-in detection will greatly suppress noise outside of the acoustic resonance frequency. Several possible common external interferences were measured to evaluate their effects and how to overcome their effects.

Clapping

A clap is a percussive sound made by striking two flat surfaces. Human clap has been reported to be up to 113 dBA,[134] louder than most car horns. A clap typically consists of several different frequencies as shown in Figure 121. Figure 122 shows several instances of clapping as measured with the measurement cell. From 40 to 90 seconds, three separate claps were made by a Smiths representative. One can see that each clap was out of phase with the modulating signal. Additionally, each clap event is identifiable because of their distinctive line-shapes. Each individual clap exhibits a sharp rise to a maximum, much faster than any absorption event, and then a much slower relaxation, which is more similar to the typical response of an absorption line event. Should all claps behave this way, one could easily avoid the effects of claps by setting a "warning" when significant negative signals are detected. In Figure 122, after 120 seconds, continuous clapping from a single source continued for 40 seconds. This resulted in a cluster of positive and negative signals which are not similar to any absorption features from TICs or other molecules.

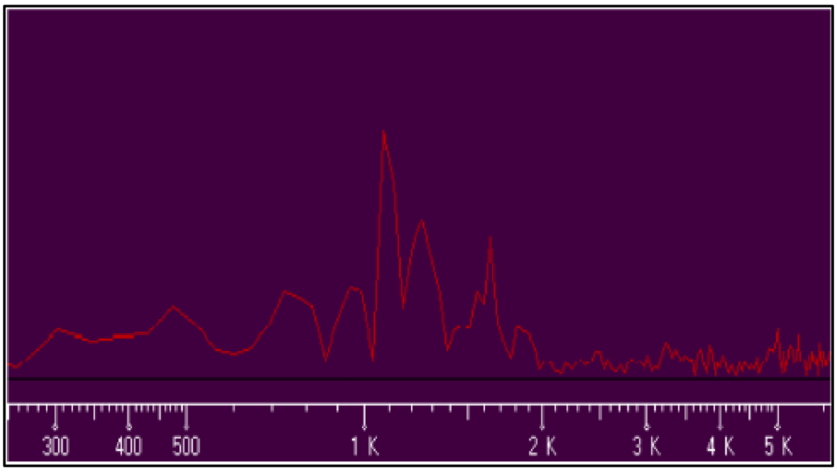

Figure 121 - Analysis spectrum of a clapping sound, reproduced from Ref. 136.

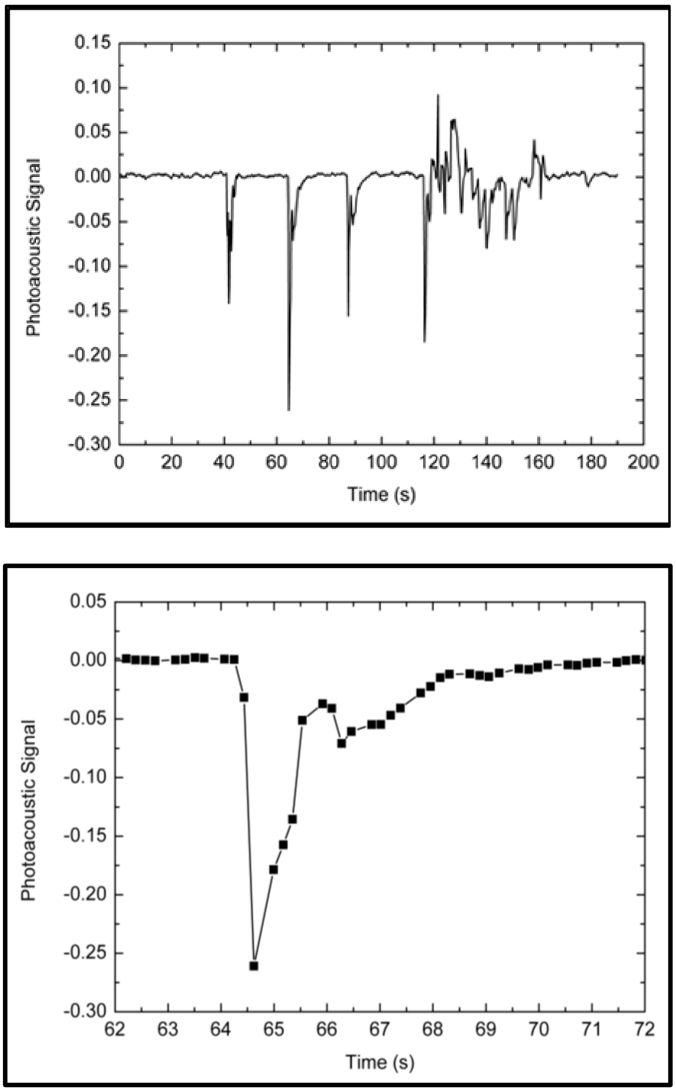

Figure 122 - Upper: A spectrum of clapping events, three single claps are shown to the left and continuous clapping shown to the right. Lower: A magnified spectrum of an individual clapping event.

A possible strategy to identify and correct clapping events could be as follow; in the eventual practical implementation of HERPAS, one could theoretically monitor the photoacoustic signal response. If a negative signal is detected. The laser will be immediately switched off; the motor retracts by a certain movement and holds. If further negative signals are detected, the laser remains unpowered. However, if no new negative signal can be detected, the laser is powered on and resumes scanning, covering the previous position to prevent providing a false negative.

Tapping on the breadboard

Vibration sensitivity can be a problem for HERPAS as the microphone may be able to pick up not only the sound from the tap but also the mechanical vibration which may oscillate the pickup plate of the microphone. In a future improved setup, this can be minimised by mechanically isolating the setup from the outside. In order to evaluate the performance of the existing setup, several taps were performed with a stainless steel rod on the aluminium breadboard to which all components were mechanically fastened. Each tap exhibited an event which is easily distinguishable from absorption acoustic signals by their characteristic sharp rise to the maximum and the slower relaxation back to zero. For some events, a negative trough is formed suggesting the tap was out of phase compared to the modulation signal received by the lock-in amplifier. Tapping on the breadboard has a rather large but easily recognisable effect.

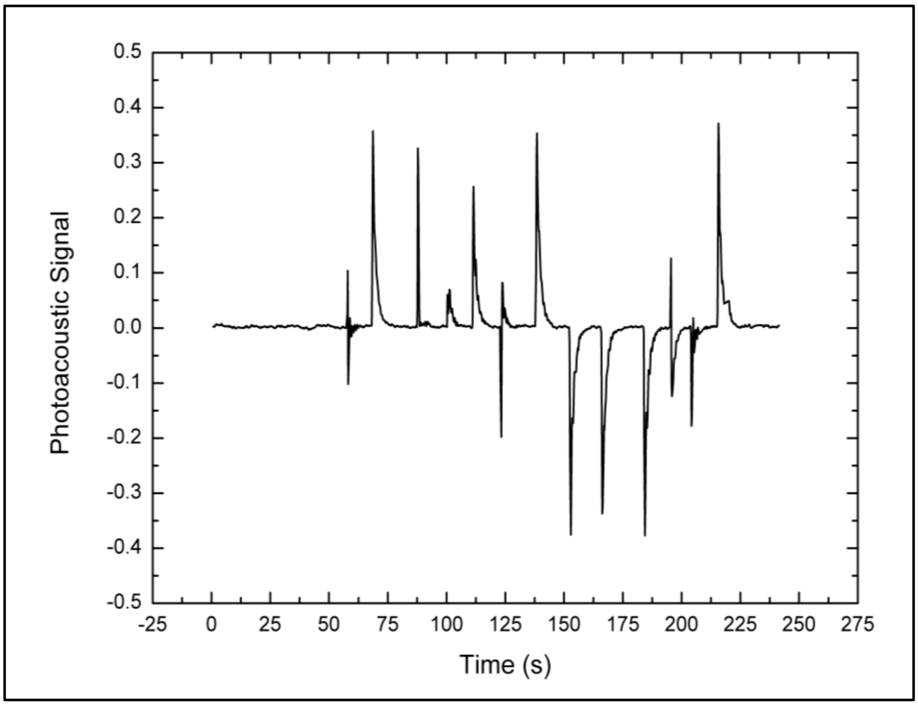

Figure 123 - A spectrum of the taps on the breadboard with a stainless steel rod.

Tapping on the optical bench

The HERPAS apparatus was assembled on the aluminium breadboard. The breadboard was cushioned on eight tennis balls which rest on an optical bench. The tennis balls help to alleviate the unavoidable vibrational background noises that are coupled to the building from road traffic, air conditioners, pumps etc. In order to investigate how effective this shielding is, quick successions of taps were made on the optical bench and the signals measured by the measurement cell are shown in Figure 124. The tapping has resulted in a series of peaks and troughs being recorded. The peak and troughs again have a distinctive sharp rise and a slower return to near zero similar to the breadboard taps. From this, it should be easy to distinguish the acoustic signal from tapping on the optical bench. In addition, this shows the effectiveness of tennis balls on dampening unwanted vibrations as the amplitude are much smaller compared to the tapping events made directly on the breadboard.

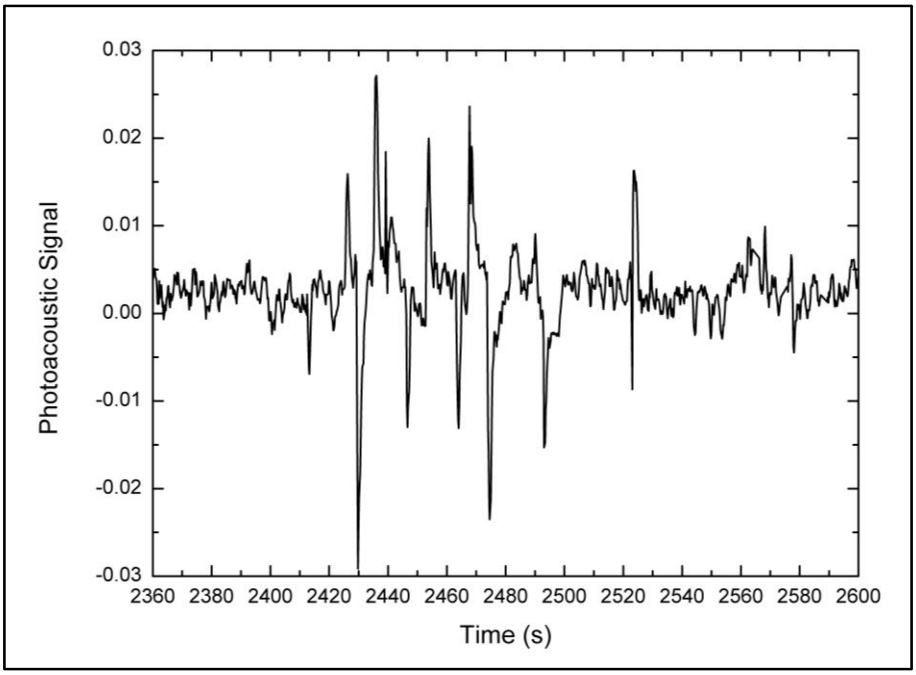

Figure 124 - A spectrum of taps on the optical bench with a stainless steel rod.

Signal Generator

All the external effects have been focused on individual, broadband frequency events. However, if the external event was a continuous, single frequency noise, it could potentially blind the detector. This was simulated by creating a single frequency noise with a signal generator app ("FuncGen") from a smartphone.

The signal generator produced a continuous sine wave output which resulted in an oscillating signal. The oscillation is caused by a mismatch in the phase of the sine wave and the reference of the lock-in amplifier, yielding both positive and negative signals. The recorded line profiles were very different compared to singular events such as clapping or tapping because there were no physical mechanical vibrations which could transmit directly through to the microphone. The effect of the signal generator was purely acoustic. Clearly, such an event does not resemble a photoacoustic spectrum and can therefore be easily distinguished.

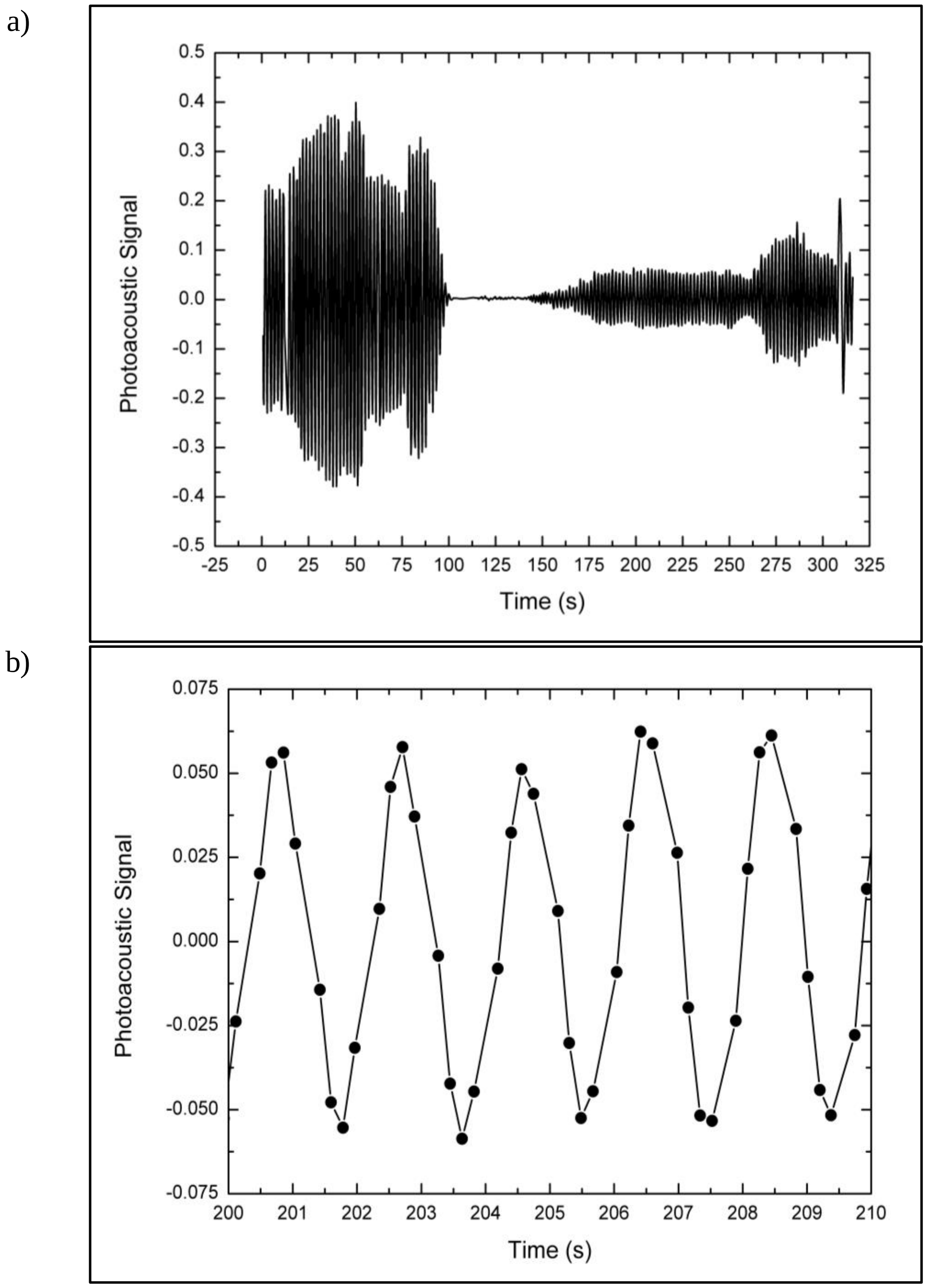

Figure 125 - a): Spectrum of two interfering continuous sound wave events at 2.25 kHz generated by a signal generator. b): Spectrum of a zoomed in region of a section of the recorded signals.

Intentional Jamming

HERPAS is reliant on the photoacoustic detection of the gas phase species. If an enemy agent discovers the resonant frequency of the resonant tube, one could in theory severely disrupt the detection operation of the HERPAS equipment by producing the same tone using a relative simple function generator and a loud speaker. To alleviate this, the HERPAS device should be shielded from external noise sources as much as possible with several physical layers to dampen and attenuate external noise sources. In addition, even if a single frequency jamming does occur, it would be relatively easily to recognise as the detector response will either be:

1. positive or negative offset - possibly saturated if signal is in perfectly in phase or perfectly out of phase with the reference lock-in signal
2. oscillating signal - phase mismatch between the jamming signal and reference lock-in signal

One solution to counter the threat of intentional jamming is to remove the acoustic resonator and to modulate the laser using a random frequency (pseudo-random binary sequencing). As there is no acoustic resonator, the detection scheme is no longer limited to a single frequency. By modulating the laser at a random sequence of frequencies, it should be impossible to jam the equipment continuously as the frequency and phase filtering from the lock-in amplifier should effectively remove the jamming signal which is not of the correct frequency. This solution, however, will reduce the sensitivity of HERPAS (by the Q- factor) due to the change from resonant photoacoustics to photoacoustics. A reduction of noise is expected from the pseudo random binary sequencing modulation of the laser but not enough to offset the factor 40 loss from lack of resonance.

One thing to note is that in one scenario HERPAS is intended to be issued on a squad-based or smaller deployment where each soldier is issued with the equipment to safeguard the service-person from potential attacks with TICS. If intentional jamming of the HERPAS equipment is encountered, one would expect the service-person to be able to hear the jamming signal before it is detected by HERPAS equipment.

Another idea is to possibly introduce a hardware acoustic filter to reduce noise transfer from the path of least resistance (possibly the gas inlet). A third approach is to deploy a common mode rejection scheme, where a second microphone which is not linked with the acoustic resonator picks up the "noise" signal. One could filter the noise signal to match the frequency of the acoustic resonator and amplify it to get the equivalent response for the detection microphone and then subtract the two to get a potentially "noise-free" signal. All possible solutions mentioned above will require extensive testing before determining which will be the most practical for potential deployment.

Whistling

Most humans whistle at a frequency between 0.5 - 5 kHz [135] typically centred on 2 kHz [136] and such human whistling tends to consist of the prominent harmonic frequency due to the mouth acting as a Helmholtz resonator and a non-harmonic component from the turbulent rushing of air past one's lips.

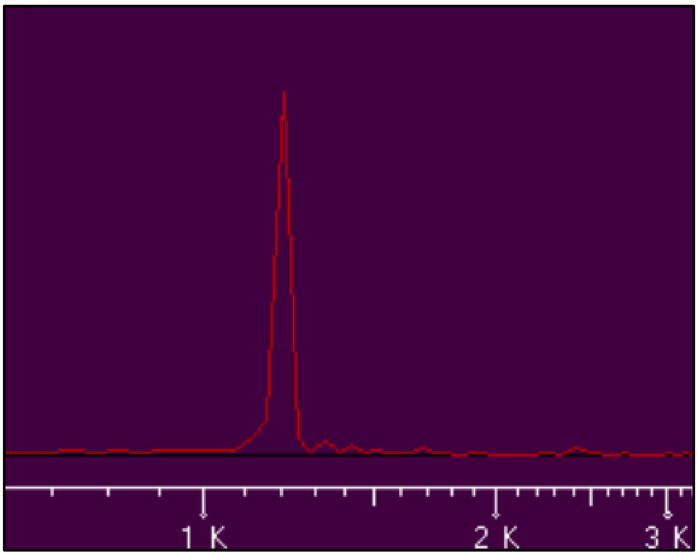

Figure 126 - Analysis spectrum of a mouth whistling sound, reproduced from Ref. 136.

For HERPAS, the whistling frequency is more important compared to the whistling amplitude because of the acoustic resonator. If the whistling frequency matches that of the acoustic resonator, it will induce an acoustic resonance which is amplified by the *Q* factor of the resonator. In Figure 126, four human whistling sounds were captured by the HERPAS. Each whistle started at a low frequency and moved up until a response was observed on screen. From, Figure 127 each whistle can be broken down to rise to a positive or negative maximum, followed by a fall through zero until reaching the opposite maximum and returning to zero.

The explanation for each of the three steps is as follows. To generate a response from HERPAS, there must be some sound waves or vibrations that reach the microphone. For whistling, it is purely acoustic. The microphone will be able to pick up all frequencies in the audible range but if the sound wave is supported by the acoustic resonator, some amplification will occur. This is picked up by the microphone and converted into an analogue electrical signal. This signal is then processed by a bandpass filter to filter out any signal above and below a frequency range. Next the filtered signal is processed by the lock-in amplifier. The lock-in can extract a signal from a carrier wave. In this case, the amplifier is fed a reference signal which is the delayed modulation signal used to modulate the laser. The lock-in amplifier integrates the filtered output in phase with the zero crossing points of the reference signal. The output of the lock-in is dependent on how much the two phases are overlapped. For the maximum positive signal, the two phases are perfectly overlapped. Between 0 and 90° phase difference, the signal will be positive, with reducing intensity as it approaches 90°. At 90° the signal will be zero as both the positive and negative portion will be integrated. Between 90° and 180° phase difference, the signal is decreasing to a maximum and at 180° the maximum negative signal will be observed.

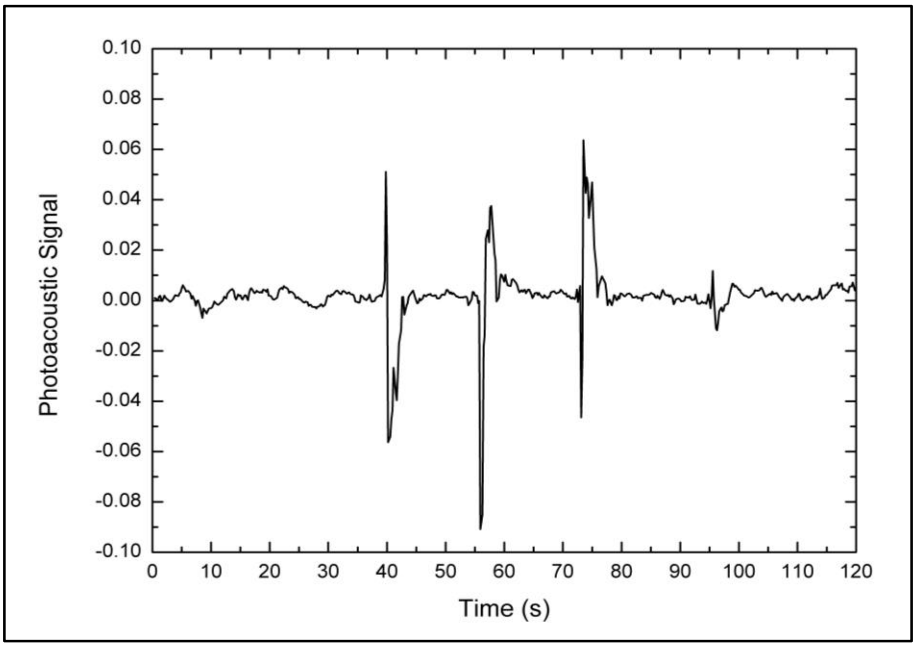

Figure 127 - A spectrum of the human whistle sounds.

Using the first event, a signal is observed. This is the result of whistle’s frequency beginning to match the acoustic resonator frequency and the phase match of the whistle and reference signal is between -90 and +90°, hence it is positive. The signal continues to rise to a maximum which can be accounted for by one of two reasons.

Either the whistle's frequency is moving into resonance with the acoustic resonator or the phase matching of the two signals is improving quickly leading to a maximum. The resonance with acoustic resonator effect will be less pronounced due to the low *Q* factor of the acoustic resonator and thus the signal rise is more likely to be due to the phase based change. The fall from maximum suggests the phase overlap is no longer optimum and hence a decrease in signal intensity occurs. The signal passes through zero and reaches the negative maximum suggesting the phase overlap reaches 90° phase difference and then finally becoming completely out of phase. The return to zero suggests the two phases are out by 270° or the whistle's frequency is rejected by the band pass filter.

Further Investigations

Power dependency

Photoacoustic spectroscopy has been demonstrated in the literature with varying laser input power ranging from low tens of mW from semiconductor laser diodes to tens of Watts from CO_2 lasers.[137] To determine the power dependency of HERPAS, the laser output was fed into a bench top, fibre coupled semiconductor optical amplifier (Thorlabs S9FC1004P) which amplifies the laser radiation. Optical amplifiers were designed for boosting or amplifying weak laser radiation in the telecommunication sectors where data, sent in the form of light pulses, travel across thousands of miles via optical fibres. As with any form of signal transmission, there are slight losses (typically <0.2 dB/km in the conventional and long wavelength bands)[138] which accumulate over such long distances such as in trans-Atlantic communication cables.

The laser was moved to a position where water traces in lab air show absorption. Different power levels were selected by the optical amplifier and the resulting photoacoustic signal was observed (see Figure 128). It can be seen that the photoacoustic response is linear from 20 mW (maximum modulated output of the ECDL without further amplification) to a boosted output of 45 mW, and by doubling the power the signal was also doubled.

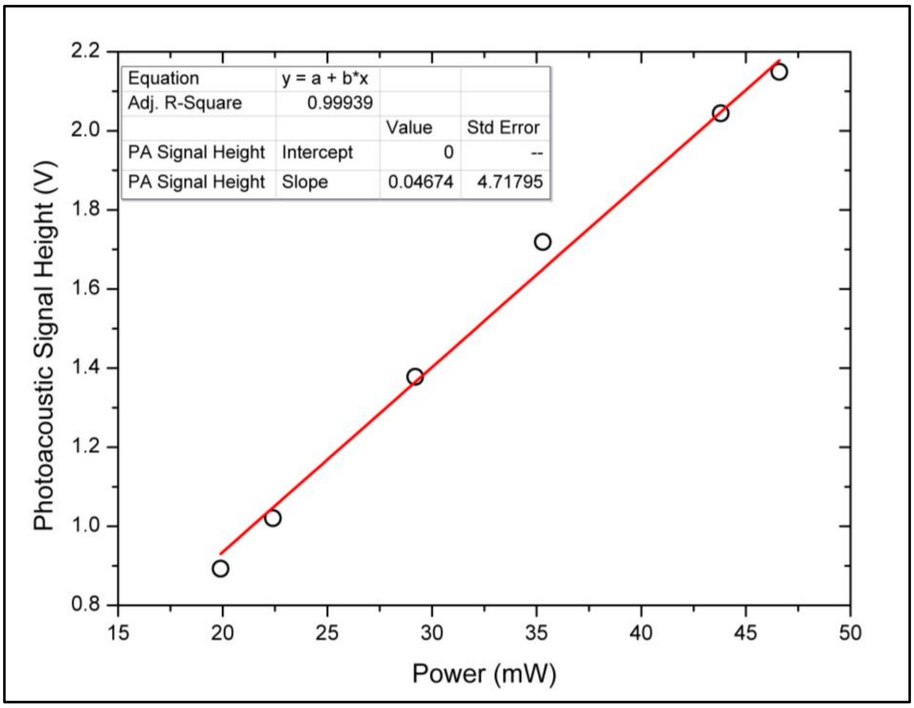

Figure 128 - A plot of photoacoustic response against optical power of a water line in 1 atm. of air.

Duty cycle

The typical reported duty cycle of laser modulation, with a sine or square waveform, is 50 % as it yields the maximum signal. All previous results refer to a 50 % square wave (on/off) modulation. This gives the maximum signal as the molecules are excited for the longest possible time whilst allowing the molecules sufficient time to relax fully. At 100 % duty cycle, the light continuously excites the molecules within the beampath. Some molecules drift out of the beampath and can undergo collisional deactivation but this occurs randomly, yielding an overall zero signal. The photoacoustic response at varying duty cycle with square wave (on/off) modulation was measured and plotted as shown in Figure 129. Theoretically, the optimum modulation should be via a sine wave, since this matches best with the acoustic wave at a single frequency. In a theoretical analysis, the present square wave is separated into sine wave contributions and only the first harmonic contribution will contribute to a first approximation to the photoacoustic signal at this frequency. Based upon the Fourier series, the frequency domain amplitude for a square wave modulation signal with a duty cycle of d and peak to peak amplitude of A, amplitude A_n of the n-th harmonic is given by:[139]

$$A_n = \frac{2A}{n\pi} sin(n\pi d) \qquad \textit{Equation 35}$$

By analysing the first harmonic, the relative amplitude of this first harmonic at different duty cycles is shown in Figure 129.

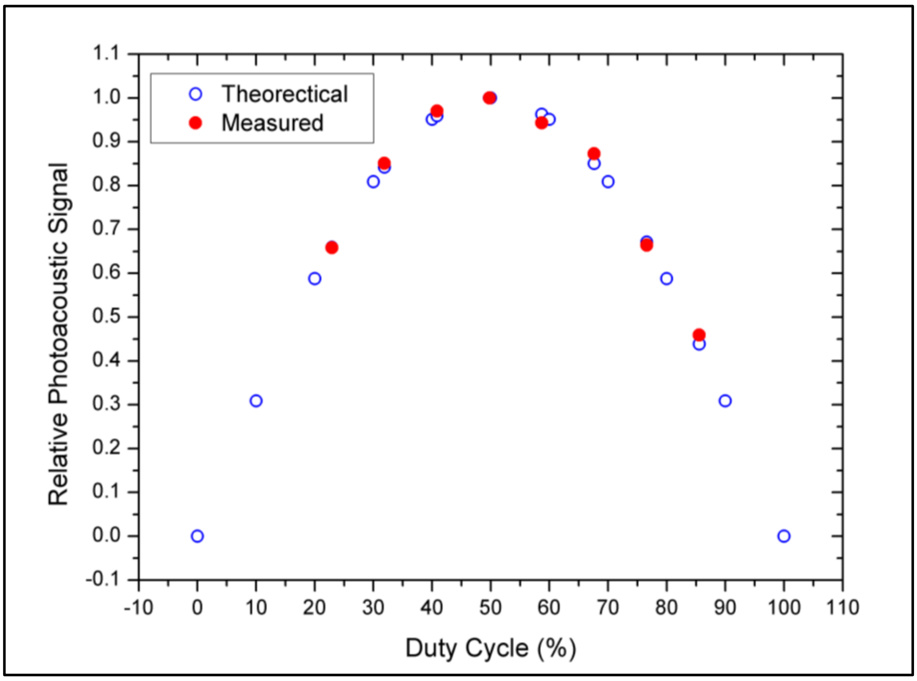

Figure 129 - Relative photoacoustic signal from equation 35 and measured from HERPAS.

Overall, the theoretical curve matches the measured one very well and the effect of the duty cycle can be well described by this theory based on sine wave functions. Reducing the duty cycle reduces the signals and thus reduces LODs; however, the saving of electrical power might offset this disadvantage in practical implementations.

Distributed feedback laser

External cavity diode lasers have the advantage of high output power with a wide tuning range. However, they are quite costly (£ 8000 for the current OEM laser system) and are rather bulky. Cheaper Fabry-Pérot diodes are available in the 1500 - 1600 nm range but most are inherently multimode due to the lack of anti-reflection coating on the output facet which allows many longitudinal modes of the laser to be supported, yielding a multimode emission. These diodes are also very difficult to tune continuously. A better alternative is distributed feedback laser diodes (DFB) as described previously.

A low cost DFB laser system was investigated to evaluate the feasibility of implementing DFB laser diodes for TICs detection. A pigtailed fiber InGaAs/InP DFB laser diode (Mitsubishi FU-650SDF-FL 49M56 D) emitting at a wavelength of 1.56868 µm at 25 °C with an output power of 4 mW was mounted on a thermoelectric cooler (Thorlabs TCLDM9). The temperature tuning coefficient was 0.1 nm/°C with a temperature tuning range of 70 °C (5 to 75 °C), a tuning range from 1566.6 to 1574 nm can be expected. The DFB laser diode was coupled to the Herriott cell and some measurements were performed on hydrogen sulfide. The DFB laser diode was tuned from 40 - 60 °C to obtain the necessary wavelength range to cover the strongest feature of the $v_1 + v_2 + v_3$ combination band at 6369.3 cm^{-1} as seen in Figure 130.

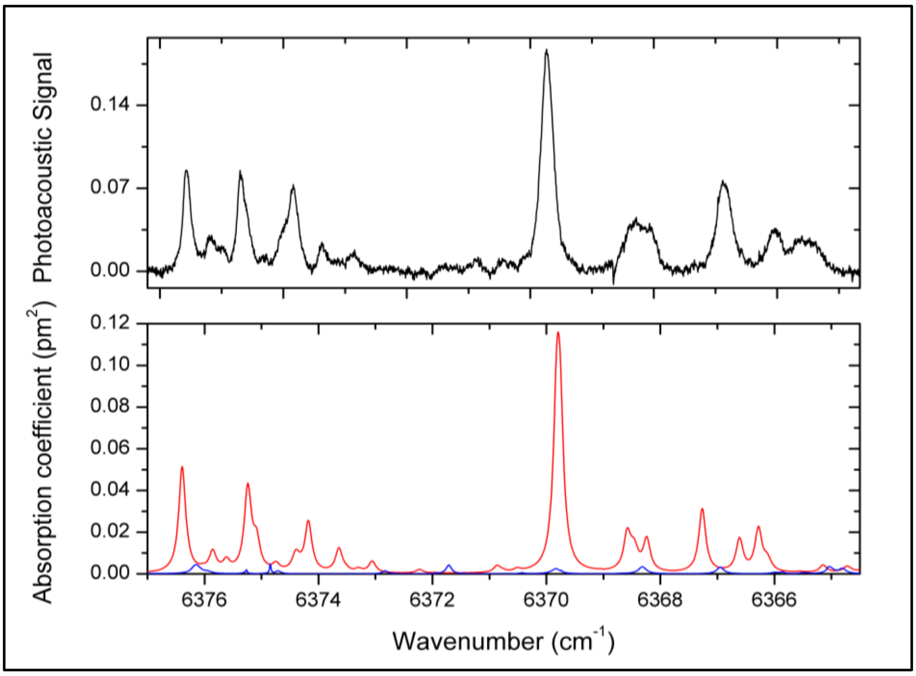

Figure 130 - Top: Measured spectrum of H_2S with DFB laser diode. Bottom: Theoretical absorption bands of H_2S (red) and water (blue).

Overall there is a good match in spectral features between the measured and predicted spectra. Some deviations in the wavelength positions are apparent. In this instance, the wavelength tuning does not appear to be linear due to occasional slight mismatch in the measured and predicted lines. The mismatch was caused by an oscillation of the temperature gradient from the thermal electric cooler which had reduced the heating load prior to achieving the desired the temperature.

In Figure 131, the photoacoustic response for the strongest H_2S line is plotted against time. The time taken for the DFB to scan across the H_2S line is approximately 5 seconds (start at 49, end at 54 second mark). The temperature tuning speed is dependent on the heat power supplied from the thermoelectric controller (TEC). With a more powerful TEC, quicker scans speeds can be obtained. A limit of detection of 31 ppm in 1 atm. of air, at 100 ms integration time with a higher noise limit of 2.7 mV was determined for this DFB laser diode at 4 mW output power. This falls within the expectation range as compared to the ECDL as the laser is approximately 10 times less powerful but nearly twice as noisy compared to the 1.4 mV of ECDL system.

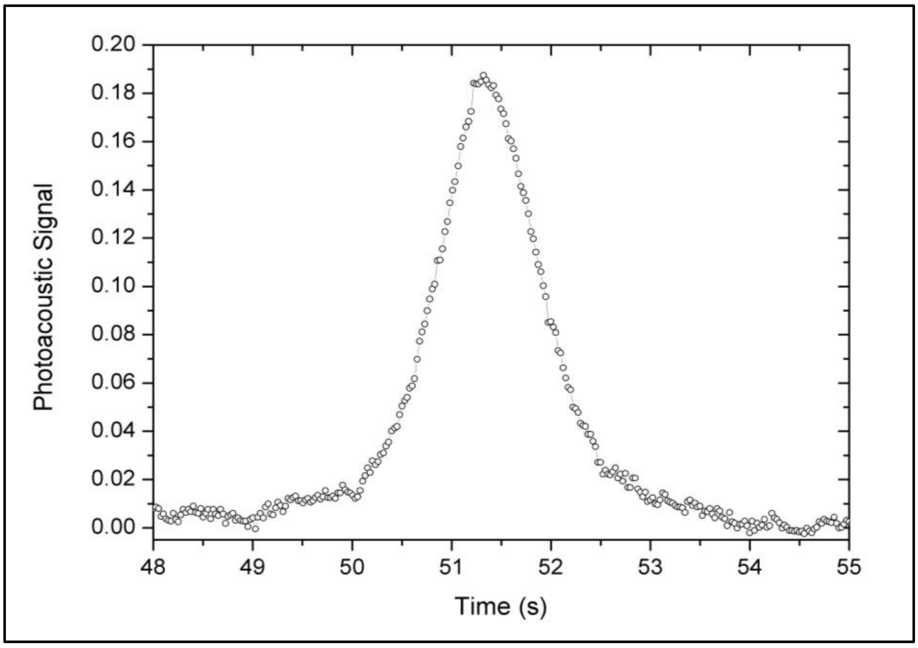

Figure 131 - A plot of measured H_2S using the DFB laser diode against time.

The full theoretical tuning range of the DFB diode from 10 to 75°C is shown in Figure 132 which has been overlaid with a theoretical H_2S spectrum. The H_2S absorption feature shown in Figure 130 and Figure 131 is marked with an asterisk. The lower limit of 10 °C is to avoid condensation of water on to the laser diode. The upper limit of 75 °C is from the manufacturer's specification sheet. It can be seen that several H_2S absorption lines are within the range of this particular DFB laser and can be selected for H_2S analysis.

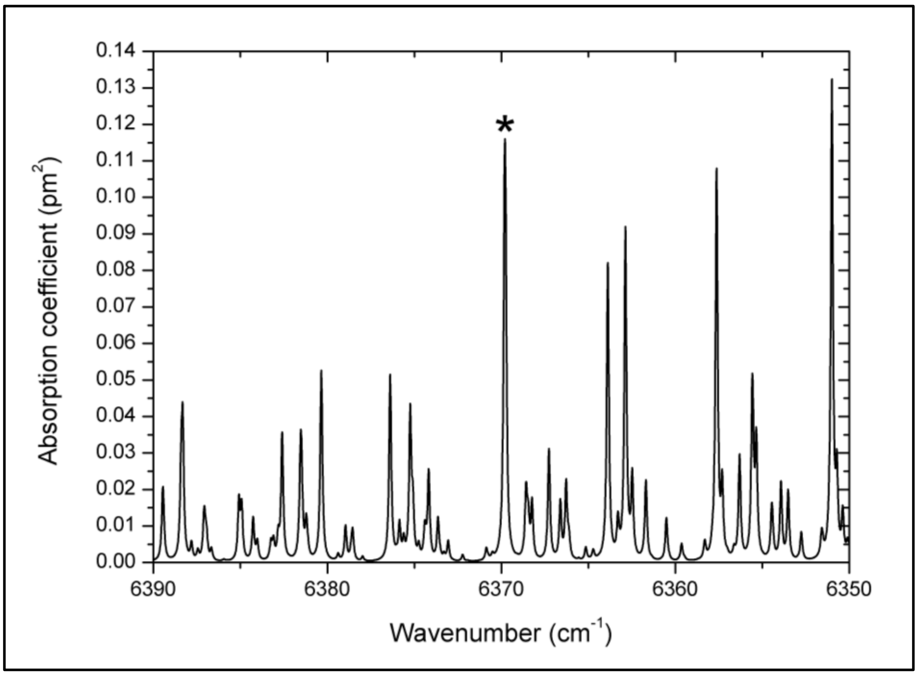

Figure 132 - Theoretical tuning range of the DFB laser diode from 10 to 75 °C.

Wavelength Calibration/Correction

The ECDL is tuned by the DC servo motor and the motor position can be used as a general guide of the wavelength. To determine an accurate wavelength, three solutions exist: monochromator, motor position, etalon fringe counting.

A monochromator would be the simplest solution as it provides a wavelength read out of the wavelength, however, off-the-shelf monochromators are expensive and bulky and would be an additional power drain.

The motor position in theory should be a good way to calibrate the wavelength. However, the motor is susceptible to hysteresis and thus is not truly reliable.

One could determine the laser's wavelength and by counting the fringes, one could provide a look up table for referencing the laser wavelength.

Etalon fringes occur when there is interference from the front and back reflections of the microscope slide acting as the gas cell window. The front and back reflections of the lasers need to overlap and was monitored by a photodiode and recorded using a DAQ card.

An example of wavelength correction is shown below. The CO_2 *R* branch was measured twice, in quick succession as shown in Figure 133. It is clearly observable that the two recorded spectra do not match up based on the motor position readout. In the absence of a monochromator with a camera operating in the NIR range, the only other method to determine the wavelength is by etalon fringe counting. The etalon fringes reveal the laser is not scanning continuously but rather mode hopping along at these motor positions. One could correct for the mismatch in motor positions by looking for the same etalon fringe and then displace the spectrum until a good match is observed.

By matching the etalon fringes, the resulting spectrum is shown in Figure 135. Wavelength calibration can be carried out in a similar manner. A factory calibration can be applied at the factory if the wavelength corresponding to each etalon fringe peak and trough is measured with a monochromator and recorded. By taking the differential of the etalon fringes, each peak and trough will become a zero crossing and thus can be looked up on the previously recorded positions. By tuning the thickness of the etalon, one could modify the interval between each recorded wavelength.

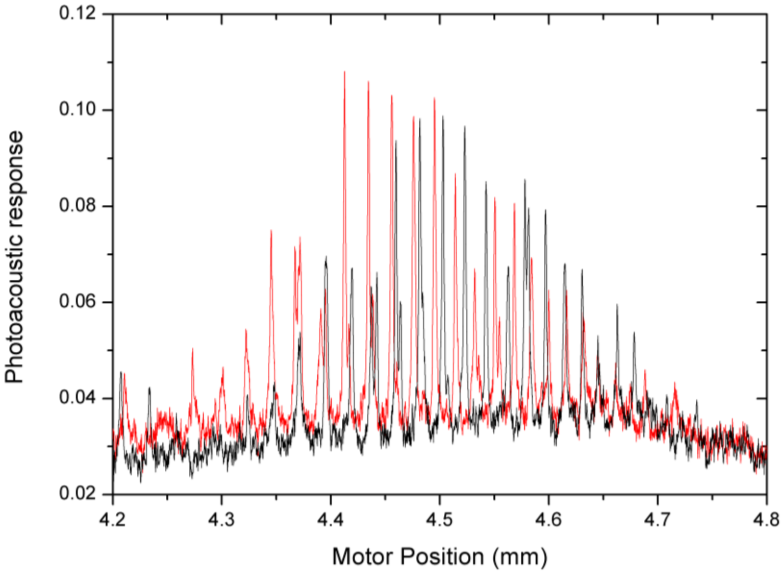

Figure 133 - Two HERPAS measurement of CO_2 from lab air plotted against the motor position.

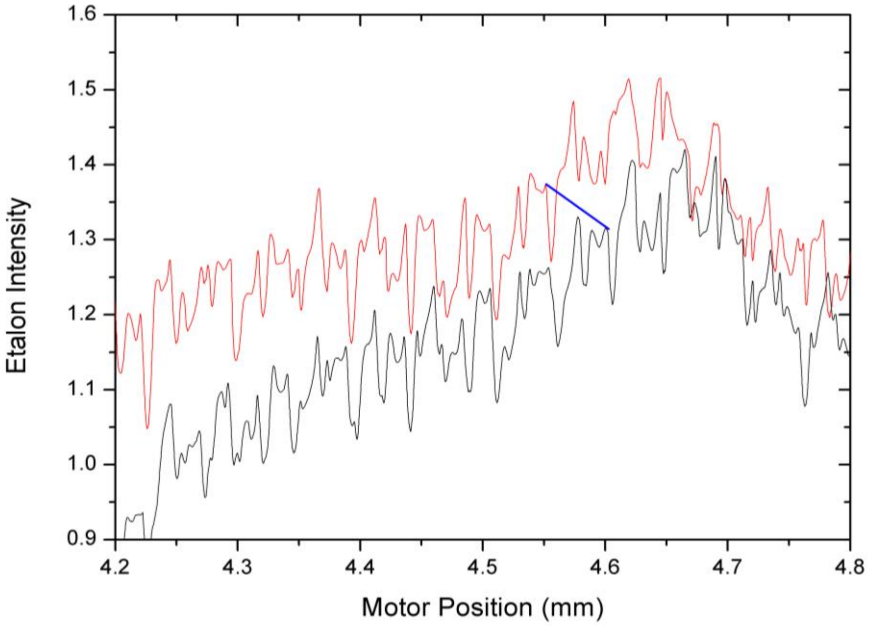

Figure 134 - Recording of the etalon fringe of the two CO_2 spectra.

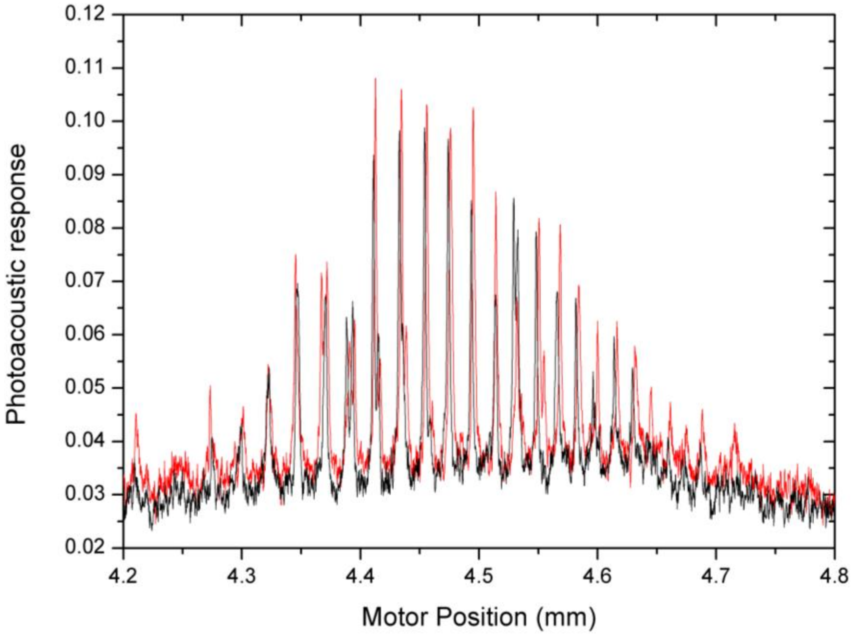

Figure 135 - Etalon corrected HERPAS spectrum of CO_2.

To conclude, external acoustical influences were investigated (clapping, tapping, internal jamming) and evaluated. Schemes to counter/negate such effects are discussed. The optical power dependency of the photoacoustic effect were also investigated with increasing laser power as well the optical duty cycle. A wavelength correction scheme by etalon fringe counting was also demonstrated even when the laser is mode-hopping.

6. Conclusion

Three different spectroscopic techniques, CERS, mid- IR CERPAS and HERPAS, were investigated and evaluated for a variety of applications of trace gas detection.

CERS

A variant of cavity-enhanced Raman spectroscopy (CERS), employs a low power diode laser which is stabilised by optical feedback to an external optical cavity composed of two highly-reflective mirrors. Using a 10 mW single mode laser diode at 635 nm, a build up of laser power inside the cavity to several Watts occurs periodically (1.5 kHz, 50 % duty cycle). This power build-up by 3 orders of magnitude allows the observation of strong Raman signals in a forward scattering collection geometry, suitable for quantitative analysis of gas phase samples, and also for more fundamental scientific applications. Variations of mirror reflectivities in the wavelength ranges where Raman transitions occur are not distorting observed intensities. Raman spectra of H_2, air, CH_4 and benzene have been recorded and analysed to demonstrate the principle. It has been shown that noise equivalent limits of detection in the ppm by volume range (1 bar sample) can be achieved with excellent linearity with a 10 mW excitation laser, demonstrating the potential of CERS with low-power diode lasers for trace gas detection. We have also demonstrated that the Gaussian spectral fitting procedure is a powerful analytical procedure, if it can be applied. With low power and compact components, the apparatus can be made battery operable and portable.

CERS has the potential to become a new standard method to monitor Raman active species, in particular important homonuclear gases like nitrogen, oxygen or hydrogen that cannot be easily detected by alternative spectroscopic techniques. Raman spectroscopy allows simultaneous multi-component analysis of gas mixtures with high sensitivity and high selectivity due to spectral resolution. Possible analytic applications include safety monitoring of hydrogen gas levels, isotope tracer studies (e.g., $^{14}N/^{15}N$ ratios), and observing isotopomers of hydrogen gas, for example monitoring radioactive tritium. CERS can also be used for more fundamental applications, for example to study vibrational interactions, intramolecular vibrational energy redistribution on fast timescales by high resolution spectroscopy, or to refine the theoretical analysis of molecular energy levels and potential energy hypersurfaces.

Mid-IR CERPAS

A mid-IR spectrometer using a 7.5 µm EC-QCL and a V-shaped optical cavity composed of three highly reflective mirrors capable of trace gas detection has been demonstrated. The V-shaped cavity geometry avoids the unwanted back-reflection whilst allowing efficient coupling of light into the optical cavity. This gives rise to a power build-up within the cavity and also stabilises the QCL to the optical cavity which greatly improves detection sensitivity to trace gases and vapours. The cavity has two acoustic resonator tubes within the beam path; these resonators are equipped with microphones which enable photoacoustic detection of light absorption. Since light is coupled into the cavity periodically at a frequency matching the acoustic resonance frequency of the resonators, sensitive detection of absorption is possible (resonant photoacoustics) which is enhanced by the power build up in the optical cavity (cavity-enhanced resonant photoacoustic spectroscopy, CERPAS). The QCL is "broadly" tuneable in the mid-IR around 7.5 µm. With this apparatus, a noise-equivalent detection limit of 50 ppt C_2H_2 in 100 mbar N_2 and 1 ppb nitromethane in

75 mbar N_2 are obtained at 1 s integration time. The apparatus was combined with a vapour generator to detect explosives' and taggants' vapours. Explosives vapours can be distinguished from interferences by spectral discrimination in order to avoid water interference. A noise-equivalent detection limit of 1.2 ppb TNT in 1 atm N_2 is obtained at 1 s integration time. In a more practical implementation, a sample gas flow is maintained through the resonators, and the pressure inside the measurement cell is reduced to 0.3 bar to avoid interferences due to water absorptions. With a rise time of about 20 s, this configuration has a reasonable time response. Noise equivalent detection limits corresponding to 5.5 ppb TNT, 7 ppb 2, 4-DNT, 11 ppb DMNB and 4 ppb TATP in 0.3 bar N_2 are obtained at 1 s integration time without the use of pre-concentrators. Note that concentrations (amount of substance per volume) are reduced inside the cell due to the reduced pressure. With longer integration times, higher optical power, or cavity mirrors with higher reflectivities, detection limits can be further improved.

The experimentation performed during the CERPAS project has yielded valuable information on the potential for this technique for the detection of vapour phase explosives and associated molecules, including by-products of the explosives manufacture process (e.g. 2,4-DNT) and taggants (e.g. DMNB). The interfacing of an explosives vapour generator with the resonator tubes has been successfully demonstrated, as has the ability to introduce the headspace vapour of additional compounds by means of Solid Phase Microextraction (SPME). The responses measured for these various compounds have confirmed the theoretical potential for the detection of explosives by the CERPAS technique.

HERPAS

A multipass enhancement of photoacoustic detection of toxic industrial gases was evaluated. The Herriott cell enables 46 passes of laser light to be coupled into an acoustic resonator, which improves the detection sensitivity to weak absorbing gases. NIR light from an extended cavity diode laser (ECDL) was coupled into a Herriott cell and an acoustic resonator. The acoustic resonator has a microphone attached which enables photoacoustic detection of light absorption. Since the light is modulated periodically to match the acoustic resonators' frequency, sensitive detection of the absorption is possible (resonant photoacoustics) which is further enhanced by a minor power build up from the Herriott cell (Herriott-cell enhanced resonant photoacoustic spectroscopy HERPAS).

The ECDL is tuneable in the NIR around 1550 nm where several selected TICS have characteristic absorption features. The various TICs can be identified by spectral discrimination from interferents and by Gaussian fitting. With this apparatus, a limit of detection (LOD) of 1.7 ppm H_2S (IDLH: 100 ppm) in 1 atm. of lab air is obtained at 100 ms integration time in a static cell measurement. LODs of 0.6 and 1.2 ppm for NH_3 (300 ppm), 28 ppm CO (1200 ppm) and 0.15 ppm C_2H_2 have been determined. The LODs are far below their respective IDLH limits. With longer integration times, higher optical power or an increase in the number of passes, LOD detection limits can be improved further.

External acoustical influences were investigated (clapping, tapping, internal jamming) and evaluated. Schemes to counter/negate such effects are discussed. The optical power dependency of the photoacoustic effect were also investigated with increasing laser power as well the optical duty cycle. A wavelength correction scheme by etalon fringe counting was also demonstrated even when the laser is mode-hopping.

7. Future Work

Improvements to each of these apparatus are discussed below. Some require advancements in manufacturing techniques while others are investigations on the design of the structures.

For CERS, further enhancements can be gained by reducing the excitation wavelength due to the wavelength dependence of the Raman scattering effect (see equation 29). With the advent of 405 nm laser diodes, commonly used in Blu-Ray(TM) players, such a modification should be plausible and easily implemented. To decrease the acquisition time, one could use multiple collection geometries and combine the Raman light collected via an optical coupler in a single monochromator. To improve on the detection limits, the camera should have a lower noise limit (operating at a lower temperature) which was demonstrated recently by Hippler.[140]

Mid-IR CERPAS

CERPAS is limited by the mirrors' reflectivities which are quite low compared what is available at more commercially available wavelengths. In addition, the noise level obtained with the ADC cards were quite high, which may have been due to electrical interference. Care has to be taken avoid build up of explosive residue on the mirrors' surface as it reduces the reflectivity and hence the performance of the spectrometer.

HERPAS

With any optical spectroscopic technique, a longer pathlength will increase the sensitivity as it allows the molecules to have more chance to interact with the light. For the Herriott cell, one can increase the number of passes (n) inside the acoustic resonator, with each additional pass there is (n+1) more light inside the resonator. This increases the amount of molecules that will be excited by the laser light and yield a proportionally stronger signal. This can be achieved by using bigger mirrors. As shown in the introduction, a Herriott cell will typically yield an elliptical or circular pattern with each reflection shown in Figure 136.

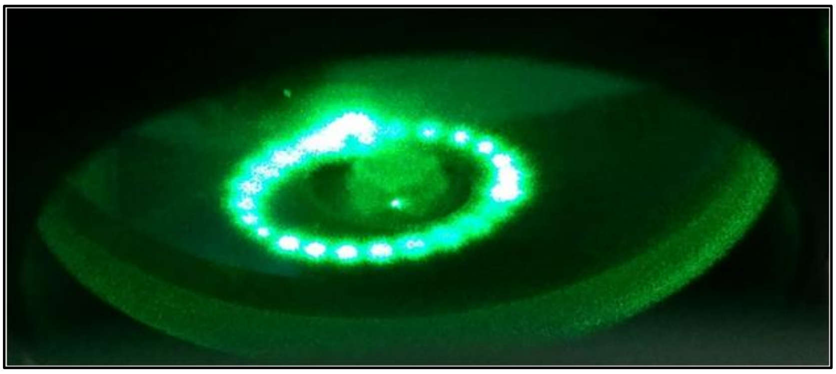

Figure 136 - Photograph of the reflected spots with a green alignment laser on the entry mirror.

One can see that it would not be possible to increase the number of passes in the current configuration as there is no more space available for any additional spots. However, by increasing the circumference, one could fit more spots and thus more reflections. Alternatively, one could fold the last reflection, using a diverting mirror, a few degrees towards the optical axis as shown in Figure 137, similar to the "perturber" approach described in the introduction of Herriott cells. A simulation (using FRED Photon Engineering) shows the addition of a small mirror allows a second ring of spots to occur which increases the sensitivity without increasing the physical size or power consumption of the apparatus.

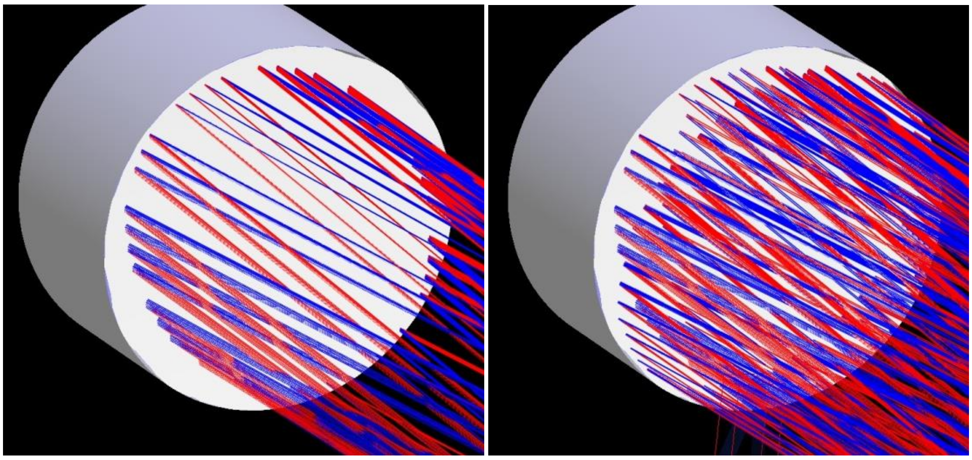

Figure 137 - Left: A simulation of laser pathway and reflections on a Herriott cell mirror. Right: A simulation of the laser pathway with a wedged shaped mirror placed at the last reflection point. Light heading towards the mirror is shown in red and the light reflected by the mirror is shown in blue.

This was trialled by attaching a small fragment of dichroic mirror by Blu-Tack®. The Blu-Tack®, shown by the red oval in Figure 138, allows the fragment to be coarse aligned as is shown below.

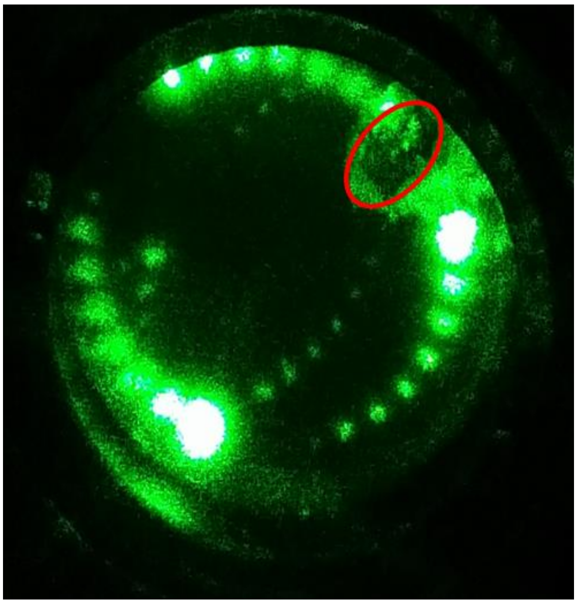

Figure 138 - Pertuber mirror (outlined in red) placed on the far Herriott cell mirror, An additional twelve spots are visible (inner broken oval of spots) and possibly more are present but not captured by the camera due to the low intensity.

Whilst, the perturber mirror does work and increases the number of passes by at least 50 %, it is difficult to align reproducibly and the Blu-Tack® prefers to adhere to the jewellers screwdriver used to bluntly adjust the perturber mirror rather than the mirror. A suitable adhesive needs to be identified. Alternatively, an astigmatic Herriott cell [7,141] can be trialled, which will give a significant improvement in the number of passes compared to the Herriot cell. However, the astigmatic mirrors tend to be custom made in metal and coated with layers of gold or silver which can be expensive. Compared to a dielectric coating, the metal mirrors will result in a minor reduction in performance due to the lower reflectivity compared to dichroic coatings but have much larger usable range (visible to mid IR). A less costly alternative can be a cylindrical variant of the multipass cell.[11,12,13]

It is also observed that the end caps have a significant acoustic enhancement factor which needs to be modelled in order to understand the reasoning behind the effect as well as optimising the enhancement for the best performance. The acoustic modelling of the enclosure may also be of benefit to the mid-IR CERPAS spectrometer.

To conclude, optical detection schemes described in this thesis can achieve high sensitivity and selectivity. CERS, mid- IR CERPAS and HERPAS will hopefully advance the field of trace gas detection further, in particular mid-IR CERPAS to detect ultratrace illegal or toxic substances or gases. HERPAS and CERPAS will hopefully be of use in monitoring gases involved in atmospheric chemistry or gases that attribute to Greenhouse Effect. Lastly, CERS has strong potential for gaseous isotopic analysis.

8. References

---

[1] T. Hubert, L. Boon-Brett, G. Black and U. Banach, *Sens. Actuators, B,* 2011, **157**, 329 – 352.

[2] C. R. Arkin, C. H. Curley, D. P. Floyd, G. R. Naylor, W. D. Haskell, M. Blalock, T. P. Griffin, D. W. Follistein, F. W. Adams and J. A. Diaz, TrAC, *Trends Anal. Chem.,* 2004, **23**, 322 – 330.

[3] A.H. Pfund, 'Atmospheric Contamination', *Science*, 1939, **90**, 326–327

[4] J. U. White, "Long Optical Paths of Large Aperture,*" J. Opt. Soc. Am.*, 1942, **32**, 285

[5] http://cluin.org/programs/21m2/openpath/tdl/ access on 07/09/2015

[6] D. Herriott, H. Kogelnik, and R. Kompfner, *Appl. Opt.*, 1964, **3**, 523 - 526

[7] J. B. McManus, P. L. Kebabian, and M. S. Zahniser, *Appl. Opt.,* 1995, **34**, 3336 - 3348

[8] D. R. Herriott and H. J. Schulte, *Appl. Opt.,* 1965, **4**, 883 - 889

[9] Béla Tuzson, Markus Mangold, Herbert Looser, Albert Manninen, and Lukas Emmenegger, *Opt. Lett.*, 2013, **38**, 257 - 259

[10] D. A. Knox , A. K. King, E. D. McNaghten, S. J. Brooks, P. A. Martin, S. M. Pimblott, *Applied Physics B*, 2015, **119**, 55 - 64

[11] L. Hao, S. Qiang, G. Wu, L. Qi, D. Feng, Q. Zhu, *Rev. Sci. Instrum.*, 2002, **73**, 2079

[12] V.L. Kasyutich P.A. Martin, *Applied Physics B*, 2007, **88**, 125 - 130

[13] C. Shen, Y. Zhang, J. Ni, *Chin. Opt. Lett.*, 2013, **11**, 091201

[14] J. M. Herbelin, J. A. McKay, M. A. Kwok, R. H. Ueunten, D. S. Urevig, D. J. Spencer, and D. J. Benard, *Appl. Optics.,* 1980, **19**, 144 - 147

[15] D. Z. Anderson, J. C. Frisch, and C. S. Masser, *Appl. Optics*, 1984, **23**, 1238 - 1245

[16] A. O'Keefe, D. A. G. Deacon, *Rev. Sci. Instrum.,* 1988, **59**, 2544 - 2551

---

[17] C. C. Harb, T. K. Boyson, A. G. Kallapur, I. R. Petersen, M. E. Calzada, T. G. Spence, K. P. Kirkbride, and D. S. Moore, *Optics Express*, 2012, **20**, 15489 - 15502, DOI: 10.1364/OE.20.015489

[18] J. D. Smith, D. B. Atkinson, *Analyst*, 2001, **126**, 1216 - 1220

[19] T. Baynard , E. R. Lovejoy , A. Pettersson , S. S. Brown , D. Lack , H. Osthoff , P. Massoli , S. Ciciora , W. P. Dube & A. R. Ravishankara, *Aerosol Science and Technology*, 2007, **41**, 447 - 462, DOI: 10.1080/02786820701222801

[20] J. Pearson, A. J. Orr-Ewing, M. N. R. Ashfold, and R. N. Dixon, The Journal of Chemical Physics, 1997, **106**, 5850, DOI: 10.1063/1.473252

[21] G. Berden, R. Engeln, P. C.M. Christianen, J. C. Maan, and G. Meijer, *Phys. Rev. A,* 1998, **58,** 3114

[22] Y. Le Grand, and A. Le Floch, *Appl. Optics*, 1990, **29**, 1244

[23] TROLAS group at IUP, University of Bremen, http://www.iup.uni-bremen.de/troposphere/images/image001crds.jpg (accessed on 05/04/11)

[24] D. Romanini, A. A. Kachanov, N, Sadeghi and F. Stoeckel, *Chem. Phys. Lett*., 1997, **264**, 316

[25] Y. He, M. Hippler and M. Quack, *Chemical Physics Letters*, 1998, **289**, 527 - 534

[26] D. J. Hamilton, M. G. D. Nix, S. G. Baran, G. Hancock, A. J. Orr-Ewing, Optical feedback cavity-enhanced absorption spectroscopy (OF-CEAS) in a ring cavity, *Applied Physics B*, 2010, **100**, 233 - 242

[27] J. W. Hahn, Y. S. Yoo, J. Y. Lee, J. W. Kim, and H.-W. Lee, *Appl. Optics*, 1999, **38**, 1859 -1866 ,DOI:10.1364/AO.38.001859

[28] M.S.I. Aziz, A. J.Orr-Ewing, J. Environ. Monit., 2012, **14**, 3094 - 3100, DOI:10.1039/C2EM30801K

[29] R. Wada and A. J. Orr-Ewing, *Analyst*, 2005, **130**, 1595 - 1600, http://dx.doi.org/10.1039/b511115c

[30] M. Pradhan, M. S. I. Aziz, R. Grilli and A. J. Orr-Ewing, *Environmental Science and Technology*, 2008, **42**, 7354 – 7359

---

[31] D. Mellon, S. J. King, J. Kim, J. P. Reid, and A. J. Orr-Ewing, *J. Phys. Chem. A*, 2011, **115,** 774 – 783, dx.doi.org/10.1021/jp109894x

[32] M. I. Cotterell, B. J. Mason, T. C. Preston, A. J. Orr-Ewing and J. P. Reid, *Phys. Chem. Chem. Phys.*, 2015, **17**, 15843

[33] S. Cheskis, I. Derzy, V.A. Lozovsky, A. Kachanov, D. Romanini, *Appl. Phys. B*, 1998, **66,** 377 – 381

[34] M. Mazurenka, A. J. Orr-Ewing, R. Peverall and G. A. D. Ritchie, *Annu. Rep. Prog. Chem., Sect. C*, 2005, **101**, 100 – 142, DOI: 10.1039/b408909j

[35] R. Lang, K. Kobayashi, *J. Quantum Electron.*, 1980, QE-16, 347- 355.

[36] A. E. Siegman, *Lasers*, University Science Books, 1986, 744 - 756.

[37] M. Hippler, C. Mohr, K. A. Keen and E. D. McNaghten, *J. Chem. Phys.*, 2010, **133**, 044308.

[38] "Exploring Different Configurations of Cavity Ringdown Spectroscopy at Highest Sensitivity", Johnny Chu, MChem thesis 2011, Dept of Chemistry, University of Sheffield.

[39] B. Dahmani, L. Hollberg, R. Drullinger, *Opt. Lett.*, 1987, **12**, 876.

[40] J. Morville, D. Romanini, A.A. Kachanov, M. Chenevier, *Appl. Phys. B*, 2004, **78,** 465 – 476

[41] D.J. Hamilton, A.J. Orr-Ewing, *Applied Physics B: Lasers and Optics*. **102**, 879 - 890

[42] A. G. Bell, *American J. of Science*, 1880, **20**, 305 - 324

[43] A. G. Bell, *Manufacturer and Builder*, 1881, **13**, 156 - 158.

[44] J.Tyndall, *Proc. R. Soc.*, 1881, **31**, 307 - 317

[45] W.C. Rontgen, *Ann. der Phys. und Chem.*, 1881, **1**, 155 - 159

[46] W. H. Preece, *Proc. R. Soc.*, 1881, **31**, 506 - 520

[47] P. Patimisco, G. Scamarcio, F. K. Tittel, V. Spagnolo, Sensors, 2014, **14**, 6165 - 6206, DOI:10.3390/s140406165

[48] E.L. Kerr and J.Atwood, *Appl. Opt.*, 1968, **7**, 915 - 921

---

[49] C.F. Dewey Jr., R.D. Kamm and C.E. Hackett, *Appl. Phys. Lett.*, 1973, **23**, 633 - 635

[50] J. Kauppinen, K. Wilcken, I. Lauppinen, V. Koskinen, Microchemical Journal, 2004, 76, 151 - 159.

[51] P. Pellegrino, R. G. Polcawich, Evolution of a MEMS Photoacoustic Chemical Sensor, US Army Research Report 2003, www.dtic.mil/cgi-bin/GetTRDoc?AD+ADA483776

[52] A. A. Kosterev, Yu. A. Bakhirkin, R. F. Curl, F. K. Tittel, *Optics Letters*, 2002, **27**, 1902 - 1904.

[53] Sir C. V. Raman, *Ind. J. Phys.*, 1928, **2**, 387.

[54] A. Smekal, *Die Naturwissenschaften*, 1923, **11**, 873 – 875.

[55] http://chemwiki.ucdavis.edu/Physical_Chemistry/Spectroscopy/Vibrational_Spectroscopy/Infrared_Spectroscopy/How_an_FTIR_Spectrometer_Operates, accessed on 16/05/2015

[56] J. Faist, F. Capasso, D.L. Sivco, C. Sirtori, A.L. Hutchinson, and A.Y. Cho, *Science*, 1994, **264**, 553 - 556.

[57] R. N. Hall, G. E. Fenner, J. D. Kinhsley, F. H. Dills, G. Lasher, *Phys. Rev. Lett.*, 1962, **9**, 366.

[58] Y. Arita, P. Ewart, *Optics Communication*, 2008, **281**, 2561 – 2566.

[59] Q. Gao, Y. Zhang, J. Yua, S. Wub, Z. Zhang, F. Zheng, X. Lou, W. Guo, *Sensors and Actuators A: Physical*, 2013, **199**, 106 – 110.

[60] A. Thompson, H. Northern, B. Williams, M. Hamilton, P. Ewart, *SENSORS AND ACTUATORS B-CHEMICAL*, 2014, **198**, 309 - 315.

[61] J. Manne , W. Jäger, J. Tulip, *Appl. Phys. B*, 2009, **94**, 337.

[62] P. J. S. Heim, Z. F. Fan, S. H. Cho, K. Nam, M. Dagenais, F. G. Johnson and R. Leavitt, *Electron. Lett.*, 1997, **33**, 1387.

[63] K. Liu and M. G. Littman, *Opt. Lett.*, 1981, **6**, 117.

[64] C. J. Hawthorn, K. P. Weber and R. E. Scholten, *Rev. Sci. Instrum.*, 2001, **72**, 4477.

[65] M. G. Littman and H. J. Metcalf , *App. Opt.*, 1978, **17**, 2224.

---

[66] Thorlabs Tunable Laser Kit User Guide, https://www.thorlabs.com/thorcat/21000/TLK-L1550M-Manual.pdf, accessed on 06/07/2015

[67] G.A. West, J.J. Barrett, D.R. Siebert, and K.V. Reddy, *Rev. Sci. Instrum.*, 1983, **54**, 797 - 817.

[68] B. Lavorel, G. Millot, M. Rotger, G. Rouillé, H. Berger, and H.W. Schrötter, *J. Mol. Struct.*, 1992, **273**, 49 - 59.

[69] *High-resolution Raman Spectroscopy of Gases*, A. Weber, in: *Handbook of High-Resolution Spectroscopy*, Ed. by M. Quack and F. Merkt (John Wiley, Chichester 2011), 1153 - 1236.

[70] C.L. Spencer, V. Watson, and M. Hippler, *Analyst*, 2012, **137,** 1384 - 1388.

[71] M. Hercher, W. Mueller, S. Klainer, R.F. Adamowicz, R.E. Meyers, and S.E. Schwartz, *Appl. Spectrosc.*,1978, **32**, 298 - 302.

[72] W.-U.L. Brillet and A. Gallagher, *Phys. Rev. A*, 1980, **22**, 1012 - 1017.

[73] E. Riedle and H.J. Neusser, *J. Chem. Phys.*, 1984, **80**, 4686 - 4693.

[74] G.J. Dixon, C.E. Tanner, and C.E.Wieman, *Optics Lett.*, 1989, **14**, 731 - 733.

[75] M. De Labachelerie, K. Nakagawa, and M. Ohtsu, *Opt. Lett.*, 1994, **19**, 840 - 842.

[76] J. A. Barnes, T. E. Gough, and M. Stoer, *Rev. Sci. Instrum.*, 1999, **70**, 3515 - 3518.

[77] M. Hippler, C. Mohr, K. Keen, and E. McNaghten, *J. Chem. Phys.*, 2010, **133**, 1 - 8.

[78] D.A. King, W.F. Carlsen, D.F. Gray, and R.J. Pittaro, US patent 5,432,610 (1995)

[79] D.A. King and R.J. Pittaro, *Opt. Lett.*, 1998, **23**, 774.

[80] D.J. Taylor, M. Glugla, and R.-D. Penzhorn, *Rev. Scient. Instrum.*, 2001, **72**, 1970.

[81] S. Ohara, S. Yamaguchi, M. Endo, K. Nanri, and T. Fujioka, *Opt. Rev.*, 2003, **10**, 342.

[82] X. Li, Y. Xia, L. Zhan, and J. Huang, *Opt. Lett.*, 2008, **33**, 2143.

[83] S. K. Sengupta, J. M. Farnham, and J. E. Whitten, *J. Chem. Educ.*, 2005, **82**, 1399.

---

[84] S. G. Baran, G. Hancock, R. Peverall, G.A.D. Ritchie, and N.J. van Leeuwen, *Analyst*, 2009, **134**, 243.

[85] I. Dabrowski, *Can. J. Phys.*, 1984, **62**, 1639.

[86] D. Papoušek and M.R. Aliev, *Molecular Vibrational-Rotational Spectra*, Elsevier, Amsterdam 1982.

[87] M. Quack, *Annu. Rev. Phys. Chem.*, 1990, **41**, 839 - 874.

[88] J.-P. Champion, M. Loëte, and G. Pierre, *Spectroscopy of the Earth's Atmosphere and Interstellar Medium*, K.N. Rao and A. Weber (Eds.), (Academic Press, Boston 1992) 339 - 442

[89] M. Hippler and M. Quack, *J. Chem. Phys.*, 2002, **116**, 6045.

[90] C. Manca Tanner and M. Quack, *Mol. Phys.*, 2012, **110**, 2111 - 2135, DOI:10.1080/00268976.2012.702934

[91] Ch. Wenger and J.-P. Champion, *J. Quant. Spectrosc. Radiat. Transfer*, 1998, **59**, 471.

[92] http://icb.u-bourgogne.fr/OMR/SMA/SHTDS/STDS.html (accessed March 2012).

[93] W.K. Bischel and G. Black, *AIP Conf. Proc.,1983,* **100**, 181 - 187, DOI:http://dx.doi.org/10.1063/1.34046

[94] M.W. Todd, R.A. Provencal, T.G. Owano, B.A. Paldus, A. Kachanov, K.L. Vodopyanov, M. Hunter, S.L. Coy, J.I. Steinfeld, and J.T. Arnold, *Appl. Phys. B*, 2002, **75,** 367 - 376.

[95] Y. He, M. Hippler, and M. Quack, *Chem.Phys.Lett.*, 1998, **289,** 527.

[96] M. Hippler, L. Oeltjen, and M. Quack, *J. Phys. Chem. A*,2007, **111**, 12659.

[97] S.S. Brown, *Chem. Rev.*, 2003, **103**, 5219 – 5238.

[98] D. Romanini, M. Chenevier, S. Kassi, M. Schmidt, C. Valant, M. Ramonet, J. Lopez, and H.-J. Jost, *Appl. Phys. B,* 2006, **83,** 659 - 667.

[99] S.G.Baran, G. Hancock, R. Peverall, G.A.D. Ritchie, and N.J. van Leeuwen, *Analyst, 2009,* **134**, 243.

---

[100] M.W. Sigrist, *Air Monitoring by Laser Photoacoustic Spectroscopy*, chapter 4 in M.W. Sigrist (Ed.), *Air Monitoring by Spectroscopic Techniques*, Chemical Analysis Series 127, (Wiley, New York 1994).

[101] P. Hess A. Miklós, and Z. Bozóki, *Rev. Sci. Instrum.,2001,* **72**, 1937.

[102] D.Z. Anderson, J.C. Frisch, and C.S. Masser, *Appl. Opt.,1984,* **23**, 1238.

[103] A. J. L. Shillings, S. M. Ball, M. J. Barber, J. Tennyson and R. L. Jones, *Atmos. Chem. Phys., 2011,* **11,** 4273 – 4287.

[104] Rothman, L.S. and Gordon, I.E. and Babikov, Y. and Barbe, A. and Benner, D. Chris and Bernath, P.F. and Birk, Manfred and Bizzocchi, L. and Boudon, V. and Brown, L.R. and Campargue, A. and Chance, Kelly and Coudert, L. H. and Devi, V. Malathy and Drouin, B.J. and Fayt, A. and Flaud, J.-M. and Gamache, R.R. and Harrison, J. and Hartmann, J.-M. and Hill, C. and Hodges, J.T. and Jacquemart, D. and Jolly, A. and Lamouroux, J. and LeRoy, R.J. and Li, G. and Long, D. and Mackie, C.J. and Massie, S.T. and Mikhailenko, S. and Müller, H.S.P. and Naumenko, O.V. and Nikitin, A.V. and Orphal, J. and Perevalov, V.I. and Perrin, A. and Polovtseva, E.R. and Richard, C. and Smith, M.A.H. and Starikova, E. and Sung, K. and Tashkun, S.A. and Tennyson, J. and Toon, G.C. and Tyuterev, Vl. G. and Wagner, G. (2013) *The HITRAN 2012 Molecular Spectroscopic Database.* Journal of Quantitative Spectroscopy and Radiative Transfer, **130**, 4 - 50

[105] S. W. Sharpe, T. J. Johnson, R. L. Sams, P. M. Chu, G. C. Rhoderick, and P. A. Johnson, *Applied Spectroscopy,* 2004, **58**, 1452 - 1461

[106] A. Kachanov, S. Koulikov, F. K. Tittel, *Appl. Phys. B,* 2013, **110**, 47 - 56

[107] J. I. Steinfeld and J. Wormhoudt, *Annu. Rev. Phys. Chem.*, 1998, **49**, 203 - 232.

[108] Containing the Threat from Illegal Bombings: An Integrated National Strategy for Marking, Tagging, Rendering Inert, and Licensing Explosives and Their Precursors", National Academy Press Washington, D.C., 1998.

[109] Y. Sun, Field Detection Technologies for Explosives, ILM Publications, 2010, ch. 6, pp. 69 - 90, ISBN-13 978-1906799021

[110] C. Patel, 2011, *Tunable quantum cascade lasers and photoacoustic detection of trace gases, TNT, TATP and precursors acetone and hydrogen peroxide,* US Patent 7903704 B2

---

[111] M.W. Todd, R.A. Provencal, T.G. Owano, B.A. Paldus, A. Kachanov, K.L. Vodopyanov, M. Hunter, S.L. Coy, J.I. Steinfeld, and J.T. Arnold, *Appl. Phys. B*, 2002, **75,** 367 - 376.

[112] P.A. Pella, *Anal. Chem.*, 1976, **48**, 1632 - 1637.

[113] M.B. Pushkarsky, I.G. Dunayevskiy, M. Prasanna, A.G. Tsekoun, R. Go, and C.K.N. Patel, *PNAS*, 2006, **103**, 19630 – 19634.

[114] J. Zhao, T. Luo, X. Zhang, Y. Lei, K. Gong, and Y. Yan, *Anal. Chem.*, 2012, **84**, 6303 - 6307, DOI: 10.1021/ac301359j

[115] J. M. Johnston, 1999, CANINE DETECTION CAPABILITIES: OPERATIONAL IMPLICATIONS OF RECENT R & D FINDINGS, available from http://barksar.org/K-9_Detection_Capabilities.pdf

[116] Summary of the Final Report of the International Task Force 25 Hazard from Industrial Chemicals, 15 April 1999.

[117] NIOSH, NIOSH respirator selection logic. Cincinnati, OH: U.S. Department of Health and Human Services, Public Health Service, Centers for Disease Control, National Institute for Occupational Safety and Health, DHHS (NIOSH). Publication No. 2005-100.

[118] J.P. Besson , S. Schilt, L. Thévenaz, *Spectrochimica Acta Part A*, 2006, **63**, 899 – 904.

[119] R.E. Lindley, A.M.Parkes, K.Keen, E.D. McNaghten, & A.J. Orr-Ewing, *Applied Physics B*, 2007, **86,** 707 - 713, DOI:10.1007/s00340-006-2543-0

[120] P. D. Goldan and K. Goto, *Journal of Applied Physics*, 1974, **45**, 4350, DOI: 10.1063/1.1663056

[121] Ch. Hornberger, M. König, S.B. Rai, W. Demtröder, *Chemical Physics*, 1995, **190**, 171-177.

[122] Specification reflectivity of E04 Coating, available from: <http://www.thorlabs.de/images/TabImages/E04ReflectionData.xlsx/>, accessed on 26/02/2015.

[123] M. Hippler, M. Stringer, J. Chu, H. McIntyre, S. Taylor, “Ultrasensitive explosives vapour detection by cavity-enhanced resonant photoacoustic spectroscopy using a quantum cascade laser (QCL-CERPAS)”, in preparation.

---

[124] A. M. Smith, *Electronics Letters*, 1980, **16**, 773 - 774.

[125] J. Sakai and T. Kimura, "Birefringence and Polarization Characteristics of Single-Mode Optical Fibers under Elastic Deformations", *IEEE Journal of Quantum Electronics*, 1981, **QE-17**, 1041-1051.

[126] R. Ulrich and A. Simon, *Applied Optics*, 1979, **18**, 13, 2241 - 2251.

[127] A. Smith, *Applied Optics*, 1980, **19**, 2060 - 2611.

[128] M. Monerie and L. Jeunhomme, *Optical and Quantum Electronics*, 1980, **12**, 449 - 461.

[129] F. B. Gorte, Acoustic design and scaling aspects of a photoacoustic sensor system for combustible gases, April 2013, Delft University of Technology

[130] L. Lechuga-Fossat, J. M. Flaud, C. Camy-Peyret, P. Arcas, M. Cuisenier, *Molecular Physics*, 1987, **61**, 23 - 32.

[131] A. M. Cubillasm, J. M. Lazaro, O. M.Conde, M. N. Petrovich, J. M. Lopez-Higuera, *Sensors*, 2009, **9**, 6261 - 6272.

[132] Centers for Disease Control and Prevention. Current Cigarette Smoking Among Adults—United States, 2005 – 2013. Morbidity and Mortality Weekly Report 2014, **63**, 1108–1112 [accessed 2015 June 30].

[133] Knowles EK-23014 specification sheet, available from <http://www.knowles.com/eng/content/download/4510/61986/version/4/file/EK-23024-000.pdf/>, accessed on 01/03/15.

[134] http://www.guinnessworldrecords.com/world-records/loudest-clap/ - accessed on 01/03/2015.

[135] M. Nilsson, Josef Ström Bartunek, Jörgen Nordberg, and Ingvar Claesson., Proceedings of the 2008 Congress on Image and Signal Processing, 5, (2008), IEEE Computer Society.:<http://www.bth.se/fou/forskinfo.nsf/0/67a079f0676c546fc12574a4002d6d38 /$file/nilsson-whistle.pdf/>

[136] G. Lopes, F. Ribeiro, P. Carvalho, " Whistle Sound Recognition in a Noisy Environment," *Proceedings of Controlo'2010 - 9th Portuguese Conference on Automatic Control*, Coimbra, Portugal (September 2010) 172–179, available from: <https://repositorium.sdum.uminho.pt/bitstream/1822/16155/1/CN07.pdf/>

---

[137] P. L. Meyer and M. W. Sigrist, *Rev. of Sci. Inst.*, 1990, **61**, 1779.

[138] Corning SMF-28 Optical Fibre Product Information, available at:<http://www.focenter.com/Fiber %20Optic %20Center %5Ccorning %5Cdatasheets %5Csmf-28.pdf/>

[139] Smith S. W., 1997,The Scientist and Engineer's Guide to Digital Signal Processing, California Technical Pub

[140] M. Hippler, *Anal. Chem*., 2015, **87**, 7803 – 7809.

[141] A. Elia, C. Di Franco, P. M. Lugarà, G. Scamarcio, *Sensors (Basel).* 2006, **6**, 1411 – 1419.